The role of the actin-binding proteins cofilin1 and INF2 on mitochondrial dynamics and cellular resilience

Dissertation

zur

Erlangung des Doktorgrades

der Naturwissenschaften

(Dr. rer. nat.)

dem

Fachbereich Pharmazie der

Philipps-Universität Marburg

vorgelegt von

Lena Hoffmann

aus Siegen

Marburg/Lahn **2020**

Erstgutachter: Prof. Dr. Carsten Culmsee

Zweitgutachter: Prof. Dr. Marco B. Rust

Eingereicht am 08.01.2020

Tag der mündlichen Prüfung am 19.02.2020

Hochschulkennziffer: 1180

Eidesstattliche Erklärung

Ich versichere, dass ich meine Dissertation

"The role of the actin-binding proteins cofilin1 and INF2 on mitochondrial dynamics and cellular resilience"

selbständig ohne unerlaubte Hilfe angefertigt und mich dabei keiner anderen als der von mir ausdrücklich bezeichneten Quellen bedient habe. Alle vollständig oder sinngemäß übernommenen Zitate sind als solche gekennzeichnet.

Die Dissertation wurde in der jetzigen oder einer ähnlichen Form noch bei keiner anderen Hochschule eingereicht und hat noch keinen sonstigen Prüfungszwecken gedient.

Marburg, den 08.01.2020

.....

(Lena Hoffmann)

Teilergebnisse der vorliegenden Arbeit wurden in folgenden Aufsätzen vorab publiziert:

(1) Actin(g) on mitochondria – a role for cofilin1 in neuronal cell death pathways / 18.01.2019 zur Veröffentlichung eingereicht bei Biological Chemistry / 16.04.2019 zur Veröffentlichung angenommen bei Biological Chemistry [76].

(2) Cofilin1-dependent actin dynamics control DRP1-mediated mitochondrial fission / 21.11.2016 zur Veröffentlichung eingereicht bei Cell Death and Disease / 27.07.2017 zur Veröffentlichung angenommen bei Cell Death and Disease [140].

Table of contents

1 Introduction

1.1 Actin dynamics

Actin dynamics, i.e. the assembly and disassembly of filamentous actin (F-actin) are essential for a plethora of fundamental cellular processes, including cell shaping and motility, cell division, contraction, organelle morphology and transport [117, 172]. Moreover, actin dynamics is crucial for neuron-specific functions such as neurite formation, differentiation, synaptogenesis and synaptic plasticity [35, 38, 145].

1.2 The family of actin-binding proteins

1.2.1 Cofilin1

In mammals, the ADF/cofilin family comprises three members: actin-depolymerizing factor (ADF, aka destrin), mainly expressed in neurons and epithelial cells, the ubiquitously expressed cofilin1 (non-muscle (n)-cofilin), which represents over 90 % of all ADF/cofilin proteins in the brain [116], and cofilin2 (muscle (m)-cofilin), which is abundant in striated muscles [164], but also present in other tissues including the brain [67].

The physiological function of ADF/cofilin in actin dynamics depends on local protein concentrations [74]. At a sub-stoichiometric ADF/cofilin-actin ratio, ADF/cofilin weakens the interaction of actin subunits, thereby promoting actin depolymerization by severing F-actin and accelerating the dissociation rate of actin subunits [175]. Conversely, saturating ADF/cofilin concentrations do not induce F-actin disassembly, but instead can nucleate actin assembly [2]. Moreover, ADF/cofilin binds to globular actin monomers (G-actin) thereby inhibiting its incorporation into F-actin [22, 108].

Interaction of ADF/cofilin with actin is controlled by post-translational modifications via phosphorylation of a conserved serine residue present in both cofilin1 isoforms 1 and 2 at position 3 (Ser3) [13]. Cofilin1 is unable to bind actin after phosphorylation at Ser3 by LIM domain kinase 1 and 2 (LIMK1, 2), and Testis-specific kinases 1 and 2 (TESK1, 2) [4, 185]. Upstream effectors of LIMK include Rho GTPases, Rac, Cdc42 and the kinases Pak1 or ROCK, which can activate LIMK by phosphorylation [27]. In contrast, activation of cofilin1 depends on Ser3 dephosphorylation by the protein phosphatases slingshot and chronophin

[60, 129]. The dephosphorylated form of cofilin1 was further found to form rod-like structures due to its high binding capacity for F-actin [33, 79, 122].

More recently, cofilin1 emerged as an important player in cell death signaling in both neuronal and non-neuronal cells, based on by findings that cofilin1 translocation to mitochondria was crucial for the progression of apoptosis [33]. Similarly, cofilin1 translocated to mitochondria upon apoptosis induction in mouse embryonic fibroblasts (MEFs), although cofilin1 knockout did not affect apoptosis signaling in these cells [139]. In MEFs, cofilin1 inactivation caused pronounced effects on mitochondrial dynamics, i.e. enhanced mitochondrial fission [140]. Therefore, the role of cofilin1 in the regulation of mitochondrial dynamics and integrity in regulated cell death may vary between cell types and tissues.

Cofilin1 is the most abundant member of the ADF/cofilin family in the central nervous system (CNS) [12]. Therefore, many studies have been conducted to understand the versatile role of cofilin1 on neuronal plasticity and behavioral aspects *in vivo* [144]. In the brain, cofilin1 serves as a main regulator of brain development and neuronal differentiation [12, 51], spine morphology [78], synaptic plasticity [66, 145], neurotransmitter release [176] and behavior [62, 157, 176]. Thus, its physiological role is indispensable. Moreover, many neurodegenerative diseases, such as Alzheimer's disease (AD) [116], Parkinson's disease (PD) [133] or Huntington's disease (HD) [123] are known to involve detrimental formation of cofilin1- and actin-rich aggregates, named cofilin-actin rods. Further, recent studies suggested an important role for cofilin-actin rods for infarct development in rodent models of ischemic stroke [151, 177]. This observation supports the view that neuronal death after acute brain damage and in neurodegenerative disorders share pathological features involving alterations in cofilin-dependent actin regulation. However, cofilin-actin rod formation is not detrimental per se, as it can also prevent mitochondrial membrane permeabilization and ATP loss in stressed neurons [14, 125].

The regulation of detrimental cofilin1 activity is not well understood. However, oxidative regulation was recently introduced as a potential mechanism for its activation under stress conditions. Human cofilin1 possesses four cysteine residues at positions 39, 80, 139 and 147, all thought to be prone for oxidation thereby activating cofilin1 [57]. For example, taurine chloramine derived from neutrophils mediated cofilin1 oxidation thereby transducing apoptotic signaling in lymphoma cells [88]. Moreover, oxidation of a specific methionine

residue (Met115) of cofilin1 prevents phosphorylation at Ser3, mediating a loss of its actin binding property and concomitantly attaining activity to translocate and bind to mitochondria, where cofilin1 induces release of cytochrome c and swelling of the organelle [107]. This effect was shown to be independent of the pro-apoptotic Bcl-2 protein Bax and can be induced by application of recombinant cofilin1 protein on isolated mitochondria, underlining that cofilin1 indeed exerts direct effects on mitochondria [23, 88, 107].

1.2.2 Inverted-formin 2 (INF2)

Mammals possess a huge variety of formin proteins, that are indispensable for actin regulation and therefore responsible for organization of different actin-based structures, including contractile rings for cytokinesis [110], force generating stress fibers [161] or filopodia, taking over a guidance role for cell migration [128]. Formins are characterized by a dimeric actin-binding structure, called formin homology 2 (FH2) domain capable of binding actin filaments at their barbed end and thereby accelerating their nucleation and elongation [73]. Inverted-formin 2 belongs to the formin family and resembles other formins in their unique FH2 domain. Notably, besides the ability to elongate actin filaments, INF2 has also properties to depolymerize actin achieved by its C-terminal actin-binding WASP homology 2 motif (WH2) [29]. The various functions of INF2 are also linked to the respective isoform. INF2 exists in two splice variants the prenylated ER-bound-CAAX- and the cytosolic non-CAAX variant [30, 90]. It is assumed, that both isoforms exert distinct functions on organelle dynamics. A knockdown model of the cytosolic non-CAAX isoform revealed a profound effect on Golgi structure [138], causing a scattered Golgi phenotype, whereas specific silencing of the CAAX-isoform results in substantial increase of mitochondrial length (2.5 times) [90].

Proper function of INF2 is physiologically relevant, as mutations in the actin-binding domains can lead to severe disease pattern, such as focal segmental glomerulosclerosis [21] or Charcot-Marie Tooth disease [20].

1.3 Regulation of mitochondrial dynamics

Mitochondrial dynamics covers the processes of mitochondrial fusion and fission in order to adapt mitochondrial function to cellular needs [54]. Mitochondrial fusion serves as a process to elongate existing mitochondria and enhances the network to ensure supply with metabolic substrates, proper distribution of mitochondrial DNA (mtDNA) and facilitate communication between mitochondria [26, 95]. The opposed fission process covers

mitochondrial separation which is necessary to ensure mitochondrial transport and distribution to locations of high energy demand [96]. A balance between fission and fusion is important for proper cellular energy production, distribution and maintenance of mtDNA, calcium homeostasis and thus for cellular survival, reviewed in [130].

Cells maintain a balance between fusion and fission balance through a multitude of mitochondrial shaping proteins. Fusion is mainly ensured by mitofusion 1 and 2 (Mfn1/2) by mediating outer mitochondrial membrane (OMM) merging, whereas inner mitochondrial membrane (IMM) fusion is achieved by optic-atrophy protein 1 (OPA1) and only the interplay of these different proteins succeeds in a fusion event [153]. The opposed process is driven by GTPase-driven dynamins, i. e. dynamin-related protein 1 (DRP1) and dynamin 2 (Dnm2) [3].

The role of actin on mitochondrial dynamics

The actin cytoskeleton is a dynamic structure that determines not only shape and morphology of a cell, but is also important for trafficking and regulation of vesicles and organelle transport [141]. In yeast, a mitochondrial membrane protein complex including maintenance of mitochondrial morphology protein 1 (Mmm1) and mitochondrial distribution and morphology proteins 10 and 12 (Mdm10, Mdm12) links the mitochondrial outer membrane to the actin cytoskeleton, which is relevant for organelle movement [16, 17]. In contrast, mitochondrial trafficking in mammals is mainly regulated by the microtubule-based motor proteins dynein and kinesin [18, 53]. Intriguingly, yeast and mammals seem to share common strategies in regulating mitochondrial dynamics, as actin stimulates constriction of the outer mitochondrial membrane in both cell types, thereby forcing a fission event together with the crucial fission factor DRP1 (in yeast Dnm1) [23, 71, 120]. In healthy cells, F-actin continuously binds to mitochondria, enhances mitochondrial fragmentation via DRP1 at mitochondrial-ER contact sites, and disassembles again to maintain steady-state dynamics of mitochondrial morphology [72, 120]. Further, it was demonstrated that F-actin plays an essential role in the recruitment of DRP1 to the outer mitochondrial membrane, leading to membrane constriction and division of the organelle [83]. F-actin polymerization induced by the inverted formin INF2 was further shown to act as a tethering structure between ER and mitochondria thereby serving as an important regulator in mitochondrial fission [90]. For this process, it is also essential that the actin-nucleating protein Spire1C binds INF2 and promotes actin assembly at the outer mitochondrial membrane. Disruption of

either Spire1C's actin- or formin-binding activities reduces mitochondrial constriction and division [111]. It was shown that application of the calcium ionophore ionomycin induced an F-actin burst, followed by enhanced mitochondrial fission. In this context, F-actin assembly preceded DRP1 oligomerization at the outer mitochondrial membrane and fission sides were enriched for F-actin as well as DRP1. Additionally, F-actin was able to directly bind DRP1 and enhance its GTPase activity, suggesting that F-actin can activate DRP1 to execute a fission event [24]. Further, mitochondrial calcium uptake plays a pivotal role for ionomycin-induced mitochondrial fission, since inhibiting mitochondrial calcium uptake by knockout of the mitochondrial calcium uniporter (MCU) significantly reduced mitochondrial fission [24]. Both, INF2 knockout and inhibition of actin polymerization by latrunculin A treatment abolished the ionomycin-induced mitochondrial calcium uptake [24], connecting local F-actin assembly to ionomycin-induced calcium burst. Impaired actin dynamics by cortactin or cofilin1 depletion can also enhance DRP1 accumulation at mitochondria [102, 140]. Further, maturation and activation of DRP1 oligomers at the mitochondrial surface induced by cofilin1 depletion increased mitochondrial fragmentation without deteriorating mitochondrial function in mouse embryonic fibroblasts (MEF) [140] (Figure 1).

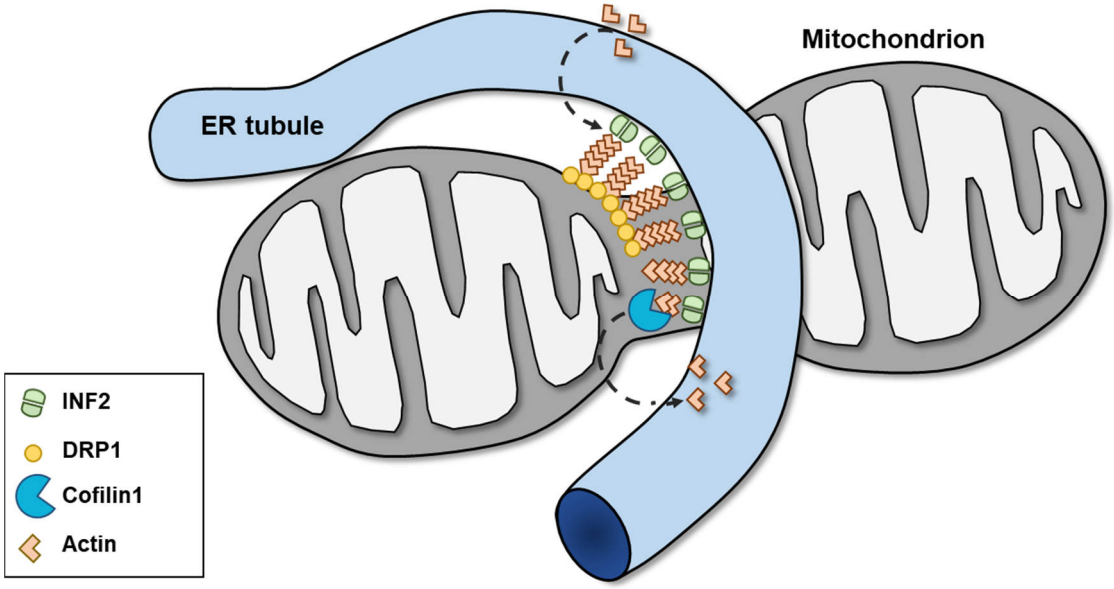

Figure 1. Model of actin-dependent control of mitochondrial dynamics via DRP1 and INF2 [140].

ER-bound INF2 triggers actin polymerization and thus facilitates recruitment of DRP1 to mitochondria. INF2 (inverted-formin 2); DRP1 (dynamin-related protein 1).

Previous studies in non-neuronal cells suggested that cofilin1 exerted direct effects on mitochondria, i.e. in tumor cells upon erucin-induced mitochondrial fission. This study revealed, that dephosphorylation at Ser3 led to mitochondrial transactivation of cofilin1 and

to an interplay with DRP1 enhancing fragmentation of the organelle [101]. Mitochondrial translocation of cofilin1 was also observed after apoptosis induction, as cofilin1 colocalization with mitochondria and subsequent induction of cytochrome c release was an early step in the cell death cascade [33, 139]. In yeast, actin binding-deficient cofilin1 mutants can enhance mitochondrial respiration, indicating that cofilin1 may also exert actin-independent effects on mitochondrial function [91]. In mammalian cells, specific amino acids at position 15-30 of the N-terminus and on position 106-166 of the C-terminus were critical for mitochondrial localization underlining that cofilin1 indeed has properties to bind directly to mitochondria [33].

The ambiguous properties of cofilin-actin rods in models of neuronal disorders

Control of actin dynamics by ADF/cofilin is crucial for actin's cellular functions. Cofilin1 exerts highest actin severing activity at a cofilin1-actin ratio around 1:800 [2]. Interestingly, several studies have shown that disrupting the balance between these proteins can lead to abnormal protein aggregation, termed cofilin-actin rods [6]. ATP depletion is a major trigger for cofilin-actin rod formation at a stoichiometry of 1:1 [115]. Cofilin1 self-assembles by intermolecular disulfide bonds to form dimers, trimers and oligomers. Finally, cofilin-actin rod formation impairs cofilin1 mediated F-actin severing and thereby actin turnover [134] (Figure 2). Effects of cofilin-actin rods at the cellular level is the result of an interplay between direct sterical impacts and indirect aspects following a decline in actin dynamics [34]. Major consequences of rod formation in neurons include abnormal distribution of cellular organelles, such as mitochondria or early endosomes, loss of pre- and postsynaptic compartments and, therefore, reduced synaptic transmission and impaired neuronal plasticity [34].

Some studies suggested protective properties for cofilin-actin rods under pathophysiological conditions. For example, in a model of heat shock stress, cofilin1 mutants unable to form rods could not rescue the cell stress phenotype, whereas one mutant (K22A) was still able to form rods and significantly protected cells from heat shock stress. These findings indicate that the rod forming ability may be beneficial under stress conditions [124]. Further, it was shown, that neurites with newly formed rods were transiently protected against loss of the mitochondrial membrane potential and decline of cellular ATP level upon cofilin-actin rod induction by overexpression of a Xenopus laevis ADF-cofilin1 chimera [14]. The authors suggested that sequestering ADF/cofilin1 and actin into rods would initially be beneficial for

the energy status of neurons and they attributed this to the reduced energy demand since normal actin dynamic processes may dissipate a critical amount of ATP. Through rod formation, actin dynamics are decreased and energy can be used for other processes enhancing the cellular resilience during stress exposure [14]. At later stages of the stress response, however, disrupted actin dynamics may counteract this positive energy-saving effect. This could also change ion transfer, i.e. decreased sodium/potassium (Na^+/K^+)-ATPase activity, and the resulting sodium accumulation in the cells could reduce the activity of sodium/calcium (Na^+/Ca^{2+}) exchanger. Elevated intracellular calcium levels are responsible especially for the detrimental effect on mitochondrial function [178].

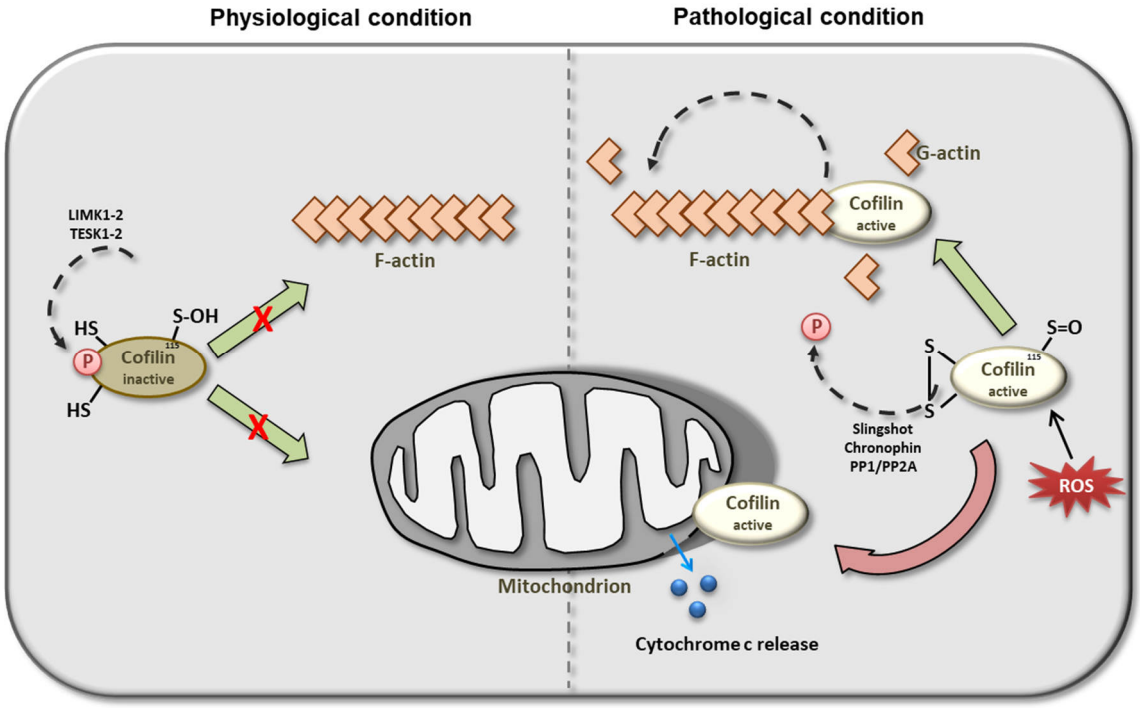

Figure 2. Cellular mechanism of cofilin1 activation under physiological and pathophysiological conditions [76].

Under physiological conditions, cofilin1 can be activated by slingshot, chronophin or protein phosphatases 1/2A by dephosphorylation of serine residue 3 in order to attain affinity to bind to F-actin for depolymerization of the filament. Under pathophysiological conditions, cofilin1 is oxidized and thus obtains activity to translocate to mitochondria and finally induce detrimental cytochrome c release and swelling of the organelle. Further, under these circumstances, cofilin1 is able to develop cofilin-actin rods, mainly observed in neurodegenerative diseases and stroke. ER (endoplasmic reticulum); F-Actin (filamentous actin); G-Actin (monomeric actin); PP1/PP2A (Protein phosphatase 1 and 2A); ROS (reactive oxygen species).

The role of cofilin1 in neurodegenerative disorders and as a putative point of action in therapeutic interventions

Neurodegenerative disorders such as AD and PD are emerging diseases in our ageing societies. In Europe, it is estimated that at least 35 % of the total disease burden is owing to

brain disorders [131]. Therefore, a better understanding of the underlying mechanisms of brain diseases is critical for future treatment strategies. Recently, cofilin1 emerged as a participant in cell death mechanisms involved in degradation of neurons. In this regard, the property of cofilin1 to form aggregates with actin seems to be important for according detrimental effects in neurons. For example, under stress conditions induced by glutamate exposure or the amyloid beta-protein, ATP levels declined and thereby induced activation of phosphatases mediating dephosphorylation, i.e. activation of cofilin1. Due to the concomitant loss of ATP in damaged neurons, ADP-actin accumulated and formed aggregates with dephosphorylated cofilin1 [7].

Until now, only symptomatic or palliative therapies available for any of the aforementioned diseases, such as AD or PD. Thus, it is necessary to develop novel and effective therapeutic intervention strategies.

Findings in a mouse model of long term depression (LTD) demonstrated that inhibition of cofilin1 stabilized dendritic spines and their functional activity. In these experiments, inhibition of cofilin was achieved in a dominant negative manner using a phosphorylated peptide containing the first 16 amino acids of cofilin1 ("p-Cofilin peptide") which inhibited cofilin1 activation through competitive binding to phosphatases [188]. The application of this phosphorylated peptide in a mouse model of AD rescued surface expression and function of AMPA and NMDA receptors. Functional cofilin1 inhibition by these peptides partially improved working memory and novel object recognition in the AD mouse model [43]. Moreover, the peptides also exerted beneficial effects in mouse models of autism [47] and neuropathic pain [136]. Besides this, there is also evidence, that overexpression of cofilin1 could rescue alpha-synuclein-driven deficits in neuronal growth and axon elongation in a PD mouse model, due to the restoration of appropriate actin turnover [159].

Whether inhibiting cofilin1-actin rod formation would also be beneficial in conditions of cellular stress leading to programmed cell death remains to be clarified. Some reports suggested that complete inhibition of rod formation could not rescue cells during heat shock stress in a mouse striatal cell line ($STHdh^{Q7/Q7}$). Notably, a cofilin1 (K22A) mutant which retained some ability for rod formation as well as an accelerated actin dynamizing activity was able to rescue the cells under stress conditions [124].

1.4 Neuronal cell death mechanisms

1.4.1 Oxidative stress-induced cell death mechanisms

Cell death induced by oxidative stress is widely considered a major factor contributing to neurodegenerative disorders, such as Alzheimer's (AD) or Parkinson's disease (PD) [69, 85]. It is widely accepted that different features of programmed cell death (PCD) occur in these pathologies leading to severe loss of neuronal function [165]. Major steps of the cell death cascade include detrimental accumulation of intracellular calcium and formation of reactive oxygen species [69, 112]. Different cell death paradigms converge at the level of mitochondria [113]. Mitochondria are dynamic organelles regulating the energy metabolism, calcium homeostasis and the cellular redox balance [10]. Thus, mitochondrial demise, including mitochondrial calcium overload, loss of the mitochondrial membrane potential, accumulation of reactive oxygen species and release of apoptosis inducing factor (AIF) are thought to be the point of no return upon cell death induction [36]. A broad understanding of the molecular mechanism involved in transducing detrimental cell death signals to mitochondria are of great importance for future clinical implications.

In this study, programmed cell death was achieved by glutamate or erastin treatment leading to cell death mechanisms called oxytosis or ferroptosis (Figure 3). Oxytosis is a well-established form of programmed cell death occurring during neuronal development, as immature neurons are especially prone to glutamate-induced toxicity [126], as well as under pathological conditions in neurodegenerative diseases [150]. Besides, ferroptosis was discovered more recently as an iron-dependent form of oxidative cell death which can be achieved by erastin treatment in neuronal HT22 cells [45, 127]. The glutamate- or erastin-induced inhibition of the cystine-glutamate (X_c^-)-antiporter leads to reduction of glutathione level by depletion of intracellular cysteine. This results in an impaired activity of the glutathione peroxidase-4 (GPX4) which implicates activation of 12/15-lipoxygenase (LOX) and accumulation of reactive oxygen species (ROS) [149, 160]. In turn, dynamin-related protein 1 (DRP1) and the pro-apoptotic protein BID attain activity to translocate to mitochondria to implicate mitochondrial ROS production and loss of the mitochondrial membrane potential by mitochondrial outer membrane permeabilization (MOMP) [64, 65, 127]. Finally, cytochrome c and apoptosis inducing factor (AIF) are released from mitochondria and translocate to the nucleus, where AIF is involved in degradation of deoxyribonucleic acid (DNA) [37, 149, 160].

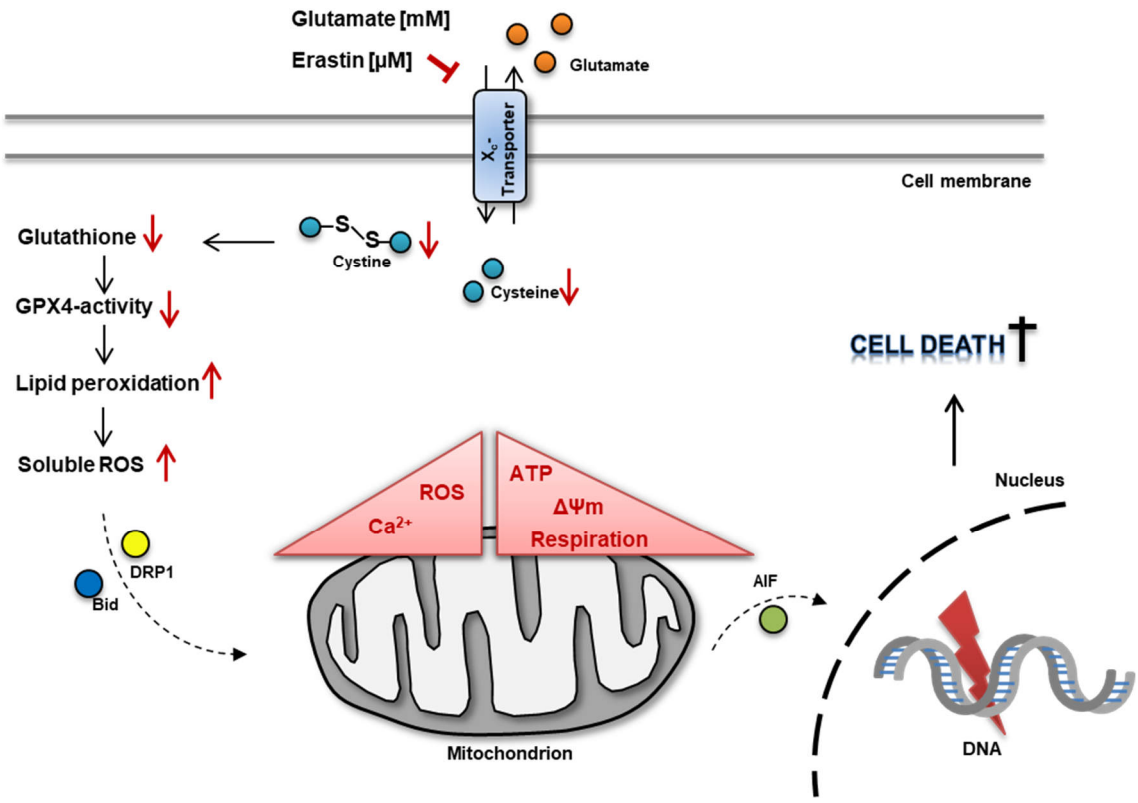

Figure 3. Model of oxidative stress-induced cell death in neuronal HT22 cells.

Main steps of the cell death cascade described in oxytosis and ferroptosis induced by glutamate or erastin are exemplified in this scheme. X_c^--transporter (glutamate/cystine antiporter); GPX4 (glutathione peroxidase 4); ROS (reactive oxygen species); DRP1 (dynamin-related protein 1); Bid (BH3-interacting domain death agonist); ATP (adenosine triphosphate); ΔΨm (mitochondrial membrane potential); AIF (apoptosis inducing factor); DNA (deoxyribonucleic acid).

Investigation of the signaling cascade of programmed cell death reveals the involvement of the actin-binding protein cofilin1 in transducing apoptotic signaling to mitochondria [33]. Cofilin1 belongs to the family of actin-binding proteins and is thus involved in regulating actin dynamics. It can also act as a direct participator in the apoptotic cell death cascade. How cofilin1 can also participate in non-apoptotic cell death paradigms remains to be elucidated. Therefore, the current study addresses the effect of cofilin1 depletion in non-apoptotic cell death induced by glutamate or erastin in neuronal HT22 cells and primary cortical neurons.

1.4.2 Excitotoxicity

Under different pathological conditions, such as neurodegenerative disorders like Alzheimer's disease [81], Parkinson's disease [11, 92], but also ischemia or brain trauma [32, 180], excessive release of the excitatory neurotransmitter glutamate from presynaptic vesicles is triggered, which leads to enhanced activation of postsynaptic glutamate receptors, such as AMPA-, NMDA or G-protein-coupled metabotropic glutamate receptors (mGlu)

[154]. Since 1969, this pathological process was specified by Olney and coworkers as excitotoxicity [132]. The activation of voltage-gated-calcium-channel (VDCC) and glutamate receptors results in detrimental influx of Ca^{2+} into the postsynaptic neuron and a second uncontrolled increase of Ca^{2+} by degradation of the major Na^{+}/Ca^{2+}-exchanger (NCX) via proteolytic cleavage by calpains [8]. Intracellularly, accumulated Ca^{2+} impacts many processes and effector proteins and, thus, needs to be tightly controlled for maintaining physiological functions. Moreover, overstimulation of AMPA-receptors and metabotropic glutamate receptors results in activation of ryanodine receptors (RyRs) and IP_3-receptors, located at the ER, and thereby leads to further Ca^{2+} release from intracellular stores, i e. endoplasmic reticulum (ER) [143, 152]. In particular, Ca^{2+}-binding to calmodulin enhances the activity of neuronal nitric oxide synthetase (nNOS) [158], which implicates production of nitric oxide (NO) and, in turn, generation of free radicals, such as peroxynitrite ($OONO^{-}$), considered as a major factor defining cell death progression and neuronal demise [182]. In turn, the major antioxidant proteins, namely glutathione peroxidase (GSH), catalase and superoxide dismutase (SOD), decreases, which results in defects of the electron transport chain (ETC), the induction of the mitochondrial permeability transition pore (mPTP) and release of apoptosis-inducing-factor (AIF) as well as detachment of cytochrome c (CytC) from the mitochondrion into the cytosol [61, 93, 183]. As a consequence, production of free radicals, such as peroxynitrite ($OONO^{-}$) and the release of AIF can both lead to DNA damage and execute cell death [146, 160] (Figure 4).

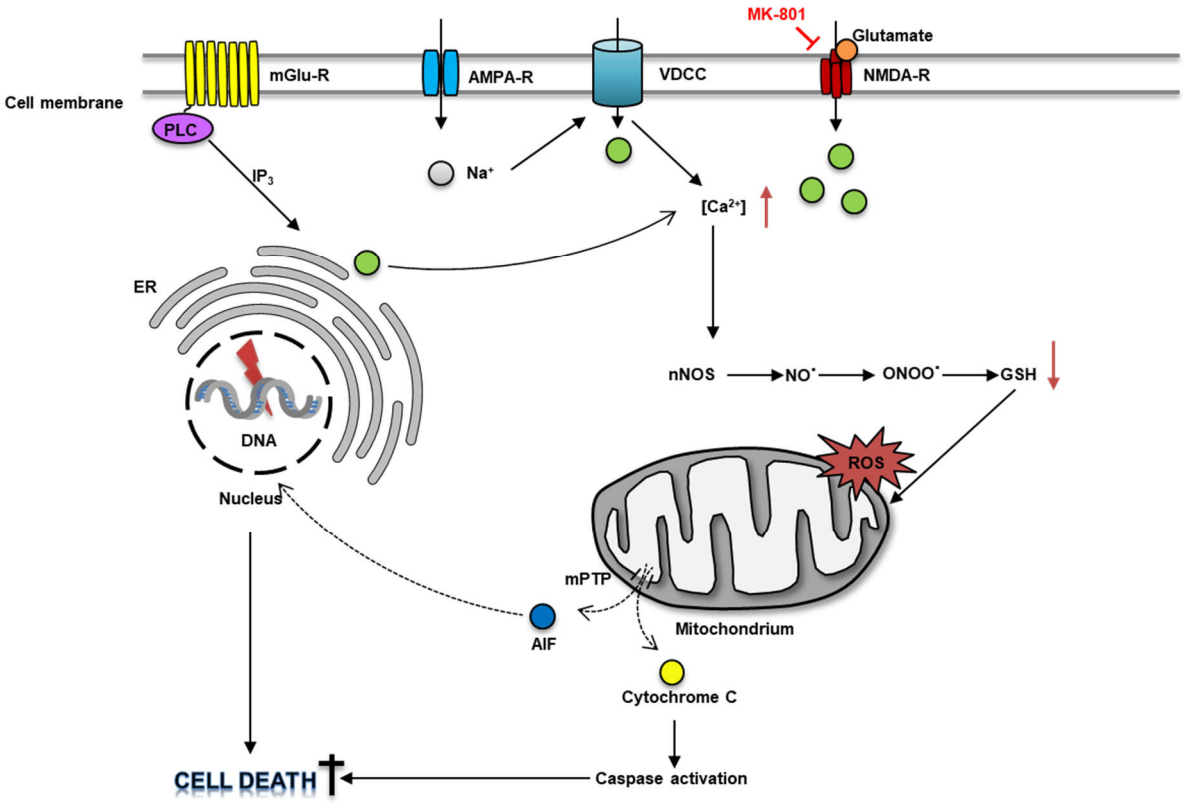

Figure 4. Cellular model of glutamate-induced neuronal excitotoxicity modified from [93].

Main steps of the cell death cascade upon excitotoxicity induction by glutamate are presented in this scheme. NMDA-R (N-methyl-D-aspartate receptor); VDCC (voltage-dependent calcium channels); AMPA-R (α-amino-3-hydroxy-5-methyl-4-isoxazolepropionic acid receptor); mGlu-R (metabotropic glutamate receptors); PLC (phospholipase C); IP_3 (inositol 1,4,5-trisphosphate); ER (endoplasmic reticulum); [Ca2+], (intracellular calcium concentration); ROS (reactive oxygen species); nNOS (neuronal nitric oxide synthase); NO (nitric oxide); $ONOO^-$ (peroxynitrite); GSH (glutathione); mPTP (mitochondrial permeability transition pore); AIF (apoptosis inducing factor); DNA (deoxyribonucleic acid).

2 Aims and objectives

Neurological diseases, such as stroke, AD or related dementias are among the four most prevalent disorders leading to death and disability worldwide [173]. The major common fatal incidences of those pathologies converge at the level of neuronal demise through oxidative stress [9].

To uncover key players of the cell death cascade induced by oxidative stress in order to decipher potential future strategies was the main goal of this study.

In particular, following objectives were addressed in the present work:

(1) To unravel the interdependence of mitochondrial dynamics and function in mouse embryonic fibroblasts (MEF cells), which were identified to exhibit DRP1-dependent mitochondrial fragmentation upon deletion of the actin-binding protein cofilin1.
(2) Evaluation of cofilin1 involvement in oxidative stress-induced cell death moieties in a hippocampal neuronal cell line (HT22) upon erastin or glutamate exposure leading to cellular damage via ferroptosis or oxytosis, respectively. Hence, this approach will provide new insight into cell death mechanisms involved in neurodegenerative diseases or ischemic stroke.
(3) Integration of the actin-regulatory protein INF2 into the described cellular pathophysiological mechanisms involved in oxytosis or ferroptosis in neuronal HT22 cells.
(4) *In vitro* characterization of cofilin1 in primary cortical neurons derived from genetically modified mice to unravel the role of cofilin1 in paradigms of glutamate-induced excitotoxicity. Hence, the perceptive comprehension about the involvement of cofilin1 would provide the basis of a discussion of cofilin1 as a potential target for cell death mechanisms contributing to pathologies leading to neurodegeneration.
(5) To decipher the ability of cofilin1 to directly influence mitochondrial integrity and function. Further, unraveling crucial cysteine residues responsible for cofilin1 activation and its detrimental impact on mitochondrial function would provide a comprehensive view on the redox regulation of cofilin1.

3 Materials and methods

3.1 Chemicals, reagents and kits

Standard chemical reagents

Standard chemical reagents were purchased from Merck KGaA (Darmstadt, Germany) if not indicated otherwise. Buffers and solutions were prepared with demineralized, ultrapure water obtained from SG Ultra Clear UV Plus Pure Water System (VWR, Darmstadt, Germany). Ultrapure water, PBS and cell culture equipment was sterilized using a steam autoclave (Systec V-40, Systec GmbH, Wettenberg, Germany). Solutions and buffers for aseptic preparations were filtered using Nalgene™ Rapid-Flow™ sterile filter (Thermo Fisher Scientific, Carlsbad, USA).

Table 1. Kits and Bioassays

Kit	Application	Company
Annexin-V-FITC Detection Kit	Cell death	Promokine, Heidelberg, Germany
Attractene Transfection Reagent	Plasmid transfection	Qiagen GmbH, Hilden, Germany
BODIPY (581/591 C11)	Lipid peroxidation	Invitrogen, Karlsruhe, Germany
CM-H_2DCFDA	Soluble ROS	Invitrogen, Karlsruhe, Germany
InviTrap® Spin Universal DNA Mini Kit	RNA/DNA purification	Stratec Molecular GmbH, Berlin, Germany
Lipofectamine RNAiMax Transfection Reagent	siRNA transfection	Invitrogen, Karlsruhe, Germany
MitoPT™ TMRE Kit	Mitochondrial membrane potential	Immunochemistry technologies, Hamburg, Germany
MitoSOX™	Mitochondrial ROS	Invitrogen, Karlsruhe, Germany

Pierce™ BCA Kit	Protein determination	ThermoFisher Scientific, Carlsbad, USA
SuperScript III One Step RT-PCR System with Platinum® Taq	RNA amplification	Invitrogen, Karlsruhe, Germany
ViaLight™ ATP Plus-Kit	ATP measurement	Lonza, Basel, Schweiz
ZymoPURE II Plasmid Midiprep Kit	Plasmid purification	Zymo Research Europe GmbH, Freiburg, Germany
Rhod-2 AM, cell-permeant	Mitochondrial Ca^{2+}	Invitrogen, Karlsruhe, Germany
REDExtract-N-Amp Tissue PCR Kit	DNA amplification	Sigma, Taufkirchen, Germany

3.2 Cell culture

Table 2. Cell culture equipment

Type	Company
T75 flasks (75 cm^2)	Greiner, Frickenhausen, Germany
6-well plates (175 cm^2)	Greiner, Frickenhausen, Germany
24-well plates	Greiner, Frickenhausen, Germany
96-well plates	Greiner, Frickenhausen, Germany
96-well plates BCA	Greiner, Frickenhausen, Germany
96-well plates µClear®	Greiner, Frickenhausen, Germany
96-well plates xCELLigence E-plates	Roche, Applied Science, Penzberg, Germany
Seahorse XFe96 FluxPaks	Agilent, CA, USA
µ-Slide 8 well	Ibidi GmbH, Gräfelfing, Germany
3.5 cm dish	Sarstedt, Nümbrecht, Germany
10 cm dish	Sarstedt, Nümbrecht, Germany
15 mL tube	Greiner, Frickenhausen, Germany
50 mL tube	Greiner, Frickenhausen, Germany
0.2; 0.5; 1.5; 2.0 mL tubes	Sarstedt, Nümbrecht, Germany

0.22 µm Whatman Puradisc™ sterile filter	Whatman, Dassel, Germany
Cell scraper	Sarstedt, Nümbrecht, Germany
1 mL syringes	Braun, Melsungen, Germany
Cannulae	Braun, Melsungen, Germany
Pipette tips	Greiner, Frickenhausen, Germany

Table 3. Phosphate buffered saline (PBS), pH 7.4

Substance	**Quantity**
NaCl	9 g
Na_2HPO_4	0.527 g
KH_2PO_4	0.144 g
HCl (0.1M)	q.s. for pH 7.4
Bidest H_2O	Ad 1 L

3.2.1 HT22 and MEF cells

Cell culture

HT4 cells originate from immortalized primary mouse hippocampal neurons by application of SV40 T-antigen [121]. Subsequently, HT22 cells were subcloned from HT4 cells due to their sensitivity to glutamate [41].

MEF cells deficient for cofilin1 were generated by Katharina Rehklau [139] and provided by Prof. Dr. Marco Rust (Philipps University of Marburg, Marburg, Germany). In brief, cofilin1$^{-/-}$ MEF cells derive from conditional cofilin1$^{flx/flx}$ mice, respectively [12]. Cofilin1 depletion in cofilin1$^{flx/flx}$ MEFs was achieved upon stable transfection of Cre recombinase inducible by 4-hydroxytamoxifen (TamOH) [139]. Cofilin1 protein expression was obviously diminished after 48 hours of TamOH treatment (Figure 9) and the respective experiments were conducted after 72 hours.

HT22 cells and MEF cells were cultured at 37 °C and 5 % CO_2 in supplemented Dulbecco's modified Eagle's medium (DMEM High Glucose; Capricorn Scientific GmbH, Ebsdorfergrund, Germany) (Table 4) in a Heracell™ 150 CO_2-incubator (Thermo Fisher Scientific, Darmstadt, Germany).

Table 4. Culture medium for HT22 and MEF cells

Substance	Quantity
FBS (Biochrom, Berlin, Germany)	50 mL
HEPES-Buffer (1M)	10 mL
Penicillin (10 000 U/mL)/Streptomycin (10 mg/mL) (Capricorn, Ebsdorfergrund, Germany)	5 mL
L-Alanyl-L-glutamine (200 mM)	5 mL
DMEM High glucose	Ad 500 mL

Every three to four days, both cell lines were subcultured at a ratio of 1:5 or 1:10. To detach cells from the 75 cm²cell culture flask, cells were washed with prewarmed PBS and incubated with trypsin-EDTA for 3 - 5 minutes (Table 5). To stop the trypsin reaction, 10 mL of preheated culture medium was added and transferred to a 50 mL tube, spun down at 1,000 x g for 3 minutes and resuspended in fresh culture medium. Afterwards, cell number was determined using a counting chamber (Neubauer Zählkammer, Brand, Wertheim, Germany). Certain cell numbers were seeded in the appropriate culture dish depending on the respective experiment (Table 6).

Table 5. Trypsin-EDTA (1xTE)

Substance	Quantity
Trypsin (7 500 U/mg)	100 mg
Ethylenediamine-tetra-acetic acid (EDTA)	40 mg
PBS	Ad 200 mL

Table 6. Cell densities HT22 and MEF cells

Plate format	HT22	MEF cells
6-well plate	150 000 – 200 000	110 000 – 130 000
24-well plate	40 000 – 50 000	4 000 – 11 000
96-well plate	6 000 – 7 000	1 4000 – 2 000
μ-Slide 8 well	14 000 – 16 000	5 000 – 8 000

3.2.2 Primary mouse neurons

Primary cortical neurons were prepared from embryonic mouse brains (E18) in 1xHBSS (Table 7) as previously described [37]. Finally, dissociated neurons were seeded at the indicated density onto poly-L-lysin coated plates (Table 9). Neuronal cultures were grown in supplemented Neurobasal™ Plus Medium (NB⁺ Plus medium) (Table 8) for the indicated time period. Every three to four days, half of the medium was replaced by fresh NB⁺ Plus medium. Glutamate treatment (25 µM) was conducted at the indicated *day in vitro* (DIV) for 24 hours. NMDA-antagonist MK801 (Merck KGaA, Darmstadt, Germany) was added as a control at a concentration of 10 µM. Rho activator II CN03 (Cytoskeleton, Denver, USA) was applied at a concentration of 1 µg/ml 3 hours prior to glutamate treatment.

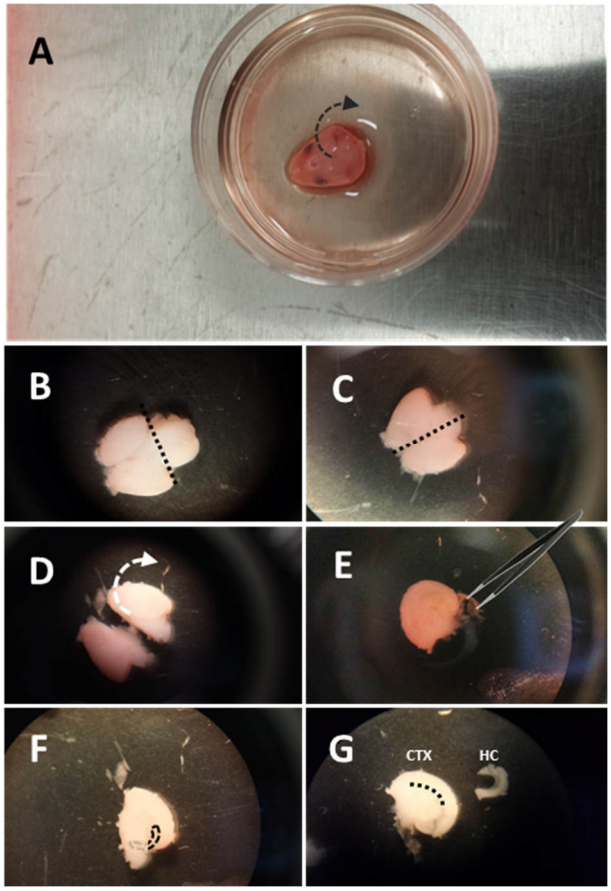

Figure 5. Isolation of cortex and hippocampus from E18 mouse embryos.

A The head of the embryo was decollated from the rest of the body using scissors and afterwards placed in a 35 mm petri dish for further preparation. **B** The brain was carefully removed from the skull using forceps. **C** The midbrain and cerebellum were removed from the basal forebrain. **D** Both cerebral hemispheres were separated carefully with forceps. **E** To exclude contamination with endothelial tissue, meninges were removed completely from the cerebral cortex. **F** The hippocampus was dissected out of the ambient brain tissue. **G** Finally, the cortical tissue was collected and both separated brain regions were collected in a 1.5 mL tube filled with 1xHBSS.

Table 7. Hank's balanced salt solution (HBSS) pH 7.2

Substance	Quantity
10x HBSS	50 mL
HEPES	1.2 g
Penicillin (10 000 U/mL)/Streptomycin (10 mg/mL)	5 mL
Bidest H_2O	Ad 500 mL

Table 8. Neurobasal™ Plus Medium (NB+ Plus)

Substance	Quantity
Neurobasal™ Plus Medium (Gibco®)	500 mL
B-27™ Plus Supplement (50X) (Gibco®)	10 mL
L-Alanyl-L-glutamine (200 mM)	5 mL
Penicillin (10.000 U/mL)/Streptomycin (10 mg/mL)	5 mL

Table 9. Cell densities for primary neurons

Plate format	Primary cortical neurons
6-well plate	550 000 – 700 000
24-well plate (Coverslips)	200 000
96-well plate	45 000 – 55 000
µ-Slide 8 well	150 000

Cofilin1$^{flx/flx}$ mice

Genetically modified mice expressing a cofilin1 gene region with exon 2 being flanked by loxP sites were used as controls, also referred to as wildtype (WT). Cofilin1 knockout was achieved by insertion of the Cre enzyme capable to recognize loxP sites and thus specifically delete exon 2 of the cofilin1 gene region, resulting in a non-functional gene product. Since a systemic knockout of cofilin1 is embryonically lethal [68], Cre expression is under the control of a CaMKIIα-promotor to specifically delete cofilin1 in excitable neurons [12, 145].

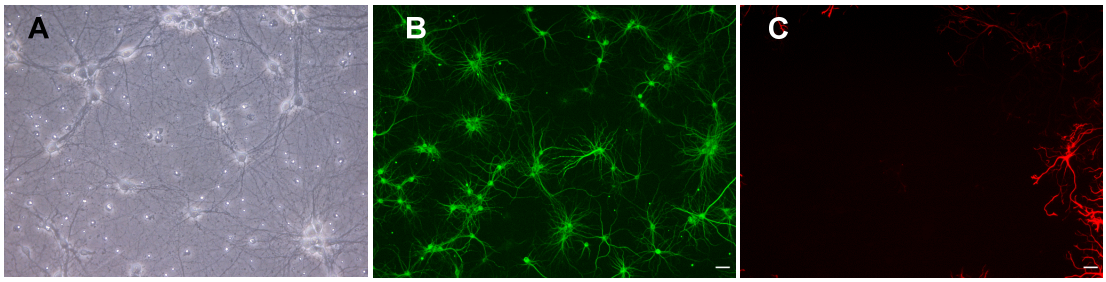

Figure 6. Primary neuronal culture from E18 cortical tissue.

A Brightfield images of neurons were captured after 10 days in vitro (DIV). **B** The neuronal culture was fixed at DIV20 and afterwards immunostained with an antibody against microtubule-associated protein 3 (MAP2) in green for specific visualization of neurons. *Scale bar* 50 µm. **C** To visualize the number of remaining astrocytes in the neuronal culture, glial fibrillary acidic protein (GFAP) was stained in red. *Scale bar* 50 µm.

For the evaluation of the genotype of the embryos, DNA from E18 pubs was isolated with REDExtract-N-Amp Tissue PCR Kit according to the manufacturer's protocol. Afterwards, specific primers (Table 35) were applied for the amplification of the genetically encoded Cre enzyme. The respective PCR program was implemented (Table 36) and PCR products were transferred onto a 1.5 % agarose gel supplemented with ethidium bromide to enable UV-based detection of the DNA.

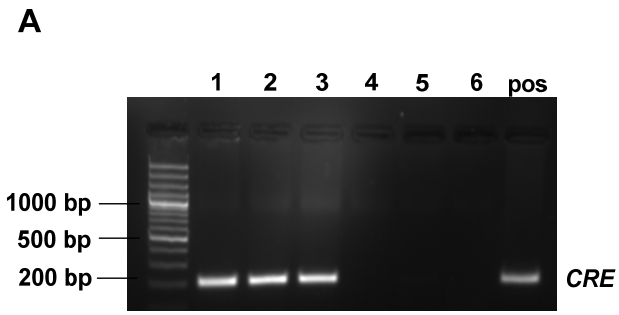

Figure 7. Determination of the genotype of E18 pubs.

A 10 µL of DNA amplification products of six different pubs were loaded onto an ethidium bromide supplemented 1.5 % agarose gel and afterwards illuminated with UV light. GeneRuler 100 bp Plus DNA ladder was used as an appropriate scale. Pos (positive control for Cre expression); bp (base pairs).

3.2.3 DNA/RNA transfection

Transfection of HT22 cells or MEF cells

Cells were seeded at Day 0 and grown for 24 hours in a 24-well plate. Afterwards, the transfection mixture was prepared consisting of 60 µL OptiMEM, 0.5 - 1.2 ug Plasmid-DNA and 3.5 µL Attractene (QIAGEN, Hilden, Germany) and finally put dropwise onto the cell culture medium.

Transfection of primary neurons

For a transfection in a 24-well plate, 100 µL NB^+ medium, 0.5 - 1 µg DNA and 1.75 µL Lipofectamine 2000 transfection reagent (ThermoFisher Scientific, Darmstadt, Germany) were mixed per well and kept at room temperature. During 30 minutes of incubation time, cells were washed with NB medium and the conditioned medium was collected in a 15 mL tube. 400 µL of NB^+ Plus medium without antibiotics and 100 µL of the transfection mixture was added onto the cells and incubated for precisely 90 minutes. Afterwards, cells were washed again with NB medium and conditioned medium was put back onto the neuronal culture.

Table 10. Plasmids

Plasmid name	Backbone	Source	Information
WT-Cofilin1	pEGFP-C3	AG Rust/AG Witke	
Alanin-Cofilin1-mutant	pEGFP-N1	AG Rust/AG Witke	
Aspartate-Cofilin1	pEGFP-N1	AG Rust/AG Witke	
Actin-Chromobody SNAP	pWPXL	AG Grosse	Cloned by Michael Melak
CMV-mito-LAR-GECO1.2	pcDNA3.1	Addgene (Plasmid #61245)	[179]
GFP control vector	pAAV-CMV-eGFP-IRES	AG Rust/AG Schratt (ETH Zürich, Austria).	Backbone derived from Cell Biolabs, Inc., San Diego, USA
GFP-CRE	pAAV-CMV-eGFP-IRES-CRE	AG Rust/AG Schratt (ETH Zürich, Austria).	Backbone derived from Cell Biolabs, Inc., San Diego, USA

siRNA transfection

For proper cofilin1 knockdown, HT22 cells were transfected with 15 nM cofilin1siRNA for 48 h. The reverse transfection was conducted according to the manufacturer's protocol. In brief, siRNA was incubated with Lipofectamine RNAiMAX (Thermo Fisher Scientific,

Darmstadt, Germany) in antibiotic-free OptiMEM for 20 minutes. Proper amount of the transfection mix was transferred to respective plates and cell suspensions were added to the mixture.

Following siRNA sequences were used:

Table 11. siRNA sequences and companies

siRNA	Abbreviation	Sequence	Conc.	Company
MISSION® Universal negative control#1 (Scrambled siRNA)	scrsiRNA	5′-UAAUGUAUUGGAA CGCAUA-3′)	q.s.	Sigma
Cofilin1siRNA 01	Cfl1si01	5′-AGACAAGGACUGCC GCUAU-3′	15 nM	GE Healthcare, Little Chalfont, England
Cofilin1siRNA 02	Cfl1si02	5′-GGAAUCAAGCAUGA AUUAC-3′	15 nM	GE Healthcare, Little Chalfont, England
INF2siRNA SMARTpool	INF2si	5′-GGACAGAGCACCCA CCUAC-3′ 5′-GGAAGAAACGUCCC UCAAG-3′ 5′-GCAACUGCCAGCAA UCCUA-3′ 5′-CUCGAGUUCUCUAG CAAUA-3′	5 nM	GE Healthcare, Little Chalfont, England
DRP1siRNA	DRP1si	5`-AAG CAG AAG AAU GGG GUA AAU TT-3´	40 nM	Eurofins, Ebersberg, Germany

Table 12. siRNA transfection protocol

	6-well plate	24-well plate	96-well plate	µ-Slide 8 Well
siRNA	5 – 40 nM	5 – 40 nM	5 – 40 nM	5 – 40 nM
Lipofectamine® RNAiMAX	4 µL	1 µL	0.24 µL	0.5 µL
Opti-MEM	Ad 400 µL	Ad 100 µL	Ad 20 µL	Ad 50 µL

3.2.4 Cell death induction by erastin or glutamate

Cell death was induced after 24, 30 or 48 h after cell seeding by 0.2-1 µM doses of erastin (Merck KGaA, Darmstadt, Germany) or 2-10 mM doses of D, L-glutamic acid monohydrate (Sigma-Aldrich, Taufkirchen, Germany). Erastin was dissolved in DMSO to a stock solution of 1 mM and glutamate was diluted in DMEM to a stock concentration of 1 M and following adjustment to a neutral pH of 7.2. Both compounds were further diluted in DMEM to the desired concentration and resulting effects were evaluated after 16 hours of treatment, if not stated differently.

3.3 Cell viability measurement

3.3.1 MTT assay

Cell viability was assessed by a colorimetric assay based on the yellow colored MTT reagent (3-(4,5-dimethyl-2-thiazolyl)-2,5-diphenyl-2H-tetrazolium bromide, 0.5 mg/ml for HT22 cells and 1 mg/ml for primary cortical neurons; Sigma-Aldrich, Munich, Germany) which is reduced to a purple colored formazan product by dehydrogenases and NAD(P)H coenzyme of metabolically active cells during 1 h incubation period at 37 °C [155]. The color of the product can be quantified by absorbance measurement at 570 nm with a reference filter at 630 nm by FluoStar OPTIMA reader (BMG Labtech, Ortenberg, Germany).

3.3.2 xCELLigence system

Cell proliferation and detachment was monitored using the xCELLigence Real-Time Cell Analysis (RTCA; Roche Diagnostics, Mannheim, Germany) system as previously described [44]. Changes in the impedance are displayed as normalized cell indices.

3.4 Measurement of mitochondrial morphology and function

3.4.1 Analysis of mitochondrial morphology

To assess mitochondrial morphology, MitoTracker® DeepRed FM (Invitrogen, Karlsruhe, Germany) was used to visualize active mitochondria by far-red fluorescence. After incubating the cells with 200 nM MitoTracker diluted in DMEM for 15-30 minutes at 37 °C, mitochondria can be visualized using an epifluorescence microscope (DMI6000B, Leica, Wetzlar, Germany) equipped with a 63 x/1.4 NA oil immersion objective. Cells were excited at a wavelength of 633 nm and emitted light was detected at 670 nm.

For quantification of mitochondrial morphology changes, mitochondria were classified into three different categories [65]. Category I mitochondria are tubular, elongated and distributed throughout the cytosol, whereas mitochondria of category II show a circular and fragmented phenotype, although still distributed in the whole cell. Mitochondria subdivided into category III are small and fragmented and located close to the nucleus. These cells also exhibit characteristic features of cell death, such as shrunken nuclei and smaller cell shape.

To evaluate not only fragmented mitochondria, but also to account for elongated mitochondria under particular conditions, automated analysis by ImageJ Software (NIH, Bethesda, USA) was used with support of a ImageJ macro first described by Ruben K. Dagda and Charleen Chu [39].

3.4.2 ATP bioluminescent assay

Cellular ATP level were measured using the ViaLight™ Plus Kit (Lonza, Verviers, Belgium) according to the manufacturer's protocol. Briefly, cells were lysed, transferred to a white-walled 96-well plate and the ATP monitoring reagent was added to the cell lysate. Afterwards, the emitted luminescence was detected with a FLUOstar OPTIMA reader (BMG Labtech, Ortenberg, Germany).

$$ATP + Luciferin + O_2 \xrightarrow[Mg^{2+}]{Luciferase} Oxyluciferin + AMP + PP_i + CO_2 + Photons$$

3.4.3 Seahorse measurement

Measurement of the mitochondrial oxygen consumption rate (OCR) and extracellular acidification rate

Determination of the mitochondrial oxygen consumption rate as an indicator of mitochondrial respiration was performed using the Seahorse XFe96 Analyzer (Agilent Technologies, Waldbronn, Germany). The measurement can either be performed with intact cells, or with isolated mitochondria from tissues.

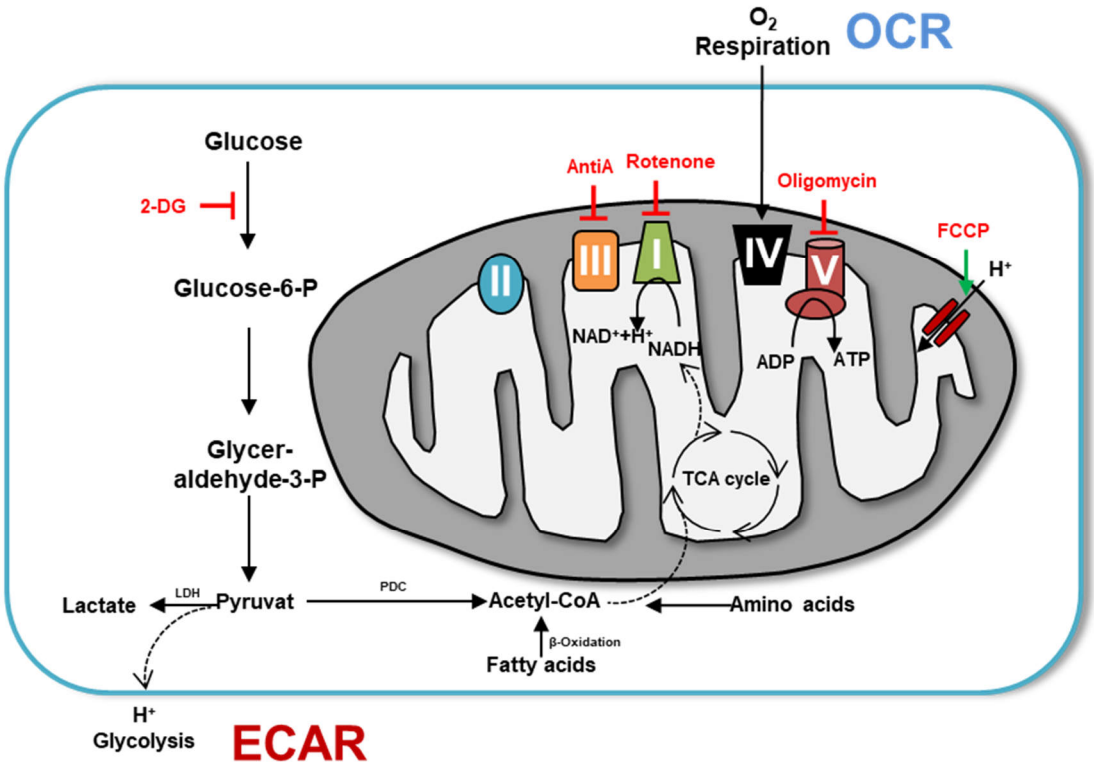

Figure 8. Molecular mechanism of Seahorse assay. Modified from Agilent.com.

OCR (oxygen consumption rate); ECAR (extracellular acidification rate); 2-DG (2-deoxy-D-glucose); TCA (tricarboxylic acid cycle); AntiA (antimycin A); FCCP (carbonyl cyanide-4-(trifluoromethoxy)phenylhydrazone) ADP (adenosine diphosphate); ATP (adenosine triphosphate); NAD^+ (oxidized form of nicotinamide adenine dinucleotide); NADH (reduced form of nicotinamide adenine dinucleotide); Glucose-6-P (glucose-6-phosphate), LDH (lactate dehydrogenase); PDC (pyruvate dehydrogenase complex); Acetyl-CoA (acetyl coenzyme A).

HT22 cells were plated in XFe96-well microplates (6000 cells/well, Seahorse Bioscience). 1 hour prior to the measurement, growth medium was replaced by the seahorse assay medium (4.5 g/l glucose, 2 mM glutamine, 1 mM pyruvate, pH 7.35). After recording three baseline measurements, four compounds were added by injection. Indicated compounds for

the injections were used in following final concentrations: 3 μM oligomycin, 0.5 μM FCCP, 0.1 μM rotenone together with 1 μM antimycin A and 150 μM 2-DG.

For MEF cells all steps were performed according to the protocol described for HT22 cells. FCCP concentration was increased to 1 μM.

Primary cortical neurons in were cultured in DMEM supplemented with 143 mM sodium chloride, 15 mM glucose, 10 mM sodium pyruvate, 2 mM glutamine, 0.04% (w/v) BSA and an adjusted pH of 7.35. For these cells, indicated compounds for the injections were used in following final concentrations: 2 μM oligomycin, 2 μM FCCP, 1 μM rotenone together with 1 μM antimycin A, and 150 mM 2-DG

After the measurement, cells were carefully washed once with PBS before adding 50 μL lysis buffer (10 mM Tris base, 0.1% (v/v) Triton X-100) per well and freezing the plate at - 80°C.

The mitochondrial coupling assay was performed for isolated mitochondria according to a previously described protocol [142]. Per well, 5-12 μg of isolated mitochondrial protein were measured in mitochondrial assay solution (Table 30) containing the complex II substrate succinate (10 mM) and the complex I inhibitor rotenone (2 μM) to focus on mainly complex II- and complex III-driven respiration. For slight attachment of the plated mitochondria at the bottom of the cell plate, a centrifugation step of the whole plate at 2,000 x g for 20 min at 4 °C was indispensable (Heraeus Megafuge 40R; Thermo Fisher Scientific, Darmstadt, Germany). Indicated compounds for the injections were used in following final concentrations: 4 mM ADP, 2.5 μg/ml oligomycin, 4 μM FCCP and 4 μM antimycin A (AA).

Three basal and three measurements after each injection were recorded.

3.4.4 Rhodamine123 measurement

After isolation of mitochondria from the cortical tissue, mitochondrial integrity was confirmed by rhodamine 123 staining as described before [186]. Isolated mitochondria (75 μg per well) were diluted in 140 μL SWP1 buffer (Table 13) and mixed with 125 nM rhodamine 123 in a black 96-well plate. The rhodamine 123 dye is completely quenched by mitochondria with an intact ΔΨm. During the measurement, FCCP (500 nM) was injected and led to depolarization of the ΔΨm resulting in immediate release of the dye and increased fluorescence measured by FLUOstar OPTIMA reader (BMG Labtech, Ortenberg, Germany) at an excitation wavelength of 485 ± 12 nm and emission wavelength of 530 ± 10 nm.

Table 13. SWP1 buffer, pH 7.3

Compound	Final concentration
Sucrose	200 mM
MOPS-Tris	10 mM
Succinate	5 mM
H_3PO_4	1 mM
EGTA	10 μM
Rotenone	2 μM

3.5 Flow cytometric measurement (FACS)

Different cellular and mitochondrial parameters of the glutamate- or erastin- induced cell death pathways were analyzed using the Guava easyCyte 6–2L flow cytometer (Merck Millipore, Darmstadt, Germany) upon the addition of respective fluorescent dyes.

3.5.1 BODIPY

Lipid peroxidation

By staining the cells with BODIPY 581/591 C11 (4,4-difluoro-5-(4-phenyl-1,3-butadienyl)-4-bora-3a,4a-diaza-s-indacene-3-undecanoic acid; Thermo Fisher Scientific, Darmstadt, Germany) oxidized lipids and membranes can be detected. Following 8 h of glutamate treatment, the cells were stained with 2 μM BODIPY dye for 1 h at 37 °C.

3.5.2 DCF

Cellular reactive oxygen species formation

The cell permeable dye 2',7'-dichlorodihydrofluorescein diacetate (H_2DCF-DA) was used to evaluate the accumulation of cellular reactive oxygen species upon 30 minutes incubation with a final concentration of 20 μM in DMEM without serum.

3.5.3 TMRE

Mitochondrial membrane potential (ΔΨm)

Mitochondrial membrane potential was measured after staining the cells with MitoPT TMRE Kit (ImmunoChemistry Technologies, Hamburg, Germany). Cells were incubated with 0.2 μM TMRE (tetramethylrhodamine ethyl ester) for 30 min at 37 °C.

For investigation of the mitochondrial membrane potential of isolated mitochondria from adult mouse brain tissue, 40 µg mitochondria were diluted in 150 µL 1xMAS (Table 30) supplemented with 2 µM rotenone and 10 mM succinate. 50 µM of the uncoupler CCCP was used as a positive control. Mitochondria were incubated with 0.2 µM TMRE for 15 minutes and then measured with Guava easyCyte 6–2L flow cytometer (Merck Millipore, Darmstadt, Germany).

3.5.4 MitoSOX

Mitochondrial superoxide formation

For evaluation of mitochondrial reactive oxygen species accumulation, MitoSOX Red indicator (Thermo Fisher Scientific, Darmstadt, Germany) was applied at a concentration of 1.25 µM for 30 min at 37 °C.

MitoSOX measurement with isolated mitochondria was conducted according to TMRE measurement (described in chapter 3.5.3 TMRE). 10 µM of the complex III-inhibitor antimycin A (AA) was used as a positive control and incubated simultaneously with MitoSOX Red indicator at a concentration of 1.25 µM.

3.5.5 Rhod2-AM

Mitochondrial calcium measurement

Staining the cells with the mitochondrial selective dye Rhod-2 AM (rhodamine-2 acetoxymethyl ester; Thermo Fisher Scientific, Darmstadt, Germany), allows for specific evaluation of mitochondrial calcium accumulation. Rhod-2 AM was reduced to Dihydrorhod-2 AM and incubated at a concentration of 2 µM in DMEM without serum for 1 hour.

3.5.6 AnnexinV/PI

Cell death

Apoptotic and late necrotic cells were identified using the Annexin V-FITC Detection Kit (Promokine, Heidelberg, Germany). AnnexinV and propidium iodide (PI) staining were performed for 5 minutes in the dark at room temperature after harvesting cells with trypsin.

3.6 Protein analysis

3.6.1 Protein sample preparation

For protein extraction and Western blot analysis, cells were washed with 1xPBS (Table 3) and afterwards destructed in protein lysis buffer (Table 14) using a cell scraper and thoroughly transferred to a 1.5 mL tube. Liquid nitrogen was used to devastate cell membranes for release of whole protein lysates. Insoluble fragments were removed by centrifugation at 10,000 x g for 15 minutes at 4 °C. The protein-containing supernatant was transferred into a fresh tube and kept on ice for measuring the protein concentration for further experiments.

Table 14. Protein lysis buffer, pH 7.8

Substance	Quantity
D-Mannitol	0.25 M
Tris-HCl	0.05 M
EDTA	1 mM
EGTA	1 mM
DTT 100 mM	1:100
Triton® X-100	1:100
PhosSTOP™ (Roche, Penzberg, Germany)	1 tablet
cOmplete™, EDTA-free Protease Inhibitor Cocktail (Roche, Penzberg, Germany)	1 tablet
Bidest. H_2O	Ad 10 mL

3.6.2 BCA assay

The total protein concentration of the sample was determined using the bicinchoninic acid (BCA)-based Pierce BCA Protein Assay Kit (Thermo Fisher Scientific, Darmstadt, Germany). The underlying biochemical reaction includes the reduction of Cu^{2+} to Cu^{+} by peptides in a stoichiometric manner. Based on this reaction, bicinchoninic acid reactis with the cuprous ion and the resulting purple colored solution can be measured with the 560±10 nm bandpass filter of FLUOstar OPTIMA reader (BMG Labtech, Ortenberg, Germany). Protein sample concentration was compared to a protein standard curve of bovine serum albumin (BSA).

3.6.3 Polyacrylamide gel electrophoresis (PAGE)

Gel electrophoresis was conducted to separate proteins based on their molecular weight.

Table 15. 1.5 M Tris-HCl, pH 8.8

Substance	Quantity
Tris-HCl	23.6 g
HCl	q.s. for pH adjustment
Bidest. H_2O	Ad 100 mL

Table 16. 0.5 M Tris-HCl, pH 6.8

Substance	Quantity
Tris-HCl	7.88 g
HCl	q.s. for pH adjustment
Bidest. H_2O	Ad 100 mL

Table 17. 10 % Sodium dodecyl sulfate (SDS)

Substance	Quantity
SDS pellets	1 g
Bidest. H_2O	Ad 10 mL

Table 18. Stacking gel 3.5 %

Substance	Quantity
Acrylamide/bisacrylamide 30 %	0.58 mL
Sodium dodecyl sulfate solution 10 %	0.05 mL
0.5 M Tris-HCl buffer, pH 6.8	1.2 mL
Ammonium persulfate solution 10 %	30 µL
Tetramethylethylenediamine (TEMED)	8 µl
Bidest. H_2O	Ad 5 mL

Table 19. Running gel 10 % / 12.5 %

Substance	10 %	12.5 %
Acrylamide/bisacrylamide 30 %	3.34 mL	4.17 mL
Sodium dodecyl sulfate solution 10 %	0.1 mL	0.1 mL
1.5 M Tris-HCl buffer, pH 8.8	2.5 mL	2.5 mL

Ammonium persulfate solution 10 %	62.5 µL	62.5 µL
Tetramethylethylenediamine (TEMED)	12.5 µL	12.5 µL
Bidest. H_2O	Ad 10 mL	Ad 10 mL

3.6.4 Western blot

After SDS-PAGE, proteins were transferred onto a PVDF membrane (Roche Diagnostics, Mannheim, Germany). Incubation with the primary antibody against the protein of interest was conducted over night at 4 °C and at room temperature on the next day for additional two hours. After washing the membrane with 1xTBST, the secondary antibody was applied for two hours and the chemiluminescent signal was visualized with Chemidoc software (Bio-Rad, Germany). Tubulin was frequently used as a loading control for total protein lysate.

Table 20. 5x SDS sample buffer; 10 mL

Substance	Quantity
1.5 MTris-HCl, pH 6.8	2 mL
Glycerol	5 mL
SDS pellets	1 g
β-Mercaptoethanol	2.5 mL
1 % Bromophenol blue	0.5 mL

Table 21. 10x SDS-PAGE buffer (Running buffer)

Substance	Quantity
Tris base	30 g
SDS pellets	10 g
Glycine	144 g
Bidest. H_2O	Ad 1 L

The 10x SDS-PAGE buffer was diluted 1:10 with aqua bidest prior to use.

Table 22. 10x Transfer buffer, pH 8.3

Substance	Quantity
Tris base	30 g
Glycine	144 g
HCl	q.s. for pH adjustment
Bidest. H_2O	Ad 1 L

To dilute the 10x transfer buffer, 70 % aqua bidest and 20 % methanol was added.

Table 23. 10x TBS, pH 7.5

Substance	Quantity
NaCl	292 g
Tris base	24.2 g
HCl	q.s. for pH adjustment
Bidest. H_2O	Ad 1 l

Table 24. 1x TBST

Substance	Quantity
10x TBS	100 mL
Tween 20	0.5 mL
Bidest. H_2O	Ad 1 L

Table 25. 5% Blocking milk

Substance	Quantity
Skim milk powder	5 g
1xTBST	100 mL

3.6.5 Antibodies

Table 26. Primary antibodies

Antibody	Dilution	MW [kDa]	Host	Company	Purpose
Cofilin1	1:1000	16	rabbit	Cell Signaling and Witke-Laboratory [12]	WB

phospho-Cofilin1 (Ser3)	1:1000	16	rabbit	Cell Signaling	WB
PGC1α	1:1000	92	rabbit	Rockland	WB
DRP1	1:1000	83	mouse	BD Bioscience	WB
α-Tubulin	1:10 000	54	mouse	Sigma-Aldrich	WB
MCU	1:1000	30	rabbit	Cell Signaling	WB
Fis1	1:500	17	rabbit	Enzo Life Science	WB
p62	1:1000	62	rabbit	Cell Signaling	WB
Actin C4 clone	1:2000	42	mouse	MP Biomedicals	WB
LC3B	1:1000	14-16	rabbit	Cell Signaling	WB
Mfn2	1:1000	80	rabbit	Cell Signaling	WB
TFAM	1:1000	28	rabbit	Abcam	WB
Nrf-1	1:1000	68	rabbit	Cell Signaling	WB
INF2	1:1000	180-200	rabbit	Proteintech	WB
GFP	1:500	27	goat	Rockland	WB
H2AX	1:2000	14	rabbit	Novus Biologicals	WB
MAP2	1:100		mouse	Abcam	Immunocyto-chemistry
GFAP	1:100		mouse	Cell Signaling	Immunocyto-chemistry
phospho-DRP1 (Ser616)	1:1000	83	rabbit	Cell Signaling	WB
phospho-DRP1 (Ser637)	1:1000	83	rabbit	Cell Signaling	WB
Tim23	1:1000	23	mouse	BD Transduction laboratories	WB

Table 27. Secondary antibodies

Antibody	Dilution	Host	Company	Purpose
Peroxidase-labeled anti-goat IgG (H+L)	1:2500	horse	Vector laboratories	WB
Peroxidase-labeled anti-mouse IgG (H+L)	1:3000	horse	Vector laboratories	WB
Peroxidase-labeled anti-rabbit IgG (H+L)	1:2500	goat	Vector laboratories	WB
Anti-mouse IgG (H+L) Dylight™ 650	1:200	goat	Thermo Scientific	Immunocytochemistry
Anti-rabbit IgG (H+L) Dylight™ 488	1:200	goat	Thermo Scientific	Immunocytochemistry

3.6.6 Immunoprecipitation

Immunoprecipitation was performed to investigate protein-protein-interactions. To achieve sufficient pulldown quantity of the protein of interest, Dynabeads™ Protein A for Immunoprecipitation (Invitrogen, Karlsruhe, Germany) were used according to the manufacturer's protocol. In brief, magnetic Dynabeads were coupled to 2.5 µg of the primary antibody diluted in 200 µL 1xPBS/0.1 % Tween20 by incubation on a rotator at room temperature for 30 minutes. Afterwards, the Dynabead-antibody complex was washed once with PBS/Tween20 by restraining the tube on a magnet following resuspension of the magnetic beads in 6 mg Crosslinker BS^3 (Thermo Fisher Scientific, Darmstadt, Germany) diluted in 250 mL aqua bidest. 750 µL PBS/Tween20 was added prior to rotation for

30 minutes at room temperature to fix the crosslinked beads with the antibody. Subsequently, the fixed complex was washed one with PBS/Tween20 and 1 mL of 30 mM Tris-HCl, pH 7.4 solution was added for 15 minutes. Then, 250 µg of protein sample diluted in 600 µL protein lysis buffer (Table 14) was added to the Dynabead-antibody-complex and incubated over night at 4 °C on a rotator. On the next day, the complex was washed three times with PBS and finally the proteins were eluted by boiling the sample with 50 µL of 2.5x SDS sample buffer (Table 20) for 10 minutes at 95 °C. The antigens were visualized by primary and secondary antibody detection after SDS-PAGE and wet blot procedure via chemiluminescence with Chemidoc software (Bio-Rad, Germany).

3.6.7 Mitochondrial isolation

Table 28. Mitochondrial isolation buffer, pH 7.2, 4 °C [147]

Substance	Final concentration	Weight
Sucrose	300 mM	102.8 g
TES	5 mM	1.146 g
EGTA	200 µM	76 mg
Bidest. H_20		add 1 L
KOH	q.s. for pH adjustment	

Mitochondrial isolation of freshly dissected cortical or hippocampal brain tissue (~50 mg) was performed as previously described [147]. Briefly, the tissue was charged with 2 mL mitochondrial isolation buffer (Table 28) and roughly homogenized with a 20G Neoject needle (Dispomed, Gelnhausen, Germany) and then sieved through a 100 µm nylon cell strainer (Corning Incorporated, Corning, NY, USA). To homogenize the tissue efficiently and extract mitochondria from the cell structure thoroughly, a cell homogenizer (Isobiotec, Heidelberg, Germany) with appropriate 1 mL gas-tight syringes (Supelco, Munich, Germany) were used and restrained into a device to ensure constant rate of 700 µL/min. The cell homogenizer contains a spherical tungsten carbide ball with a clearance of 10 µm to decompose the tissue but simultaneously maintain the integrity of mitochondria. The cell homogenate was transferred into 1.5 mL tubes and centrifuged at 800 x g for 10 min at 4 °C to remove cell debris. Afterwards, the supernatant was transferred into a fresh tube and centrifuged at 10 000 x g, again for 10 min at 4°C (Heraeus™ Fresco™ 17 Mikrozentrifuge; Thermo Fisher Scientific, Darmstadt, Germany). The resulting pellet consists of a crude

mitochondrial fraction, which was finally resuspended in MSHE-BSA buffer (Table 29). All steps were performed on ice or at 4 °C. Pierce™ BCA Kit was used to determine the protein amount of the mitochondrial fraction.

Table 29. MSHE-BSA buffer, pH 7.2

Substance	Final concentration	Weight
Sucrose	70 mM	24 g
Mannitol	210 mM	38.26 g
HEPES	5 mM	1.19 g
EGTA	1 mM	0.38 g
BSA (freshly added)	0.5 % (w/v)	5 g
Bidest. H_2O		ad 1 L
KOH	q.s. for pH adjustment	ad 1 L H2O

Table 30. 1xMitochondrial Assay Solution (1xMAS), pH 7.2

Substance	Final concentration	Weight
Sucrose	70 mM	24 g
Mannitol	220 mM	40.08 g
KH_2PO_4	10 mM	1.36 g
$MgCl_2$	5 mM	0.476 g
HEPES	2 mM	0.476 g
EGTA	1 mM	0.380 g
BSA (freshly added)	0.20 % (w/v)	2 g
Bidest. H_2O		ad 1 L
KOH	q.s. for pH adjustment	

3.7 DNA/RNA analysis

3.7.1 RNA sample preparation for RT-PCR

For semi-quantitative reverse transcription PCR, mRNA was isolated by using InviTrap Spin Universal RNA Mini Kit (Stratec Biomedical, Birkenfeld, Germany). For each well of a 6-well plate, 350 µL lysis buffer was prepared with 1 % β-mercaptoethanol and the RNA isolation kit was used according to the manufacturer's protocol. The resulting RNA was eluted with

40 µL of elution buffer and stored on ice, until further handling and determination of RNA amounts.

All primers were obtained from EurofinsGenomics (Ebersberg, Germany) and the following sequences were used for amplification:

Table 31. Primers for RT-PCR

Primer	Sequence	Amplicon size
Gapdh	forward 5′-CGTCTTCACCACCATGGAGAAGGC-3′	399 bp
	reverse 5′-AAGGCCATGCCAGTGAGCTTCCC-3′	
Cofilin1	forward 5′-GCCAACTTCTAACCACAATAG-3′	146b p
	reverse 5′-CCTTACTGGTCCTGCTTCC-3′	
DRP1	Forward 5′-ACAGGAGAAGAAAATGGAGTTTGAAGCAG-′3	860 bp
	Reverse 5′-AACAAATCCTAGCACCACGCAT-3′	

Table 32. PCR program *DRP1*

Steps	Temperature	Duration	Cycles
Initial denaturation	95 °C	1 min	
Reverse transcription (RT)	60 °C	30 min	
RT inactivation	95 °C	2 min	
Denaturation	95 °C	30 sec	26x
Annealing	57 °C	1 min	
Extension	70 °C	2 min	
Final extension	70 °C	10 min	
Soak/cooling	4 °C	∞	

Table 33. PCR program *cofilin1*

Steps	Temperature	Duration	Cycles
Initial denaturation	95 °C	1 min	

Reverse transcription (RT)	52 °C	30 min	
RT inactivation	95 °C	2 min	
Denaturation	95 °C	30 sec	
Annealing	52 °C	30 sec	25x
Extension	68 °C	30 sec	
Final extension	68 °C	5 min	
Soak/cooling	4 °C	∞	

Table 34. PCR program *GAPDH*

Steps	Temperature	Duration	Cycles
Reverse transcription (RT)	55 °C	30 min	
RT inactivation	95 °C	2 min	
Denaturation	95 °C	30 sec	
Annealing	60 °C	30 sec	27x
Extension	70 °C	1 min	
Final extension	70 °C	10 min	
Soak/cooling	4 °C	∞	

3.7.2 DNA extraction and genotype

REDEextract-N-Amp Tissue PCR Kit-Sigma (Taufkirchen, Germany)

PCR reaction:

-6 µL REDExtract-N-Amp PCR Reaction Mix

-2 µL Primer (composed of 0.5µL of each primer)

-2 µL DNA

Table 35. PCR primers for Cre-genotype determination

Primer	Sequence	Amplicon size
Cre recombinase	forward 5‘-GAACGCACTGATTTCGACCA-3‘	200 bp
	reverse 5‘-AACCAGCGTTTTCGTTCTGC-3‘	

Mitochondria oIMR7338	Forward 5‘- CTAGGCCACAGAATTGAAAGATCT-3‘	324 bp
oIMR7339	Reverse 5‘- GTAGGTGGAAATTCTAGCATC ATCC-3‘	

Table 36. PCR program Cre and internal control (Mito primer)

Cre primer			**Mito primer (internal control)**		
Temperature	**Duration**	**Cycles**	**Temperature**	**Duration**	**Cycles**
95 °C	3 min		94 °C	1.5 min	
95 °C	45 sec		94 °C	30 sec	
58 °C	45 sec	35x	60 °C	1 min	35x
72 °C	45 sec		72 °C	1 min	
72 °C	10 min		72 °C	2 min	
4 °C	∞		4 °C	∞	

3.7.3 RT-PCR and agarose gel electrophoresis

DNA or RNA absorbance was measured at 260 nm by a spectrophotometric system using the NanoPhotometer™ (Implen, Munich, Germany). Afterwards, above specified RT-PCR components (Table 37) were carefully transferred into 0.2 mL PCR reaction tubes and the respective PCR program were run at T-personal thermocycler (Biometra GmbH, Göttingen, Germany).

Table 37. RT-PCR components

Substance	**Quantity**
2x reaction buffer	12.5 µL
RNA sample	100-500 ng
Forward primer	1 µL
Reverse primer	1 µL
SuperScript III enzyme	0.5 µL
Nuclease-free water	ad 25 µL

After amplification of the PCR product, 10 % 10x loading dye (Table 38) was added, mixed thoroughly and finally loaded onto a 1.5 % agarose gel stained with ethidium bromide. Additionally, GeneRuler 100 bp Plus DNA ladder (Thermo Fisher Scientific, Darmstadt, Germany) was used as a reference for PCR product size. Agarose gel electrophoresis was conducted at 80 V and illumination by Chemidoc-XRS Imaging system (Bio-Rad, Munich, Germany) was used for visualization of the respective PCR products.

Table 38. 10x Loading dye

Compound	Quantity
Tris base	60.57 mg
40 % glycerol	20 mL
EDTA	168.2 mg
Orange G 0,25 %	125 mg
Bidest H_2O	Ad 50 mL

3.7.4 Quantitative PCR

Two-step reverse transcription quantitative PCR (RT-qPCR) was performed with the StepOnePlus Real-Time PCR System (Fisher Scientific GmbH, Schwerte, Germany) in the lab of Prof. Marco Rust. mRNA was isolated with InviTrap Spin Universal RNA Mini Kit (Stratec Biomedical, Birkenfeld, Germany) from indicated cell types cultured in 6-well plates. The RNA amount was determined using a NanoPhotometer (Implen, Munich, Germany). To remove remaining genomic DNA, Turbo DNA-free Kit (Thermo Fisher Scientific, Darmstadt, Germany) was used according to the manufacturer's protocol. 200 ng of purified RNA was applied for cDNA synthesis with iScript cDNA Synthesis Kit (Bio-Rad Laboratories, Hercules, CA, USA). The resulting cDNA was diluted 1:5 with aqua bidest, 4 µL of cDNA, appropriate amounts of iTaq Universal SYBR Green Supermix (Bio-Rad Laboratories, Hercules, CA, USA) and the respective primer pair were carefully transferred into a MicroAmp Fast Optical 96-well Reaction Plate (Thermo Fisher Scientific, Darmstadt, Germany). To avoid evaporation, the plate was tightly sealed with MicroAmp Optical Adhesive Film (Thermo Fisher Scientific, Darmstadt, Germany). Triplicates were used for each measurement and evaluated by double delta Cτ analysis by subtracting Cτ values of the housekeeping gene 18S from the gene of interest and subsequently calculating the ratio

between control and the favored experimental condition. mRNA expression fold change is shown as $2^{-\Delta\Delta C\tau}$.

Table 39. cDNA synthesis

Temperature	Duration
25 °C	5 min
42 °C	30 min
85 °C	5 min

Table 40. RT-qPCR program

Temperature	Duration	Cycles
95 °C	10 min	
95 °C	15 sec	50x
60 °C	1 min	50x
95 °C	15 sec	
60 °C	1 min	
95 °C	15 sec	

3.7.5 PCR Primer

Table 41. RT-qPCR primers

Primer	Sequence
PGC1α	For 5′-ACTGACGGCCTAACTCCACCCA-3′
	Rev 5′-ACTCGGATTGCTCCGGCCCT-3′
TFAM	For 5′-ATTCCGAAGTGTTTTTCCAGCA-3
	Rev 5′-TCTGAAAGTTTTGCATCTGGGT-3′
Nrf-1	For 5′-AGCACGGAGTGACCCAAAC-3′
	Rev 5′-TGTACGTGGCTACATGGACCT-3′
Nrf-2	For 5′-TCCGCCAGCTACTCCAGGTTGG-3′
	Rev 5′-TGGGCCCTGATGAGGGGCAGTG-3′
18S	For 5′-CTTAGAGGGACAAGTGGCG-3′
	Rev 5′-ACGCTGAGCCAGTCAGTGTA-3′
MCU	For 5′-AAAGGAGCCAAAAAGTCACG-3′

	Rev 5′-AACGGCGTGAGTTACAAACA-3′
p62	For 5′-TGCTCTTCGGAAGTCAGCAA-3′
	Rev 5′-CCCGACTCCATCTGTTCCTC-3′
mtDNA	For 5′-ACCGCGGTCATACGATTAAC-3′
	Rev 5′-CCCAGTTTGGGTCTTAGCTG-3′

3.8 Calcium imaging

3.8.1 Cytosolic calcium measurement

Calcium imaging using acetoxy-methyl-ester Fura-2 (Fura-2 AM) is a reliable method to record spontaneous synchronized network activity of neuronal cultures as an alternative to measuring electrical activity by patch-clamp electrophysiology or field electrodes. Fura2-AM is a commonly used ratiometric and cell-permeant calcium indicator, which is intracellularly cleaved by esterases to the cell-impermeant acidic form Fura2. The accumulated dye is able to bind intracellular calcium, which changes its excitation peak from 340 nm to 380 nm. By calculating the ratio between both wavelengths, the signal is independent of the dye concentration, illumination intensity and photobleaching artifacts, optical path length or uneven distribution of the dye [42].

Cells were seeded on poly-L-lysine coated coverslips (Ø 12 mm) and cultured as described above (Chapter 3.2.2 Primary mouse neurons) for 23-27 days. At the day of the measurement, NB$^+$ Plus medium was replaced by HEPES-Ringer buffer (Table 42) for 1 hour at 37 °C. Afterwards, cells were incubated with 3 µM of Fura2-AM for 30 minutes and finally washed for another 30 minutes in HEPES-Ringer buffer in the humidified 37 °C incubator with a 5 % CO_2 supply.

For calcium imaging, a Leica DMI6000 inverted epifluorescence microscope (Leica, Wetzlar, Germany) was used equipped with a 20x/0.40 Leica HCX PL FLUOTAR objective. Images were acquired every 800 ms using a Leica DFC 360FX camera. 37 °C temperature was achieved using a heating unit and a suitable PeCon® Inkubator BL (PeCon® GmbH, Erbach, Germany). Eleven regions of interest (ROI) were selected and fluorescence intensities were quantified by Leica Application Suite software (Leica, Wetzlar, Germany). Data are presented as the Fura2-ratio of both recorded wavelengths (340/380 nm).

Table 42. HEPES-Ringer buffer, pH 7.4

Substance	Concentration
NaCl	136.4 mM
KCl	5.6 mM
$MgCl_2$	1 mM
$CaCl_2$	2.2 mM
HEPES	10 mM
Glucose	5 mM
BSA (added at the day of measurement)	0.2% (w/v)

3.8.2 Mitochondrial calcium measurement

For evaluation of mitochondrial calcium uptake upon stimulation with either potassium chloride (KCl, 60 mM) or calcium chloride ($CaCl_2$, 60 mM), MEF cells were grown for 72 hours and primary cells were grown for eight to ten days in µ-Slide 8 well and transfected with mito-LAR GECO1.2 plasmid for 48 hours. Prior to the measurement, medium was replaced by 25 mM HEPES-buffered Hank's Balanced Salt Solution (HBSS; Thermo Fisher Scientific, Darmstadt, Germany). Fluorescence intensities were acquired with Leica DMI6000 inverted epifluorescence microscope (Leica, Wetzlar, Germany). 40x/0.60 Leica HCX PL FLUOTAR objective was used for magnification. Images were recorded every 1-2 sec at 37 °C using a Leica DFC 360FX camera. Time lapse recordings were processed with ImageJ software (National Institutes of Health, Bethesda, MD, USA) or by Leica Application Suite software (Leica, Wetzlar, Germany).

3.9 Protein purification

Cloning and mutagenesis

Human cofilin1 was amplified by PCR using specific oligonucleotides (forward: 5'-CATATGGCCTCCGGTGTG-3', reverse: 5'-GGATCCTCACAAAGGCTTGCCCTC-3') and cloned into the pET-15b vector (Novagen, Millipore, UK). By using site-directed mutagenesis, the cysteine residues of cofilin1 were changed into serine using complementary oligonucleotides harboring the nucleotide exchanges (Cys39Ser: forward: 5'-GTGCTCTTCTCCCTGAGTG-3', reverse: 5'-CACTCAGGGAGAAGAGCAC-3'; Cys139Ser: forward: 5'-CAAGCAAACTCCTACGAGGAG-3', reverse: 5'-CTCCTCGTAGGAGTTTGCTTG-3'; Cys147Ser: forward: 5'-GACCGCTCCACCCTGG-3',

reverse: 5'-CCAGGGTGGAGCGGTC-3') and the KOD Hot Start Mastermix (Merck, Darmstadt, Germany). The plasmids were confirmed by sequencing (Seqlab, Göttingen, Germany).

Expression, purification and thermal stability

The human cofilin1 WT and the mutant Cys139/147Ser were expressed as His-Tag fusion proteins in *E. coli* as described before [70]. The proteins were purified by immobilized metal affinity chromatography using the His Trap Kit from GE Healthcare Life Science, USA. Expression and purification efficiency were analyzed by SDS-PAGE using precast gels from BioRad, USA, and Coomassie staining. The thermal stability of the proteins was analyzed by recording the emission at 600 nm over time with increasing temperature from 20 °C to 70 °C (2 °C per 3 min) using the Shimadzu UV1800.

To investigate direct actin-independent effects of recombinant cofilin1 protein on mitochondrial parameters, such as respiration, ROS production or the membrane potential, freshly isolated mitochondria from adult mouse cortex were prepared as previously described (Chapter 3.6.7 Mitochondrial isolation). Cofilin1 recombinant protein was either used in the native way, oxidized by 100 µM H_2O_2 incubation for 30 minutes, or reduced with 10 mM freshly dissolved dithiothreitol (DTT) for 30 minutes. The remaining elution buffer from the protein purification process was substituted by PBS using sephadex-based PD MidiTrap G-25 columns (GE Healthcare, Chicago, USA). Afterwards, protein amount was determined by NanoPhotometer™ (Implen, Munich, Germany). 0.13-0.25 µg recombinant protein was used per µg mitochondrial protein and incubated for 30 - 60 minutes at room temperature and another 10 minutes at 37 °C. The assays were performed as described in chapters 3.4.3 Seahorse measurement, 3.5.3 TMRE and 3.5.4 MitoSOX.

3.10 Actin-rod induction

Actin-rod formation was induced by treating primary neurons (DIV6) plated on glass-coverslips (Ø 12 mm) with ATP-depleting medium composed of 10 mM sodium azide (NaN_3) and 6 mM 2-deoxy-D-glucose (2-DG) diluted in EBSS for 30 minutes at 37 °C as previously described [15, 115]. The actin-chromobody SNAP-tag plasmid (0.5 µg/well) was transfected two days prior to ATP depletion. SNAP-Cell® TMR Star (New England Biolabs, Ipswich, England) was incubated at a concentration of 1:3,000 for 24 hours the day prior to

the treatment. Afterwards, cells were washed once with PBS and fixed with 4% formaldehyde (Pierce™ diluted from 16 % Formaldehyde (w/v), Methanol-free; Thermo Fisher Scientific, Darmstadt, Germany). Subsequently, glass coverslips were fixed on precleaned microscope slides (MENZEL-Gläser, Braunschweig, Germany) with fluorescence mounting medium (Dako North America Inc., Carpinteria, USA).

Images were obtained using an LSM 700 confocal microscope with a 63x/1.4 NA oil objective (Zeiss). A 488 nm laser was used for GFP constructs and a 555 nm laser for SNAP-Cell® TMR Star. Images were acquired of single cells showing expression of Actin Chromobody SNAP as well as Cre-GFP or IRES-GFP, respectively. Maximum intensity projections of 30 confocal slices (Z-stacks) per cell were calculated using FIJI (NIH, Bethesda, USA). After thresholding the images to a certain particle size of less than 10 μm [115] the number of spots with the highest fluorescence intensity (actin rods) was acquired by FIJI.

3.11 Statistical analysis

Presented data are shown as mean values with standard deviation (SD). The statistical analysis of the present data was performed using the one-way analysis of variance (ANOVA) followed by Scheffé's- or Fisher's LSD post-hoc test (for Western blot analysis) to correct for multiple comparison. Calculations were done using WinSTAT standard statistical software (R. Fitch Software, Bad Krozingen, Germany) or GraphPad Prism 8 (San Diego, USA). For comparison of two groups, the unpaired t-test was used. Data with $p<0.05$ (*); $p<0.01$ (**) or $p<0.001$ (***) were considered statistically significant different.

Quantification and comparison of RNA or Western blot signals was realized by Image Lab 4.0.1 Software (Bio-Rad, Munich, Germany). By using the rectangular tool, bands were specifically orbited and signal intensities were calculated by background subtraction as percent of the intensity of the respective band of a housekeeping gene or protein.

4 Results

4.1 Effects of cofilin1 knockout on mitochondrial dynamics and function in MEF cells

Mitochondrial dynamics is highly regulated by a multitude of mitochondrial shaping proteins, such as DRP1, Fis1, Mitofusion1/2 or OPA1, as previously reviewed [148]. Recently, actin dynamics emerged as an additional key factor for DRP1 recruitment to mitochondria, and therefore attains relevance in the regulation of mitochondrial dynamics [83]. In this regard, this study addressed the role of the actin-binding proteins cofilin1 and INF2 on mitochondrial dynamics. For this purpose, mouse embryonic fibroblasts (MEF) were used containing a floxed cofilin1 gene region ($MEF^{flx/flx}$), which can be modulated by Cre recombinase. Cre is a bacterial protein, but upon transfection into mammalian cells and subsequent activation, it binds and cuts the floxed gene regions which results in specific deletions of these genetic areas. In the present experimental setup, Cre activation was induced by 1 μM 4-hydroxytamoxifen (TamOH) for 24 – 72 hours. Western blot analysis of protein lysates from permanent expressing Cre-MEFs (MEF $MerCreMer^{flx/flx}$) revealed a robust knockdown after 48 hours after TamOH addition (Figure 9 A). In MEF cells, which only carry the floxed cofilin1-gene region, but no Cre enzyme, cofilin1 protein levels were unaltered after TamOH treatment (Figure 9 A). Both, cofilin1 and INF2 are essential regulators of actin dynamics. Hence, mutual regulation was studied by assessing INF2 protein expression upon cofilin1 depletion. INF2 increased significantly upon cofilin1 downregulation (Figure 9 B), underlining counteracting properties of both actin-binding proteins.

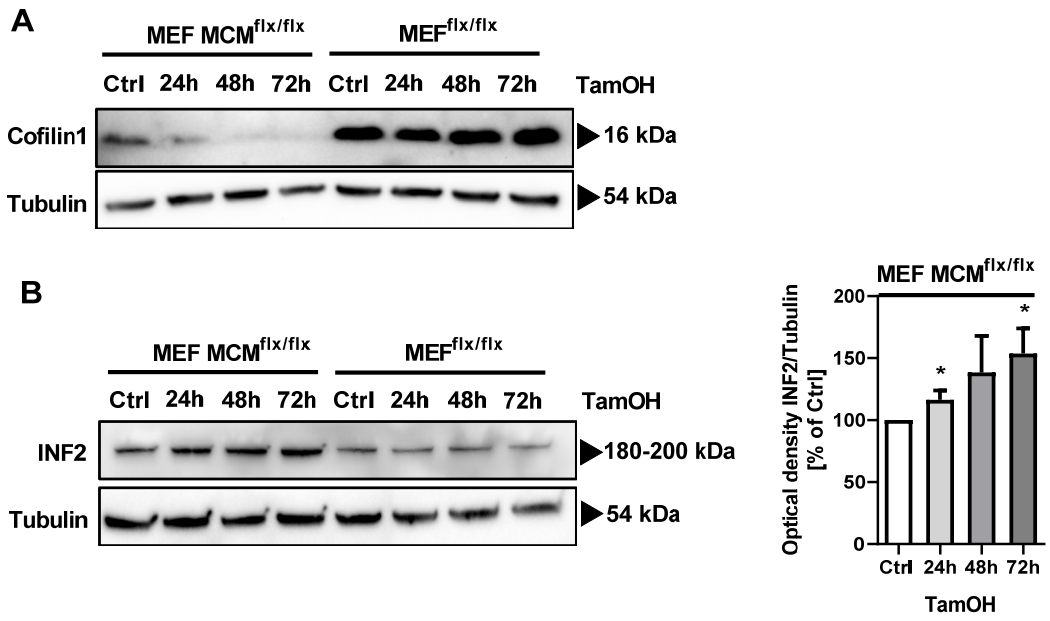

Figure 9. Cofilin1 knockout was achieved by 4-OH-tamoxifen (TamOH) treatment for 24 to 72 hours.

A Cofilin1 levels were evaluated by Western blot analysis either in MEF MCM$^{flx/flx}$ cells or in MEF$^{flx/flx}$ cells after 24 - 72 hours of 1 µM 4-hydroxytamoxifen treatment. **B** In MEF MCM$^{flx/flx}$ cells or in MEF$^{flx/flx}$ cells INF2 levels were analyzed after 1 µM TamOH treatment for the indicated time and subsequently quantified. (Mean + SD is shown of three replicates). Ctrl (control); TamOH (4-hydroxytamoxifen). *p<0.05 compared to Ctrl (ANOVA, Scheffé's-test).

4.1.1 Cofilin1 knockout leads to mitochondrial fragmentation via activation of DRP1

In the current study, the role of the actin-binding proteins on mitochondrial dynamics was determined, since actin acts as a scaffold to recruit DRP1. Mitochondrial morphology was assessed after staining active mitochondria with MitoTracker® Deep Red and by following categorization: Category I-mitochondria represents a tubular and elongated phenotype, whereas mitochondria of category II are fragmented and visible as dot-like structures, but still distributed throughout the cytosol. Category III is fragmented and localized closely to the nucleus, indicating cell damage and imminent cell death. Quantification of mitochondrial morphology of MEF MCM$^{flx/flx}$ cells revealed a predominantly fragmented mitochondrial phenotype (the amount of category II mitochondria increased from ~33 % to ~75 %; Figure 10 B) upon cofilin1 knockout induced by TamOH treatment. MEF$^{flx/flx}$ cells were used as a negative control to prove the specificity of this finding, as these cells do not show any tendency towards mitochondrial fragmentation upon TamOH treatment over the indicated time (Figure 10 C).

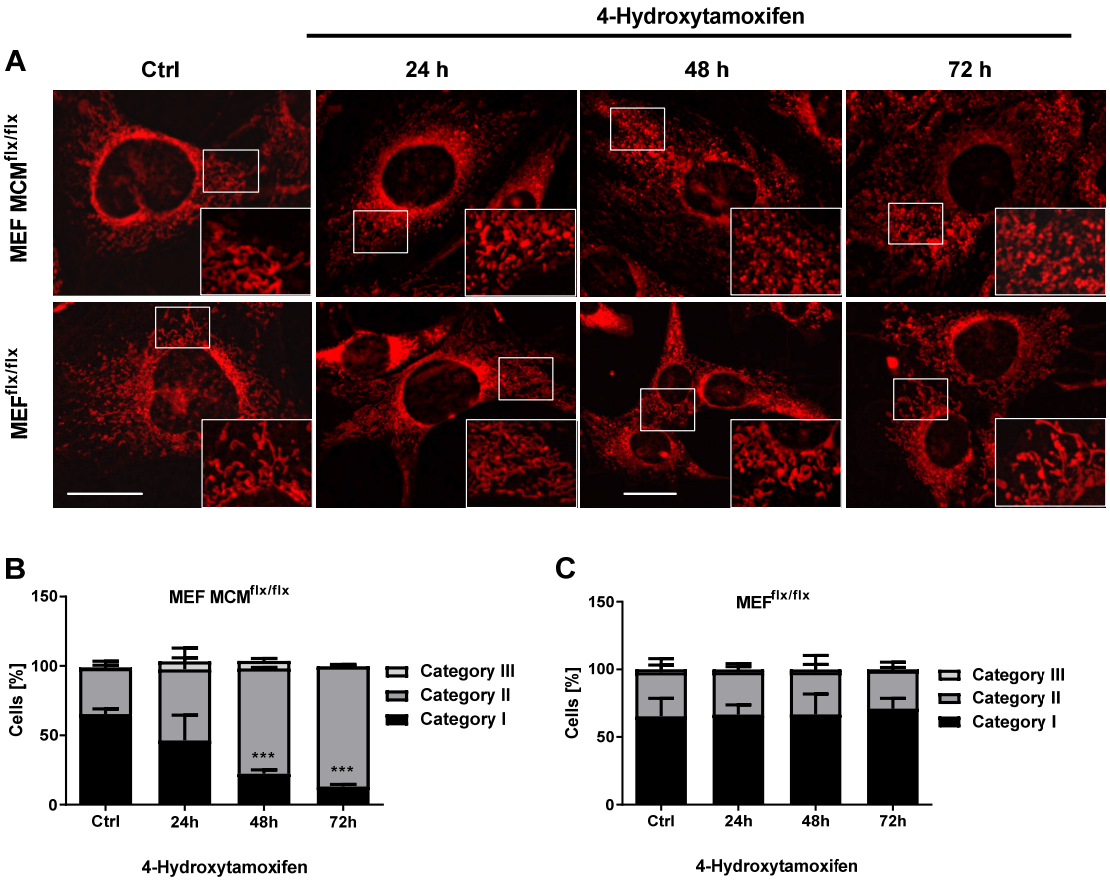

Figure 10. Mitochondrial morphology was influenced by cofilin1 knockout.

A Changes in mitochondrial morphology were visualized after 24 – 72 hours of 4-hydroxytamoxifen treatment using MitoTracker® Deep Red. *Scale bar* 25 µm. **B, C** Three hundred cells per condition were counted and rated into three categories according to the mitochondrial appearance (Category 1: elongated; Category 2: intermediate; Category 3: fragmented) and quantified as percentage of counted cells (mean + SD of three experiments). Ctrl (control). ***$p < 0.001$ compared to Ctrl (ANOVA, Scheffé's-test).

Further addressing the crucial role of a loss of cofilin1 on mitochondrial fragmentation, a rescue experiment was performed in cofilin1-deficient MEFs with either the wildtype-variant or alanin- or aspartate-mutants of serine residue 3. Accordingly, cells expressing the WT-cofilin1 protein exhibited a rescued mitochondrial phenotype comparable with cofilin1-retaining control cells (Figure 11). The active alanin-mutant was also able to restore the tubular network of mitochondria, whereas eGFP expressing cells, or cells transfected with the inactive aspartate-mutant showed a fragmented mitochondrial morphology (Figure 11), already described before (Figure 9 and Figure 10).

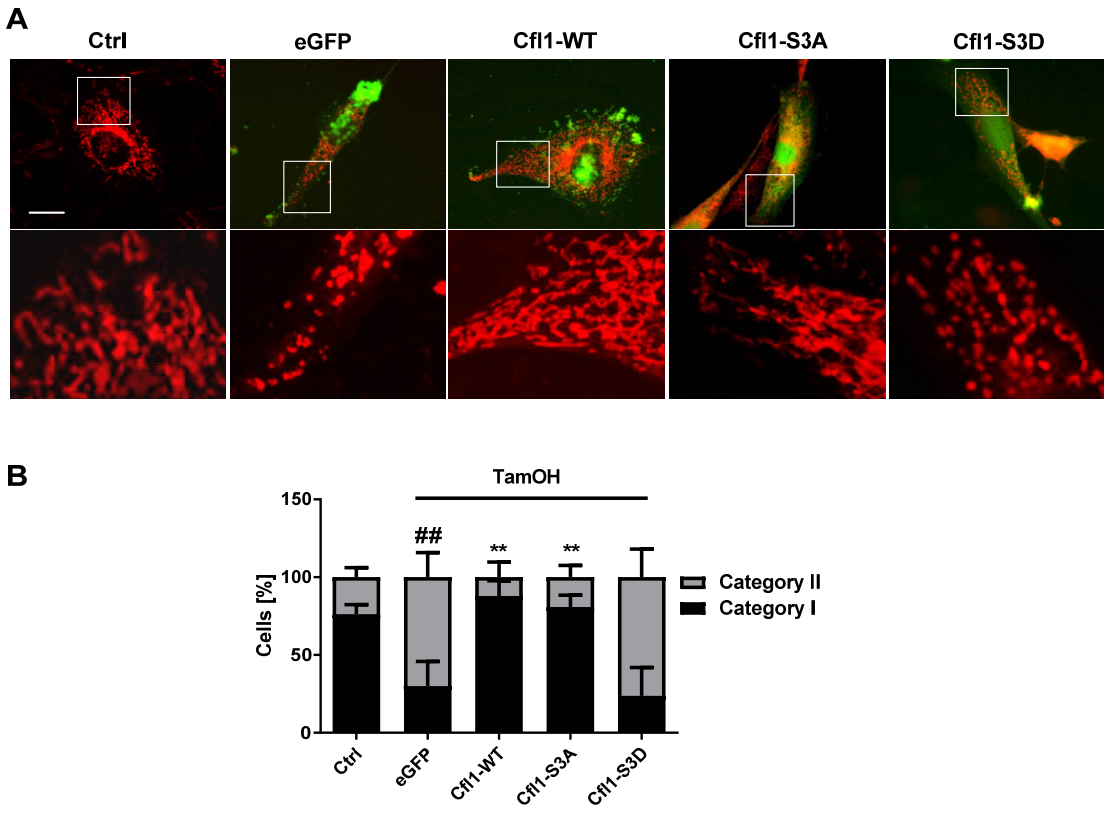

Figure 11. Cofilin1 reexpression resulted in recovery of mitochondrial morphology.

A Changes in mitochondrial morphology were visualized after 48 hours of 4-hydroxytamoxifen treatment and cofilin1-reexpression using MitoTracker® Deep Red. *Scale bar* 25 µm. **B** Three hundred cells per condition were counted and rated into three categories according to the mitochondrial appearance (Category 1: elongated; Category 2: intermediate; Category 3: fragmented) and quantified as percentage of counted cells (mean + SD of three experiments). Ctrl (control); Cfl1 (cofilin1); WT (wildtype); S3A (Ser3→Alanin mutation); S3D (Ser3→Aspartate mutation). ##p<0.01 compared to eGFP; **p<0.01 compared to Ctrl (ANOVA, Scheffé's-test).

Mitochondrial fragmentation is mostly attributed to the main fission-regulating protein dynamin-related protein 1 (DRP1). Therefore, DRP1 involvement was examined by addressing *DRP1* mRNA levels, and the phosphorylation state of serine residue 616 and 637 by Western blot, which influences DRP1 activity. DRP1 is active after phosphorylation of Ser616 alongside dephosphorylation at Ser637 [56]. Cofilin1 depletion resulted in increased *DRP1* mRNA levels (Figure 12 A), although the upregulation was not significant due to high variation. The phosphorylation state of the two crucial serine residues of DRP1 underlined that the protein is activated upon cofilin1 knockout (Figure 12 B, C), emphasizing the hypotheses that DRP1 is involved in actin-dependent control of mitochondrial dynamics upon cofilin1 depletion.

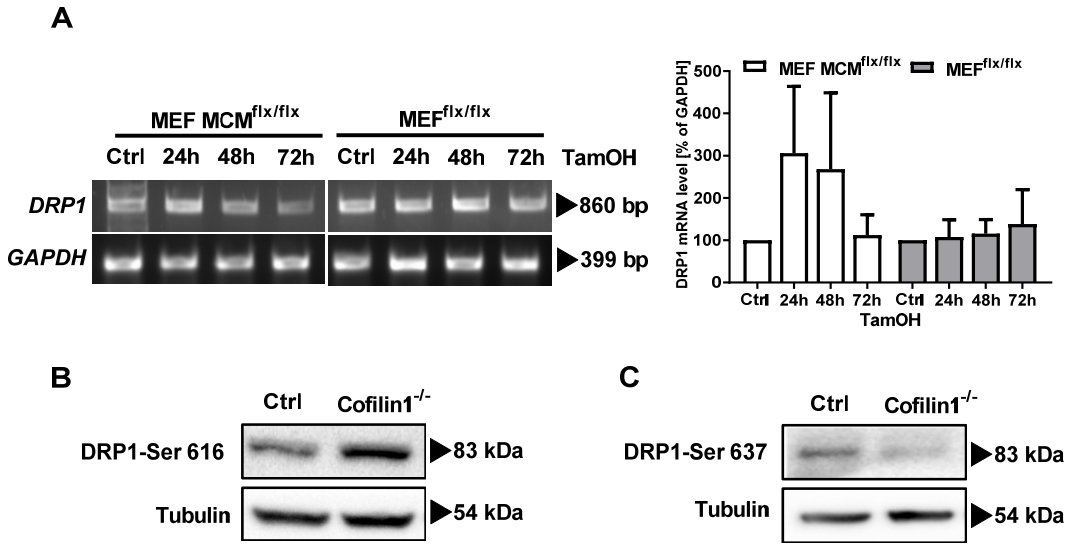

Figure 12. DRP1 was activated upon cofilin1 depletion.

A *DRP1 mRNA* level were evalutated by RT-PCR following visualization by ethidium bromide in an agarose gel in MEF MCM$^{flx/flx}$ and MEF$^{flx/flx}$ cells after 4-hydroxytamoxifen treatment. Three experiments were quantified (mean + SD). **B** DRP1 activation was examined by Western blot analysis of serine residue 637 and **C** serine residue 616 of DRP1 protein after cofilin1 knockdown by 4-hydroxytamoxifen in MEF MCM$^{flx/flx}$ cells.

To link mitochondrial fragmentation after cofilin1 knockout to the increased DRP1 activity, the influence of DRP1siRNA was investigated in this experimental setup. The efficiency of the siRNA was evaluated by Western blot analysis (Figure 13 C) and afterwards applied to MEF MCM$^{flx/flx}$ cells preincubated with TamOH. The mitochondrial morphology was analyzed after Mitotracker® Deep Red staining as previously described in this chapter. Silencing of DRP1 increased the number of category I-mitochondria significantly from 35 % to 68 % (Figure 13 B) in cofilin1-knockout MEFs underlining that DRP1 is the crucial mediator of actin-dependent mitochondrial fragmentation.

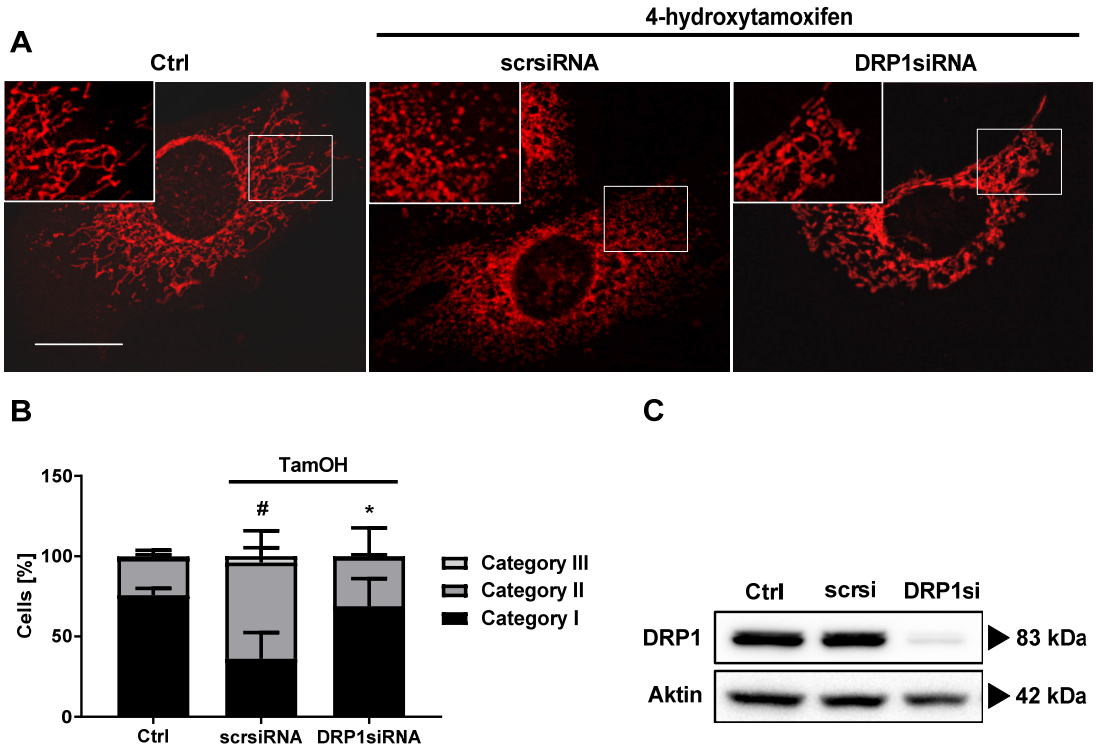

Figure 13. DRP1 silencing rescued mitochondrial fragmentation in cofilin1 knockout cells.

A Changes in mitochondrial morphology were visualized after 48 hours of 4-hydroxytamoxifen treatment and DRP1-silencing with siRNA using MitoTracker® Deep Red. *Scale bar* 25 µm. **B** Three hundred cells per condition were counted and rated into three categories according to the mitochondrial appearance (Category 1: elongated; Category 2: intermediate; Category 3: fragmented) and quantified as percentage of counted cells (mean + SD of three experiments). #p<0.05 compared to Ctrl; *p<0.05 compared to scrsiRNA transfection (ANOVA Scheffé's-test). **C** DRP1 downregulation was confirmed by Western blot analysis of MEF MCM$^{flx/flx}$ cells 48 hours after siRNA transfection. Ctrl (control); scrsi (scrambled siRNA); DRPsi (DRP1 siRNA); TamOH (4-hydroxytamoxifen).

4.1.2 Mitochondrial function is not impaired upon cofilin1 depletion

Mitochondrial fragmentation represents a prerequisite for cellular damage and subsequent cell death. However, in the recent study it is demonstrated that enhanced mitochondrial fragmentation due to altered actin dynamics is not accompanied by impaired mitochondrial function or cell death (Figure 14 and Figure 15). To address mitochondrial function, metabolic parameters were determined using a Seahorse XFe96 Analyzer. Here, the oxygen consumption rate (OCR), an indicator of mitochondrial respiration and the extracellular acidification rate (ECAR), representing the glycolysis rate, were measured simultaneously. The determined OCR of control MEFs and cofilin1$^{-/-}$ MEFs showed similar values, indicating that mitochondrial respiration was not impaired upon alterations in the mitochondrial phenotype (Figure 14 A). According to this finding, cofilin1$^{-/-}$ MEFs are able to cover their

energy demand by oxidative phosphorylation (OXPHOS) and do not rely on glycolysis (Figure 14 B).

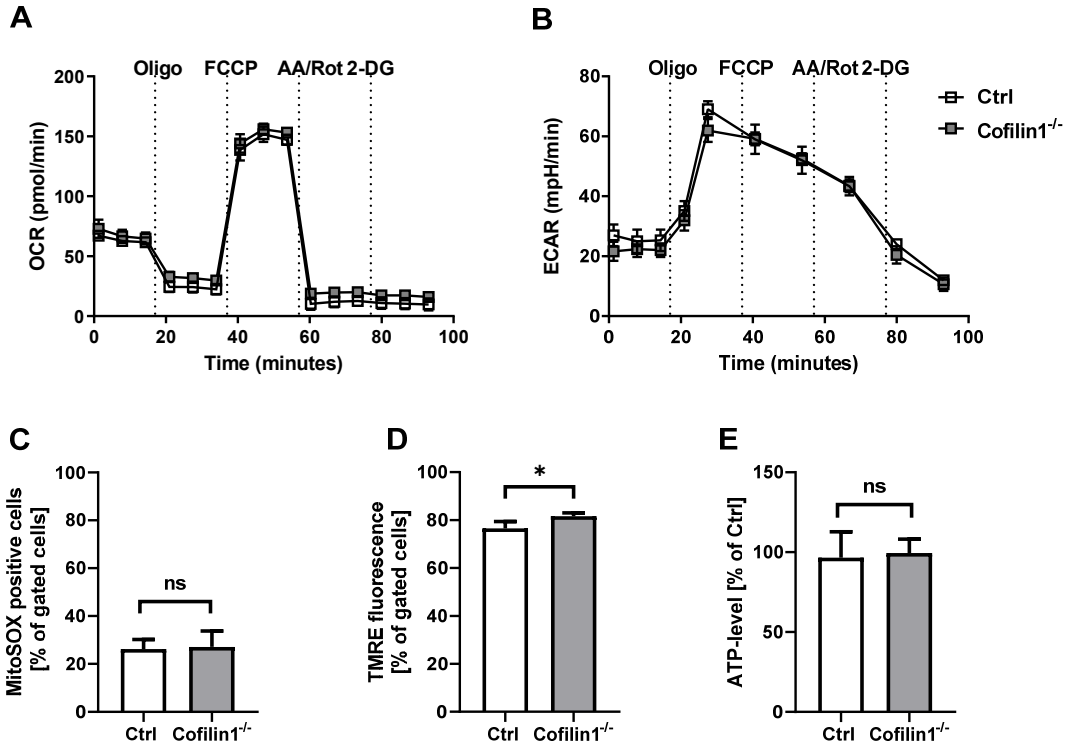

Figure 14. Mitochondrial function was not impacted by cofilin1 depletion.

A A representative seahorse measurement of control and cofilin1 knockdown MEF MCM$^{flx/flx}$ (TamOH treatment for 48 hours) cells was performed and the oxygen consumption rate (OCR) and **B** the extracellular acidification rate (ECAR) is shown. Four injections were necessary to metabolically perturb the respiration of cells: Oligo (oligomycin); FCCP (Carbonyl cyanide-4-(trifluoromethoxy)phenylhydrazone); AA (antimycin A); Rot (rotenone); 2-DG (2-deoxy-D-glucose). Mean values ± SD of n=6-8 replicates are presented. **C** Superoxides produced by mitochondria were investigated by flow cytometry and MitoSOX staining. Three replicates per condition are shown (mean + SD; 3,000 cells per replicate). **D** The mitochondrial membrane potential was evaluated by application of the fluorescent dye TMRE and following analysis via flow cytometry. Three replicates per condition are shown (mean + SD; 5,000 cells per replicate). **E** ATP levels were quantified by luminescence-based measurement and one representative measurement with n=8 replicates is shown (mean + SD). *p<0.05 compared to Ctrl; ns (not significant) (unpaired t-test).

Mitochondrial reactive oxygen species (ROS) are predominantly generated under pathological conditions and cellular disbalance, e.g. upon cell damage induced by glutamate or erastin. In these conditions, mitochondrial fragmentation is considered as a hallmark of the cell death cascade, involving mitochondrial ROS generation as a stress response to cellular ROS and lipid peroxidation. Here, mitochondrial ROS formation was investigated in cofilin1$^{-/-}$ MEFs to address, whether enhanced mitochondrial fragmentation implicitly induces mitochondrial ROS accumulation. These presented data substantiate, that the MitoSOX signal was not increased upon cofilin1 depletion in MEF cells (Figure 14 C). The

mitochondrial membrane potential was also examined to analyze potential mitochondrial impairment in cofilin1$^{-/-}$ cells. Surprisingly, the TMRE signal of cofilin1-deficient MEFs was slightly elevated compared to control cells (Figure 14 D). In accordance with the unaltered mitochondrial OCR data, ATP level were also unchanged in MEFs that lack the actin-binding protein cofilin1 (Figure 14 E).

In line with the maintained mitochondrial function in cofilin1$^{-/-}$ MEFs, FACS-based AnnexinV/PI measurements revealed constant ratios of early apoptotic or late necrotic features in the cofilin1-knockout MEFs compared to control cells (Figure 15), indicating that neither mitochondrial function nor cell death is affected upon cofilin1 deletion. To further evaluate the impact of cofilin1 knockout on cellular resilience upon erastin or glutamate exposure in MEF cells, the number of dead cells was quantified accordingly. Cofilin1 depletion in MEF cells had no impact on cellular resistance in these model systems.

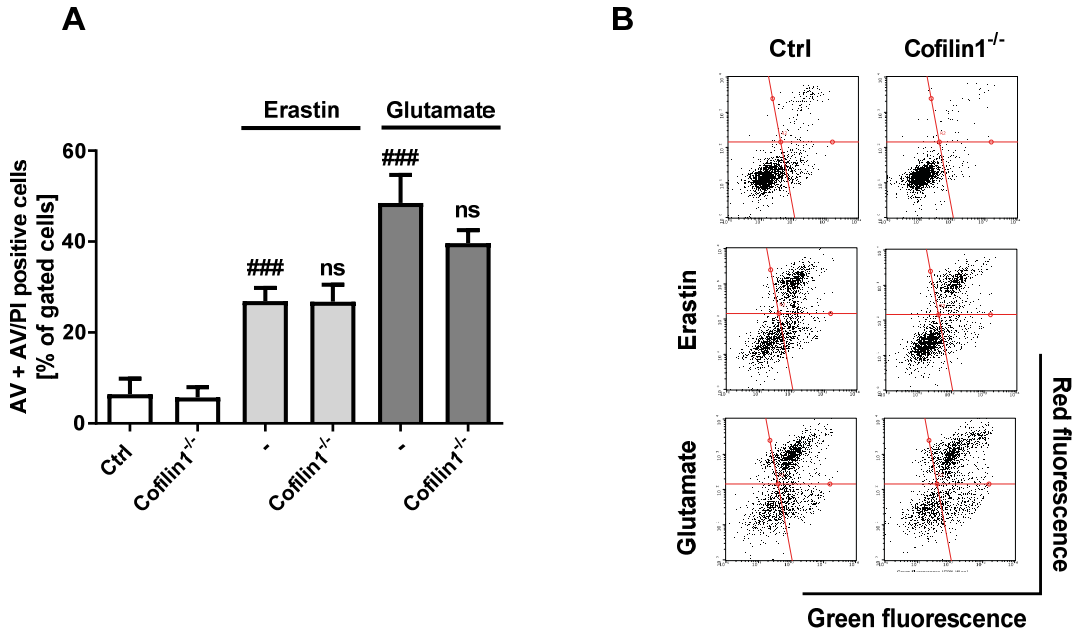

Figure 15. Cofilin1 knockout was not accompanied by enhanced cell death.

A AnnexinV (AV) and propidium iodide (PI) were used to visualize the amount of early apoptotic and late necrotic cells. Each bar represents the sum of AV and AV/PI positive cells (lower and upper right corner of the dot plot). 0.5 µM erastin or 5 mM glutamate was applied to induce cell death. **B** Representative dot plots exemplify the distribution of AV positive (lower right corner) or AV/PI positive (upper right corner) cells. Three replicates per condition are shown (mean + SD; 5,000 cells). ###p<0.001 (ANOVA; Scheffè's-test).

An altered mitochondrial phenotype requires not only an investigation of mitochondrial shaping proteins, but also of mitochondrial biogenesis markers and mitochondrial DNA (mtDNA) content representative for the mitochondrial mass. Therefore, the most important

mitochondrial biogenesis marker were assessed by qRT-PCR. Mitochondrial DNA was increased in cofilin1-knockout cells, suggesting an increased mitochondrial mass (Figure 16 A). In line with increased mtDNA, the *mRNA* of the nuclear respiratory factor 1 (Nrf-1), a key transcription factor for of mitochondrial DNA replication [169], was also significantly upregulated (Figure 16 D). Furthermore, the *mRNA* of the main mitochondrial biogenesis marker PGC1α was significantly elevated (Figure 16 F). The *mRNA* of the other proteins, such as p62, the mitochondrial transcription factor A (TFAM) and nuclear factor erythroid-2 related factor 2 (Nrf-2) remained unaffected by cofilin1 depletion (Figure 16).

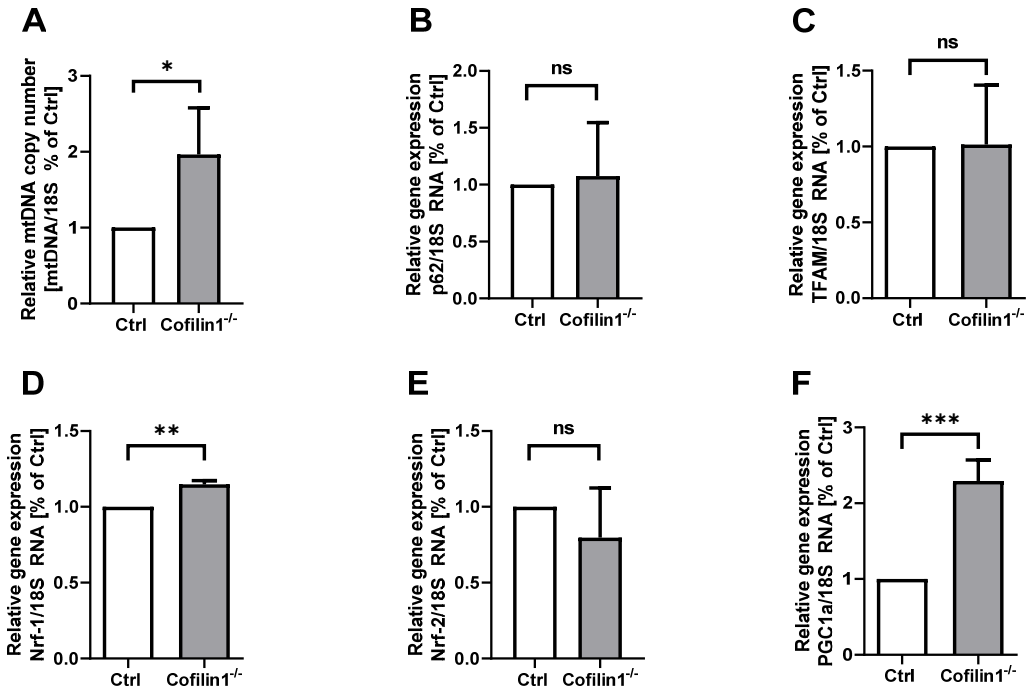

Figure 16. Proteins with impact on mitochondrial shape and biogenesis were evaluated by qRT-PCR of control and cofilin1$^{-/-}$ MEF MCM$^{flx/flx}$ cells.

A Relative mtDNA levels comparative to the reference gene 18S were quantified and the control cells were normalized to 1.0. **B** Relative *p62* mRNA levels normalized to 18S were quantified. **C** Relative *TFAM* mRNA levels normalized to 18S were quantified. **D** Relative *Nrf-1* mRNA levels normalized to 18S were quantified. **E** Relative *Nrf-2* mRNA levels normalized to 18S were quantified. **F** Relative *PGC1α* mRNA levels normalized to 18S were quantified. Values are given as mean + SD of n=3 replicates). ns= not significant; *p<0.05 compared to Ctrl; **p<0.01 compared to Ctrl; ***p<0.001 compared to Ctrl (unpaired t-test).

4.1.3 Cofilin1 knockout impacts mitochondrial Ca^{2+} levels

Previous studies demonstrate a role for INF2-mediated actin polymerization on ER-mitochondrial contacts impacting ER-mitochondrial Ca^{2+} transfer [24]. Thus, mitochondrial Ca^{2+} might also be influenced by altered actin dynamics due to a cofilin1-knockout. Here, the positively charged, cell-permeable, mitochondrial-specific Rhod-2 tetra-acetoxymethyester

(AM) dye was used to investigate basal mitochondrial Ca^{2+} levels in control MEFs and cofilin1$^{-/-}$ cells. Following flow cytometry analysis, cofilin1$^{-/-}$ MEFs (42 %) showed a higher basal signal of the Ca^{2+} indicator Rhod-2 AM than control MEFs (24 %) (Figure 17). This tendency was not observable in cells that lack the Cre recombinase, suggesting specific effects of cofilin1 knockout.

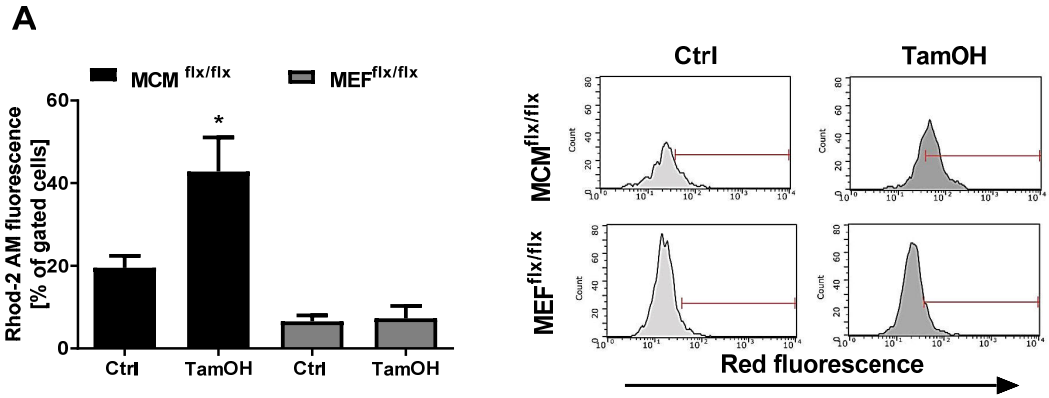

Figure 17. Basal mitochondrial Ca^{2+} levels increased upon cofilin1 depletion.

A The mitochondrial specific Ca^{2+} indicator Rhod-2 AM was added to the cells and subsequent flow cytometric measurement was performed with MEF MCM$^{flx/flx}$ cells and MEF$^{flx/flx}$ cells after TamOH treatment for 48 hours. Three replicates are shown (mean + SD). *p<0.05 (unpaired t-test). **B** Representative blots exemplify the intensity of red fluorescent cells. Ctrl (control); TamOH (4-hydroxytamoxifen).

Acute mitochondrial Ca^{2+} transients can be specifically measured by a mitochondrial-targeted red-fluorescent Ca^{2+} indicator mito-LAR GECO1.2 [179]. The mitochondrial localization of the indicator is demonstrated in Figure 18, as the signal of the Ca^{2+} indicator and mito-GFP perfectly overlap (Figure 18 C). Time lapse imaging of the mito-LAR GECO1.2 signal upon $CaCl_2$ stimulation revealed an attenuated mitochondrial Ca^{2+} uptake in cofilin1$^{-/-}$ MEFs compared to control cells (Figure 18 D).

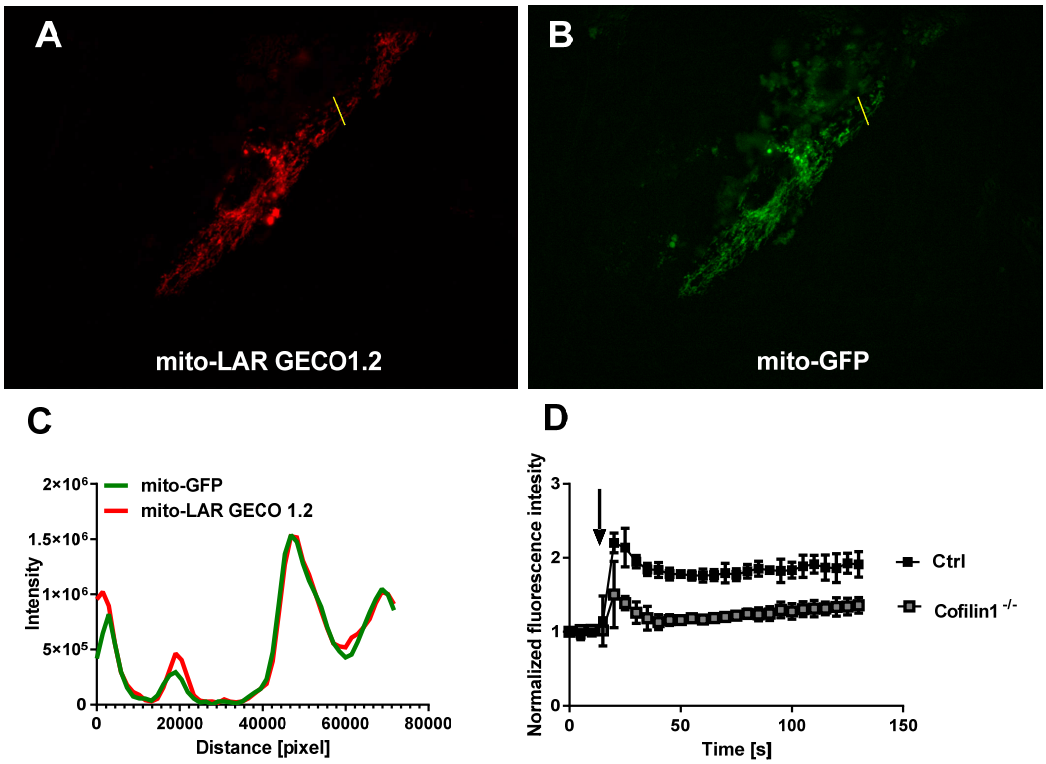

Figure 18. Mito-LAR GECO1.2 colocalized with the mitochondrial-specific GFP signal and revealed lower acute mitochondrial Ca^{2+} uptake in cofilin1$^{-/-}$ MEFs.

A The low-affinity mitochondrial Ca^{2+} indicator mito-LAR GECO1.2 was transfected in MEF MCM$^{flx/flx}$ cells and the expression pattern was visualized 48 hours later at an inverted epifluorescence microscope (40 x magnification). **B** Mitochondrial-targeted GFP was transfected for 48 hours and visualized accordingly. **C** The colocalization of mito-LAR GECO1.2 and mitochondria was quantified by intensity course over a certain distance (yellow line). **D** Control MEFs and cofilin1$^{-/-}$ MEFs were transfected with mito-LAR GECO1.2 plasmid and 48 hours later fluorescent intensity was recorded for 130 seconds. After 15 seconds, 60 mM $CaCl_2$ was applied to induce calcium uptake into mitochondria.

4.1.4 Mitochondrial calcium uniporter (MCU) expression alters in cofilin1 knockout cells

The inner mitochondrial membrane-located mitochondrial calcium uniporter was identified as the most important regulator of Ca^{2+} homeostasis between mitochondria and the cytosol. The MCU emerged as a pore-forming complex with several regulatory subunits. In cofilin1$^{-/-}$ cells, MCU protein abundance was significantly elevated, whereas in control cells (MEF$^{flx/flx}$) MCU levels were unaltered (Figure 19 A, B). In contrast, the analyzed protein levels of the regulatory subunits MCUR1, MICU1 and MICU2 were unchanged (Figure 19 B, C, D).

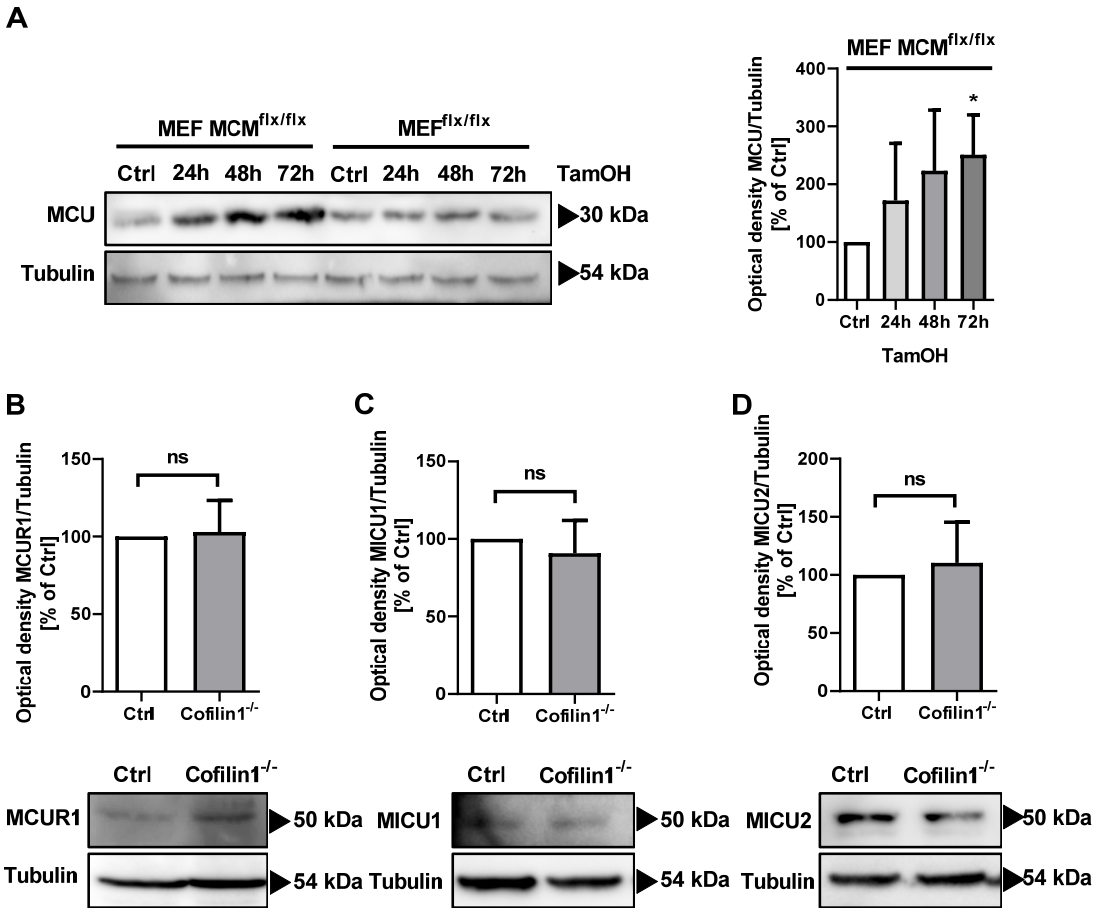

Figure 19. Mitochondrial calcium uniporter expression increased upon cofilin1 depletion.

A Western blot analysis of MCU expression was evaluated in MEF MCM$^{flx/flx}$ and MEF$^{flx/flx}$ cells upon 1 μM TamOH treatment for the indicated time period. The bar graph represents values from three experiments (mean + SD). **B** Western blot analysis of MCUR1 expression was evaluated in MEF MCM$^{flx/flx}$ either untreated or treated for 48 hours with 1 μM TamOH. The bar graph represents values from five experiments (mean + SD). **C** Western blot analysis of MICU1 expression was evaluated in MEF MCM$^{flx/flx}$ either untreated or treated for 48 hours with 1 μM TamOH. The bar graph represents values from three experiments (mean + SD). **D** Western blot analysis of MICU2 expression was evaluated in MEF MCM$^{flx/flx}$ either untreated or treated for 48 hours with 1 μM TamOH. The bar graph represents values from five experiments (mean + SD). Ctrl (control); TamOH (4-hydroxytamoxifen). ns= not significant; $p<0.05$ compared to Ctrl (unpaired t-test).

4.1.5 Autophagic flux is not altered in cofilin knockout MEFs

Autophagy is considered the main mechanism to remove dysfunctional or misfolded cellular proteins and organelles. In the past, the actin cytoskeleton was uncovered as an important regulator on autophagosome formation [1]. Therefore, putative impacts of cofilin1 knockout on autophagy were examined by Western blot analysis of the major autophagy protein LC3B. Upon autophagy induction by bafilomycin A, LC3B-I and II levels were evaluated in MEF MCM$^{flx/flx}$ cells with or without TamOH induction. The results of the Western blot analysis and subsequent quantification suggest that cofilin1 knockout exerted no effect on the induction of autophagosomal proteins (Figure 20 A, B), indicating that despite alterations at

the level of actin regulatory proteins, actin dynamics is still functional with regard to autophagosome formation.

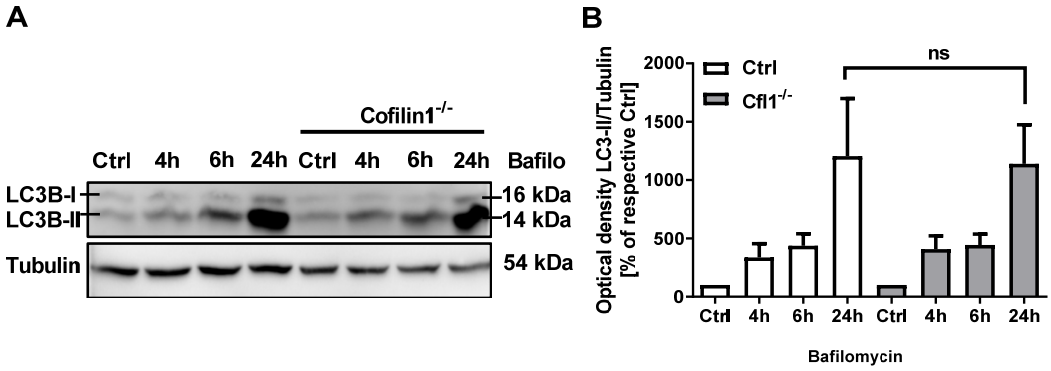

Figure 20. Autophagy regulation was independent of cofilin1 depletion.

A MEF MCM$^{flx/flx}$ were either used untreated or pretreated with 1 μM TamOH for 48 hours to induce cofilin1 knockout. Afterwards, bafilomycin A1 was added at a concentration of 10 nM for the indicated time. Western blot analysis was performed to evaluate LC3B I and LC3B-II level upon bafilomycin A1 treatment. **B** Quantification of LC3B-II was calculated from three experiments and presented as mean + SD. ns = not significant (ANOVA, LSD-test). Ctrl (control); Cfl1 (Cofilin1); Bafilo (Bafilomycin A1).

4.2 Oxidative cell death in HT22 cells

4.2.1 Cofilin1 depletion prevents oxidative stress-induced cell death

The small molecule erastin and the neurotransmitter glutamate are inducers of oxidative cell death in neuronal HT22 cells by inhibiting the X_c^--glutamate-cystine antiporter (Figure 3). Cells undergo cell death upon treatment with 0.2 – 1 μM erastin or 2 – 10 mM glutamate within less than 16 hours of exposure. These cells show characteristic features of cellular damage, such as a shrunken cell morphology as well as detachment from the surface of the cell culture plate, whereas healthy cells exhibit an even cellular network and a stretched morphology (Figure 21).

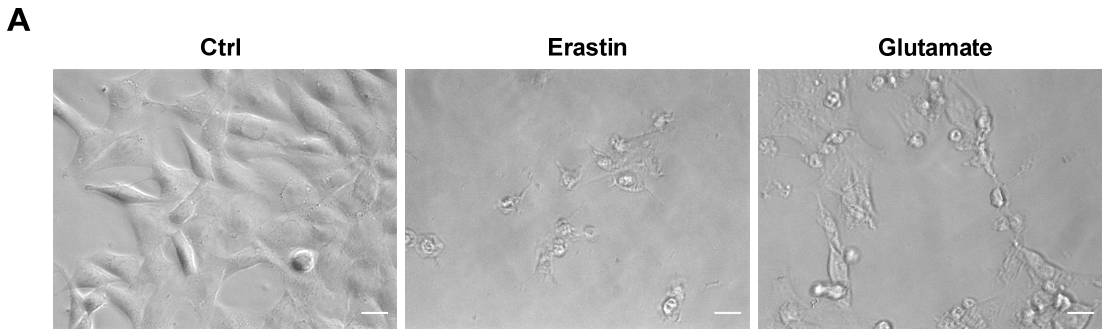

Figure 21. HT22 cells exhibited characteristic morphological features of cell death upon erastin or glutamate treatment.

A HT22 cells were plated into 8 well μ-slide and the cellular shape was investigated by brightfield microscopy 16 hours after challenging the cells with erastin or glutamate. *Scale bar* 25 μm.

Cofilin1 is among other actin-binding proteins one of the most important actin depolymerizing proteins. The activity of cofilin1 either to bind F-actin or to attain activity for translocation to mitochondria in terms of cell death transmission is regulated by the phosphorylation state of serine residue 3 [13]. Phosphatases, such as slingshot, chronophin or protein phosphatase 1/2A (PP1/2A) are able to dephosphorylate cofilin1 resulting in an activation of the protein, whereas phosphorylation is mediated by LIM domain kinase 1 and 2 (LIMK1, 2), and Testis-specific kinases 1 and 2 (TESK1, 2) causing its inactivation. Here, the activity status of cofilin1 upon cell death induction by erastin or glutamate was examined by Western blot analysis of serine residue 3. Interestingly, between 8 and 14 hours of erastin or glutamate exposure, cofilin1 is significantly dephosphorylated and thereby activated during oxytosis or ferroptosis (Figure 22 A, B).

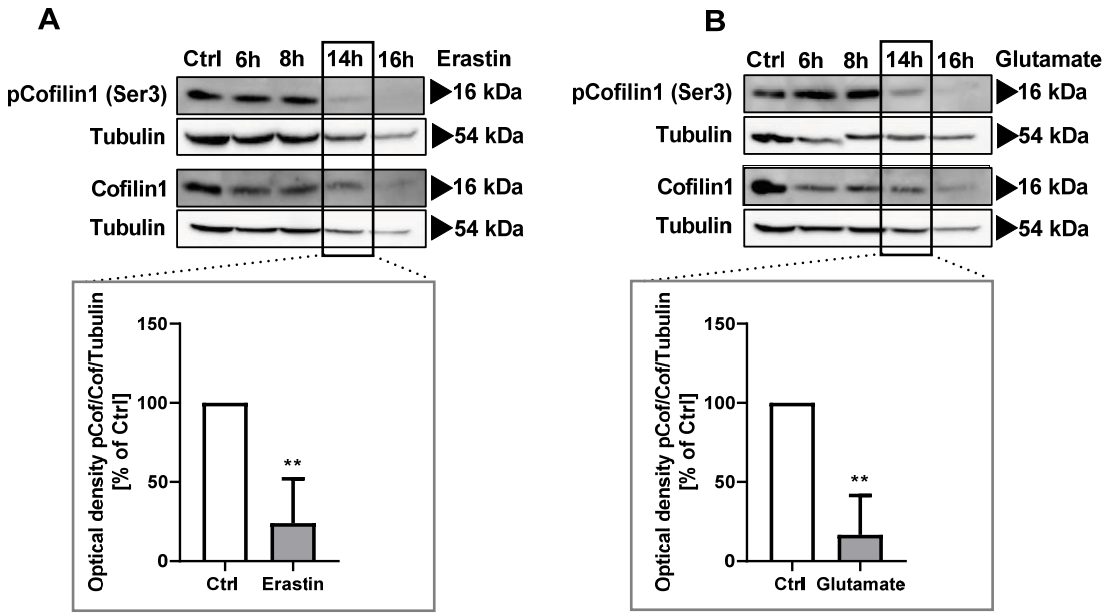

Figure 22. Cofilin1 was activated via dephosphorylation at serine residue 3 after erastin- or glutamate treatment.

A HT22 cells were challenged with 1 μM erastin for the indicated time and afterwards phosphorylated cofilin1 was analyzed via Western blot. Three blots were quantified (mean + SD). **B** Accordingly, HT22 cells were treated with 10 mM glutamate for the specified time period and quantified from three independent blots. (mean + SD). Ctrl (control), pCof (phosphorylated cofilin1-serine 3), Cof (cofilin1). **p<0.01 compared to Ctrl (unpaired t-test).

To further analyze effects of cofilin1 in model systems of oxidative stress-induced cell death in neuronal HT22 cells, a loss-of-function approach was used by transfecting a specific cofilin1 siRNA. The knockdown was evaluated by Western blot analysis and additionally confirmed by RT-PCR (Figure 23 A, B). In order to investigate the impact of cofilin1 on critical features of the cell death cascade upstream of mitochondria, oxidation of lipids and membranes were evaluated by BODIPY staining and following flow cytometry. This measurement revealed an increase of lipid peroxidation after 9 hours of erastin or glutamate exposure, which was unaffected by cofilin1 silencing (Figure 23 C). In line with this, cytosolic reactive oxygen species were elevated in control cells, as well as in cofilin1-knockdown cells after erastin or glutamate challenge (Figure 23 D).

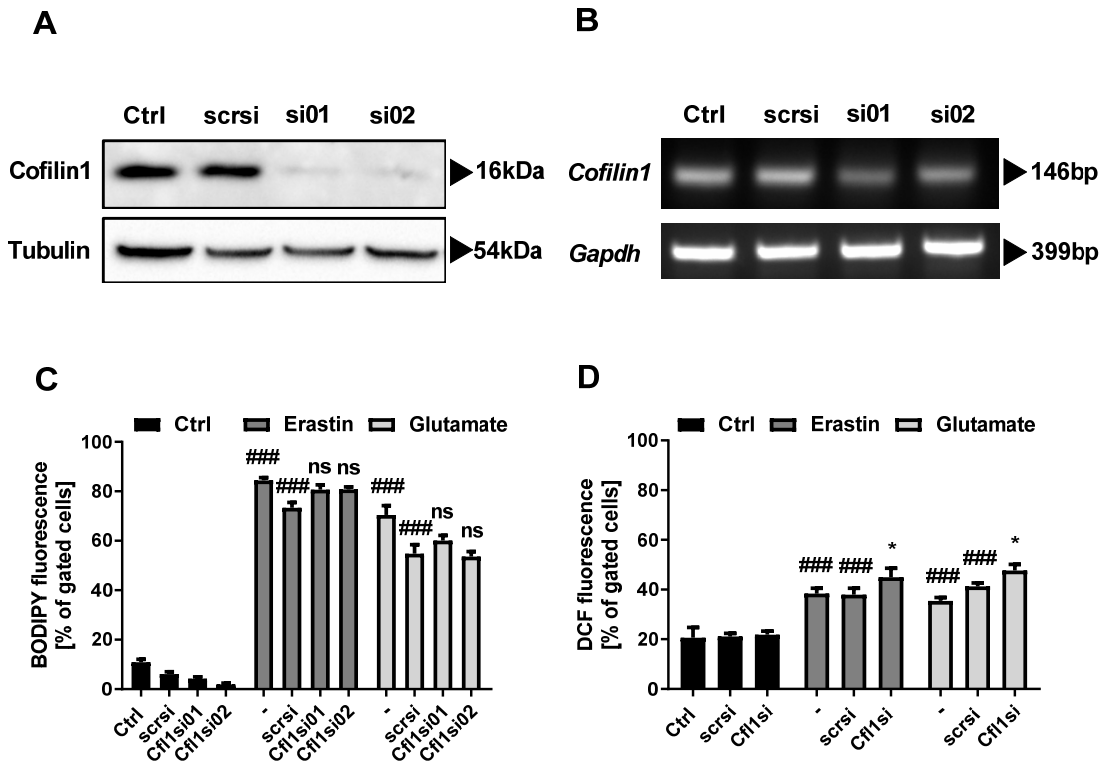

Figure 23. Knockdown of cofilin1 with a specific siRNA had no impact on lipid peroxidation and soluble ROS formation.

A 15 nM cofilin1 siRNA was incubated for 48 h and subsequently protein levels were evaluated by Western blot. Tubulin was used as a loading control for total protein amount. **B** Cofilin1 mRNA level were assessed by RT-PCR 48 h after siRNA transfection. Gapdh was used as an internal control. **C** Lipid peroxidation was determined 9 h after challenging the cells with 0.5 μM erastin or 5 mM glutamate with BODIPY fluorescencent dye and subsequent FACS measurement. **D** The amount of soluble ROS was measured after 0.8 μM erastin or 7 mM glutamate treatment for 10 h following DCF staining and FACS analysis. Data are given as mean + SD; 5,000 cells per replicate of n=3 replicates. Ctrl (control); scrsi (scrambled siRNA); Cfl1si (cofilin1 siRNA), ###p<0.001 compared to untreated ctrl; ns = not significant; *p<0.05 compared to erastin- or glutamate-treated Ctrl (ANOVA, Scheffé's-test).

4.2.2 Cofilin1 silencing rescues mitochondrial function upon glutamate- or erastin treatment

In order to characterize cofilin1's precise point of action, mitochondrial parameters of erastin- or glutamate treated HT22 cells were analyzed after cofilin1 knockdown. Interestingly, cofilin1 knockdown entirely prevented mitochondrial ROS production in HT22 cells challenged with erastin or glutamate, whereas in control cells or in cells transfected with an unspecific siRNA, MitoSOX fluorescence exceeded 60 % of the gated signal (Figure 24 A, B). Mitochondrial Ca^{2+} overload is considered as one of the major detrimental steps in the cell death cascade upon oxidative stress induction. Therefore, Rhod-2 AM fluorescent Ca^{2+} indicator was used to specifically monitor mitochondrial Ca^{2+} levels upon glutamate or erastin treatment. These results suggested, that cofilin1 silencing is

capable to reduce mitochondrial Ca^{2+} overload to a certain extent (erastin: scrsi 86 % vs. cofilin1si 68 %; glutamate: scrsi 68 % vs. cofilin1si 39%), indicating that cofilin1 plays a role in Ca^{2+}-dependent cell death transmission upstream of mitochondria.

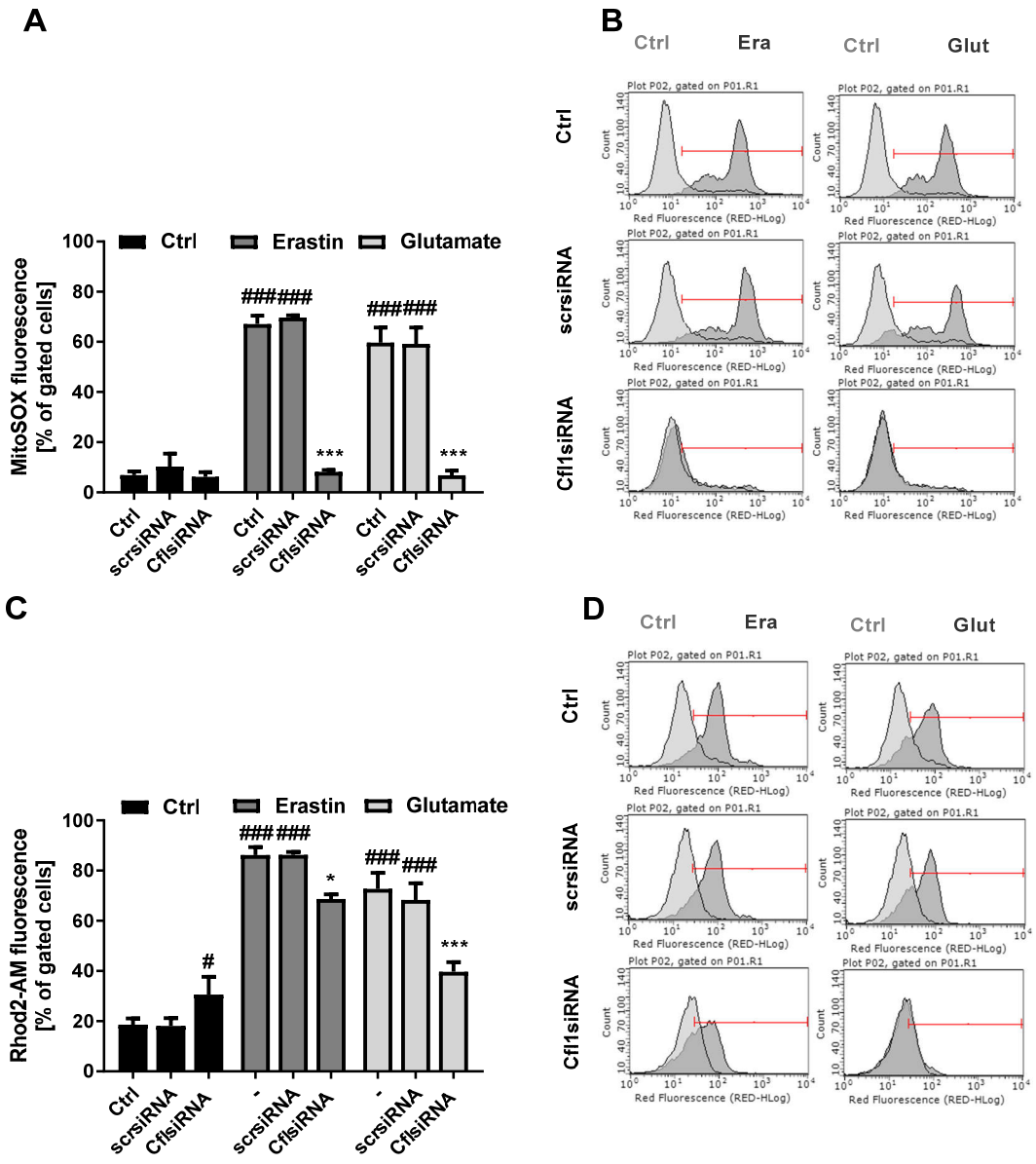

Figure 24. Detrimental mitochondrial ROS accumulation was abolished and mitochondrial Ca^{2+} overload was attenuated in cofilin1 knockout cells upon erastin or glutamate treatment.

A Mitochondrial ROS accumulation was measured by MitoSOX staining and FACS analysis after 16 hours treatment with 0.5 µM erastin 4 mM glutamate. Beforehand, cofilin1siRNA was incubated for 30 hours. Data are presented as mean + SD; 5,000 cells per replicate of n=3 replicates. **B** Representative images from the MitoSOX measurement are provided. **C** Rhod-2 acetoxymethyl ester (Rhod-2 AM) was used to specifically measure mitochondrial Ca^{2+} level after 16-hours treatment with 0.8 µM erastin or 8 mM glutamate. Values are projected as mean + SD; 5,000 cells per replicate of n=3 replicates. **D** Representative histograms from the Rhod-2 AM measurement are provided. Ctrl (control); scrsi (scrambled siRNA); Cfl1si (cofilin1 siRNA), #p<0.05 and ###p<0.001 compared to untreated ctrl, *p<0.05 compared to erastin- or glutamate-treated ctrl, ***p<0.001 compared to erastin- or glutamate-treated ctrl (ANOVA, Scheffé's-test).

The mitochondrial membrane potential ($\Delta\Psi_m$) is considered as one of the major factors defining the vitality and functional capability of these organelles. Sustained changes of the $\Delta\Psi_m$ are deleterious to a cell, since oxidative phosphorylation (OXPHOS) is derogated and the required clearance of defective mitochondria is impaired [189]. To evaluate the impact of cofilin1 depletion on this important mitochondrial parameter, $\Delta\Psi_m$ was evaluated by the fluorescence indicator TMRE. Considerably, the $\Delta\Psi_m$ was extensively preserved in cofilin1-knockdown HT22 cells after erastin or glutamate exposure compared to the control conditions (Ctrl; scrsiRNA) (Figure 25).

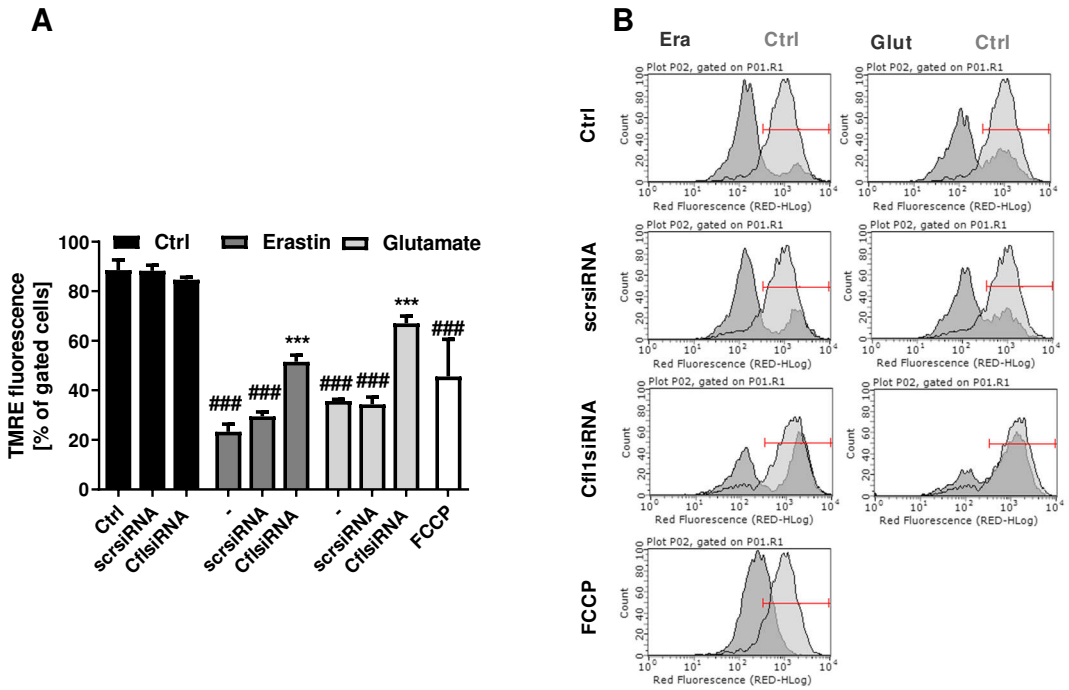

Figure 25. Mitochondrial membrane potential was preserved in cofilin1 knockout cells upon erastin or glutamate challenge.

A The mitochondrial membrane potential was evaluated by an appropriate cell permeant, positively-charged TMRE dye and following FACS analysis after 16 hours treatment with 1 µM erastin or 10 mM glutamate. Beforehand, cofilin1siRNA was incubated for 30 hours (mean + SD; 5,000 cells per replicate of n=3 replicates). **B** Representative histograms from the TMRE measurement are provided. The light grey curves show the untreated control condition, whereas the dark grey parts represent the left shifted TMRE fluorescence after erastin or glutamate treatment, or addition of the uncoupler FCCP. Ctrl (control); scrsi (scrambled siRNA); Cfl1si (cofilin1 siRNA), ###p<0.001 compared to untreated ctrl, ***p<0.001 compared to erastin- or glutamate-treated ctrl (ANOVA, Scheffé's-test).

The transmembrane potential generated by the proton gradient is directly harnessed to generate ATP [189]. As such, OXPHOS function is dependent on intact $\Delta\Psi_m$. Thus, the question arises how erastin and glutamate affect the mitochondrial respiration in control and cofilin1-silenced HT22 cells. The Seahorse XFe Analyzer was used to measure the oxygen consumption rate (OCR), representing mitochondrial respiration, and the extracellular acidification rate (ECAR), an indicator of glycolysis, simultaneously. After 9 hours of erastin

or glutamate exposure, control cells showed a decline of OCR and ECAR, suggesting that there is almost no energy production in these cells. Surprisingly, cofilin1siRNA transfected cells are also impaired in their mitochondrial respiration under basal conditions and after erastin or glutamate treatment (Figure 26 A, C), but the rate of glycolysis was largely preserved (Figure 26 B, D).

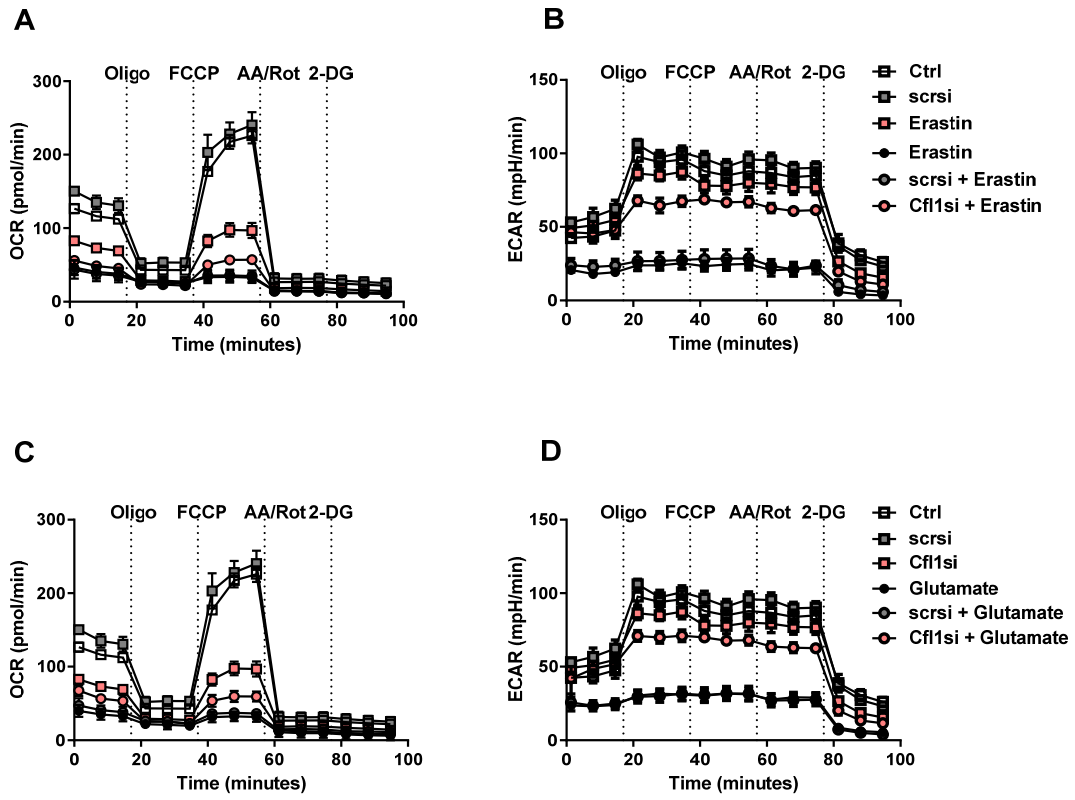

Figure 26. Cofilin1 knockdown preserved cellular ECAR in models of oxidative stress, whereas mitochondrial respiration was impaired.

Cofilin1siRNA was transfected for 48 hours. Afterwards, cells were damaged for 9 hours with 0.5 μM erastin or 7 mM glutamate. **A, C** Afterwards, the oxygen consumption rate (OCR) and **B, D** the extracellular acidification rate (ECAR) were determined by a Seahorse XFe96 Analyzer. Data of 3-6 replicates per condition are shown as mean ± SD. Oligo (oligomycin); FCCP (carbonyl cyanide 4-(trifluoromethoxy)phenylhydrazone); AA (antimycin A) Rot (rotenone); 2-DG (2-deoxy-D-glucose). Ctrl (control); scrsi (scrambled siRNA); Cfl1si (cofilin1 siRNA).

In addition to OCR and ECAR measurements, ATP levels were determined. To this end, HT22 cells were challenged with erastin or glutamate for 9 hours and following luminescence-based measurements of ATP levels. This revealed a significant decline of ATP production upon erastin or glutamate exposure under control conditions. However, in cofilin1-knockdown cells, ATP production was significantly preserved (Figure 27 A), underlining functional glycolysis despite loss of mitochondrial respiration. In this regard,

correlation between OCR and ECAR illustrates the metabolic potential of the cells, measured under baseline and stressed conditions by FCCP injection (Figure 27 B).

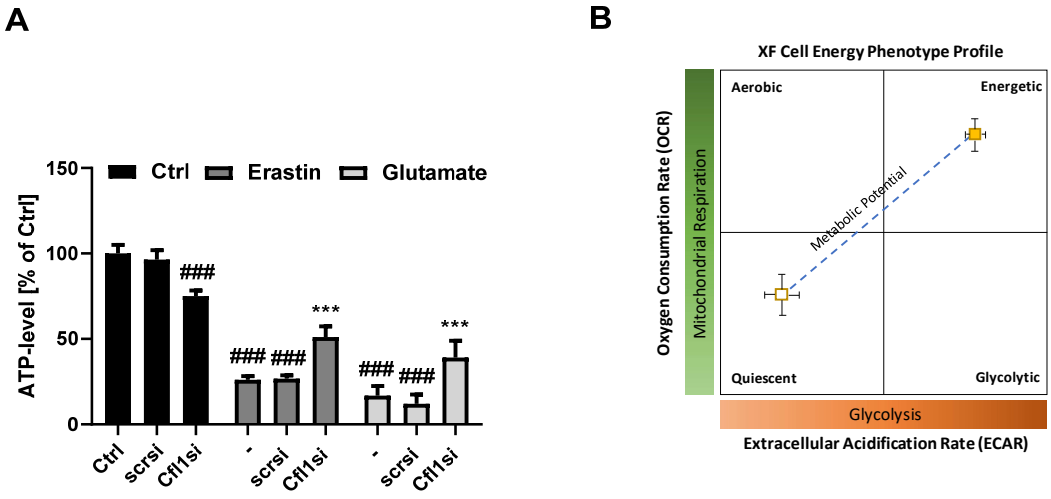

Figure 27. ATP levels were preserved upon cofilin1 knockdown in models of oxidative stress.

A Cofilin1 knockdown was achieved by siRNA incubation for 48 hours. Afterwards, cells were challenged for 8 hours with 0.7 µM erastin or 7 mM glutamate. Finally, ATP content was measured by luminescence-based measurement. Values are shown as mean + SD (n=8). Ctrl (control); scrsi (scrambled siRNA); Cfl1si (cofilin1 siRNA), ###p<0.001 compared to untreated ctrl, ***p<0.001 compared to erastin- or glutamate-treated ctrl (ANOVA, Scheffé's-test). **B** XF Cell Energy Phenotype Profile represents the metabolic potential of cells under basal and under stress conditions, e.g. after FCCP injection during the seahorse measurement.

Especially after glutamate or erastin treatment, metabolic bioenergetics underwent a mostly quiescent state in control conditions, whereas cells deficient for cofilin1 exhibited a considerably higher metabolic potential, indicating a functional energy production during oxidative stress (Figure 28). Of note, under control conditions, cofilin1 knockdown itself impaired the metabolic potential to a great extent (Figure 28; Yellow box).

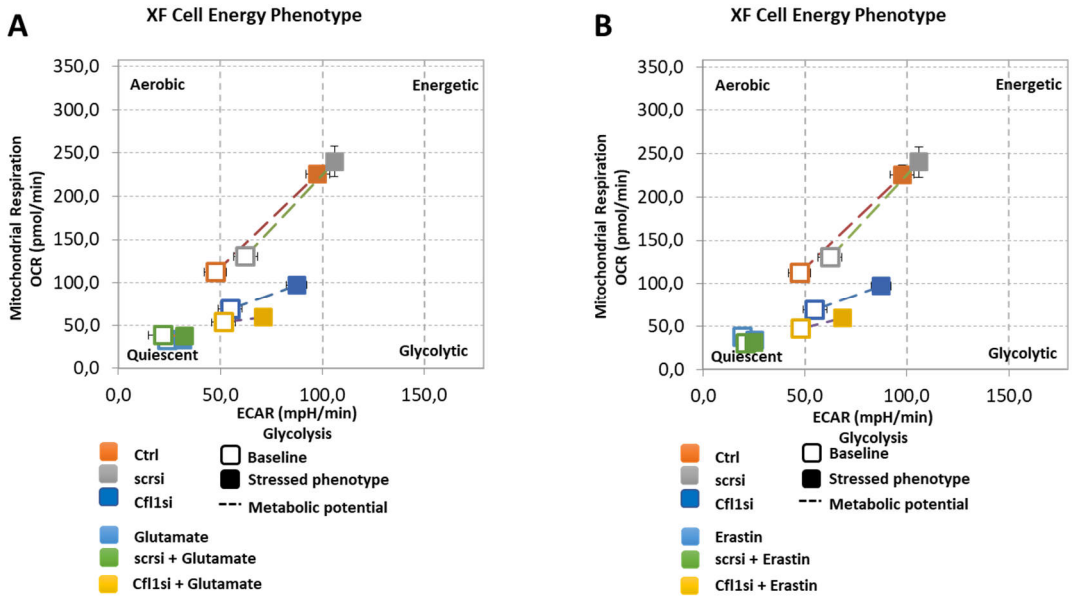

Figure 28. Metabolic profile of cofilin1 silenced HT22 cells under basal and under stress conditions.

A, B The cell energy phenotype correlates the OCR and the ECAR of the cells at basal conditions (open dot) measured before the first compound was injected by the system and after FCCP injection, representing a stressed phenotype (filled dot). The displayed metabolic potential (dashed line) represents the capacity to meet the required energy demand under conditions of stress. Ctrl (control); scrsi (scrambled siRNA); Cfl1si (cofilin1 siRNA).

To further investigate the mechanism by which cofilin1-knockdown cells switch to glycolysis under conditions of cellular damage, major glycolytic enzymes and their regulation were evaluated by Western blot. The regulating properties of c-Myc are well described in cancer cells, in which ATP is mostly generated by glycolysis (Warburg effect). Here, c-Myc is considered to regulate a variety of genes encoding glycolytic enzymes and thus drives energy production towards glycolysis [40, 59]. The present data suggests a role for c-Myc in recovering the energy production of cofilin1-knockdown cells after erastin or glutamate exposure, as the protein level of c-Myc under these conditions increase evidently (Figure 29 A; Figure 30 A). One major protein regulating cellular bioenergetic pathways under hypoxic condition is the Hypoxia-inducing factor 1α (Hif1α). It is described as a trigger for glycolysis, as it enhances the conversion of glucose to pyruvate and subsequently to lactate. Moreover, by transcriptional activation of the pyruvate dehyrogenase kinase 1 (PDK1) Hif1α can actively suppress the tricarboxylic acid cycle (TCA) [87]. In neuronal HT22 cells, Hif1α protein level increased after 9 hours of erastin or glutamate exposure in cells transfected with an unspecific siRNA, whereas cofilin1-deficient cells exerted decreased Hif1α levels (Figure 29 B; Figure 30 B). While PDK1 protein expression was initially lower in cofilin1-deficient cells, the level converged with the expression in control cells after 9 hours, indicating that

PDK1 expression increases upon erastin or glutamate treatment in cofilin1-knockdown cells (Figure 29 C; Figure 30 C).

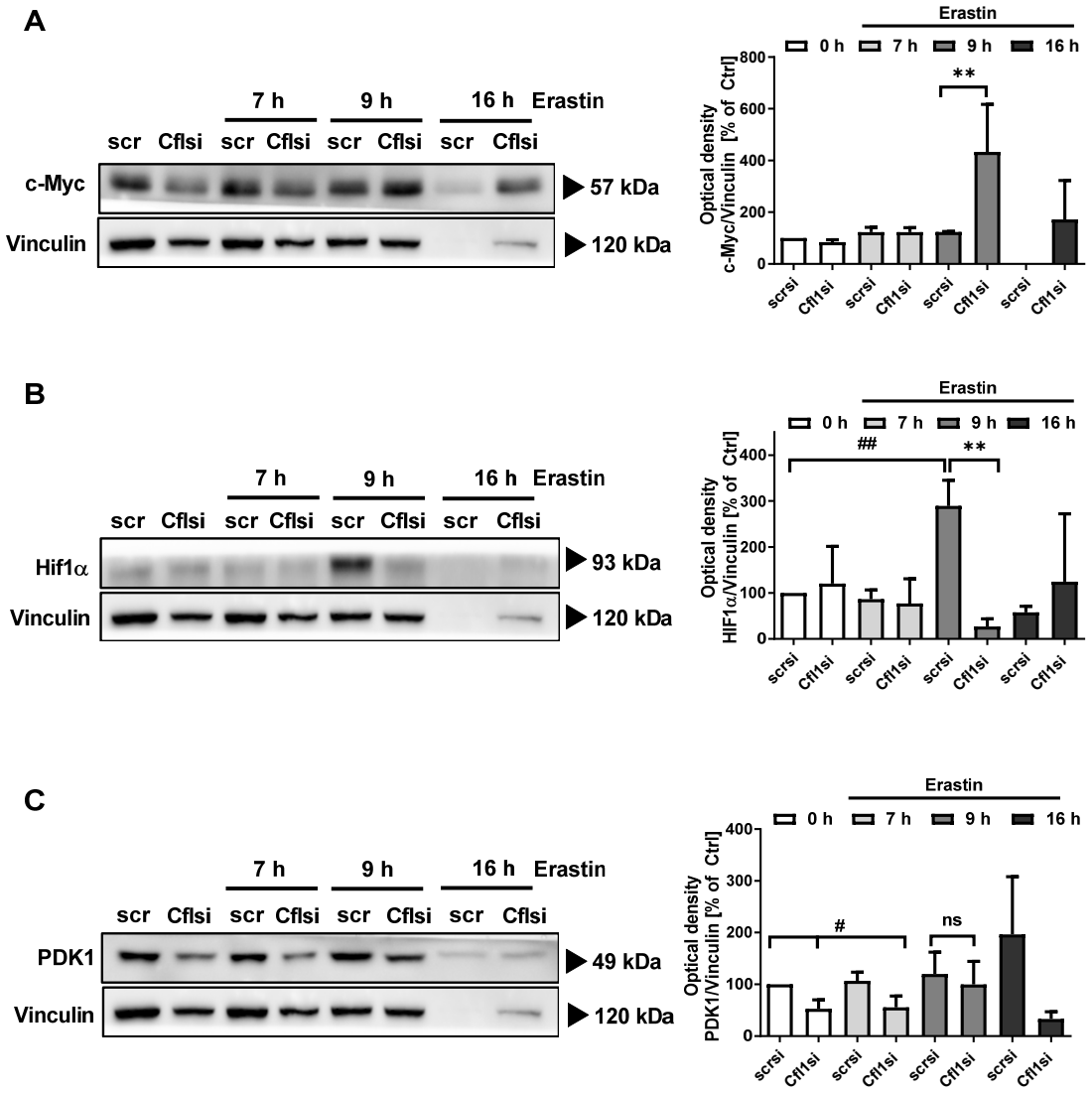

Figure 29. Protein abundance of major glycolysis-regulating proteins under erastin treatment in cofilin1-knockdown cells.

A c-Myc protein expression **B** Hif1α protein expression or **C** PDK1 protein levels were evaluated after 7, 9 or 16 hours of 1 μM erastin treatment by Western blot. Quantification of the data was realized by densitometric analysis of the Western blot signals and normalization to Vinculin. Data are presented as mean + SEM (n = 3). Scrsi (scrambled siRNA); Cfl1si (cofilin1siRNA). #p<0.05 and ##p<0.01 compared to scrsi ctrl; **p<0.01; ns (not significant) compared to erastin-treated scrsi (ANOVA, LSD-test).

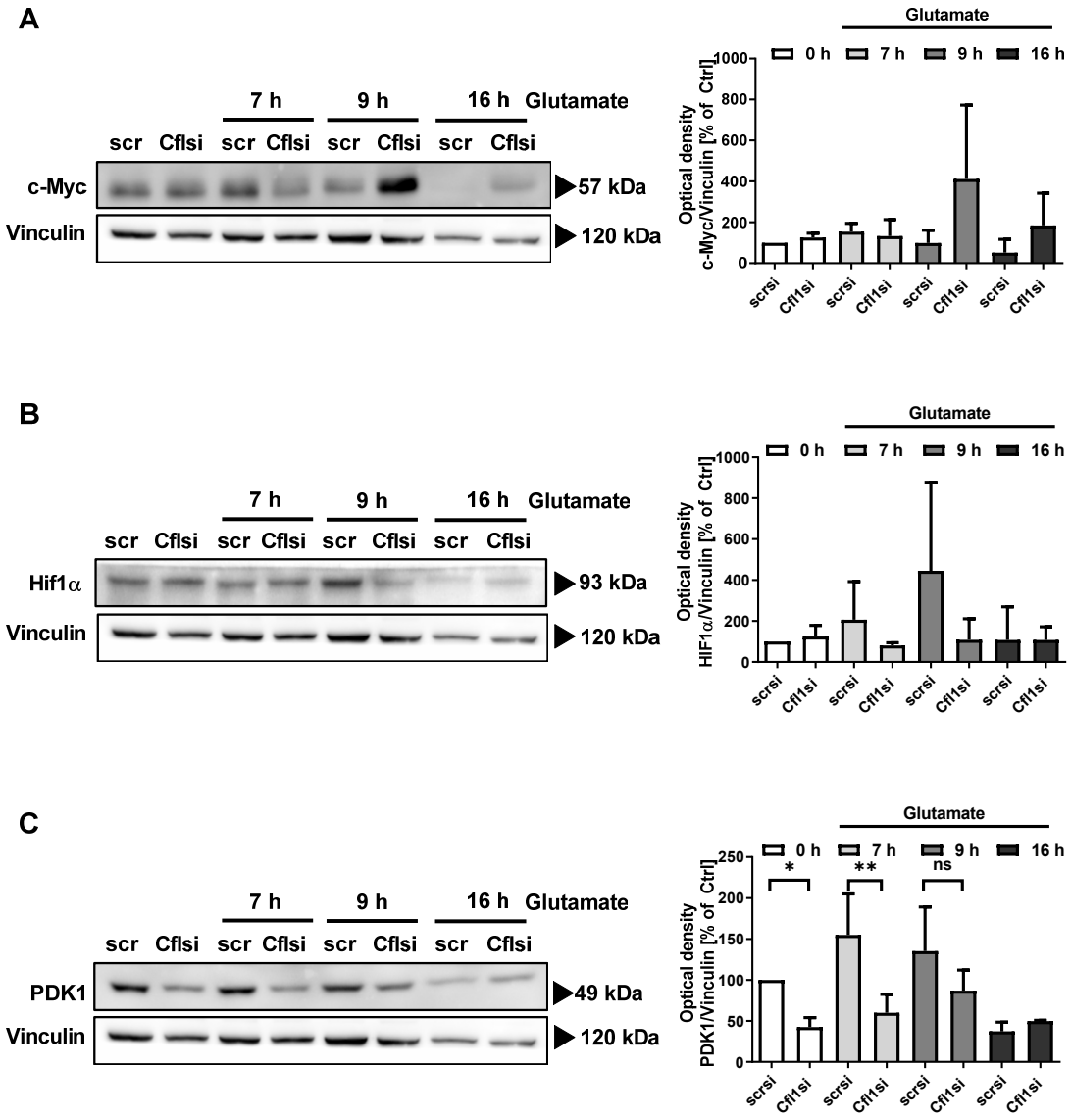

Figure 30. Protein abundance of major glycolysis-regulating proteins under glutamate treatment in cofilin1-knockdown cells.

A c-Myc protein expression **B** Hif1α protein expression or **C** PDK1 protein levels were evaluated after 7, 9 or 16 hours of 10 mM glutamate treatment by Western blot. Quantification of the data was realized by densitometric analysis of the Western blot signals and normalization to Vinculin. Data are presented as mean + SEM (n = 3). Scrsi (scrambled siRNA); Cfl1si (cofilin1siRNA). *p<0.05 and **p<0.01 compared to respective scrsi; ns (not significant) compared to glutamate-treated scrsiRNA ctrl (ANOVA, LSD-test).

Cofilin1 was described as a dispensable part in apoptosis induced by staurosporine in mouse embryonic fibroblasts (MEF), as cofilin1-deficient cells were still prone to cell death progression in this paradigm [139]. In this regard, it was interesting to examine cell death pathways in neuronal cells in order to understand possible discrepancies between different cell types. Therefore, neuronal HT22 cells were exposed to erastin or glutamate and the number of dead cells was determined by AnnexinV and propidium iodide (PI) staining. This

measurement revealed an increase of AnnexinV and PI positive cells upon erastin or glutamate treatment, which was anticipated in neuronal HT22 cells deficient for cofilin1 (Figure 31 A, B). This finding was confirmed by MTT assay to assess the metabolic activity of damaged cells under control and cofilin1-knockdown conditions. Addition of erastin or glutamate to the plated cells significantly decreased the metabolic activity of control and unspecific siRNA transfected cells, whereas the metabolic activity of cofilin1-silenced HT22 cells was significantly preserved (Figure 31 C, D). Further, cell impedance measurements were performed by xCELLigence system to monitor cell growth or cell detachment in a real-time manner, referred to as normalized cell index. Upon erastin or glutamate exposure, cell detach within five to ten hours due to cell shrinkage and cell death. Cofilin1siRNA was able to attenuate cell damage under the applied treatment conditions, represented by a considerably preserved normalized cell index (Figure 31 E, F).

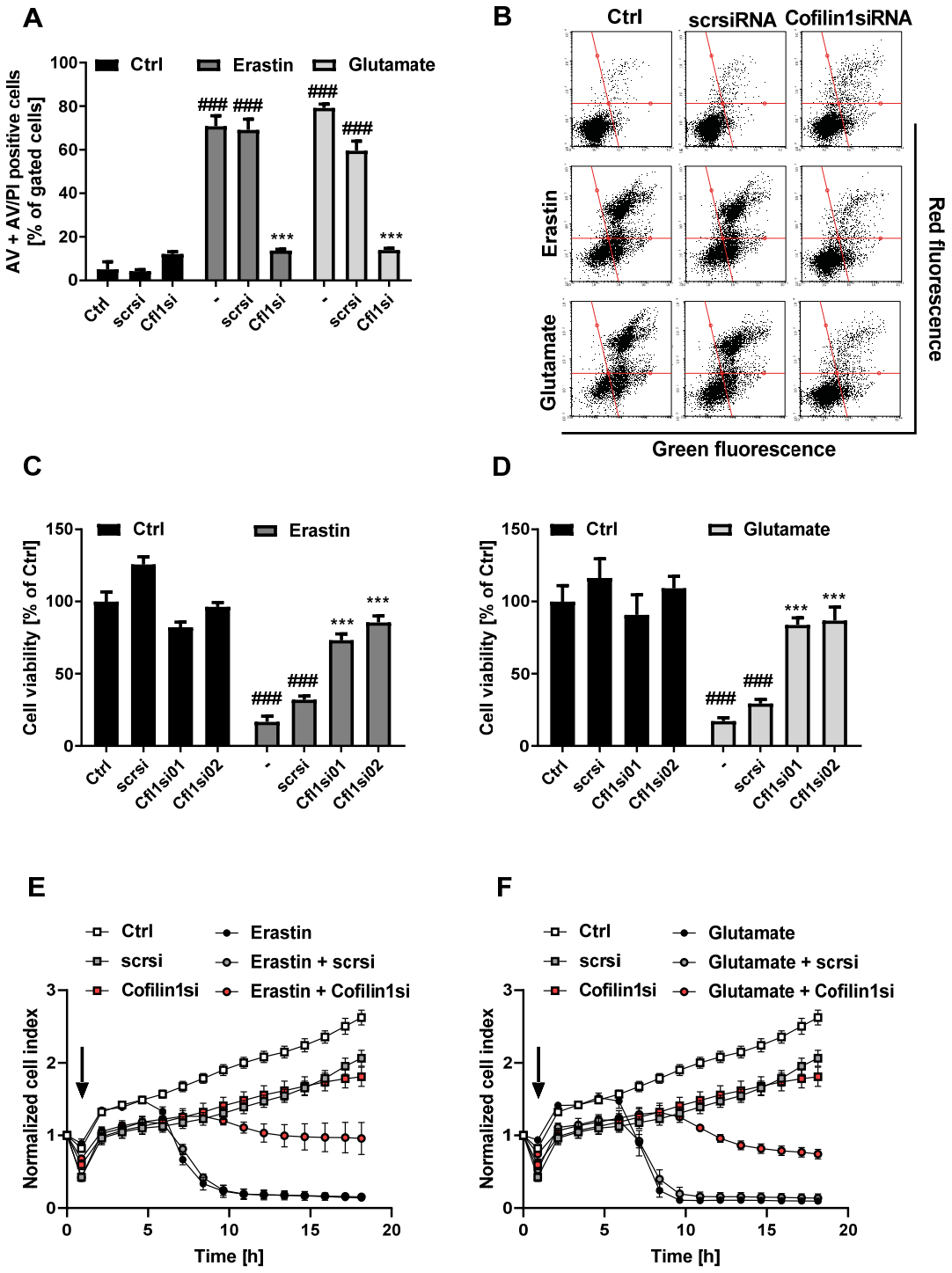

Figure 31. Cofilin1 silencing attenuated erastin- and glutamate-induced cell death in neuronal HT22 cells.

A AnnexinV and PI staining was conducted after 30 h of siRNA incubation and following 16 h of erastin 0.5 µM or glutamate 2 mM treatment. (mean + SD; 5,000 cells per replicate of n=3 replicates) **B** The dot plots show representative replicates of each condition of AnnexinV/PI FACS measurement. **C, D** Cells were treated with 0.2 µM erastin or 2 mM glutamate for 16 h and finally stained with MTT reagent. Values are shown as mean + SD; n=8 replicates. **E, F** xCELLigence measurement was performed after siRNA incubation for 30 h. The arrow indicates the time of application of 0.75 µM erastin and 8 mM glutamate. Data are given as mean + SD; n=8 replicates. Ctrl (control); scrsi (scrambled siRNA); Cfl1si (cofilin1 siRNA), ###p<0.001 compared to untreated Ctrl; ***p<0.001 compared to erastin- or glutamate-treated Ctrl (ANOVA, Scheffé's-test).

Cofilin1 was identified as a crucial mediator of oxytosis and ferroptosis in this study. As detected before by Western blot analysis, activation of cofilin1 was achieved by dephosphorylation (Figure 22). Due to cofilin1's deactivating phosphorylation, the impact of upstream inhibition on cellular resistance after administration of slingshot- or phosphatase 1/2A inhibitor in terms of oxidative stress-induced cell death mechanisms was addressed. Intriguingly, the inhibition of either slingshot or phosphatases or both substances, partially rescued the metabolic activity, but did not completely rescue cells upon erastin or glutamate exposure, indicating, that in these paradigms of cellular damage other pathways might contribute in addition to the activation of cofilin1 besides slingshot and phosphatase 1/2A (Figure 32).

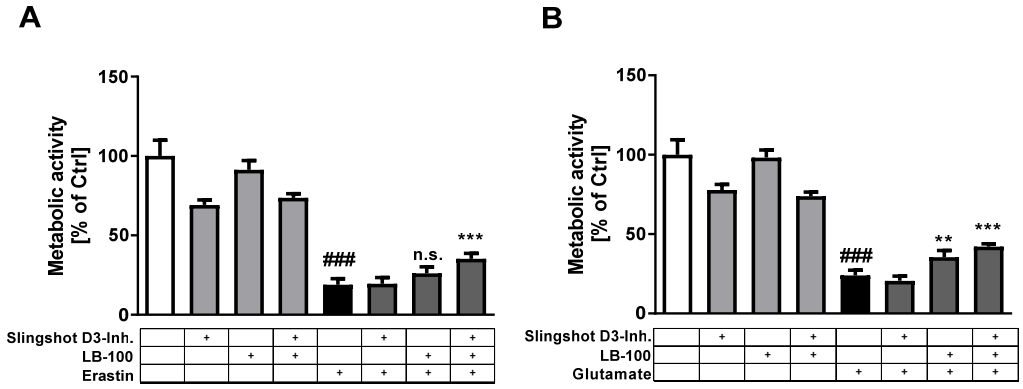

Figure 32. Slingshot and phosphatase inhibition revealed a slight protection upon erastin or glutamate exposure.

A HT22 cells were preincubated for 7 hours with 5 μM of the phosphatase inhibitor LB-100 and 15 μM Slingshot D3 inhibitor and afterwards challenged with 1 μM erastin or **B** 10 mM glutamate, respectively. Data are shown as mean + SD (n=8). **p<0.01 compared to erastin- or glutamate treated ctrl; ***p<0.001 compared to erastin- or glutamate treated ctrl; ###p<0.001 compared to untreated ctrl.

Further, cofilin1 was tested in an overexpression model in neuronal HT22 cells to evaluate effects of excessive cofilin1 expression on cell viability under basal conditions or in addition to erastin or glutamate application. Therefore, HT22 cells were transfected either with a plasmid encoding the wildtype cofilin1 protein, an active serine 3→alanine mutant (S3A), or an inactive serine 3→ aspartate mutant (S3D), respectively. The obtained data revealed a detrimental effect of the active cofilin1 versions (WT/S3A) on cell survival under basal condition, which could not be exacerbated by additional erastin or glutamate treatment for 7 hours. Intriguingly, the effect on cell death by expression of the inactive cofilin1 mutant S3D was significantly less pronounced, suggesting that the serine residue at position 3 of cofilin1 is decisive for functional consequences regarding cell impairment.

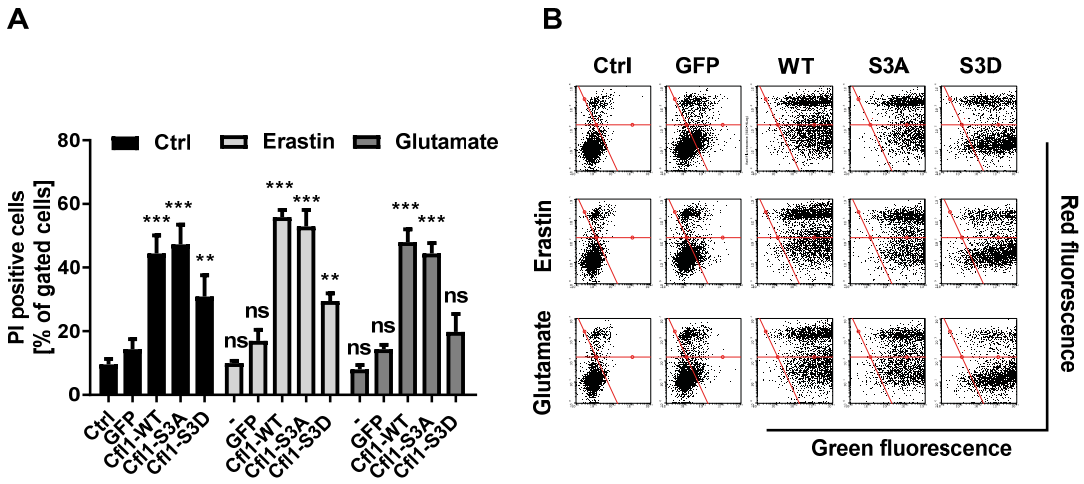

Figure 33. Cofilin1 overexpression resulted in enhanced cell death in neuronal HT22 cells.

A HT22 cells were transfected with the respective plasmids for 30 hours and afterwards treated with 1 μM erastin or 10 mM glutamate, respectively. FACS analysis was performed after staining with propidium iodide (PI) and 5,000 cells were measured per condition. Mean + SD from three replicates are presented. ns (not significant); **p<0.01 and ***p<0.001 compared to GFP-transfected ctrl (ANOVA, Scheffé's test). **B** Representative dot plots are shown for each condition.

Cofilin1 not only serves as an important actin-regulating protein with depolymerizing properties, but was also described to directly translocate to mitochondria upon cell death induction by staurosporine in mammalian cells [139]. How cofilin1 is transactivated to mitochondria and if other proteins besides actin are necessary for cofilin1's subcellular guidance and distribution is yet poorly understood. Therefore, the interaction of cofilin1 and DRP1, a known mitochondrial-targeted protein in cell death mechanisms [50, 64], was examined by co-immunoprecipitation assays after DRP1-pulldown upon erastin or glutamate treatment. The Western blot analysis of protein lysates after erastin or glutamate exposure for 6 – 8 hours and subsequent specific DRP1 precipitation revealed no direct interaction of cofilin1 and DRP1 (Figure 34), whereas the BCL2 associated X protein (BAX) interacted with DRP1 under these circumstances [84].

Figure 34. DRP1 pulldown after erastin- or glutamate exposure revealed an interaction with BAX, but not with cofilin1.

A HT22 cells were challenged with 1 μM erastin or 10 mM glutamate for 6 – 8 hours. From protein lysates, DRP1 was specifically culled and possible interacting proteins, such as BAX and cofilin1 were determined by Western blot. The input represents proteins detectable in the whole protein lysate.

4.2.3 INF2 depletion abrogates loss of mitochondrial function and cell death upon glutamate or erastin treatment

Considering that the actin-depolymerizing protein cofilin1 is attributed to major regulatory functions in cell death pathways, other actin-binding proteins might also take part in this context. Therefore, inverted-formin 2 emerged as an interesting candidate in neuronal cell death pathways. For a loss of function approach, a SMARTpool siRNA of four different sequences specifically targeted to INF2 was applied to neuronal HT22 cells. The efficiency on protein level was validated by Western blot analysis (Figure 35 A). To specify the point of action of INF2, cytosolic ROS formation was measured by DCF fluorescence indication and following flow cytometry. This measurement revealed a significant increase of the DCF signal in control cells and cells transfected with an unspecific siRNA (scrsiRNA) after erastin or glutamate exposure. Under these circumstances, INF2-knockdown cells exerted even higher or comparable soluble ROS levels as control cells (Figure 35 B), indicating that soluble ROS formation was not affected in the absence of INF2. Further, the amount of membrane and free fatty acid oxidation, an early hallmark in the cell death cascade induced by erastin or glutamate, was assessed by BODIPY staining and flow cytometry analysis. The BODIPY signal of control or scrsiRNA-transfected cells increased up to 40 – 60 % after 9 hours after cell death induction by erastin or glutamate. Surprisingly, also INF2siRNA-transfected cells contained similar amounts of the oxidized BODIPY signal as control cells (Figure 35 C), suggesting no impact of INF2 on early cell death parameters, such as lipid peroxidation.

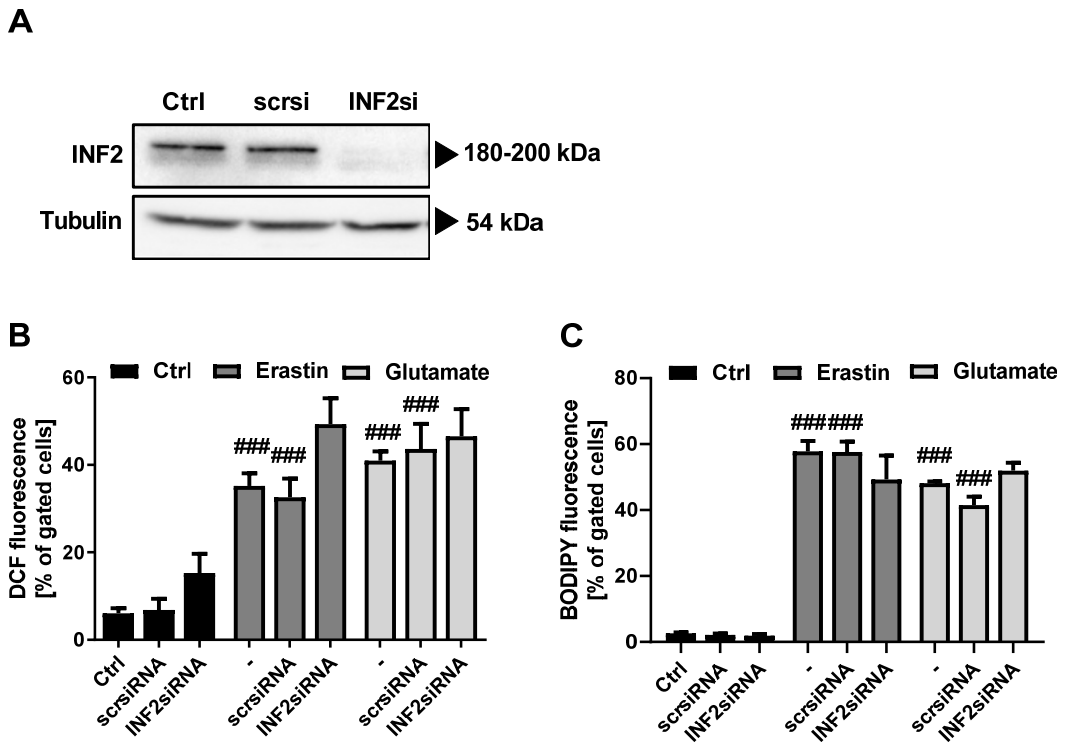

Figure 35. Soluble ROS formation and lipid peroxidation occurred independently of INF2 downregulation after cell death induction with erastin or glutamate.

A INF2 was downregulated by SMARTpool siRNA of four different RNA sequences. The knockdown was confirmed by Western blot analysis after application of 5 nM of the specific siRNA pool for 48 hours. **B** The amount of soluble ROS was measured after 0.6 μM erastin 7 mM glutamate treatment for 10 h following DCF staining and FACS analysis. Data are given as mean + SD; 5,000 cells per replicate of n=3 replicates. **C** Lipid peroxidation was determined 9 h after challenging the cells with 0.7 μM erastin or 8 mM glutamate with BODIPY fluorescent dye and subsequent FACS analysis. Ctrl (control); scrsi (scrambled siRNA); ###p<0.001 compared to untreated ctrl (ANOVA, Scheffé's-test).

Mitochondrial demise is considered the 'point of no return' upon cell death induction in the model of glutamate-induced oxytosis [97]. To address the question, whether actin-binding proteins besides cofilin1 play a decisive role in cell death progression, mitochondrial parameters were investigated in INF2siRNA-transfected HT22 cells after erastin or glutamate exposure. Mitochondrial ROS production was assessed by MitoSOX staining and following flow cytometry. This measurement revealed a substantial increase of mitochondrial ROS accumulation in control and scrambled siRNA transfected cells, which was prohibited by silencing INF2 (Figure 36 A, B). Further, mitochondrial Ca^{2+} accumulation was analyzed by the cell-permeable mitochondrial specific Ca^{2+}-indicator Rhod-2 AM. Here, INF2 silencing almost completely averted detrimental mitochondrial Ca^{2} overload induced by erastin or glutamate treatment (Figure 36 C, D). This suggested that preventing

mitochondrial Ca^{2+} accumulation might be the centerpiece of cellular protection of INF2-knockdown cells.

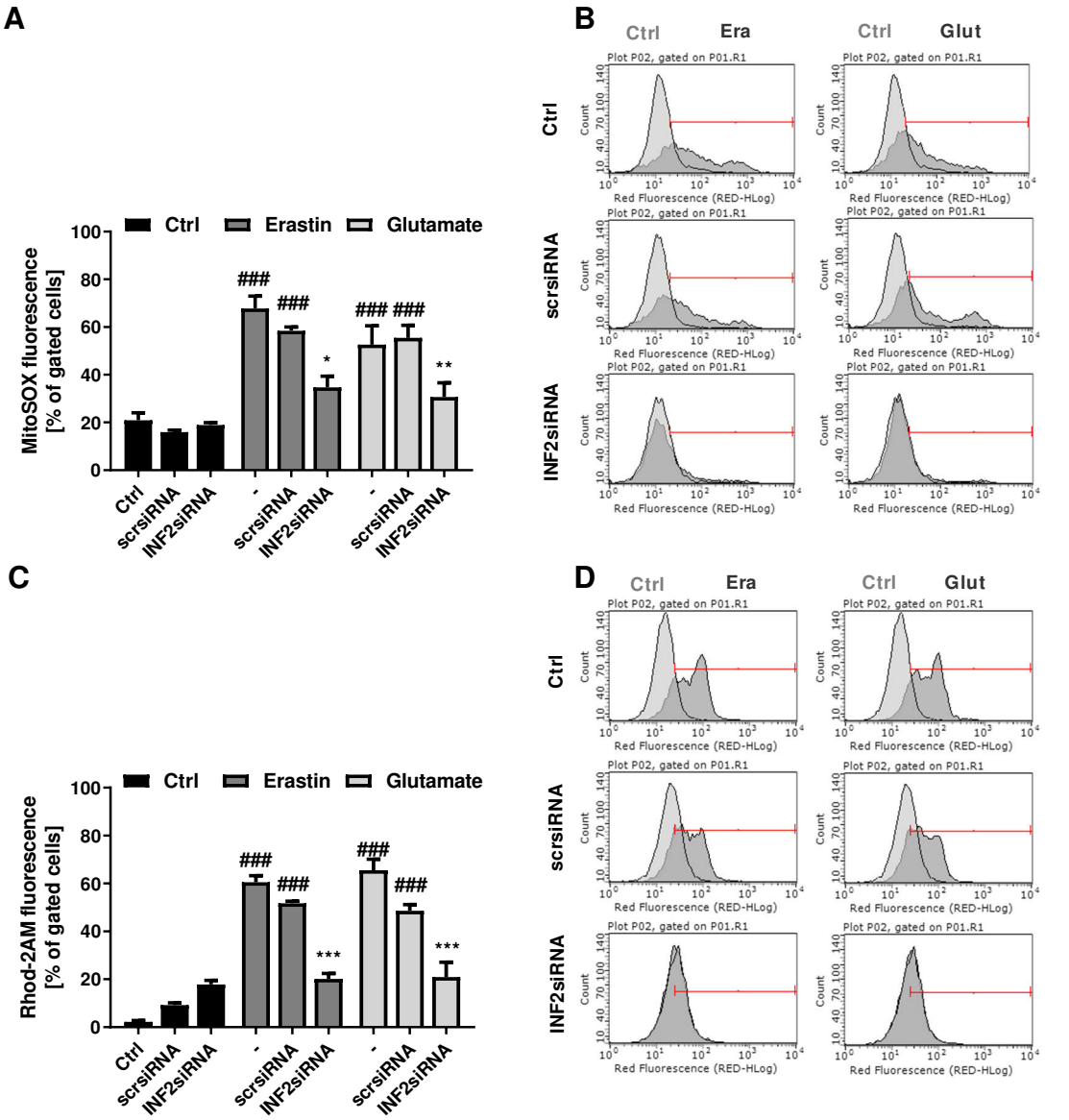

Figure 36. Mitochondrial ROS accumulation and detrimental mitochondrial calcium overload were diminished in INF2-deficient HT22 cells in terms of oxidative stress.

A Mitochondrial ROS accumulation was measured by MitoSOX staining and FACS analysis after 16 hours treatment with 0.7 µM erastin 9 mM glutamate. Beforehand, INF2siRNA was incubated for 30 hours. Data are presented as mean + SD; 5,000 cells per replicate of n=3 replicates. **B** Representative histograms from the MitoSOX measurement are provided. **C** Rhod-2 acetoxymethyl ester (Rhod-2 AM) was used to specifically measure mitochondrial calcium level after 16-hour treatment with 0.8 µM erastin or 6 mM glutamate, again after silencing INF2 with siRNA. Values are projected as mean + SD; 5,000 cells per replicate of n=3 replicates. **D** Representative images from the Rhod-2 AM measurement are provided. Ctrl (control); scrsi (scrambled siRNA); ###p<0.001 compared to untreated ctrl, *p<0.05 compared to erastin- or glutamate-treated ctrl, **p<0.01 compared to erastin- or glutamate-treated ctrl, ***p<0.001 compared to erastin- or glutamate-treated ctrl (ANOVA, Scheffé's-test).

To further validate the obtained data, the mitochondrial membrane potential was measured by the positively charged indicator TMRE. In line with the previous data, the mitochondrial membrane potential was completely preserved upon erastin or glutamate treatment by INF2siRNA (Figure 37 A, B), indicating an entire protection of mitochondrial integrity upon INF2 downregulation.

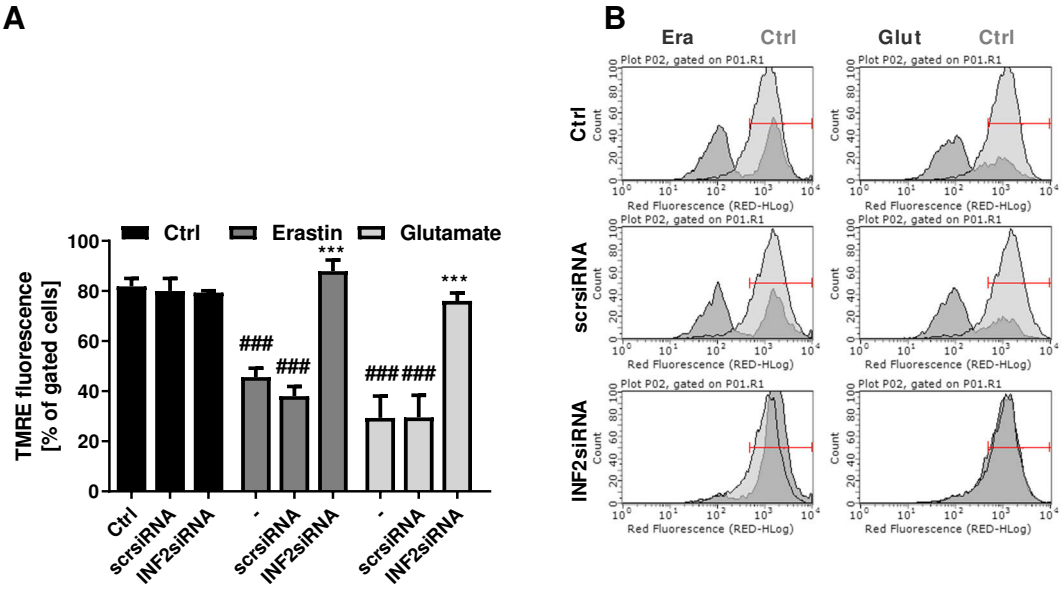

Figure 37. INF2 knockdown mediated full protection against loss of the mitochondrial membrane potential in paradigms of erastin or glutamate-induced cell death.

A The mitochondrial membrane potential was evaluated by an appropriate cell permeant, positively-charged TMRE dye and following FACS analysis after 16 hours treatment with 0.7 µM erastin or 7 mM glutamate. Beforehand, INF2siRNA was incubated for 30 hours. Values are given as mean + SD; 5,000 cells per replicate of n=3 replicates. **B** Representative histograms from the TMRE FACS measurement are provided. Ctrl (control); scrsi (scrambled siRNA); ###p<0.001 compared to untreated ctrl, ***p<0.001 compared to erastin- or glutamate-treated ctrl (ANOVA, Scheffé's-test).

In addition, the ATP content represents the energy production by mitochondrial and non-mitochondrial respiration, required for the health and survival of cells. After erastin or glutamate exposure, ATP levels declined to a minimum of 20-40 %. INF2 knockdown partially preserved ATP production in neuronal HT22 cells after cellular damage by erastin or glutamate (Figure 38 A). To focus on mitochondrial respiration, oxygen consumption was measured by the Seahorse XFe Analyzer. This measurement revealed, that mitochondrial respiration of control or scrambled siRNA-transfected HT22 cells treated with erastin or glutamate is completely abolished. INF2-knockout under these treatment conditions showed a partial preservation of the OCR, but not of the spare respiratory capacity (Figure 38 B, D). Intriguingly, the non-mitochondrial respiration, measured via the extracellular acidification

rate (ECAR) showed a tremendous decline of glycolysis in control and scrsiRNA-transfected HT22 cells damaged by erastin or glutamate but only a minor impairment in INF2 knockdown cells (Figure 38 C, E).

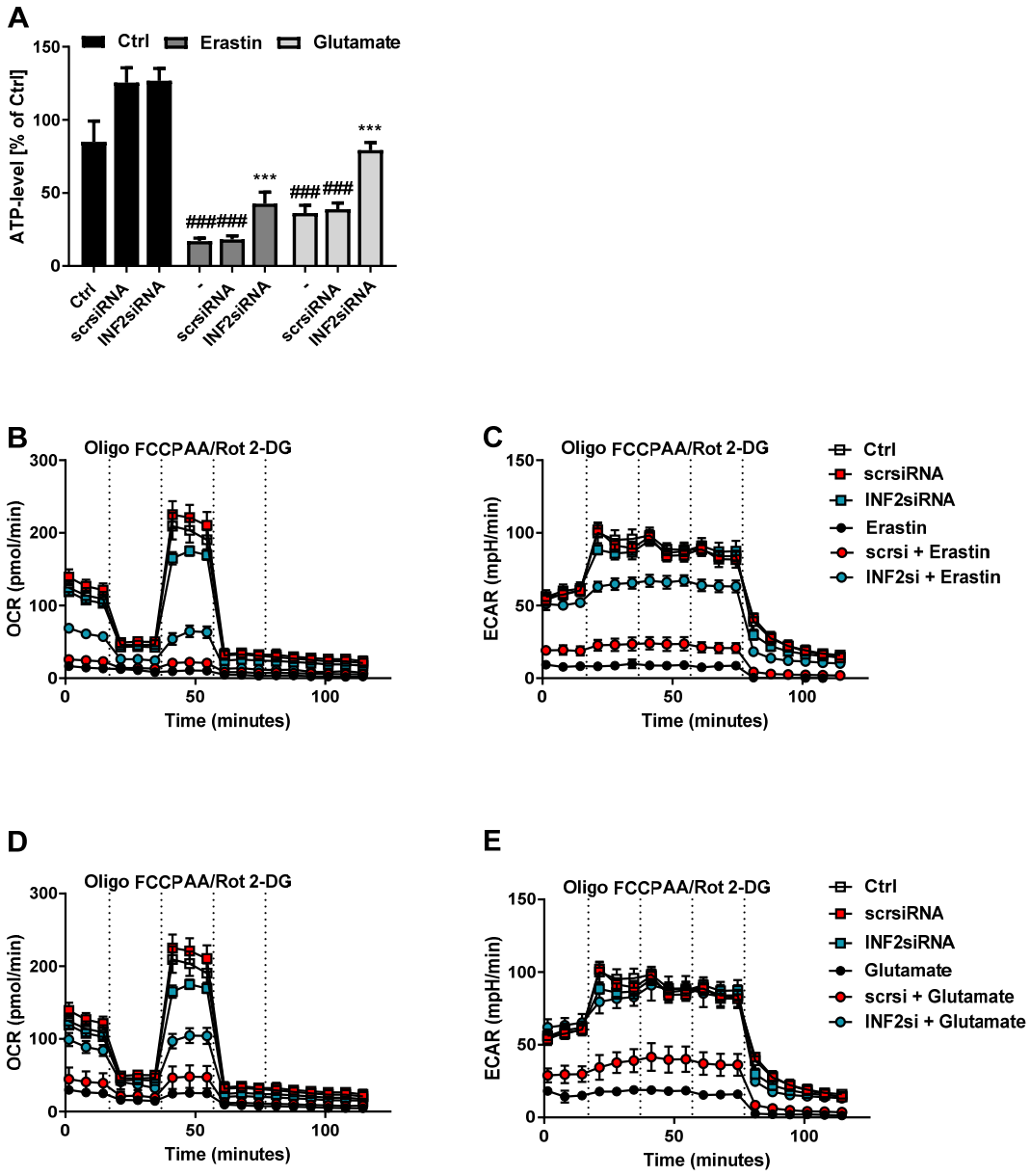

Figure 38. ATP content, mitochondrial respiration and the glycolysis rate were preserved after INF2 downregulation in models of oxidative stress-induced cell death.

A INF2 knockdown was achieved by siRNA incubation for 48 hours. Afterwards, cells were challenged for 10 hours with 0.5 µM erastin or 6 mM glutamate. Finally, ATP content was measured by luminescence-based measurement. Values are shown as mean +SD (n=8). Ctrl (control); scrsi (scrambled siRNA); ###p<0.001 compared to untreated ctrl, ***p<0.001 compared to erastin- or glutamate-treated ctrl (ANOVA, Scheffé's-test). **B, C, D, E** INF2siRNA was transfected for 48 hours. Afterwards, cells were damaged for 9 hours with 0.5 µM erastin or 5 mM glutamate. The OCR and ECAR were determined by a Seahorse XFe96 Analyzer. Data of 3-6 replicates per condition are shown as mean ± SD. Oligo (oligomycin); FCCP (carbonyl cyanide 4-(trifluoromethoxy)phenylhydrazone); AA (antimycin A) Rot (rotenone); 2-DG (2-deoxy-D-glucose). Ctrl (control); scrsi (scrambled siRNA).

To get further insight into the cellular bioenergetic profile of cells, the OCR was plotted against the ECAR to display the energetic phenotype between baseline and stressed conditions (FCCP treatment) (Figure 39 A, B). This analysis suggests a partial preserved metabolic potential upon erastin or glutamate exposure in INF2-knockdown cells compared to control or scrsiRNA-transfected cells, underlining that INF2 gene silencing contributes to the preservation of the energy homeostasis, directly related to cellular survival and health [94] (Figure 39 A, B).

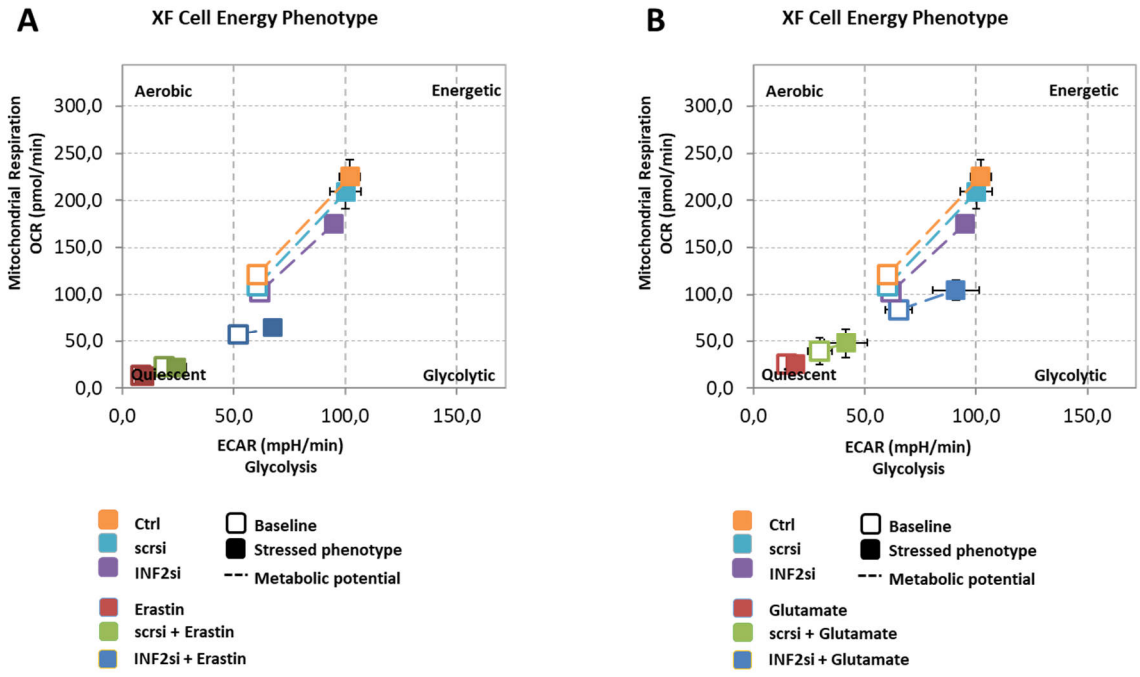

Figure 39. Metabolic profile of INF2 knockdown cells under basal and under stress conditions.

A, B The cell energy phenotype correlates the OCR and the ECAR of the cells at basal conditions (open dot) measured before the first compound was injected by the system and after FCCP injection, representing a stressed phenotype (filled dot). The displayed metabolic potential (dashed line) represents the capacity to meet the required energy demand under conditions of stress, i.e. after 9-hours treatment with 0.5 µM erastin or 5 mM glutamate.

To finally address the impact of INF2 knockdown on cellular viability in models of oxidative stress induced cell death, the number of AnnexinV and propidium iodide (PI) positive cells was determined by flow cytometry measurement. This measurement captures early apoptotic and late necrotic/apoptotic cells, here observable in control cells or scrambled siRNA-transfected cells upon erastin or glutamate exposure (Figure 40 A). This increase of cell death was partly reversed by specifically silencing INF2 (Figure 40 A). Accordingly, MTT assays measuring metabolic activity also revealed a decrease in cellular survival upon erastin or glutamate treatment in control and scrsiRNA-transfected cells, but INF2-knockout

attenuated the deleterious impact of these substances (Figure 40 B), emphasizing that INF2 plays a crucial role in the cell death progression in models of oxidative stress.

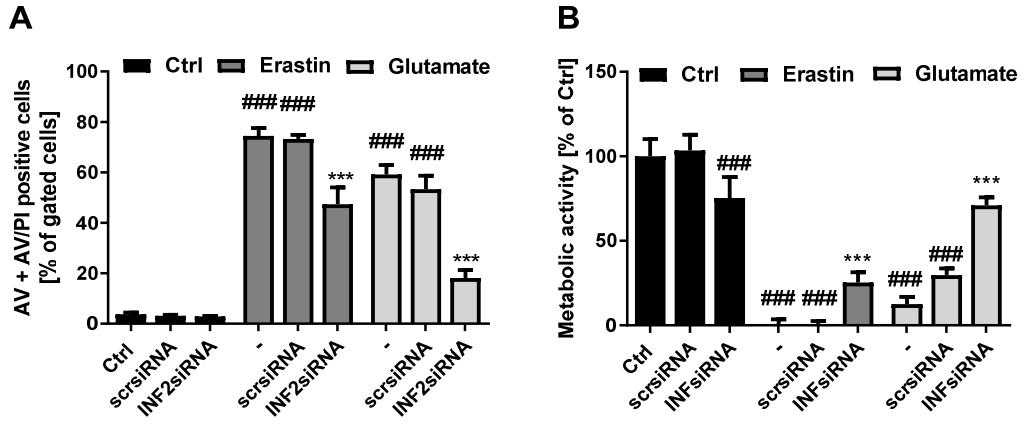

Figure 40. Attenuating cell death progression after erastin or glutamate exposure was a major attribute of INF2-knockout HT22 cells.

A AnnexinV and PI staining was conducted after 30 h of siRNA incubation and following 16 h of erastin 0.4 μM or glutamate 5 mM treatment. Values are given as mean + SD; 5,000 cells per replicate of n=3 replicates). **B** Cells were treated with 0.4 μM erastin or 5 mM glutamate for 16 h and finally stained with MTT reagent. Values are shown as mean + SD; n=8 replicates. Data are given as mean + SD; n=8 replicates. Ctrl (control); scrsi (scrambled siRNA); ###p<0.001 compared to untreated ctrl, ***p<0.001 compared to erastin- or glutamate-treated ctrl (ANOVA, Scheffé's-test).

Mitochondrial Ca^{2+} overload is one of the major steps after cell death induction leading to mitochondrial dysfunction and cellular impairment [178], mainly regulated by the mitochondrial calcium uniporter (MCU), which was also identified as the crucial regulator of Ca^{2+} assimilation under conditions of oxidative stress [103]. In this regard, it would be of interest to study the impact of INF2 on MCU abundance by Western blot analysis, which was previously reported in U2OS cells [24]. In this experimental setup in HT22 cells, a slight increase of MCU protein levels were observable in control cells after erastin exposure, which was partly reversed by INF2 silencing (Figure 41 A). After glutamate exposure, MCU abundance only changed marginally without further modulation by an INF2 knockout (Figure 41 A). Additionally, the impact of INF2 knockdown on the actin-depolymerizing protein cofilin1 was evaluated and quantified by Western blot. Surprisingly, upon INF2 downregulation, cofilin1 levels also decreased to a considerable extent under basal conditions, whereas challenging the cells with erastin or glutamate led to an increase of cofilin1 levels under INF2-deficiency compared to control cells (Figure 41 B).

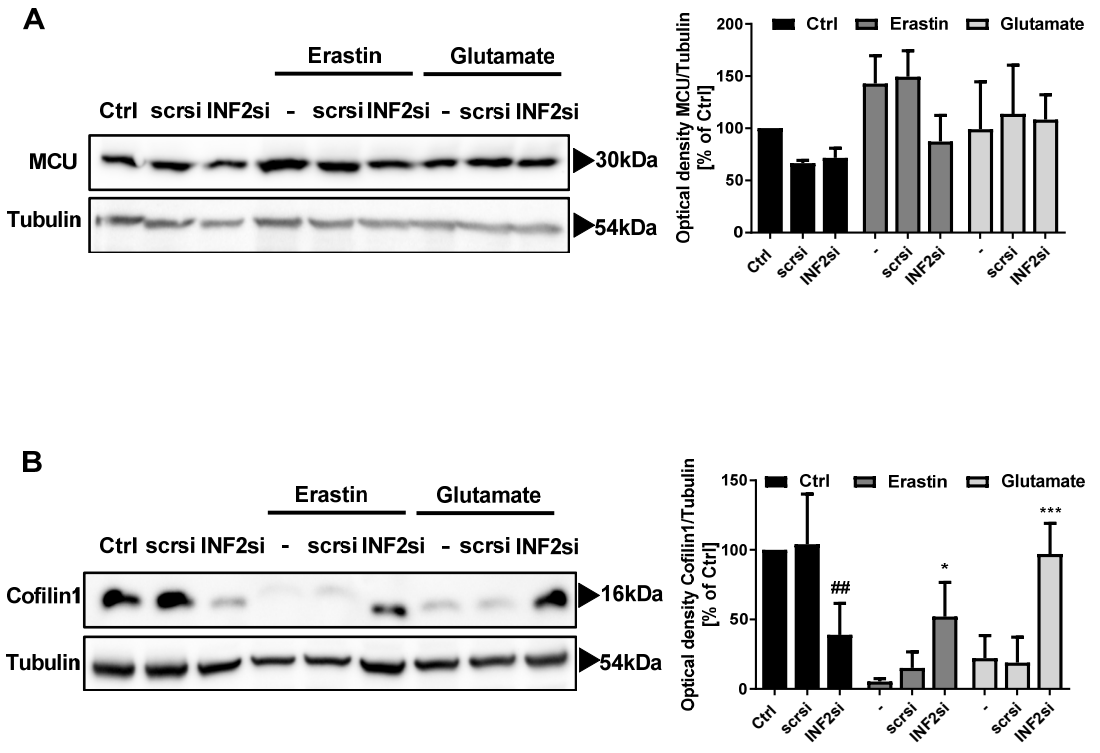

Figure 41. Protein expression levels of MCU and cofilin1 in INF2-knockdown HT22 cells after erastin- or glutamate exposure.

A MCU and **B** Cofilin1 protein levels were analyzed by Western blot after 9 hours of erastin- or glutamate exposure and afterwards relative protein abundance was quantified from three experiments. Data is presented as mean + SD. Ctrl (control); scrsi (scrambled siRNA); INF2si (INF2siRNA). ##p<0.01 compared to scrsi; *p<0.05 and ***p<0.001 compared to erastin- or glutamate-treated scrsi (ANOVA, LSD-test).

To substantiate the positive effect of INF2 deficiency on mitochondrial parameters and cellular viability, the major mitochondrial biogenesis marker PGC1α and the mitochondrial fusion protein MFN2 were analyzed by Western blot. In line with the previous results on mitochondrial resistance of INF2-siRNA transfected cells, also the expression of the mitochondrial biogenesis protein was significantly preserved after exposure with erastin or glutamate, potentially also contributing to the beneficial effects of INF2 knockout on mitochondrial biogenesis (Figure 42 A). MFN2 was not significantly affected, neither by erastin or glutamate treatment, nor by INF2 knockout (Figure 42 B).

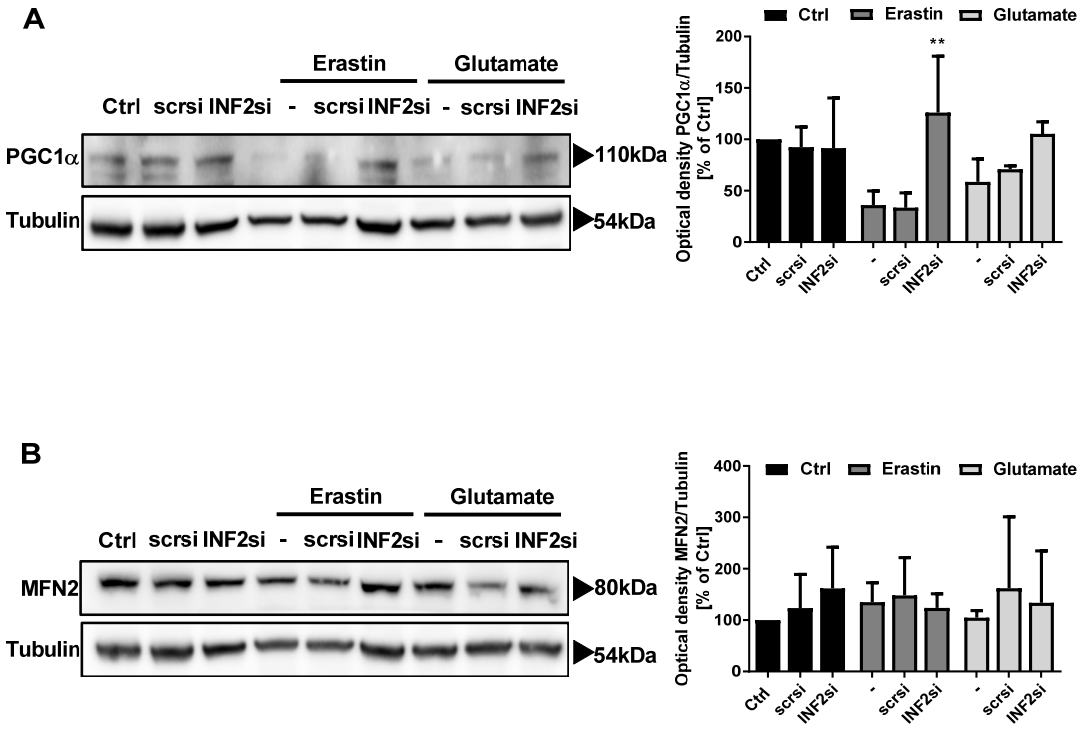

Figure 42. Protein expression levels of PGC1α and MFN2 in INF2-knockdown HT22 cells after erastin- or glutamate exposure.

A PGC1α and **B** MFN2 protein levels were assessed by Western blot after 9 hours of erastin- or glutamate exposure and afterwards relative protein expression was quantified from three experiments. Data is presented as mean + SD. Ctrl (control); scrsi (scrambled siRNA); INF2si (INF2siRNA). **p<0.01 compared to erastin-treated scrsi (ANOVA, LSD-test).

4.2.4 INF2 knockdown leads to mitochondrial elongation

Mitochondrial division is a fundamental step in maintaining energy homeostasis and therefore cellular welfare. Recent findings suggest that ER-bound INF2 acts as a crucial regulator of F-actin polymerization at putative mitochondrial constriction sides, due to its ability to recruit DRP1 from the cytosol to the point of action [90]. Predicated on these observations, it was of great interest to investigate possible effects of INF2 gene silencing on mitochondrial dynamics in neuronal HT22 cells. Intriguingly, knockdown of INF2 revealed significantly elongated mitochondria compared to control or unspecific transfected HT22 cells (Figure 43 A, B).

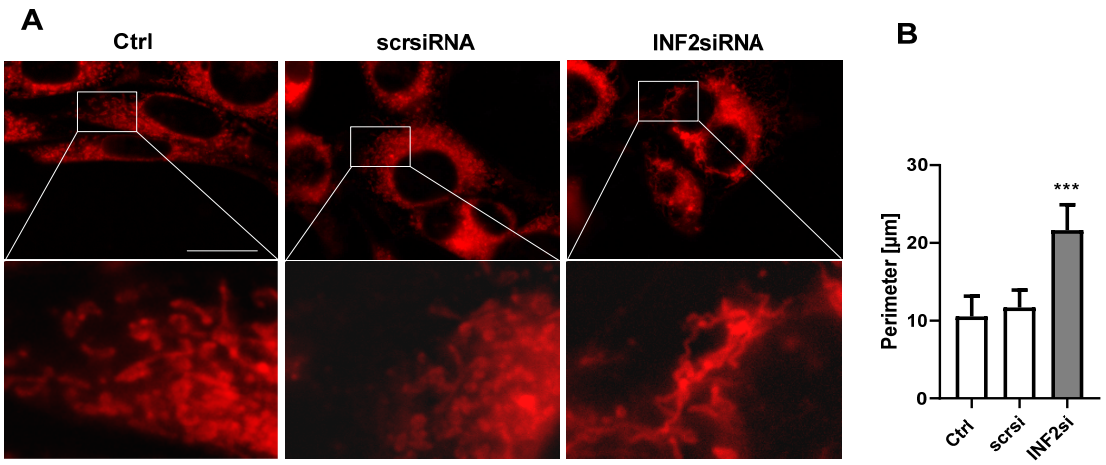

Figure 43. Determination of the mitochondrial morphology in INF2 knockdown cells exhibited an elongated phenotype.

A HT22 cells were seeded in 8-well µ-slide and simultaneously transfected with 5 nM scrsiRNA of INF2siRNA for 48 hours. Afterwards, cells were stained with Mitotracker® Deep Red and fixed with 4 % formaldehyde. Images were acquired by an inverted fluorescence microscope. *Scale bar* 25 µm. **B** The mitochondrial perimeter was measured by application of the ImageJ Plugin by Ruben K. Dagda [39]. n=30 per condition. Data are presented as mean + SD. ***p<0.001 compared to scrsiRNA-transfected cells (ANOVA, Scheffé's test).

On basis of this observation, it is highly relevant to explore the underlying mechanism of mitochondrial morphology changes. Therefore, the most important mitochondrial biogenesis markers were analyzed by qRT-PCR. However, the observed differences were overall not significant due to high standard deviations. Nevertheless, *PCG1α* and *TFAM mRNA* levels were increased after INF2 silencing compared to scrsiRNA-transfected cells (Figure 44 A, E). The mitochondrial DNA content showed also an upward tendency (Figure 44 H), whereas *DRP1 mRNA* levels were slightly reduced (Figure 44 G). The remaining analyzed values, namely *Nrf-1, Nrf-2, p62* and *MCU* were not affected at all by INF2 knockdown (Figure 44 B, C, D, F).

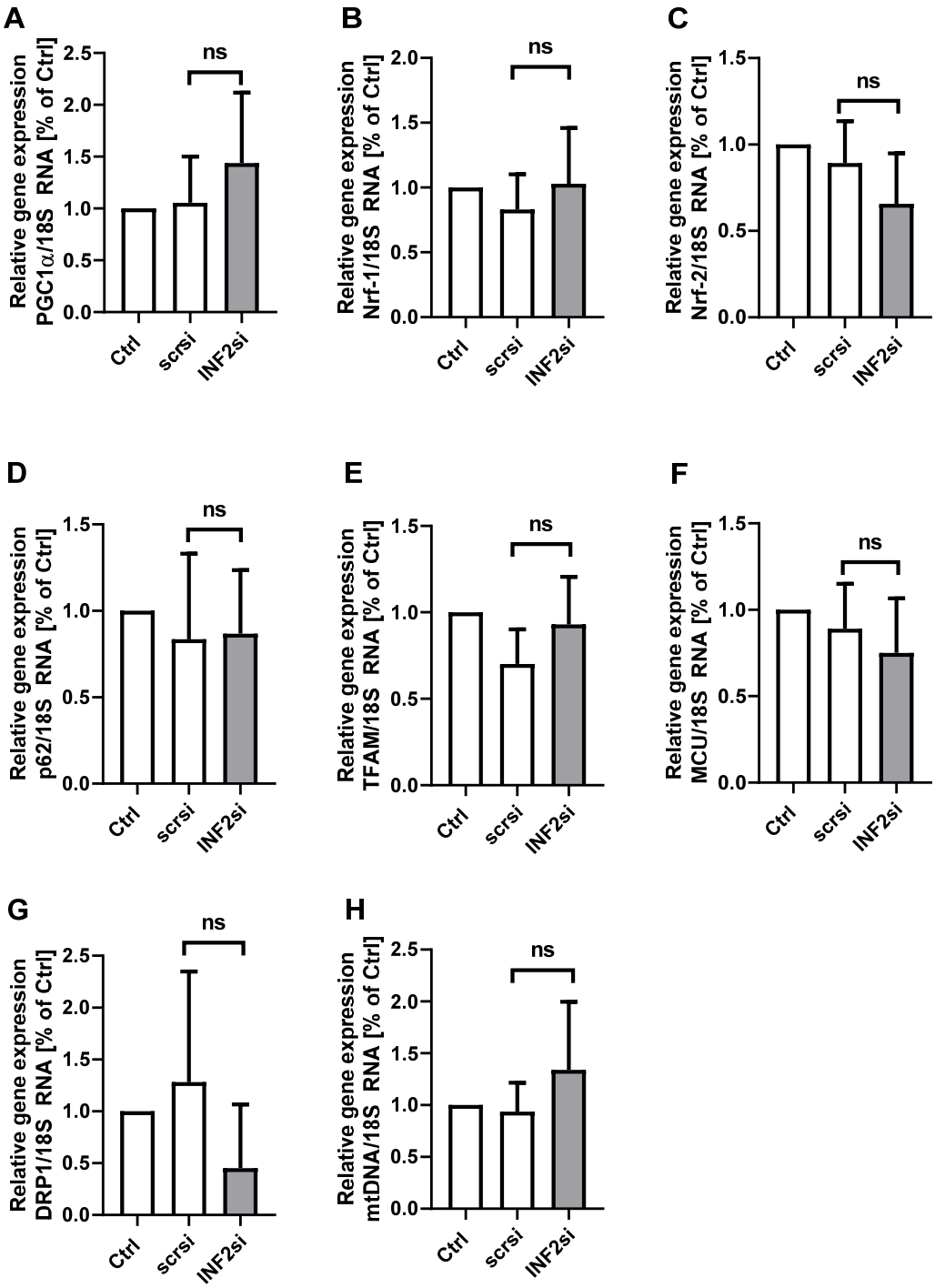

Figure 44. Proteins with impact on mitochondrial shape and biogenesis were evaluated by qRT-PCR after silencing INF2.

A Relative *PGC1α* mRNA levels comparative to the reference gene 18S were quantified by qRT-PCR and the control was normalized to 1.0. **B** Relative *Nrf-1* mRNA levels normalized to 18S were quantified by qRT-PCR. **C** Relative *Nrf-2* mRNA levels normalized to 18S were quantified by qRT-PCR. **D** Relative *p62*mRNA levels normalized to 18S were quantified by qRT-PCR. **E** Relative *TFAM* mRNA levels normalized to 18S were quantified by qRT-PCR. **F** Relative *MCU* mRNA levels normalized to 18S were quantified by qRT-PCR. **G** Relative *DRP1* mRNA levels normalized to 18S were quantified by qRT-PCR. **H** Relative *mtDNA* levels normalized to 18S were quantified by qRT-PCR. Values are given as mean + SD of n=3-4 replicates). ns= not significant (unpaired t-test).

Evaluation of protein expression levels is a meaningful tool to indirectly receive conclusions about the activity. Therefore, DRP1 abundance upon INF2 knockdown was investigated by Western blot. The densiometric-based quantification of the resulting signals revealed a substantial decrease of DRP1 expression levels after INF2-knockdown compared to scrsiRNA transfected cells (Figure 45 A). This finding aligns with mitochondrial elongation after INF2 silencing (Figure 43). Interestingly, also the expression of actin-depolymerizing cofilin1 tended towards lower protein expression levels (Figure 45 B). Based on the study of Chakrabarti and coworkers, MCU expression was analyzed upon INF2 knockout. Contrary to the results from Chakrabarti obtained in bone osteosarcoma-derived U2OS cells [24], the recent data demonstrated no substantial change in the regulation of MCU or MICU1 expression in neuronal HT22 cells, respectively (Figure 45 C, D).

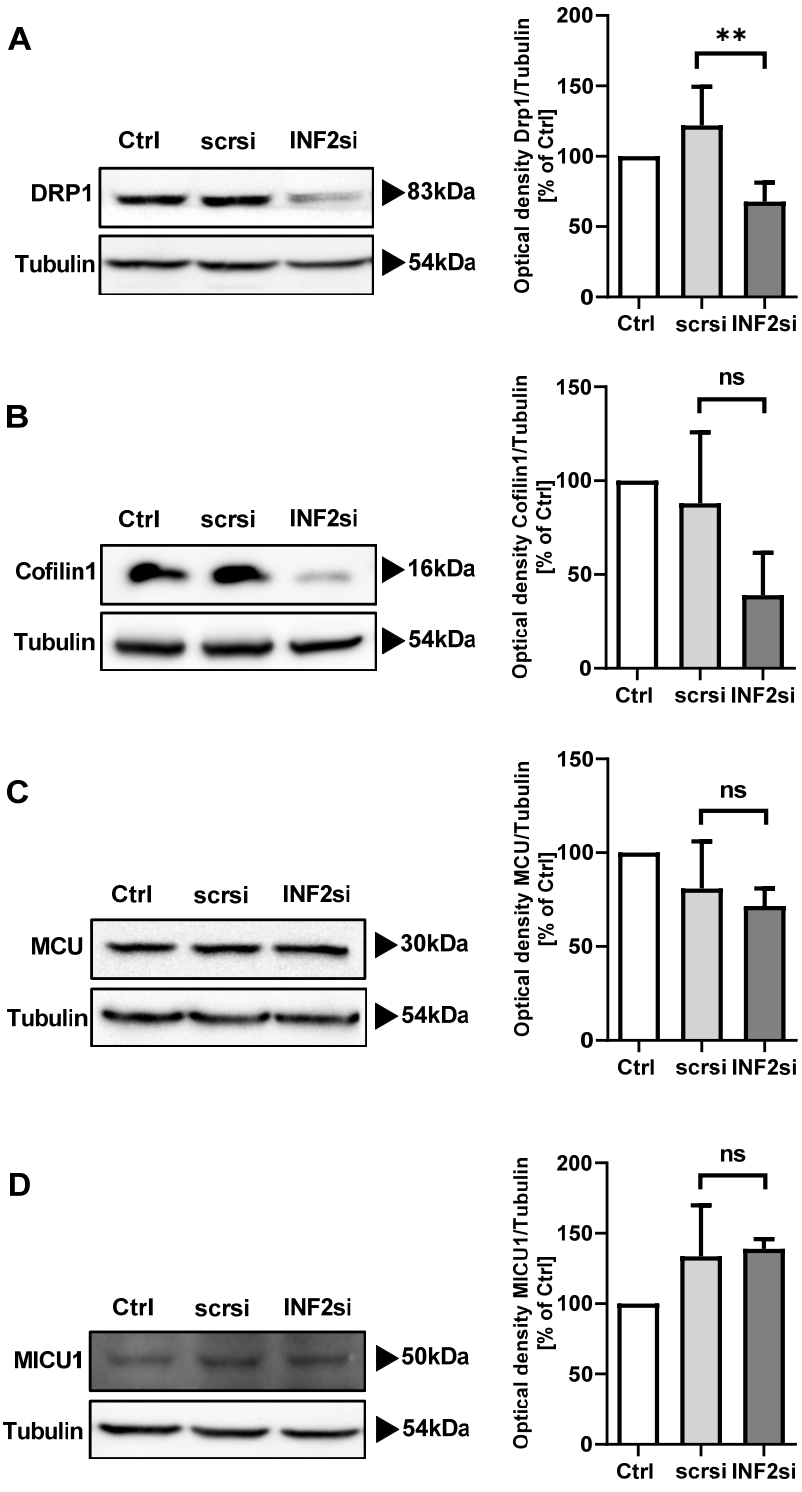

Figure 45. INF2 knockout HT22 cells revealed decreased DRP1 protein expression.

A INF2 knockdown was achieved by reverse transfection of a specific siRNA for 48 hours. Afterwards, DRP1 **B** Cofilin1 **C** MCU and **D** MICU1 protein levels were analyzed by Western blot and quantified from three to six blots (mean + SD). Ctrl (control); scrsi (scrambled siRNA); INF2si (INF2siRNA). ns=not significant; **p<0.01 compared to scrsiRNA (unpaired t-test).

4.3 Primary neurons

4.3.1 Primary neurons deficient of cofilin1 are protected against glutamate excitotoxicity

The actin-binding protein cofilin1 is highly relevant for proper actin-turnover and thus for dendritic spine formation and synaptic plasticity in neurons [77, 78, 144, 145]. In addition, recent findings demonstrated a role for cofilin1 in the neuronal HT22 cell line in paradigms of oxidative stress-induced cell death. The present study further investigated the relevance of cofilin1 in models of glutamate-induced excitotoxicity to study the effect of this specific actin-regulating protein on mitochondrial and cellular resistance. To validate the regulation of cofilin1 activity in cell death models induced by micromolar concentrations of glutamate in cortical neurons, the phosphorylation status of serine residue 3 was evaluated by Western blot. The observed dephosphorylation (Ser3) clearly underlined an activation of cofilin1 during glutamate-induced excitotoxicity.

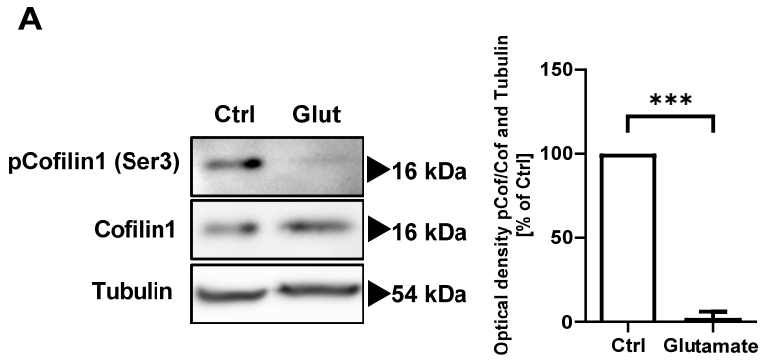

Figure 46. Cofilin1 was activated by dephosphorylation of serine 3 in models of glutamate-induced excitotoxicity.

A DIV9 primary cortical neurons were challenges with 25 μM glutamate for 24 hours and subsequently the phosphorylation status of serine residue 3 of cofilin1 was analyzed with a specific antibody. The quantification was realized by densiometric evaluation of the resulting signal and compared to total cofilin1 and to the α-Tubulin signal. ***p<0.001 compared to control (unpaired t-test). Ctrl (control); Glut (glutamate); pCofilin1 (phosphorylated cofilin1); Ser3 (serine residue 3).

Further, the metabolic profile of neurons exposed to the excitotoxic challenge was evaluated between wildtype (WT ≡ Cofilin1$^{flx/flx}$) and cofilin1$^{-/-}$ (Cofilin1$^{flx/flx,\ CaMKII\alpha\text{-}Cre}$) cells to investigate cofilin1's impact in this cellular model. The mitochondrial respiration in WT cell, represented as the oxygen consumption rate (OCR), revealed a substantial impairment after glutamate exposure, which was antagonized by the NDMA-receptor antagonist MK-801 (Figure 47 A). Notably, the bioenergetic profile of neurons deficient for cofilin1 perfectly overlap with the glutamate antagonist MK-801 (Figure 47 B) proving evidence that the absence of cofilin1 exerts a considerable protective mechanism upstream of mitochondria in primary cortical neurons in paradigms of excitotoxicity. To closely assess the difference between WT and cofilin1$^{-/-}$ neurons upon glutamate treatment, the basal respiration, measured before the first substance was injected by the Seahorse XFe Analyzer, was evaluated. Glutamate treatment resulted in a significant loss of mitochondrial respiration, whereas cofilin1$^{-/-}$ neurons exhibited a preserved basal respiration rate. Accordingly, the maximal respiration of WT neurons after FCCP injection was significantly impaired after challenging the cells with glutamate, which was circumvented by cofilin1 deficiency. In addition, the glycolysis rate was assessed indirectly by measuring the extracellular acidification rate. In WT neurons, glycolytic activity was abandoned upon glutamate application (Figure 47 E), whereas cofilin1$^{-/-}$ neurons retained glycolysis under stress conditions induced by glutamate (Figure 47 F).

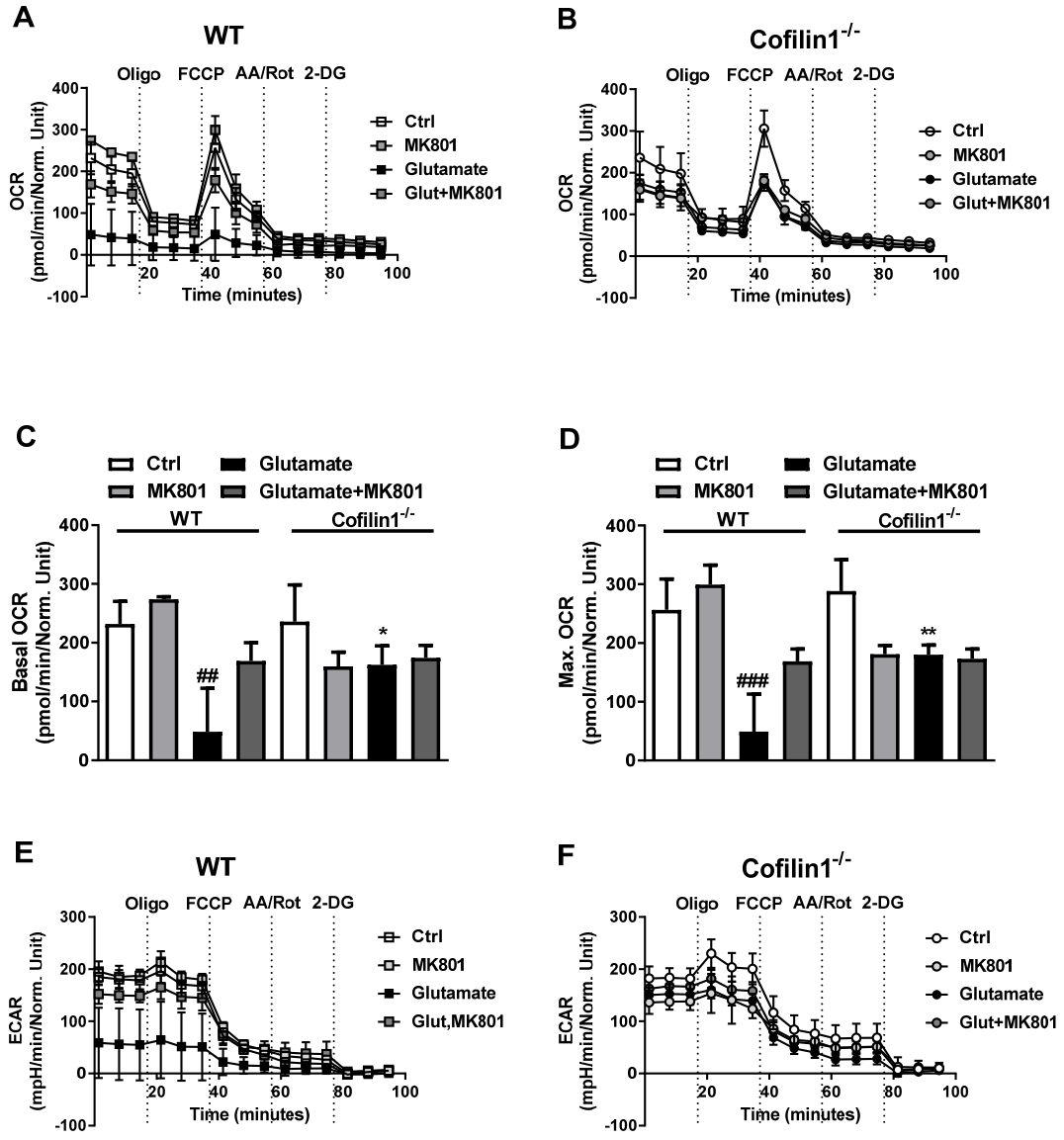

Figure 47. Mitochondrial respiration and glycolysis rate were preserved in cofilin1 knockout primary neurons in models of glutamate-induced excitotoxicity.

A OCR of WT and **B** cofilin1$^{-/-}$ neurons was measured at 30 days in vitro after 25 µM glutamate challenge for 24 hours. 20 µM MK801 was applied simultaneously and serves as a control for NMDA-R blockade. **C** Quantification of the basal OCR of WT and cofilin1$^{-/-}$ neurons, measured before the first compound was injected and **D** maximal OCR after FCCP injection of n=3-5 replicates. Mean values ± SD are given. ##p<0.01 compared to untreated ctrl, *p<0.05 compared to glutamate-treated ctrl, **p<0.01 compared to glutamate-treated ctrl (ANOVA, Scheffé's-test). **E** ECAR of WT and **F** cofilin1$^{-/-}$ neurons was also determined at 30 days in vitro after 25 µM glutamate challenge for 24 hours and MK801 cotreatment. Values of n=3-5 replicates are presented shown as mean ± SD. Oligo (oligomycin); FCCP (carbonyl cyanide 4-(trifluoromethoxy)phenylhydrazone); AA (antimycin A) Rot (rotenone); 2-DG (2-deoxy-D-glucose).

Accordingly, the recent study unraveled a role for cofilin1 upstream of mitochondrial demise in conditions of glutamate-induced excitotoxicity. To support this finding and draw conclusions on the impact of cofilin1 deficiency on cell viability, MTT assays were performed and quantified afterwards. The number of viable WT cells was significantly diminished

(Figure 48 A), whereas the cell viability of cofilin1$^{-/-}$ neurons was conspicuously preserved upon glutamate exposure (Figure 48 A).

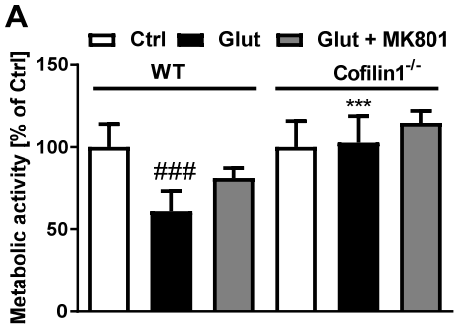

Figure 48. Cofilin1 knockout in primary cortical neurons revealed protection after glutamate exposure.

A Metabolic activity of DIV30 WT and cofilin1$^{-/-}$ neurons was determined by MTT assay after glutamate exposure for 24 hours. MK801 cotreatment serves as a control for NMDA-receptor blockade. Mean values + SD of n=5 replicates are shown. ###p<0.001 compared to untreated ctrl, ***p<0.001 compared to glutamate-treated ctrl (ANOVA, Scheffé's-test).

The phosphorylation status of cofilin1's serine residue 3 is considered as a decisive determinant for the activation of the protein. Since the Rho-ROCK pathway was identified to activate LIM domain kinase 1 and 2 (LIMK1, 2) [27], a crucial cofilin1 phosphorylating enzyme, the Rho activator CN03 was administered for induction of cofilin1 phosphorylation and thus deactivation. The effect of this manipulation was assessed in the MTT assay to quantify metabolically active cells. Interestingly, a 3-hour pretreatment with 1 µg/mL CN03 was able to rescue the loss of metabolic activity induced by 24-hour exposure of glutamate (Figure 49 A). This beneficial effect was comparable to the potent NMDA-receptor antagonist MK-801 (Figure 49 A). To validate the effect of CN03 exposure on cofilin1 phosphorylation, Western blot was performed using a specific antibody against phosphorylated Ser3-cofilin1. As previously demonstrated (Figure 46 A), cofilin1 is dephosphorylated after glutamate exposure, whereas CN03 preserved its phosphorylation status (Figure 49 B), although, this tendency was not significant due to high variations of the Western blot signal (Figure 49 B).

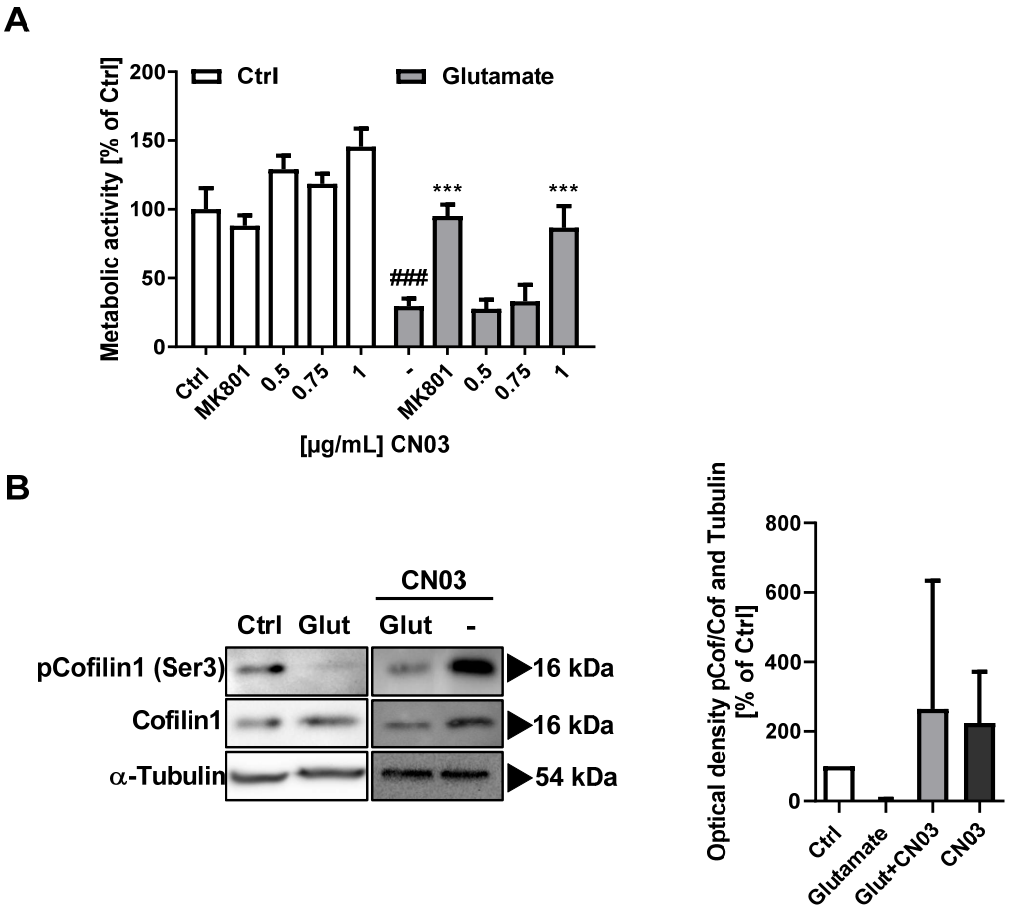

Figure 49. Cofilin1 inhibition by CN03-induced phosphorylation at serine 3 revealed protection of glutamate exposed primary neurons.

A Primary cortical neurons from wildtype E18 pubs were exposed to the indicated concentration of CN03 3 hours prior to 25 µM glutamate treatment for 24 hours at DIV9. Data from n=6 are shown as mean + SD. **B** Western blot analysis of phosphorylated Ser3-cofilin1 was performed after 3 hours pretreatment with 1 µg/mL CN03 and additional 24 hours treatment with 25 µM glutamate. Quantification of the resulting signal was realized by densiometric analysis from n=4 blots. The intensities of pCofilin1 (Ser 3) were compared to the cofilin1 signal and to α-Tubulin as a loading control and presented as mean + SD. ###p<0.001 compared to control; ***p<0.001 compared to glutamate-treated control (ANOVA, Scheffé's-test). Ctrl (control); Glut (glutamate).

4.3.2 Fura-2 measurement of synchronized spontaneous network activity of mature wildtype and cofilin1 knockout neurons

The chemical Ca^{2+} chelator and fluorophore Fura-2 AM enables dual wavelength excitation, allowing to monitor Ca^{2+} oscillations in a mature neuronal network in a real-time manner [42]. In a Ca^{2+}-bound state, Fura-2 AM is excitable at 340 nm, whereas after Ca^{2+} release, the excitation wavelength is shifted to 380 nm (Figure 50 A, B). This ratiometric measurement is less prone towards imaging artifacts, such as alterations in intracellular dye concentrations [63]. Precisely, in the present study, Fura-2 AM was administered to specifically monitor the network activity of WT and cofilin1$^{-/-}$ neurons, based on intracellular Ca^{2+} transients achieved

by depolarization-induced Ca^{2+} influx and subsequent release. The quantification was realized by Leica LAS Software and the ratio 340/380 nm was displayed, afterwards the spontaneous spikes were quantified. This unraveled a difference of the peak frequency between WT and cofilin1$^{-/-}$ neurons. Cells deficient for cofilin1 fired more frequently during the observed time frame (Figure 50 C, D, E).

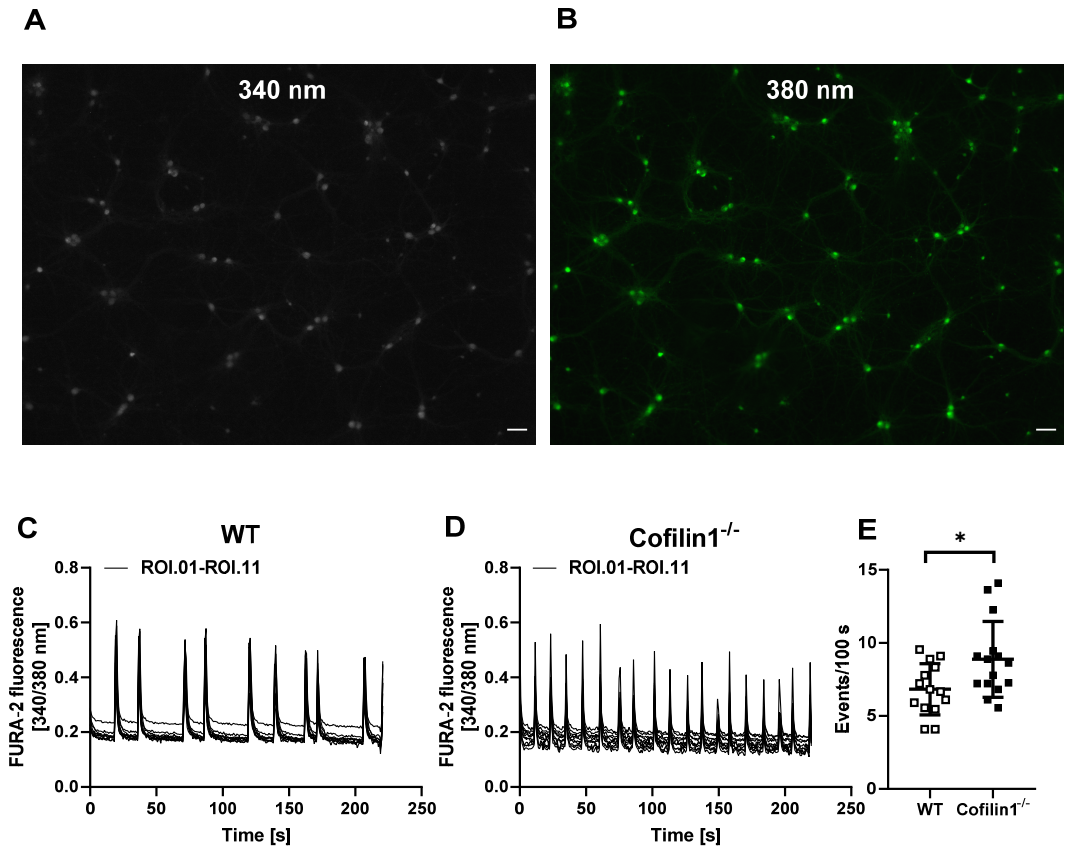

Figure 50. Spontaneous network activity of mature WT and cofilin1$^{-/-}$ primary cortical neurons.

A Primary cortical neurons were plated on coated glass coverslips and imaged at day 24 – 28 in vitro. The representative picture shows the Ca^{2+}-bound state at an excitation wavelength of 340 nm of the Ca^{2+} selective fluorescent indicator Fura-2 AM. *Scale bar* 50 µm. **B** The picture shows the fluorescence of Fura-2 AM in a Ca^{2+}-free state at an excitation wavelength of 380 nm. *Scale bar* 50 µm. **C** Wildtype neurons (flx/flx) or **D** cofilin1$^{-/-}$ neurons were loaded with the Fura-2 AM dye and fluorescence was recorded for 220 sec. Spontaneous network activity is represented by Ca^{2+} oscillations calculated by the Fura-2 AM ratio of 340/380 nm of eleven regions of interest (ROI.01-ROI.11). **E** The quantity of spontaneous events per 100 seconds was counted and presented individually and as mean + SD. *p<0.05 compared to WT (unpaired t-test).

4.3.3 Mitochondrial calcium regulation in cofilin1 knockout neurons

Previous reports in human osteosarcoma cells (U2OS) suggested, that mitochondrial Ca^{2+} regulation was directly influenced by actin dynamics [24]. Thus, in this study, effects of altered actin dynamics achieved by cofilin1-knockdown on mitochondrial calcium uniporter (MCU) expression and on mitochondrial Ca^{2+} uptake upon depolarization were specifically

addressed. MCU protein expression levels were analyzed at 24 days *in vitro* (DIV) and DIV 30 by Western blot. This analysis revealed a tendency towards increased MCU abundance around 24 days *in vitro* (Figure 51 A), but this tendency did not become significant and could not be observed later at DIV 30 (Figure 51 B). Of note, respective *mRNA* expression levels were significantly increased in cofilin1$^{-/-}$ neurons compared to WT.

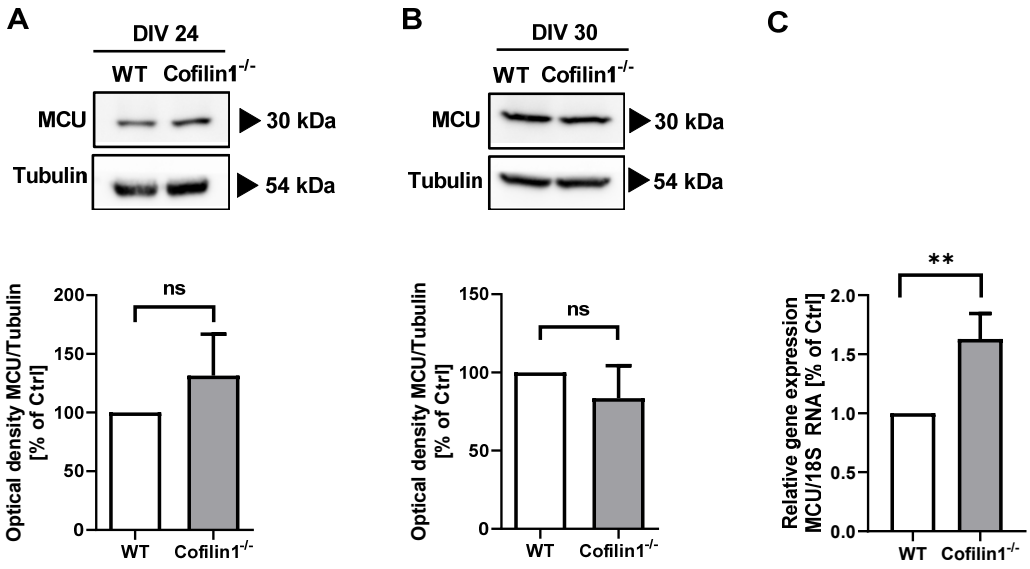

Figure 51. MCU abundance was analyzed on protein and mRNA level in primary cortical neurons.

A At DIV24 protein lysates from WT (flx/flx) and cofilin1$^{-/-}$ embryos were collected and MCU expression levels were assessed by Western blot. Three experiments were quantified and shown as mean + SD. **B** MCU expression was analyzed from DIV30 primary cortical neurons and quantified afterwards from six experiments (mean + SD). **C** Relative *MCU* mRNA levels of DIV28-30 neurons normalized to the reference gene 18S were quantified by qRT-PCR and displayed as mean + SD. **p<0.01 compared to WT (unpaired t-test).

Single cell experiments were conducted after pAAV-CMV-eGFP-IRES-CRE transfection to induce a cofilin1 knockout in neurons equipped with a floxed cofilin1 gene region. GFP expression enables identification of successful Cre transfection. The Cre activity was verified in MEF$^{flx/flx}$ cells and the knockdown of cofilin1 on protein level was validated by Western blot (Figure 52 A, B).

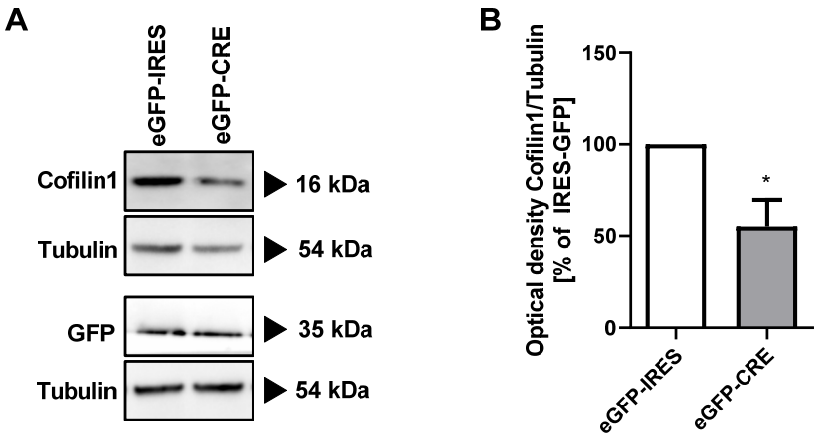

Figure 52. eGFP-CRE transfection downregulated cofilin1 protein levels significantly.

A $MEF^{flx/flx}$ cells were used to confirm the activity of the transfected Cre-recombinase after 48 hours by assessing cofilin1 protein level by Western blot. GFP-IRES was used as a control vector. To ensure equal protein amount of both samples, tubulin and GFP were used as loading control. **B** Quantification of cofilin1 protein level were realized by blotting the mean and SD from three blots. *p<0.05 compared to WT (unpaired t-test).

Further, a comparative analysis of mitochondrial Ca^{2+} uptake in WT and $cofilin1^{-/-}$ neurons was conducted. Primary cortical neurons were transfected with the genetically encoded low-affinity Ca^{2+} indicator mito-LAR-GECO1.2 [179] and an eGFP-IRES or eGFP-CRE construct, respectively (Figure 53 A, B). Surprisingly, neurons deficient for cofilin1 accommodated significantly less Ca^{2+} in mitochondria as WT cells upon depolarization by KCl, underlining an impact of the actin-regulating protein cofilin1 on mitochondrial Ca^{2+} regulation (Figure 53 C, D).

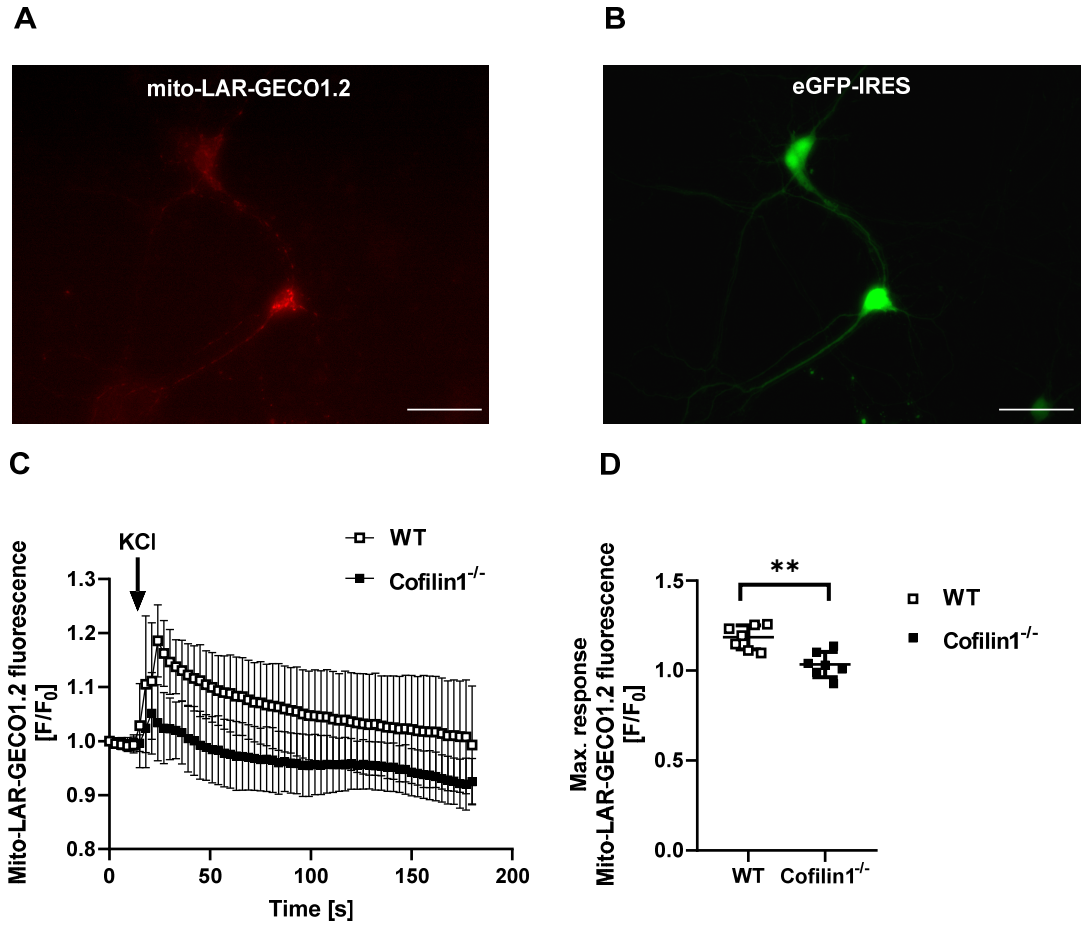

Figure 53. Mitochondrial Ca^{2+} uptake upon depolarization was assessed by mito-LAR GECO1.2 in primary cortical neurons.

A, B Primary cortical neurons from WT (eGFP-IRES-transfected) and cofilin1$^{-/-}$ (eGFP-CRE-transfected) E18-embryos were seeded into a coated µ-slide 8 well and transfected with eGFP-IRES or eGFP-CRE and mito-LAR GECO1.2 plasmids at DIV 6 and measured 48 hours later. *Scale bar* 50 µm. **C** Pooled data from seven measurements are shown as mean ± SD. **D** The maximal response upon 60 mM KCl stimulation is shown as mean ± SD. **p<0.01 compared to WT (unpaired t-test).

Cofilin-actin rod formation emerged as one of the most detrimental hallmarks occurring under pathological conditions in the brain, e.g. in neurodegenerative disorders [5, 6]. ATP decline is considered as a major trigger for the induction of cofilin-actin rods in mammalian cells [115]. In the present study, the impact of cofilin1 deletion on actin rod formation was evaluated by microscopy studies upon cofilin1 deficiency under ATP depleted conditions in primary cortical neurons. This analysis revealed a considerable difference between the number of actin rods per neuron, as cofilin1$^{-/-}$ neurons developed significantly less actin rods per neuron than WT cells under conditions of ATP deprivation (Figure 54).

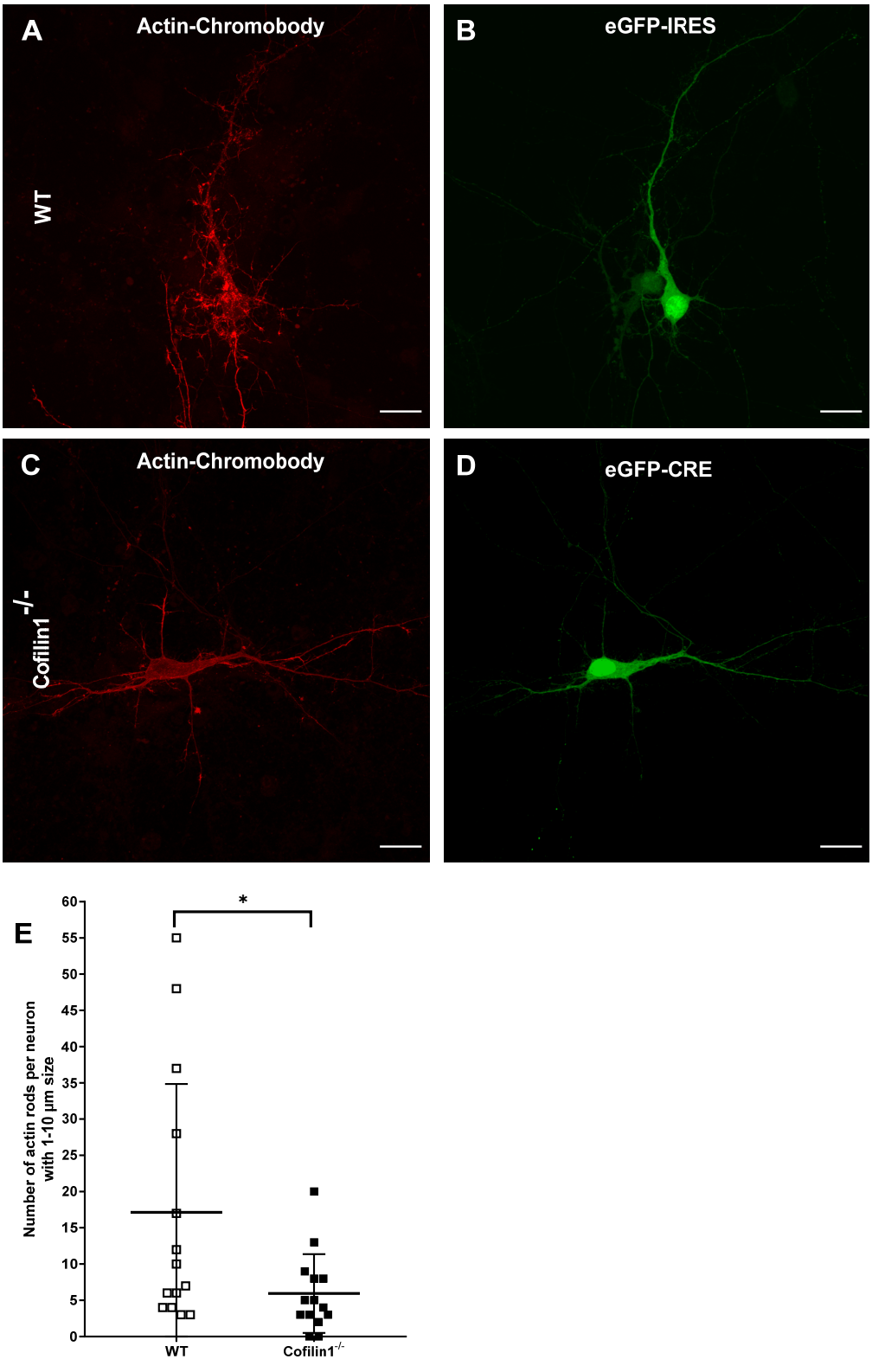

Figure 54. Actin rod formation under ATP depleted conditions of WT and cofilin1$^{-/-}$ neurons.

A, B Actin-chromobody-SNAP® was used to visualize actin rods upon ATP depletion in WT (eGFP-IRES-transfected) neurons or **C, D** cofilin1$^{-/-}$ (eGFP-CRE-transfected) neurons at DIV 6. **E** The number of actin rods per neuron with a size between 1 – 10 µm was calculated by application of a specific threshold by FIJI software. (n=14 per condition are shown as mean ± SD). *Scale bar* 20 µm. *p<0.05 compared to WT (unpaired t-test).

Mitochondrial dynamics is highly regulated by a multitude of mitochondrial shaping proteins as described previously (Chapter 1.3 Regulation of mitochondrial dynamics). Data obtained in MEF cells suggested a role for the actin-binding protein cofilin1 in the regulation of mitochondrial shape [140]. Therefore, it was highly relevant to investigate mitochondrial dynamics also in other cell types, e.g. in primary cortical neurons. For this purpose, mitochondria were visualized after transfection with a mitochondrial-targeted RFP and simultaneously transfected with either eGFP-IRES construct as a control or an eGFP-CRE plasmid to induce a specific cofilin1 knockout. The mitochondrial perimeter (Figure 55 B), representing the magnitude of each particle and the average circularity index (Figure 55 C), an indicative value for the sphericity of mitochondria, were determined by ImageJ Plugin by Ruben K. Dagda [39]. This analysis revealed a fragmented and spherical mitochondrial phenotype of cofilin1$^{-/-}$ neurons compared to WT (Figure 55), in line with data obtained in MEF cells (Chapter 4.1.1 Cofilin1 knockout leads to mitochondrial fragmentation via activation of DRP1).

Figure 55. Primary neurons deficient for cofilin1 exerted a fragmented mitochondrial phenotype.

A Primary cortical neurons were isolated from E18-embryos and cultivated for 7 days in vitro and afterwards tranfected with mito-RFP or pAAV-CMV-eGFP-IRES or pAAV-CMV-eGFP-IRES-CRE for another 4 days and finally fixed with formaldehyde 4 %. Images were acquired with an inverted fluorescence microscope Leica DMI6000. *Scale bar* 25 µm. **B** The mitochondrial shape was assessed using ImageJ Plugin Mito Macro by Ruben K. Dagda to calculate the mitochondrial perimeter or **C** the average circularity index. (eGFP IRES n=21; eGFP CRE n=29 are shown as box-plots 'min. to max.'). ***p<0.001 compared to eGFP-IRES transfected neurons (unpaired t-test).

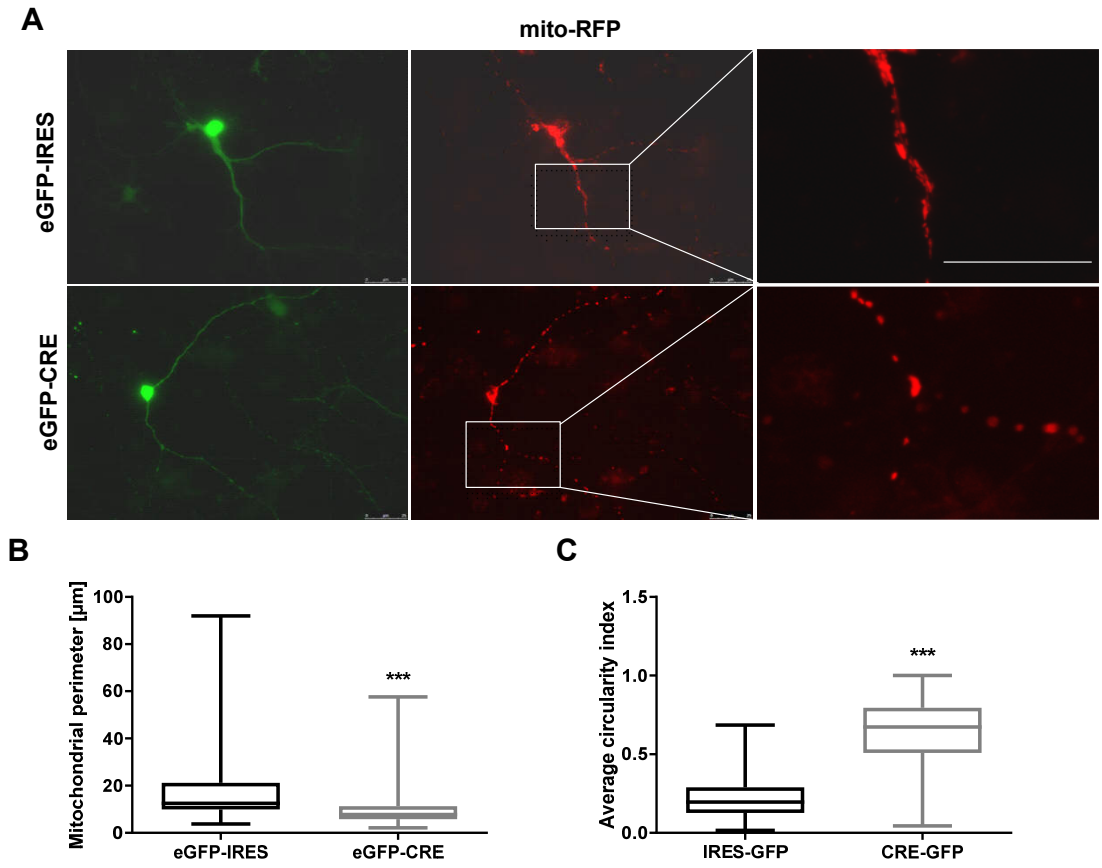

To evaluate if changed mitochondrial dynamics is also associated with changes in the transcription of mitochondrial biogenesis marker, the mRNAs of the key biogenesis proteins were quantified by qRT-PCR. *TFAM*, *PGC1α* and *Nrf-1* tended to be elevated (Figure 56 A,B,C), whereas *Nrf-2*, the mitochondrial DNA content and the autophagy marker *p62* were apparently unaffected (Figure 56 D, E, F).

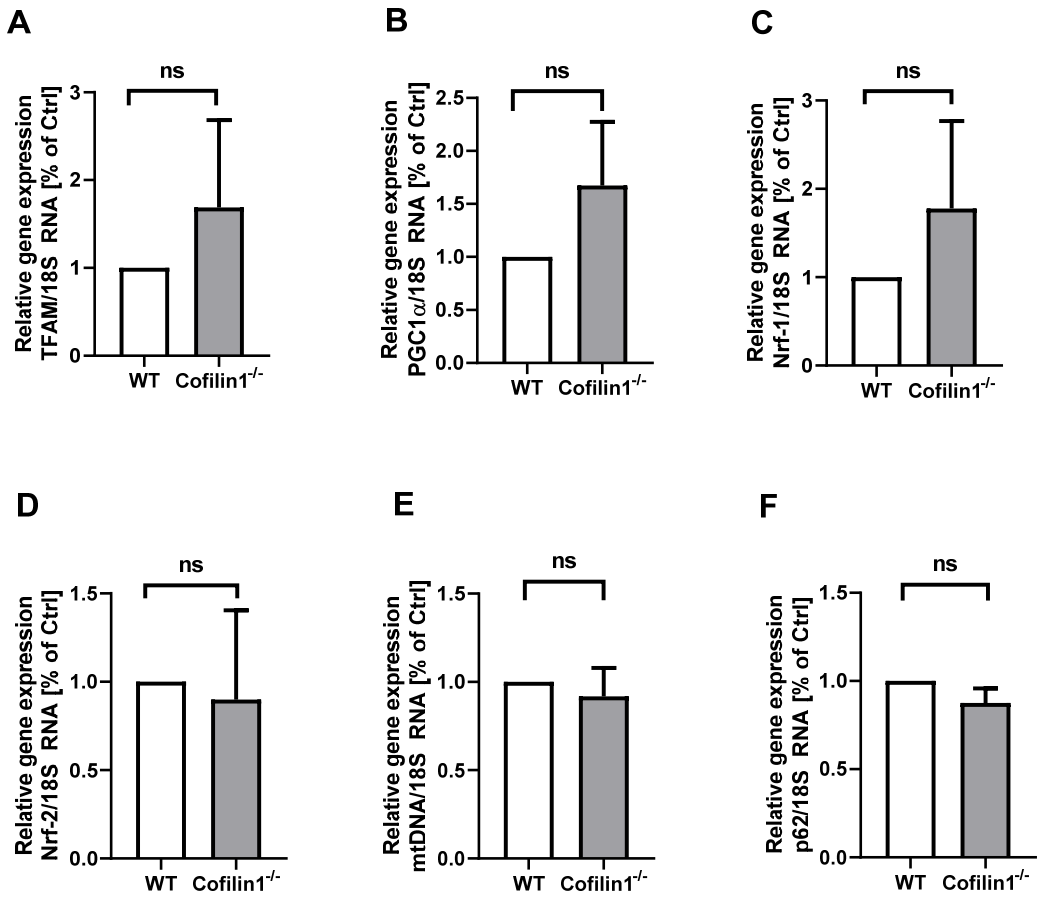

Figure 56. Proteins with impact on mitochondrial shape and biogenesis were evaluated by qRT-PCR of wildtype and cofilin1$^{-/-}$ neurons.

RNA yield from DIV25-DIV30 wildtype or cofilin1$^{-/-}$ neurons was collected and afterwards transcribed into cDNA for qRT-PCR evaluation**. A** Relative *TFAM* mRNA levels comparative to the reference gene 18S were quantified by qRT-PCR and the wildtype neurons were normalized to 1.0. **B** Relative *PGC1α* mRNA levels normalized 18S were quantified by qRT-PCR. **C** Relative *Nrf-1* mRNA levels normalized 18S were quantified by qRT-PCR. **D** Relative *Nrf-2* mRNA levels normalized to 18S were quantified by qRT-PCR. **E** Relative *mtDNA* mRNA levels normalized to 18S were quantified by qRT-PCR. **F** Relative *p62* mRNA levels normalized to 18S were quantified by qRT-PCR. Values are given as mean + SD of n=3 replicates). ns= not significant; (unpaired t-test).

In order to study a relation between DRP1 activation and mitochondrial alterations in primary cortical neurons, the phosphorylation state of DRP1 at serine 616 and 637 was evaluated by Western blot (Figure 57). DRP1 was previously shown to be in an active state, if serine 616 is phosphorylated, while serine 637 is simultaneously dephosphorylated [104]. The present study conveyed evidence, that cofilin1$^{-/-}$ depletion in neurons led to an activation of the pro-fission protein DRP1, as both crucial phosphorylation sides were significantly altered compared to WT neurons (Figure 57 B, C), whereas total DRP1 abundance was not significantly changed (Figure 57 A).

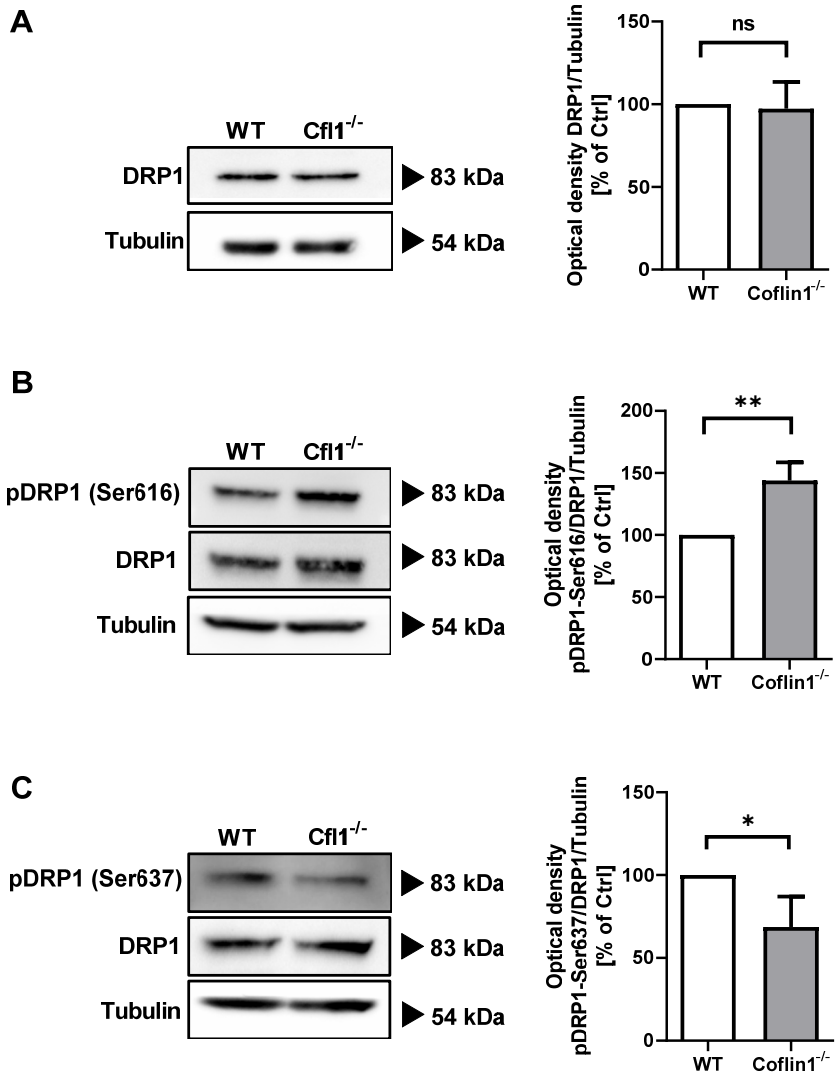

Figure 57. DRP1 was activated in cofilin1-knockout neurons.

A Protein lysates were collected at DIV30 from primary cortical neurons of E18 mouse embryos. DRP1 protein abundance was evaluated by Western blot and quantified from three blots (mean + SD). **B** DRP1 phosphorylation of serine residue on position 616 and **C** serine residue 637 was analyzed by specific antibodies, respectively. Quantification was conducted by normalization to DRP1 and α-Tubulin from three experiments and data are presented as mean + SD. ns= not significant; *p<0.05 compared to WT; **p<0.01 compared to WT (unpaired t-test). WT (wildtype=flx/flx); $Cfl1^{-/-}$ (cofilin1-knockout).

Cofilin1 is an important actin regulator, that is important for a huge variety of cellular functions and more specifically for brain development and synapse formation. In addition, after short-term deletion of cofilin1 *in vitro* mitochondrial integrity was completely preserved, although changes in mitochondrial dynamics emerged (Chapter 4.1.2 Mitochondrial function is not impaired upon cofilin1 depletion). In order to study long-term effects of cofilin1 deletion on mitochondrial function, hippocampi of adult mice were studied by the Seahorse XFe Analyzer. By measurement of the oxygen consumption

rate after biochemical disturbance with different inhibitors of the respiratory chain complexes, the bioenergetic profile of mitochondria was assessed, representing the viability and respiratory capacity of mitochondria. The measurements of isolated mitochondria revealed a sustained mitochondrial respiration of WT and cofilin1$^{-/-}$ animals (Figure 58), uncovered by compendious presentation of all three analyzed WT and cofilin1$^{-/-}$ animals (Figure 58 B), indicating that long-term cofilin1-depletion exerts no detrimental effects on mitochondrial function.

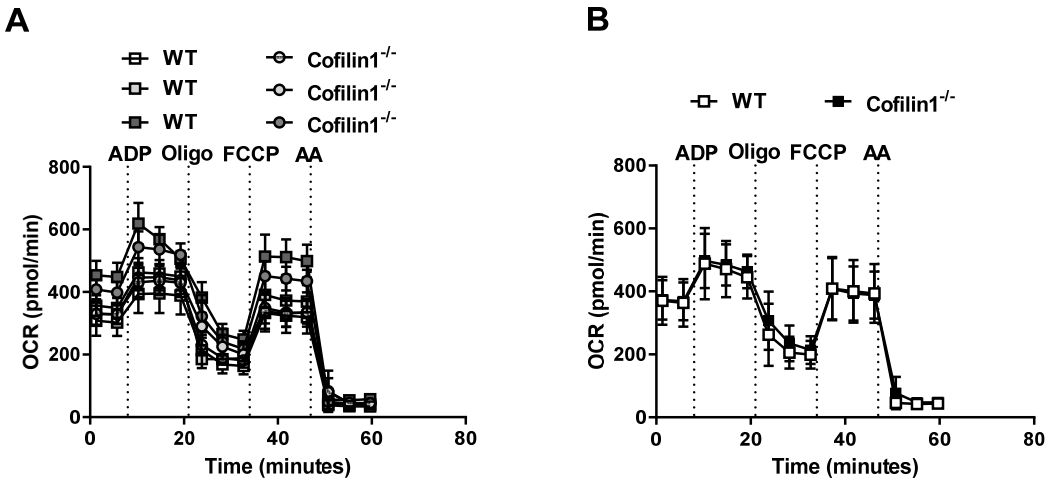

Figure 58. Isolated mitochondria from HC of adult WT and cofilin1$^{-/-}$ mice were measured by Seahorse XFe Analyzer.

A The OCR measurement of three independent, four to six-month old wildtype (flx/flx) or cofilin1$^{-/-}$ (Cfl1$^{flx/flx}$,CaMKIIα-Cre) mice was conducted after isolation of mitochondria from the HC. Values are presented as mean ± SD from 5-9 wells per condition. **B** Pooled data from three WT-mice and three cofilin1$^{-/-}$ mice (shown in A) are presented as mean ± SD.

4.4 Effects of recombinant cofilin1 protein on isolated mitochondria

Cofilin1 was identified as a crucial protein involved in several physiological and pathological mechanisms and phenotypes. Besides regulation of actin dynamics, more precisely, the enforcement of actin depolymerization, it was also described to participate in cell death mechanisms induced by oxidative stress, e.g. induced by the oxidant taurine chloramine [88] or H_2O_2 [168]. In order to study direct effects of recombinant cofilin1 on mitochondrial parameters, isolated mitochondria from adult mouse cortex were incubated with recombinant cofilin1 and afterwards analyzed by fluorescence-based cell analysis or Seahorse Xfe Analyzer. To unhinge mitochondria from an intact brain tissue, a cell homogenizer was applied for proper decomposition. Different cellular fractions, i.e. the mitochondrial and the nuclear fraction were afterwards enriched by centrifugation.

Successful fractionation was confirmed by immunoblotting for α-Tubulin, as a cytosolic marker, Tim23, a protein of the inner mitochondrial membrane and the nucleus-specific protein HDAC (Figure 59 A). The integrity of mitochondria after isolation was verified by the cationic fluorescent dye rhodamine 123, which is readily sequestered in intact mitochondria and released by treatment with the uncoupler FCCP (Figure 59 B).

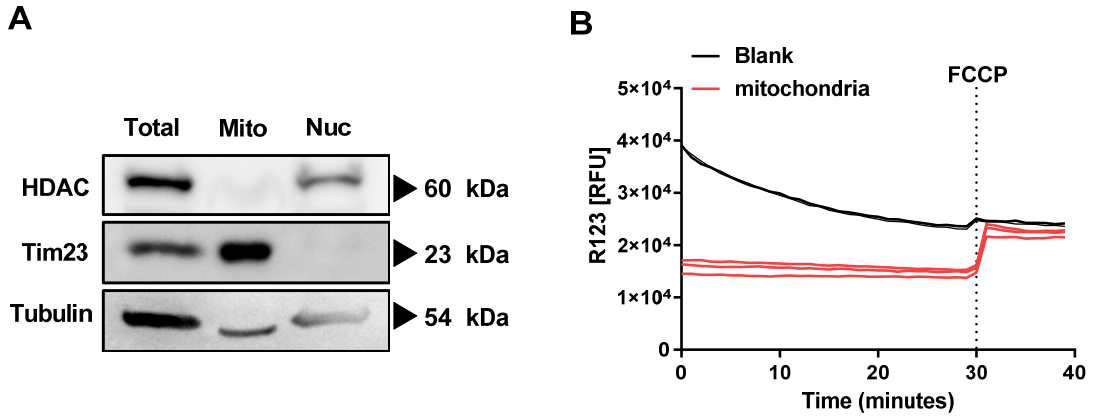

Figure 59. Implementation of a cell homogenizer to mouse brain cortex revealed enrichment of a crude mitochondrial fraction with a preserved mitochondrial integrity.

A Western blot analysis of total protein lysate, the mitochondrial and the nuclear fraction shows different signals of the cytosolic microtubule protein tubulin, the nucleus marker HDAC and the inner mitochondrial membrane protein Tim23. **B** Rhodamine123 was used to examine the integrity of mitochondria upon isolation with the cell homogenizer and required centrifugation processes. Total (total lysate); Mito (mitochondrial fraction); Nuc (nucleus fraction); R123 (Rhodamine 123).

Cofilin1 possesses several cysteine residues essential for the quaternary structure of the protein by forming intra- or intermolecular disulfide bonds. Four crucial cysteines are described in humans at position 39, 80, 139 and 147 prone to oxidation [88, 181]. Dephosphorylation of serine 3 and oxidation of the aforementioned cysteine residues are considered as crucial prerequisites for mitochondrial localization after apoptosis induction [33, 88, 118]. To specifically address the impact of different cofilin1 mutants (**2Cys**: Cys139Ser/Cys147Ser; **4Cys**: Cys39Ser, Cys80Ser, Cys139Ser, Cys147Ser) on mitochondrial ROS formation, mitochondrial membrane potential and mitochondrial respiration, isolated mitochondria were incubated with the respective cofilin1 variants under basal, oxidized (H_2O_2) or reduced conditions (DTT). Oxidation or reduction exerted no effect on the protein amount, as evaluated by Western blot (Figure 60 A). Strikingly, the reduced form of WT cofilin1 had no impact on the membrane potential, whereas application of WT cofilin1 either in the natural form or in the oxidized state decreased the membrane potential. Further, the

Cys139/147Ser mutation as well as conversion of all four cysteines to serine completely abolished the deleterious effect of the protein (Figure 60 B, C).

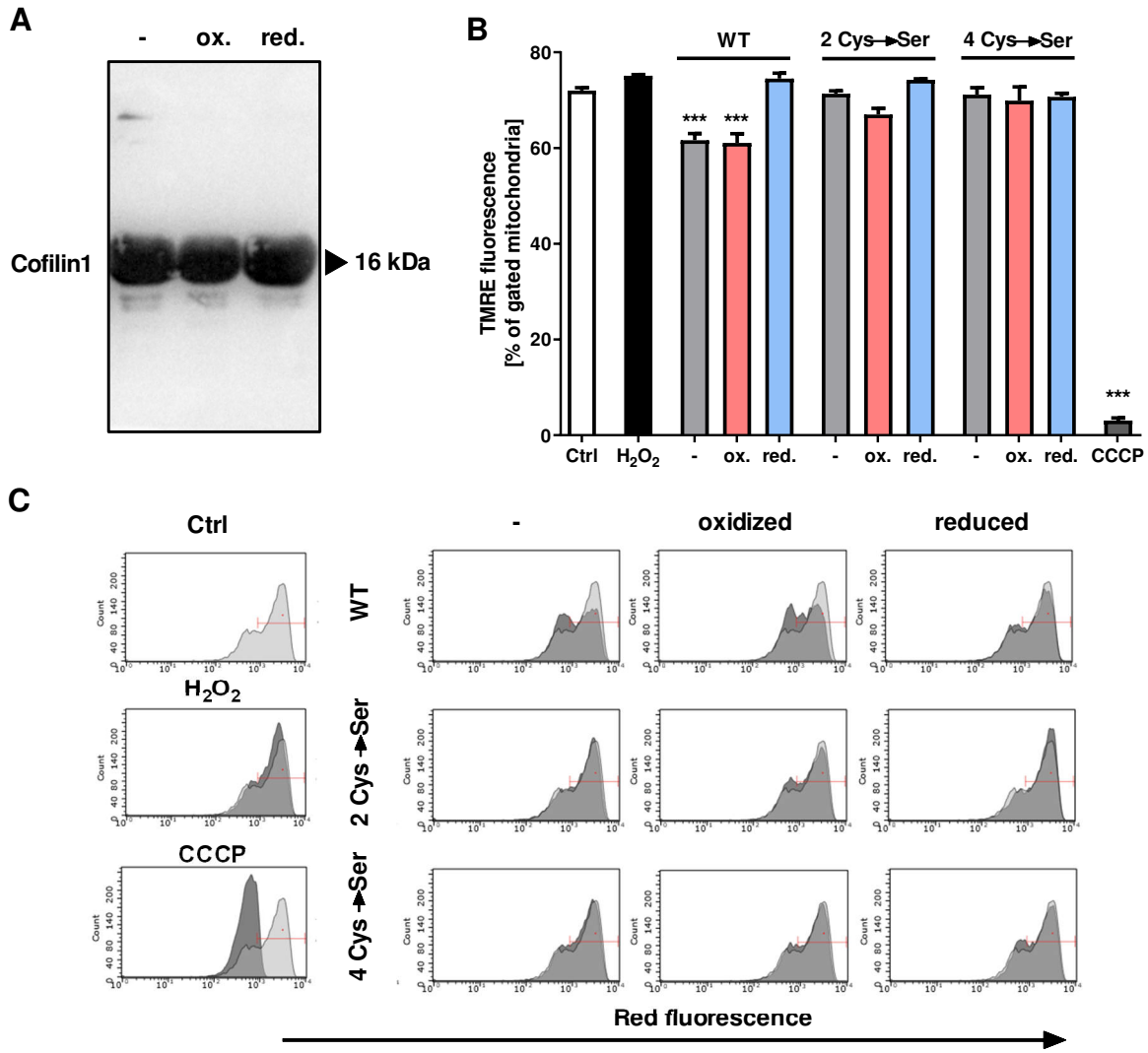

Figure 60. Isolated mitochondria were incubated with cofilin1 recombinant protein and the impact on the mitochondrial membrane potential was assessed by TMRE staining.

A Recombinant cofilin1 protein was applied in the native, the oxidized (50 µM H_2O_2) or in the reduced form (10 mM DTT) to SDS-PAGE and Western blot. **B** 75 µg mitochondria were incubated with 10 µg protein for 20 minutes at 37 °C and finally stained with TMRE (1:1,000). 50 µM CCCP served as a positive control. 10,000 total events were measured and shown as mean + SD (n=3 replicates). **C** Representative histograms of the TMRE FACS analysis are shown. WT (wildtype cofilin1 protein); 2Cys (Cys139/Cys147 → serine mutation); 4Cys (39, 80, 139, 147 → serine mutation) ***p<0.001 compared to ctrl (ANOVA, Scheffé's-test).

To elucidate the impact of the WT protein and the 2Cys-cofilin1 mutant on a broader spectrum of mitochondrial parameters of isolated mitochondria, mitochondrial ROS generation was measured after MitoSOX staining and subsequent quantification of the red fluorescence intensities. The maximal effect of mitochondrial ROS generation was evoked by antimycin A treatment, a potent complex III-inhibitor of the respiratory chain [170] (Figure

61 B). Surprisingly, the oxidized form of the WT protein also induced a significant burst of mitochondrial ROS, whereas the reduced WT protein and the 2Cys-mutant generated comparable ROS levels to mitochondria of the untreated control group (Figure 61 A). Antimycin A (AA) was used as a positive control to demonstrate the highest inducible amount of mitochondrial ROS.

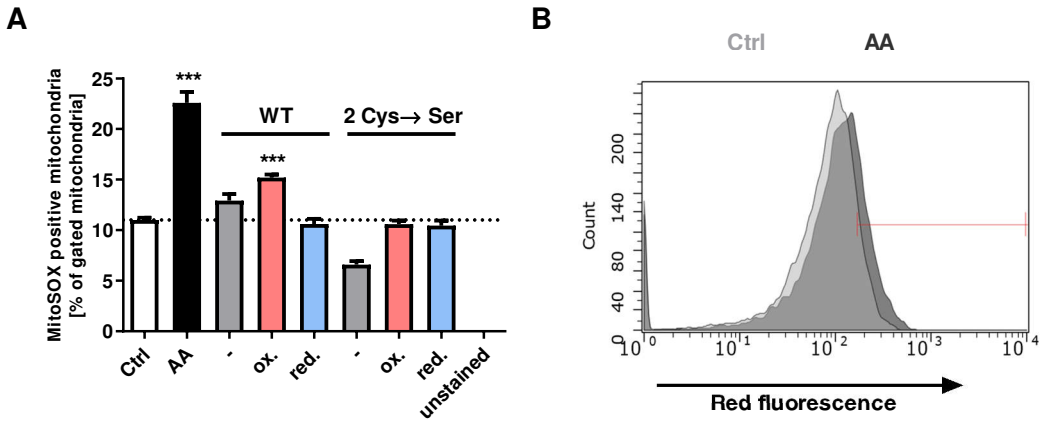

Figure 61. MitoSOX measurement of isolated mitochondria incubated with cofilin1 recombinant protein.

A 75 µg mitochondria were incubated with 10 µg protein for 20 minutes at 37 °C and finally stained with MitoSOX red fluorescent dye (1:1,000). 10 µM Antimycin A served as a positive control. 10,000 total events were measured and shown as mean + SD (n=3 replicates). **B** A representative histogram of the MitoSOX FACS analysis of ctrl and AA treated mitochondria is illustrated to show the maximal effect. AA (Antimycin A); WT (wildtype cofilin1 protein); 2Cys (Cys139/Cys147 → serine mutation); ***p<0.001 compared to ctrl (ANOVA, Scheffé's-test).

Finally, to understand the effect of recombinant cofilin1 proteins on a functional level, mitochondrial bioenergetics were evaluated by Seahorse XFe Analyzer. This measurement facilitates detailed evaluation of specific steps of mitochondrial respiration. The mitochondrial assay buffer (MAS) contained succinate to specifically assess complex II-driven respiration and rotenone to prevent reverse electron flow. ADP injection allows the specific calculation of the phosphorylating capacity to produce ATP. In the current study, the analysis of the ADP-driven activity revealed a significant difference ($p<0.02$) between the control condition and mitochondria challenged with the oxidized WT cofilin1 protein (Figure 62 A, C). The oxidized form of the 2Cys mutant mediated extenuated detrimental impact on the ADP-induced respiration, but still significant ($p<0.04$), which was completely reversed by reduction of the present cysteine residues (Figure 62 B, C). Oligomycin, a potent ATP synthase inhibitor (complex V), allows for estimating the proton leak across the inner mitochondrial membrane, which was not apparently affected after application of either the oxidized or reduced form of the recombinant protein (Figure 62 A, B). Injection of the

uncoupler FCCP disrupts the proton gradient to facilitate maximal respiration. Again, this state of mitochondrial respiration was not compromised by neither the WT cofilin1 recombinant protein, nor the 2Cys cofilin1 mutant (Figure 62 A, B, D). The present data suggests a role for the oxidized form of cofilin1 cysteine residues in mediating deleterious effects on mitochondrial integrity and function, which was attenuated if the either all cysteines, or at least the residues at position 139 and 147 were mutated to serine.

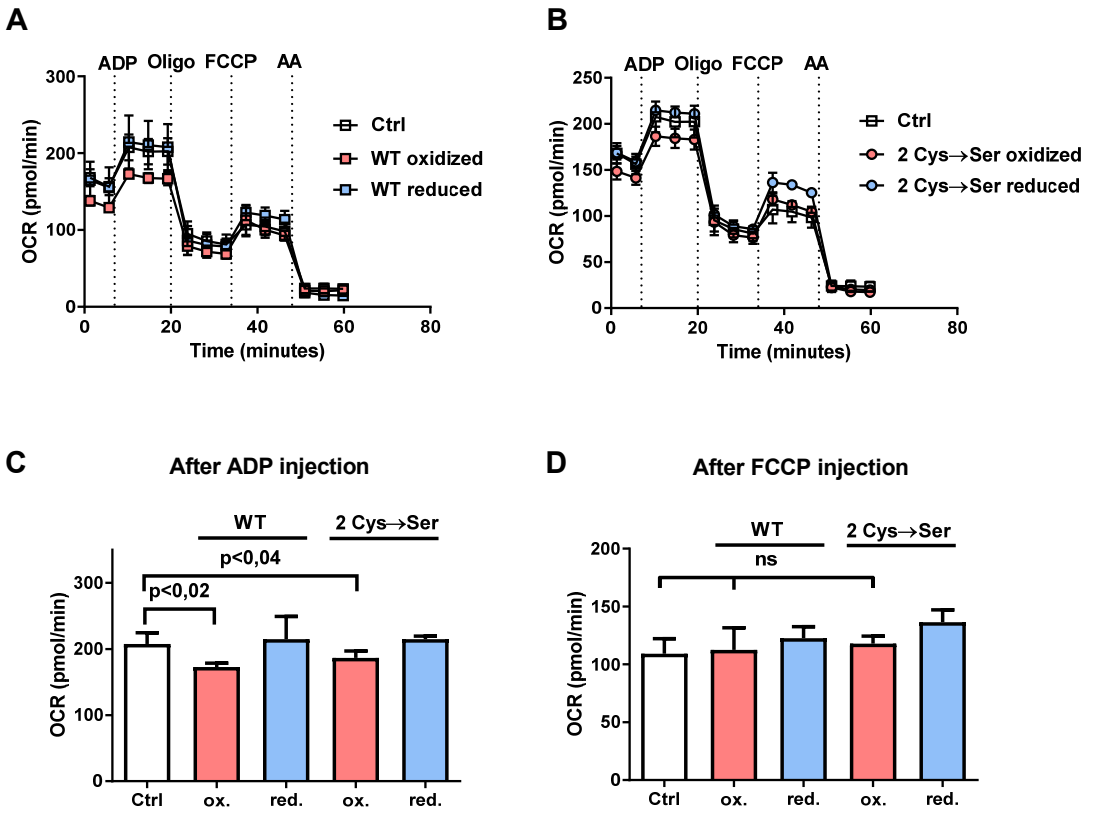

Figure 62 Evaluation of the impact of cofilin1 recombinant protein on mitochondrial respiration.

A 10 µg mitochondria per well were incubated with 1 µg WT protein or **B** with the 2 Cys mutant either in the native form, the oxidized form (50 µM H_2O_2) or in the reduced form (10 mM DTT) for 30 minutes at 37 °C and finally administered to the Seahorse Analyzer. Mean + SD (n=5-9 replicates). **C** Quantification of mitochondrial activity was conducted with the values delivered after the injection of ADP as a substrate for the OXPHOS phosphorylating capacity. **D** FCCP uncouples the oxygen consumption from ATP production and is used to assess maximal respiratory activity. ns (not significant); WT (wildtype cofilin1 protein); 2 Cys (Cys139/Cys147 → serine mutation); ***p<0.001 compared to ctrl (ANOVA, Scheffé's-test).

5 Discussion

5.1 Cofilin1 knockout in MEF cells led to mitochondrial fragmentation without deleterious effects on mitochondrial function

Mitochondrial dynamics, i.e. the balance between fusion and fission is important for the whole organism to maintain cellular bioenergetics, retain intracellular calcium homeostasis and facilitate energy supply to regions of high demand. An imbalance of these dynamic processes were associated with neurodegenerative disorders, such as Parkinson's disease, Alzheimer's disease or Charcot-Marie Tooth neuropathy [25]. Mitochondrial fragmentation, mediated by a major mitochondrial fission protein, namely dynamin-related protein 1 (DRP1), was previously associated with cell death progression upon apoptosis induction with staurosporine, etoposide or γ-irradiation [52], but also during mitotic division of cells to ensure proper distribution of mitochondria to the daughter cell [48].

In the present study, implications of actin-disturbance by deletion of the major actin-binding protein cofilin1 on mitochondrial dynamics were examined. Of note, the mitochondrial phenotype upon deletion of cofilin1 was considerably changed towards a disassembled, highly fragmented appearance, which was confirmed by enhanced DRP1-activity, as assessed by Western blot analysis of two crucial phosphorylation sites (Figure 12). Actin-dependent recruitment of DRP1 leads to constriction of the outer mitochondrial membrane (OMM), but need further stimuli, such as mitochondrial Ca^{2+} uptake through MCU to drive a productive fission event [24, 31]. Therefore, three prerequisites for mitochondrial constriction and subsequent fission are required and eventually fulfilled in cofilin1$^{-/-}$-MEFs: First, cofilin1 deletion leads to enhanced actin-polymerization by increasing filamentous actin proportion, represented by an almost doubled F/G-actin ratio [140]. Filamentous actin (F-actin) was described to be essential for DRP1-recruitment to mitochondria [72, 90]. Thus, an increase in F-actin seems to proportionally increase DRP1 recruitment. Second, subcellular DRP1 distribution is not only shifted towards mitochondria, the protein is also in its active state, as the crucial serine residue 616 is phosphorylated, whereas serine 637 is dephosphorylated (Figure 12). Ultimately, specific evaluation with the mitochondrial Ca^{2+}-sensitive dye Rhod-2 AM revealed elevated basal mitochondrial Ca^{2+} levels and increased mitochondrial uniporter (MCU) expression upon cofilin1 deletion (Figure 19), suggesting that the major requirements for a productive fission event are fulfilled (Figure 17). How

cofilin1 deficiency affects MCU transcription and protein expression is not clear until now. Potentially, ER-mitochondrial contacts are altered towards longer distances triggered by enhanced INF2-induced actin-polymerization at ER-mitochondrial contact sides. Therefore, Ca^{2+} transfer from ER to mitochondria might be aggravated and thus MCU is upregulated as a compensatory response, as previously discussed in $Mfn2^{-/-}$ cells. The authors claimed, that Mnf2 acts as a negative regulator of ER–mitochondrial tethering, thereby regulating ER-mitochondrial Ca^{2+} transfer and MCU expression [49, 137].

Surprisingly, existing data obtained after transfection with genetically encoded low-affinity Ca^{2+}-indicator mito-LAR GECO1.2 and subsequent stimulated Ca^{2+} uptake into mitochondria, revealed a lower capacity of $cofilin1^{-/-}$ MEFs to accumulate Ca^{2+} after acute stimulation compared to control cells (Figure 18). If all results are taken into consideration, cofilin1 depletion eventually lead to increased MCU expression, thus basal mitochondrial Ca^{2+} levels might be saturated. Hence, after acute stimulation of mitochondrial Ca^{2+} uptake, these organelles incorporated significantly less Ca^{2+} after cofilin1-knockout as control MEFs.

However, it still remains elusive, whether decreased acute mitochondrial Ca^{2+} uptake occurred only due to saturated basal mitochondrial Ca^{2+} levels or if other mechanisms further contributed to the observed effect. Yet, another possible explanation for the observed changes in mitochondrial Ca^{2+} uptake is an altered distance of ER-mitochondrial contacts through enhanced actin polymerization upon cofilin1 deletion (Figure 63). Evidence for this assumption was given by Chakrabarti and coworkers [24]. They demonstrated that INF2-depletion in U2OS cells diminished mitochondrial Ca^{2+} uptake after stimulation with either histamine or the ionophore ionomycin [24]. EM micrographs revealed insight into the distance between ER and mitochondria. Distances smaller than 30 nm were considered as close ER-mitochondrial contacts necessary for ER-mitochondrial Ca^{2+} transfer. Surprisingly, ionomycin evoked a significant increase of close contacts between both organelles in WT cells, but not in INF2-deficient U2OS cells, indicating that INF2-mediated actin polymerization between ER and mitochondria is necessary for the formation of close contact sides [24]. A final conclusion on ER-mitochondrial distances in the present study is unfeasible, as this moiety was not addressed until now.

Previous studies repeatedly reported a deleterious impact of mitochondrial fragmentation, as mitochondrial fission and associated functional impairments and the organelles' disintegration were suggested as a 'point of no return' in many cell death pathways [36, 82].

In the current work, it was clearly demonstrated that mitochondrial fragmentation was neither dependent on mitochondrial ROS accumulation [55] nor accompanied by mitochondrial demise, shown by preserved ATP levels, mitochondrial respiration, and an intact mitochondrial membrane potential (Figure 14). In line with these observations, also the amount of damaged or dead cells, addressed by AnnexinV and propidium iodide (PI) staining, was unaffected upon cofilin1 deletion (Figure 15). Intriguingly, under conditions of oxidative stress induced by glutamate, the amount of cell death was neither exaggerated nor diminished in cofilin1$^{-/-}$ MEFs compared to controls (Figure 15). However, mitochondrial fragmentation in other paradigms lead to higher susceptibility to ROS-induced mitophagy [171]. Detailed analysis of a specific form of cell death, namely apoptosis, revealed that cofilin1 was dispensable for cell death progression in MEF cells, although a transactivation of cofilin1 from the cytosol to mitochondria was demonstrated [139].

Enhanced transcription of the major mitochondrial biogenesis markers Nrf-1 and PGC1α might counteract the fragmented mitochondrial phenotype (Figure 16), as previous studies demonstrated, that newly synthesized mitochondria induced by AICAR treatment appeared elongated [75]. AICAR is able to induce mitochondrial biogenesis and mitochondrial elongation via AMPK-mediated Nrf-1 activation [75]. Additionally, mitochondria of cofilin1$^{-/-}$ cells were still able to fuse [140], contributing to the notion that under these circumstances mitochondria are in an intact and healthy condition.

In order to explore the option that mitochondrial fragmentation in cofilin1$^{-/-}$ cells is due to accumulation of inoperable mitochondria, the quantitative analysis of protein expression levels of the major autophagy marker LC3B-II was assessed by Western blot after autophagy-induction with Bafilomycin A. Under these treatment conditions, the protein abundance in control and cofilin1$^{-/-}$ MEFs was equally increased, suggesting that mitochondrial fragmentation is not due to enhanced gathering of defective organelles (Figure 20).

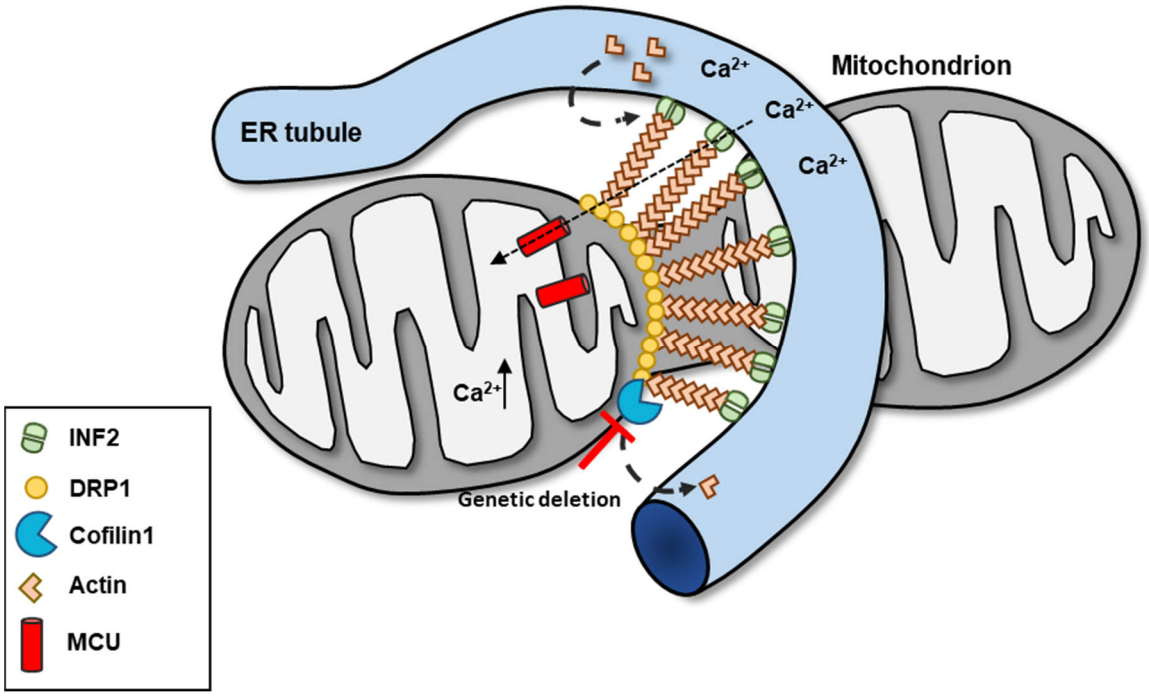

Figure 63. Model of MCU regulation after genetic cofilin1 deletion in MEF cells.

Genetic deletion of cofilin1 in MEF cells lead to increased MCU protein abundance and thus to higher basal mitochondrial Ca^{2+} levels putatively triggered by enhanced INF2-induced actin-polymerization between ER and mitochondria.

Finally, the recent study lack data on the detailed mitochondrial structure in cofilin1$^{-/-}$ MEF cells obtained with an electron microscope. As such, whether complete mitochondrial fragmentation is present cannot be faithfully determined due to the resolution limit of fluorescence microscopy. Emerging evidence suggests that mitochondria can form thin double-membrane protrusions that allow the communication of distant mitochondria, so called 'nanotunnels' [167, 184]. Until now, inter-mitochondrial nanotunnels are described in skeletal muscle [166], cardiomyocytes [80] and kidney cells [19]; and depending on the cell type, the diameter of these protrusions can vary between 40 and 200 nm [167] and, thus, they are hardly detectable. Surprisingly, changes in mitochondrial Ca^{2+} were attributed to mitochondrial nanotunnel formation [98] underlining the possibility that the observed mitochondrial fragmentation was not only a result of DRP1-transactivation and mitochondrial fission, but also based on nanotunnel formation between non-adjacent mitochondria due to elevated mitochondrial Ca^{2+} levels in cofilin1$^{-/-}$ MEFs.

5.2 Neuronal HT22 cells deficient for the actin-regulatory proteins cofilin1 or INF2 exerted higher resilience in models of oxidative stress

Among others, oxidative stress and subsequent mitochondrial impairment are one of the most harmful factors contributing to functional demise of neurons in neurodegenerative diseases [105]. In the current study, the role of cofilin1 in the paradigms of erastin and glutamate-induced cell death in neuronal HT22 cells were examined with specific focus on mitochondrial function, as mitochondrial impairment is considered as 'the point of no return' after cell death induction. However, the role of cofilin1 in apoptosis progression is contradictory until now, as studies obtained in lymphoma cells or T-cells claimed, that oxidized cofilin1 plays an important role in mediating apoptotic signaling to mitochondria by cofilin1-transactivation and subsequent induction of mitochondrial swelling [33, 88, 168], whereas, in contrast, in mouse embryonic fibroblasts (MEF) cofilin1 was found to be dispensable in regulated cellular death mechanisms [139]. The present study emphasizes for the first time, that cofilin1 is activated in neuronal cells by dephosphorylation at serine residue 3 (Ser3) in cell death paradigm of oxytosis and ferroptosis. Importantly, cofilin1-silencing significantly attenuated cell death progression (Figure 22), which is perfectly in line with previous findings on oxidative stress-induced activation of cofilin1 [86]. More precisely, the definite point of action of cofilin1 after oxytosis or ferroptosis induction was located upstream of mitochondria, but downstream of lipid peroxidation and soluble ROS accumulation. BODIPY measurement addresses the amount of oxidized cytosolic or membrane lipids, whereas H_2DCF is an indicative value for the generation ROS, such as hydrogen peroxide, nitrate and hypochlorous acid. Both indicators emphasized that cofilin1 depletion exerted no effects on early hallmarks of the cell death cascade, suggesting that lipid peroxidation as well as soluble ROS generation upon cell death induction occurred upstream and potentially induce a noxious, oxidized form of cofilin1 (Figure 23). However, mitochondrial parameters, such as mitochondria-derived ROS, detrimental mitochondrial Ca^{2+} overload, and the mitochondrial membrane potential were preserved in cofilin1 silenced neuronal HT22 cells upon erastin or glutamate exposure (Figure 24 and Figure 25).

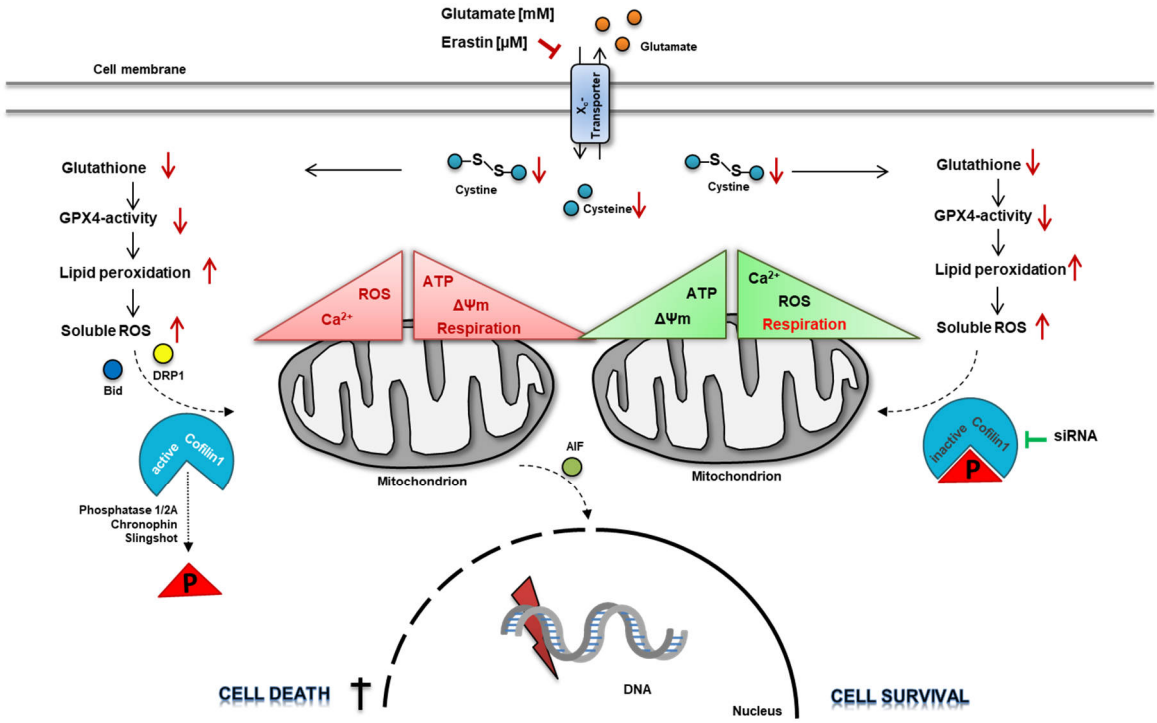

Figure 64. Putative mechanism of cofilin1 transactivation in models of erastin- or glutamate-induced cellular damage.

Oxytosis and ferroptosis share common features of the cell death cascade, such as glutathione depletion leading to diminished glutathione-peroxidase 4 activity and subsequent enhanced peroxidation of cellular or membrane lipids. Transactivation of pro-apoptotic proteins, such as Bid or Bax, are a leading cause of mitochondrial demise. Dephosphorylated cofiin1 was identified as a key regulator in the cell death progression after erastin or glutamate treatment. Cofilin1 silencing with a specific siRNA was shown to protect mitochondrial damage, by preservation of an intact mitochondrial membrane potential and circumvention of mitochondrial ROS accumulation of detrimental Ca^{2+} overload. X_c^--transporter (glutamate/cystine antiporter); GPX4 (glutathione peroxidase 4); ROS (reactive oxygen species); DRP1 (dynamin-related protein 1); Bid (BH3-interacting domain death agonist); ATP (adenosine triphosphate); ΔΨm (mitochondrial membrane potential); AIF (apoptosis inducing factor); DNA (deoxyribonucleic acid); Ca^{2+} (Calcium); P (Phosphorylation at serine 3).

Surprisingly, the maintenance of mitochondrial respiration, assessed by Seahorse XFe Analyzer, was negligible in cofilin-deficient cells after erastin or glutamate exposure, whereas the rate of glycolysis was entirely sustained (Figure 26). These findings suggested, that cells deficient for the actin-binding protein cofilin1 shifted their metabolic status towards glycolysis to match their energy demand. Accordingly, ATP levels of cofilin1-siRNA transfected cells were significantly preserved after cell death induction with erastin or glutamate (Figure 27). This phenomenon was previously described in cancer cells and referred to as 'Warburg effect' [163]. For detailed examination of the expression levels of key glycolytic enzymes, such as hypoxia-inducible factor 1 (Hif1α), c-Myc and pyruvate dehydrogenase kinase 1 (PDK1), Western blot analysis was performed and quantified afterwards. In particular, one major consequence of Hifα activation is the blockage of

pyruvate to enter the TCA cycle by enhancement of PDK1 activity, which, in turn, inhibits pyruvate dehydrogenase (PDH)-mediated conversion of pyruvate to acetyl-CoA [87]. Finally, this results in attenuated mitochondrial respiration. Surprisingly, Hif1α level are increased upon 9 hours treatment with erastin or glutamate in control cells (scrambled siRNA), but not after cofilin1-silencing, suggesting that control cells try to fix their energy production by enhancing Hif1α and PDK1-driven OXPHOS attenuation and glycolysis promotion, which is not sufficient to rescue the energy production of control cells under erastin or glutamate treatment (Figure 29 and Figure 30). However, cofilin1 siRNA-transfected cells operated differently under conditions of oxidative stress. They showed increased expression levels of c-Myc after 9-hour erastin or glutamate exposure (Figure 29 and Figure 30). C-Myc is a major regulator of glycolytic gene expression, such as LDH-A or enolase, thus, c-Myc activation mainly results in pronounced enhancement of glycolysis, until now, a mechanism only described in tumor cells [114, 187]. C-Myc and cofilin1 were recently described to underlie a direct interdependence, as c-Myc exerts properties on cofilin1 activation, nuclear translocation and F-actin reorganization in medulloblastoma cells [100]. Whether the activation cascade of c-Myc and cofilin1 can also occur *vice versa* has not been studied. The current study therefore suggested a new role for cofilin1 in the regulation of mitochondrial bioenergetic regulation, in particular, cofilin1-deficiency enforced the energy production towards glycolysis via c-Myc activation, leading to potent activation of glycolysis, whereas in erastin or glutamate-treated control cells Hif1α-PDK1 axis activation is insufficient to rescue energy production in terms of oxidative stress.

The recent data clearly demonstrate, that cofilin1 activation acts as a checkpoint in oxidative stress-induced cell death. Moreover, cofilin1-overexpression of the wildtype form or in the constitutively active form (Ser3→Ala) in neuronal HT22 cells itself exerted deleterious effects resulting in cellular damage evaluated by AnnexinV/PI staining, independently of additional noxious matter (Figure 33), which is consistent with previous studies addressing cofilin1 activity on cell death [88, 168]. These data suggest, that cofilin1 alone can induce collapse of mitochondrial integrity finally leading to cell death. If cofilin1 transactivation depends on other factors, such as DRP1 – a known protein involved in mitochondrial translocation upon cell death induction [64] – is not entirely resolved. Previous studies revealed a requirement for the pro-fission protein DRP1 in cofilin1-mediated apoptosis signaling induced by the natural compound 4-methylthiobutyl isothiocyanate (erucin) in human breast cancer cells [101]. To examine the possibility that cofilin1 needs the interaction with DRP1 in neuronal

systems, immunoprecipitation was conducted, which revealed, unlike the above-mentioned finding, no direct interaction of both proteins during oxytosis or ferroptosis (Figure 34). Interestingly, in this regard, a previous study established that the interaction of cofilin1 with p53 in models of Aβ-induced apoptosis exerts stronger deleterious effects on mitochondria than cofilin1 alone [106]. Further elucidation is needed to finally answer the question of putative interaction partners of cofilin1 in models of erastin or glutamate-induced neuronal cell death.

Another prevailing perception of the current study is the protective effect of INF2-knockout on mitochondrial parameters and cellular survival under oxidative stress conditions in neuronal HT22 cells (Chapter 4.2.3 INF2 depletion abrogates loss of mitochondrial function and cell death upon glutamate or erastin treatment). Hence, the respective findings demonstrate, for the first time, that besides cofilin1, another important actin-regulatory protein plays a fundamental role in cell death progression (Figure 40). In line with these findings, a recent study in a human keratinocyte cell line claimed, that INF2 is upregulated upon cell death induction with H_2O_2 and, in turn, its loss provided protection under oxidative stress conditions [28]. They demonstrated that this effect was mediated by maintaining mitochondrial dynamics and function and promoting mitochondrial energy metabolism on the molecular basis of Hif1-OPA1 signaling pathway, as inhibition of Hif1 abolished the valuable effect of INF2 deletion [28].

Mitochondrial Ca^{2+} homeostasis is considered a major factor defining the function and integrity of these organelles. Proper mitochondrial Ca^{2+} regulation, i.e. the uptake and the release across the inner mitochondrial membrane, is required for many mitochondrial processes, such as oxidative phosphorylation (OXPHOS) by direct activation of complex I, III and IV of the electron transport chain [58] or for key proteins of the tricarboxylic acid cycle (TCA) [162]. Intriguingly, if matrix Ca^{2+} concentration exceeds approximately 10 µM, a pathological state is accomplished, referred to as mitochondrial permeability transition (mPT) [174] and represents a major prerequisite for cell death progression [99]. Importantly, the presented data suggested, that INF2 substantially abolished massive mitochondrial Ca^{2+} overload assessed by Rhod-2 AM staining and quantification by fluorescent cell analysis (Figure 36 C, D) after cell death induction by erastin or glutamate, potentially contributing to beneficial effects on cellular survival under these circumstances. In accordance, a study from Chakrabarti demonstrated, that INF2-deficiency entirely averted acute ER-derived mitochondrial Ca^{2+} uptake stimulated by histamine or ionomycin [24]. Putative lower

mitochondrial Ca^{2+} concentration together with decreased expression levels of the pro-fission protein DRP1 resulted in alterations of mitochondrial dynamics, in especially to mitochondrial elongation of hippocampal HT22 cells (Figure 41). These observations are perfectly in line with previous findings emphasizing a role for INF2-induced actin polymerization on DRP1 recruitment and thus representing a critical step for productive mitochondrial fission [90, 119]. If mitochondrial elongation, previously defined as a protective moiety [109], contributes to the distinctive cellular resilience of INF2-knockout HT22 cells in conditions of oxidative stress, remains elusive and needs further conclusive investigation.

5.3 Mitochondrial demise and cell death of primary cortical neurons was averted by genetic cofilin1 deletion

Neurons are excessively prone to mitochondrial impairments, as this cell type inquire substantial energy demand, either for neuronal processes themselves or for proper energy distribution throughout the extensive network of axons or dendrites. Therefore, the present study spotlighted mitochondrial dynamics and function in conditions of cofilin1 deletion in primary neurons either under basal conditions or upon glutamate-induced excitotoxicity.

Major implications obtained in mouse embryonic fibroblasts, demonstrated a role of the actin-regulatory protein cofilin1 for mitochondrial dynamics. To address this phenotype also in neuronal cells, analysis of mitochondrial morphology was conducted upon Cre-transfection of cofilin1$^{flx/flx}$ neurons. Intriguingly, mitochondria of cofilin1-depleted neurons showed an impressively increased circularity index, representing the sphericity of particles and a decreased mitochondrial perimeter. Thus, this phenotype also transmits to primary neurons deficient for cofilin1, representing a conserved mechanism. Accordingly, activation of DRP1 was demonstrated by Western blot analysis of both critical serine residues 616 and 637 and thereby confirming DRP1 activation in cofilin1-deficient neurons, again without deleterious effects on mitochondrial function and cellular survival (Figure 47; Figure 48). Besides the observed similarities between MEF cells and neurons with regard to the role of cofilin1 on mitochondrial morphology, also the evaluated dynamics of mitochondrial Ca^{2+} uptake were comparable. In particular, mitochondria from cofilin1$^{-/-}$ neurons comprised significantly less Ca^{2+} after acute stimulation with KCl than wildtype-neurons (Figure 53), indicative for similar mechanisms as observed and discussed in MEF cells (Chapter 5.1

Cofilin1 knockout in MEF cells led to mitochondrial fragmentation without

deleterious effects on mitochondrial function). To evaluate the long-term effects of cofilin1-knockout on mitochondrial function, mitochondria were isolated from the hippocampus of adult cofilin1$^{flx/flx}$ (WT) and cofilin1$^{flx/flx}$CaMKIIα-Cre (cofilin1$^{-/-}$) mice and evaluated by Seahorse XFe Analyzer (Figure 58). In the hippocampus, cofilin1-downregulation in cofilin1$^{flx/flx}$CaMKIIα-Cre mice starts between postnatal day 1 and 21 and reaches almost entire suppression of protein translation between day 21 and day 50 after birth [145]. Evaluation of the mitochondrial bioenergetic profile revealed overlapping values of WT and cofilin1$^{-/-}$ of four to six-month old mice, suggesting, that even after long-term deletion of cofilin1, mitochondrial function is unaffected.

Although neurodegenerative diseases, such as Alzheimer's, Parkinson's or Huntington's disease, are often predicated to a divers genetic etiology, various studies implicate that they share common pathological pathways, e.g. major hallmarks of excitotoxicity [46]. Hence, the applied model of glutamate-induced excitotoxicity in primary cortical mouse neurons represents a suitable system to study the cellular response under the applied conditions in wildtype neurons and upon genetic deletion of the actin-regulatory protein cofilin1$^{-/-}$. Thus, the recent findings are transmissible for a variety of neurodegenerative disorders. Generally, cofilin1 was found to be highly relevant for cell death signaling in neurons, thus endorsing new insights into the pathophysiological role of cofilin1. In particular, genetic deletion of cofilin1 by CaMKIIα-driven Cre expression, thereby specifically targeted to excitable neurons, was demonstrated to increase cellular resilience in primary neurons in paradigms of glutamate-induced cell death (Figure 48). Additionally, in line with data obtained in hippocampal HT22 cells, mitochondrial respiration was preserved to the same extent as achieved by MK-801-mediated NMDA-receptor inhibition after glutamate exposure (Figure 47). NMDA-receptor activation was demonstrated to result in cofilin1 dephosphorylation, thereby promoting cofilin1 activation achieved by initialization of the phosphatase slingshot [135]. Accordingly, in the present study, inhibition of cofilin1 by facilitating serine 3 phosphorylation via Rho-ROCK-LIMK pathway induced by the Rho-activator CN03 achieved similar results (Figure 65), particularly an increase of neuronal resilience after glutamate exposure (Figure 49). In models of ischemic stroke, administration of the Rho activator CN03 or overexpression of LIMK1 could significantly reduce the percentage of cofilin-actin rods per neuron upon ATP depletion or in vivo after MCAO reperfusion [151] (Shu et al., 2018). Cofilin1 phosphorylation also preserved the number and morphology of synapses, whereas under control conditions synapse density was strongly decreased.

Functional consequences of cofilin1 phosphorylation were assessed by measuring the amplitude and frequency of miniature excitatory postsynaptic currents (mEPSC) in control neurons and in neurons overexpressing LIMK1. Further, LIMK overexpression and associated functional cofilin1 repression was associated with increased synaptic transmission under ATP depleting conditions [151]. The obtained data together with recent publications suggests, that it would be advantageous to consider cofilin1 phosphorylation as putative target for cellular protection in pathologies leading to neuronal disorders.

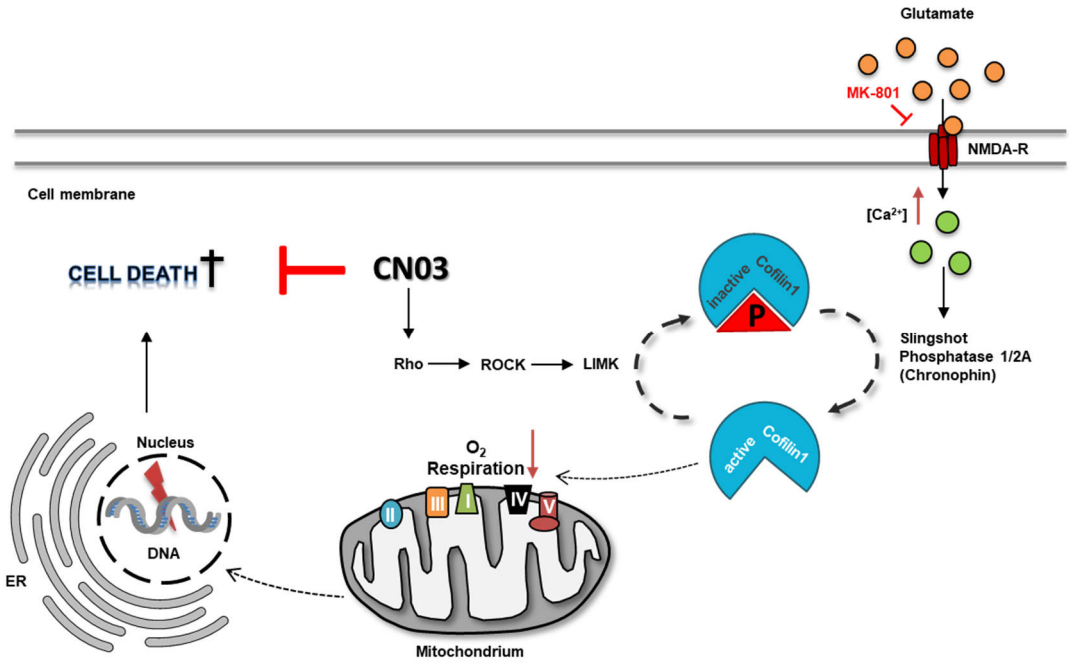

Figure 65. Putative model of glutamate-induced activation of cofilin1 in models of neuronal excitotoxicity.

Micromolar doses of glutamate stimulated excessive Ca^{2+} entry into neurons, a pathologic condition known as excitotoxicity. By application of CN03 protein, a known Rho-activator, cofilin1 is deactivated via ROCK-LIMK pathways thereby promoting neuronal protection by circumventing cofilin1 activation and mitochondrial demise. NMDA-R (N-methyl-D-aspartate receptor); ER (endoplasmic reticulum); [Ca^{2+}] (intracellular calcium concentration); P (Ser 3-phosphorylation); ROCK (Rho-associated serine/threonine kinase); LIMK (LIM kinase); DNA (deoxyribonucleic acid); roman numerals representing complex I-V of the respiratory chain.

In neurons, the function of the actin-regulatory protein cofilin1 is extremely divers. In particular, cofilin1 was demonstrated to link actin dynamics and postsynaptic plasticity, and together with ADF affected actin turnover to such a great extent, that assembly and exocytosis of synaptic vesicles in hippocampal synapses was tremendously impaired if neurons are deficient for both actin-binding proteins [176]. Synaptic transmission is especially crucial for neuronal connectivity and proper signal transduction throughout the whole brain [156]. The impact of cofilin1 on neuronal network formation and activity *in vitro* was determined by Fura-2 AM measurement and subsequent evaluation of the firing

frequency over time. Surprisingly, neurons derived from cofilin1-deficient animals exhibited a significantly more frequent spontaneous firing pattern as wildtype neurons (Figure 50). A rough hint for the interpretation of these results were delivered by Koch and coworkers [89]. They demonstrated that deletion of the Arp2/3-activator syndapin I, critically increased the firing rate of the neuronal network after activation with kainic acid. Considerably, besides the ability of syndapins to promote actin nucleation via Arp2/3-complex activation, this protein family is also known to regulate vesicle trafficking in synapses, thereby probably also impacting neuronal network activity [89]. A similar actin-dependent mechanism might also explain the increased firing frequency upon cofilin1 deletion.

Cofilin-actin rods are pathophysiological cytoplasmic or nuclear protein-aggregations and a major cause of neuronal demise in neurodegenerative diseases [6], such as Alzheimer's disease [5] or Huntington's disease [123], but recently also discovered in ischemic brain injuries [151, 177]. ATP depletion is considered as a major trigger for deleterious cofilin-actin rod formation in the brain. Preliminary confocal microscopy studies were conducted to address the imperative question for the very first time whether the absence of cofilin1 would be a beneficial condition for attenuation of actin rod formation in primary cortical neurons. Intriguingly, cofilin1-deficient neurons were still capable to form rods, but the number of actin rods was significantly reduced compared to neurons from a wildtype animal (Figure 54). On the functional level, the question remains whether deletion of cofilin1 and thereby reduction of cofilin-actin rods would lead to an improved neuronal outcome. To this end, closing remarks on cofilin1 as a potential therapeutic target are still infeasible, although the recent study provides important new insights into the properties of cofilin1 particularly under pathological conditions.

5.4 Impairments in mitochondrial function revealed a direct effect of cofilin1 on mitochondria

In order to distinguish potential indirect actin-based cofilin1 effects from those which are directly mediated by cofilin1, isolated mitochondria were incubated with recombinantly produced cofilin1 protein and afterwards analyzed either by FACS measurement or with the Seahorse XFe Analyzer. First hints of direct cofilin1-mediated impacts on mitochondria were given by Chua and coworkers in 2003 [33]. A few years later, four cysteine (39/80/139/147) and three methionine residues were identified, which are all prone to oxidation, but only the oxidized cysteines were linked to mitochondrial demise [88]. In particular, a detrimental role

for the oxidized form of cofilin1 upstream of mitochondria was unraveled in cell death models induced by the oxidants H_2O_2 or taurine chloramine (TnCl) [88, 168]. Under these circumstances, cofilin1 attains activity to translocate to mitochondria and induces mitochondrial swelling, cytochrome c release and opening of the mitochondrial permeability transition pore (mPTP). The activation of the protein was even observable under basal conditions without any further stimulus, if the cells express the oxidation-mimetic glycine residues at position 39 or 80, respectively [168]. Apparently, cysteines do not only serve as redox sensors, they are also crucial for the correct formation of the protein. Especially Cys39 and Cys80 were described to form intramolecular disulfide bonds and their oxidation eventually lead to protein dephosphorylation (Ser3) after oxidation due to sterical implications [57]. Cys139 and Cys147 are able to form both, intra- and intermolecular disulfide bonds, thus presenting a prerequisite for oligomerization and cofilin-actin rod formation [15]. In the present study, specific mutations of either two (Cys139/147) or all four cysteine residues of the recombinant protein were realized to address the question which specific cysteine residues contribute to the deleterious effects of the protein after oxidation. Specific evaluation of mitochondrial parameters after incubation of the protein and the enriched mitochondrial fraction facilitates insight into the direct mechanism of the protein without any cellular contributors. Intriguingly, the mitochondrial membrane potential, addressed by TMRE staining and following fluorescence-based quantification of the TMRE signal revealed, that the wildtype form of the protein significantly impaired the mitochondrial integrity by decreasing the mitochondrial membrane potential, which was attenuated if cofilin1 residues at position 139 and 147 are mutated to the non-oxidizable amino acid serine (Figure 60). This detrimental impact was completely averted if all four cysteine residues were substituted by serine. These data unravel that oxidation of the wildtype form of cofilin1 lead to a significant impairment of the mitochondrial respiration. Accordingly, mitochondrial ROS accumulation was enhanced by the oxidized form of cofilin1 and, in line with the TMRE measurement, the 2Cys mutant form prevented this incidence, which entirely fit to the finding from Klamt *et. al* who evaluated the Cys139/147 mutant in a cellular environment by transfection of respective cofilin1-mutated plasmids [88] (Figure 61). Evaluation of the mitochondrial respiration revealed, that the wildtype form of cofilin1 impaired the oxygen consumption upon ADP injection, an indicator of complex II, III and V-driven respiration. Although the mutation of Cys139 and 147 still lead to a decrease of mitochondrial respiration, the effect was less pronounced (Figure 62). In conclusion, the

deleterious effect of cofilin1 was attenuated if either all cysteine residues of the protein were substituted be the non-oxidizable serines, or if cysteine residues at position 139 and 147 are mutated to serine residues, indicating that both positions 139 and 147 are crucial in mediating the direct damaging impact on mitochondria.

6 Summary

Neurological diseases, such as stroke, Alzheimer's disease and related dementias are among the most prevalent disorders leading to disability and death worldwide. Many cell death pathways, including apoptosis, necrosis and necroptosis, oxytosis or ferroptosis, relevant for these pathologies, converge at the level of neuronal demise through oxidative stress. In the last decades, many efforts were accomplished to identify underlying pathophysiological mechanisms leading to neuronal demise and subsequent deficits in brain function. However, it still remains obscure which molecular mechanisms contribute to these pathologies and how they are interconnected. The role of mitochondria and respective dynamics dependent on the actin-binding proteins cofilin1 and INF2 contributing to mitochondrial regulation and to neuronal demise are illuminated in the present work. In particular, cofilin1 loss-of-function studies in MEF cells, demonstrated that absence of this actin-binding protein indirectly contributes to mitochondrial fission via DRP1 activation. Mitochondrial dynamics is especially substantial for the generation as well as delivery of ATP to cellular areas with high energy demand; and fission events are frequently associated with impaired mitochondrial function as a prerequisite for cell death. In the case of cofilin1 knockdown, however, mitochondrial fragmentation, was not associated with any mitochondrial impairment, substantiated by an identical bioenergetic profile of cofilin1$^{-/-}$ cells and control cells, unaltered ATP levels and a preserved mitochondrial integrity as assessed by TMRE measurements. Additionally, cofilin1 knockout was linked to increased basal mitochondrial Ca^{2+} level through elevated MCU expression, putatively contributing to mitochondrial fission. The role of cofilin1 in cell death paradigms induced by erastin or glutamate was negligible in MEF cells, and deletion of the protein had no relevant effect on cellular resilience.

In neuronal cells, however, cofilin1 was identified, for the first time, as a redox sensor in oxidative stress-induced cell death pathways, namely oxytosis and ferroptosis, thereby linking detrimental cellular ROS accumulation to mitochondrial demise through this actin-regulating protein. In particular, cofilin1 deletion in neuronal HT22 cells exerted substantial beneficial effects on mitochondrial resilience, assessed by quantification of mitochondrial ROS production, mitochondrial membrane potential or bioluminescent-based measurement of ATP levels. Intriguingly, HT22 cells deficient for cofilin1 exhibited a profound glycolytic shift as a response to erastin or glutamate toxicity to meet their energy demand, whereas

control cells were metabolically inactive. Surprisingly, interfering with another actin-binding protein, namely INF2, exerted similar effects on cellular resistance of neuronal HT22 cells comparable to cofilin1 knockdown. Accordingly, mitochondrial parameters were significantly preserved after oxytosis and ferroptosis induction resulting in enhanced cellular survival. Recent findings from this study and by others, suggesting that actin dynamics is directly linked to the regulation of mitochondrial fusion and fission, guided this project towards uncovering the potential of INF2 to impact mitochondrial morphology. This study unraveled an indirect role for INF2 on the regulation of mitochondrial fission by affecting actin dynamics and DRP1 activity in neuronal cells.

Notably, cofilin1 was confirmed being as a key player under pathophysiological conditions induced by glutamate in primary cortical neurons, as cofilin1 deficient cells were substantially protected against the induced excitotoxicity. Mitochondrial respiration was significantly preserved in cofilin1$^{-/-}$ primary neurons under excitotoxic conditions, thereby maintaining cellular survival. Additionally, decrease of cofilin-actin rod formation in cofilin1$^{-/-}$ deficient neurons might also contribute to the observed protective effects.

The present data on isolated mitochondria treated with the recombinant cofilin1 protein provide a further link to toxicity-related mitochondrial impairment by cofilin1 itself. Direct effects of cofilin1 were demonstrated by assessing the mitochondrial membrane potential, mitochondrial ROS accumulation and mitochondrial respiration. Interestingly, the detrimental impact of cofilin1 on mitochondria is dependent on oxidation of crucial cysteine residues at position 139 and 147, as mutations of these cysteine residues to serine abolished the noxious character of cofilin1.

Overall, the present findings reveal, for the first time, that the actin-binding proteins cofilin1 and INF2 play a crucial role in paradigms of oxidative stress and that inhibition of these proteins results in protective effects in neuronal cells that were particularly attributed to the preserved mitochondrial integrity and function. Thus, interfering with the pathological activation of actin-binding proteins, such as cofilin1 or INF2 may offer an effective therapeutic strategy in neurodegenerative diseases.

7 Zusammenfassung

Neurologische Erkrankungen, wie Schlaganfall oder Morbus Alzheimer, gehören weltweit zu den häufigsten Ursachen für Invalidität und Tod. Viele für diese Erkrankungen relevante Zelltodmechanismen, einschließlich der Apoptose, Nekrose und Nekroptose, Oxytose oder Ferroptose, führen über vermehrten oxidativen Stress zum neuronalen Zelluntergang. Zahlreiche Untersuchungen der letzten Jahre haben bereits wichtige Erkenntnisse über die zugrunde liegenden pathophysiologischen Mechanismen gebracht, die zum neuronalen Untergang und entsprechenden Einschränkungen der Gehirnfunktion führen. Es ist jedoch immer noch unklar, welche weiteren Faktoren und molekularen Mechanismen zu diesen Erkrankungen beitragen und wie diese miteinander verbunden sind. Die Rolle der Mitochondrien und ihrer dynamischen Regulierung, sowie die Charakterisierung der Aktin-bindenden Proteine Cofilin1 und INF2 im Kontext der mitochondrialen Dynamik und neuronalen Zelltodmechanismen, ist Gegenstand der vorliegenden Arbeit. Die Ergebnisse aus den Untersuchungen in MEF-Zellen zeigen, dass eine Deletion der Cofilin1-kodierenden Genregion indirekt zur mitochondrialen Fragmentierung durch DRP1-Aktivierung beiträgt. Die mitochondriale Dynamik ist besonders wichtig für die Bereitstellung von Energie in zellulären Bereichen mit hohem ATP-Bedarf. Die beobachtete mitochondriale Fragmentierung in Cofilin1$^{-/-}$ Zellen hat in den vorliegenden Untersuchungen nicht zu einer Beeinträchtigung der mitochondrialen Funktion geführt, was durch ein unverändertes bioenergetisches Profil, konstante ATP-Level und eine erhaltene mitochondriale Integrität belegt werden konnte. Die Deletion von Cofilin1 war außerdem mit erhöhten basalen mitochondrialen Ca^{2+}-Spiegeln, sowie mit einer erhöhten Proteinexpression des mitochondrialen Ca^{2+} Transporters (MCU) verbunden, was vermutlich zur mitochondrialen Fragmentierung beiträgt. Die Rolle von Cofilin1 nach Erastin- oder Glutamat-induziertem Zelltod in MEF-Zellen ist jedoch vernachlässigbar, da die Deletion des Proteins keinen relevanten Einfluss auf die zelluläre Widerstandsfähigkeit hatte.

Im Gegensatz zu den Fibroblasten wurde in der vorliegenden Arbeit in neuronalen HT22 Zellen Cofilin1 als Redox-Sensor identifiziert. In den Modellsystemen der Glutamat-induzierten Oxytose und der Erastin-induzierten Ferroptose in den hippocampalen HT22 Zellen wurden hier erstmals die kritische zelluläre ROS-Akkumulation über die Aktivierung von Cofilin1 mit der mitochondrialen Schädigung in Verbindung gebracht. Insbesondere die Cofilin1-Deletion in neuronalen HT22 Zellen zeigte erhebliche positive Auswirkungen auf

die mitochondriale Resilienz, die durch Quantifizierung der mitochondrialen ROS-Produktion, des mitochondrialen Membranpotenzials oder der Biolumineszenz-basierten Messung der zellulären ATP-Spiegel nachgewiesen wurde. Zellen mit Cofilin1-Depletion zeigen eine deutliche metabolische Verschiebung hin zur Glykolyse, um ihren Energiebedarf nach Erastin- oder Glutamatbehandlung zu decken, während Kontrollzellen unter diesen Behandlungsbedingungen deutlich geschädigt wurden und somit metabolisch inaktiv blieben. Überraschenderweise übte die Depletion eines anderen Aktin-bindenden Proteins, nämlich INF2, ähnliche Effekte auf die zelluläre Resistenz neuronaler HT22 Zellen aus. Dementsprechend waren die mitochondrialen Parameter nach Oxytose und Ferroptoseinduktion geschützt, was zu einem verbesserten Zellüberleben führte. Weitere Ergebnisse der Studie zeigen eindeutig, dass INF2 indirekt an der Regulierung der mitochondrialen Fragmentierung durch Beeinflussung der Aktindynamik und der DRP1-Aktivität beteiligt ist.

Cofilin1 konnte unter pathophysiologischen Bedingungen in primären kortikalen Neuronen nach Glutamatbehandlung als Schlüsselfaktor identifiziert werden, da Cofilin1-defiziente Zellen geschützt waren. Die mitochondriale Atmung war in primären Cofilin1$^{-/-}$ Neuronen unter der Glutamatbehandlung erhalten, was letztendlich zu einem verbesserten Gesamtüberleben der Neurone führte. Zusätzlich könnte die Tatsache, dass Cofilin1$^{-/-}$ Neurone weniger Cofilin-Aktin-Polymer-Ablagerungen pro Neuron nach ATP-Depletion entwickelten, auch zum protektiven Effekt in Cofilin1-defizienten Neuronen beitragen. Ein wichtiger Nachweis für die positiven Auswirkungen der Deletion von Cofilin1 ist die Tatsache, dass Cofilin1 direkte schädliche Effekte auf das Membranpotenzial, die mitochondrialen ROS-Akkumulation und die mitochondriale Atmung ausübte. Diese Eigenschaft ist von der Oxidation spezifischer Cysteine an den Positionen 139 und 147 abhängig; entsprechende Mutationen zu Serin verminderten die schädigende Funktion von Cofilin1.

Insgesamt zeigen die vorliegenden Ergebnisse, dass die Aktin-regulierenden Proteine Cofilin1 und INF2 eine entscheidende Rolle bei den intrazellulären Zelltodmechanismen spielen, die an der Pathophysiologie neurodegenerativer Erkrankungen beteiligt sind.

8 Abbreviations

A

ADF	Actin-depolymerizing factor
ADP	Adenosine diphosphate
AICAR	5-Aminoimidazole-4-carboxamide ribonucleotide
AIF	Apoptosis inducing factor
AM	Acetoxymethyl
AMPA	α-Amino-3-hydroxy-5-methyl-4-isoxazolepropionate
ANOVA	Analysis of variance
Arp2/3	Actin related protein 2/actin related protein 3
ATP	Adenosine triphosphate

B

BAX	Bcl-2-associated X protein
BCA	Bicinchoninic acid
BID	BH3-interacting domain death agonist
Bp	Base pair
BSA	Bovine serum albumin

C

Ca^{2+}	Calcium
CaMKII	Calcium/calmodulin-dependent protein kinase II
CCCP	Carbonyl cyanide 3-chlorophenylhydrazone
CTX	Cortex
CytC	Cytochrome C
Cys	Cysteine

D

$\Delta\Psi m$	Mitochondrial membrane potential
2-DG	2-Deoxy-D-glucose
DIV	Days in vitro
DMEM	Dulbecco's modified Eagle's medium
DMSO	Dimethyl sulfoxide
DNA	Deoxyribonucleic acid
DNase	Deoxyribonuclease
DRP1	Dynamin-related protein1
DTT	Dithiothreitol

E

E18	Embryonic day 18
EBSS	Earle's balanced salt solution
ECAR	Extracellular acidification rate
EM	Electron microscopy
ER	Endoplasmic reticulum
ETC	Electron transport chain

F

FACS	Fluorescence-activated cell sorting

FBS	Fetal bovine serum
FCCP	Carbonyl cyanide-4-(trifluoromethoxy)phenylhydrazone
G	
GFAP	Glial fibrillary acidic protein
GFP	Green fluorescent protein
flx	floxed
GPX4	Glutathione peroxidase 4
GSH	Glutathione
H	
HBSS	Hank's balanced salt solution
HC	Hippocampus
Hif1α	Hypoxia-inducible factor 1α
I	
IMM	Inner mitochondrial membrane
INF2	Inverted-formin 2
K	
KCl	Potassium chloride
L	
LC3B	Light chain 3 isoform B
LOX	Lipoxygenase
M	
MAP	Microtubule-associated protein
MCAO	Middle Cerebral Artery Occlusion
MCM	MerCreMer
mEPSC	Miniature excitatory postsynaptic currents
MCU	Mitochondrial calcium uniporter
MEF	Mouse embryonic fibroblasts
Mfn	Mitofusin
Mito-LAR GECO	mitochondrial-targeted Low Affinity Red Genetically Encoded Calcium indicators for Optical imaging
mPTP	Mitochondrial permeability transition pore
mtDNA	Mitochondrial DNA
MTT	3-(4,5-Dimethyl-2-thiazolyl)-2,5-diphenyl-2H-tetrazolium bromide
N	
NA	Numerische Apertur
NMDA	N-methyl-D-aspartate
NO	Nitric oxide
NOS	Nitric oxide synthase
Nrf-1	Nuclear respiratory factor 1
Nrf-2	Nuclear factor erythroid 2–related factor 2
O	
OCR	Oxygen consumption rate

OMM	Outer mitochondrial membrane
OPA1	Optic atrophy 1
OXPHOS	Oxidative phosphorylation

P

PBS	Phosphate buffered saline
PCR	Polymerase chain reaction
PDK1	Pyruvate dehydrogenase kinase 1
PFA	Paraformaldehyde
PGC1α	Peroxisome proliferator-activated receptor gamma coactivator 1α
PI	Propidium iodide
PLL	Poly-L-lysine
PVDF	Polyvinylidene difluoride

R

ROCK	Rho-associated serine/threonine kinase
ROI	Region of interest
ROS	Reactive oxygen species
RTCA	Real-time cell analysis

S

SD	Standard deviation
SDS-PAGE	Sodium dodecyl sulfate polyacrylamide gel electrophoresis
Ser	Serine
siRNA	Small interfering RNA

T

TamOH	4-hydroxytamoxifen
TCA	Tricarboxylic acid cycle
TMRE	Tetramethylrhodamine ethyl ester
TnCl	Taurine chloramine

W

WT	Wildtype

9 References

[1] Aguilera, M. O., Berón, W., and Colombo, M. I. 2012. The actin cytoskeleton participates in the early events of autophagosome formation upon starvation induced autophagy. *Autophagy* 8, 11, 1590–1603.

[2] Andrianantoandro, E. and Pollard, T. D. 2006. Mechanism of actin filament turnover by severing and nucleation at different concentrations of ADF/cofilin. *Molecular cell* 24, 1, 13–23.

[3] Antonny, B., Burd, C., Camilli, P. de, Chen, E., Daumke, O., Faelber, K., Ford, M., Frolov, V. A., Frost, A., Hinshaw, J. E., Kirchhausen, T., Kozlov, M. M., Lenz, M., Low, H. H., McMahon, H., Merrifield, C., Pollard, T. D., Robinson, P. J., Roux, A., and Schmid, S. 2016. Membrane fission by dynamin: what we know and what we need to know. *The EMBO journal* 35, 21, 2270–2284.

[4] Arber, S., Barbayannis, F. A., Hanser, H., Schneider, C., Stanyon, C. A., Bernard, O., and Caroni, P. 1998. Regulation of actin dynamics through phosphorylation of cofilin by LIM-kinase. *Nature* 393, 6687, 805–809.

[5] Bamburg, J. R. and Bernstein, B. W. 2016. Actin dynamics and cofilin-actin rods in Alzheimer disease. *Cytoskeleton (Hoboken, N.J.)* 73, 9, 477–497.

[6] Bamburg, J. R., Bernstein, B. W., Davis, R. C., Flynn, K. C., Goldsbury, C., Jensen, J. R., Maloney, M. T., Marsden, I. T., Minamide, L. S., Pak, C. W., Shaw, A. E., Whiteman, I., and Wiggan, O. 2010. ADF/cofilin-actin rods in neurodegenerative diseases. *Current Alzheimer research* 7, 3, 241–250.

[7] Bamburg, J. R., Bernstein, B. W., Davis, R.C., Flynn, K. C., Goldsbury, C., Jensen, J. R., Maloney, M. T., Marsden, I. T., Minamide, L. S., Pak, C. W., Shaw, A. E., Whiteman, I., and Wiggan, O. 2010. ADF/Cofilin-Actin Rods in Neurodegenerative Diseases. *CAR* 7, 3, 241–250.

[8] Bano, D., Young, K. W., Guerin, C. J., Lefeuvre, R., Rothwell, N. J., Naldini, L., Rizzuto, R., Carafoli, E., and Nicotera, P. 2005. Cleavage of the plasma membrane Na+/Ca2+ exchanger in excitotoxicity. *Cell* 120, 2, 275–285.

[9] Barnham, K. J., Masters, C. L., and Bush, A. I. 2004. Neurodegenerative diseases and oxidative stress. *Nature reviews. Drug discovery* 3, 3, 205–214.

[10] Baughman, J. M., Perocchi, F., Girgis, H. S., Plovanich, M., Belcher-Timme, C. A., Sancak, Y., Bao, X. R., Strittmatter, L., Goldberger, O., Bogorad, R. L., Koteliansky, V., and Mootha, V. K. 2011. Integrative genomics identifies MCU as an essential component of the mitochondrial calcium uniporter. *Nature* 476, 7360, 341–345.

[11] Beal, M. F. 1998. Excitotoxicity and nitric oxide in Parkinson's disease pathogenesis. *Annals of neurology* 44, 3 Suppl 1, S110-4.

[12] Bellenchi, G. C., Gurniak, C. B., Perlas, E., Middei, S., Ammassari-Teule, M., and Witke, W. 2007. N-cofilin is associated with neuronal migration disorders and cell cycle control in the cerebral cortex. *Genes & development* 21, 18, 2347–2357.

[13] Bernstein, B. W. and Bamburg, J. R. 2010. ADF/cofilin: a functional node in cell biology. *Trends in cell biology* 20, 4, 187–195.

[14] Bernstein, B. W., Chen, H., Boyle, J. A., and Bamburg, J. R. 2006. Formation of actin-ADF/cofilin rods transiently retards decline of mitochondrial potential and ATP in stressed neurons. *American journal of physiology. Cell physiology* 291, 5, C828-39.

[15] Bernstein, B. W., Shaw, A. E., Minamide, L. S., Pak, C. W., and Bamburg, J. R. 2012. Incorporation of Cofilin into Rods Depends on Disulfide Intermolecular Bonds: Implications for Actin Regulation and Neurodegenerative Disease. *Journal of Neuroscience* 32, 19, 6670–6681.

[16] Boldogh, I. R., Nowakowski, D. W., Yang, H.-C., Chung, H., Karmon, S., Royes, P., and Pon, L. A. 2003. A protein complex containing Mdm10p, Mdm12p, and Mmm1p links mitochondrial membranes and DNA to the cytoskeleton-based segregation machinery. *Molecular biology of the cell* 14, 11, 4618–4627.

[17] Boldogh, I. R. and Pon, L. A. 2006. Interactions of mitochondria with the actin cytoskeleton. *Biochimica et biophysica acta* 1763, 5-6, 450–462.

[18] Boldogh, I. R. and Pon, L. A. 2007. Mitochondria on the move. *Trends in cell biology* 17, 10, 502–510.

[19] Bowes, T. and Gupta, R. S. 2008. Novel mitochondrial extensions provide evidence for a link between microtubule-directed movement and mitochondrial fission. *Biochemical and biophysical research communications* 376, 1, 40–45.

[20] Boyer, O., Nevo, F., Plaisier, E., Funalot, B., Gribouval, O., Benoit, G., Huynh Cong, E., Arrondel, C., Tête, M.-J., Montjean, R., Richard, L., Karras, A., Pouteil-Noble, C., Balafrej, L., Bonnardeaux, A., Canaud, G., Charasse, C., Dantal, J., Deschenes, G., Deteix, P., Dubourg, O., Petiot, P., Pouthier, D., Leguern, E., Guiochon-Mantel, A., Broutin, I., Gubler, M.-C., Saunier, S., Ronco, P., Vallat, J.-M., Alonso, M. A., Antignac, C., and Mollet, G. 2011. INF2 mutations in Charcot-Marie-Tooth disease with glomerulopathy. *The New England journal of medicine* 365, 25, 2377–2388.

[21] Brown, E. J., Schlöndorff, J. S., Becker, D. J., Tsukaguchi, H., Tonna, S. J., Uscinski, A. L., Higgs, H. N., Henderson, J. M., and Pollak, M. R. 2010. Mutations in the formin gene INF2 cause focal segmental glomerulosclerosis. *Nature genetics* 42, 1, 72–76.

[22] Carlier, M.-F., Laurent, V., Santolini, J., Melki, R., Didry, D., Xia, G.-X., Hong, Y., Chua, N.-H., and Pantaloni, D. 1997. Actin Depolymerizing Factor (ADF/Cofilin) Enhances the Rate of Filament Turnover: Implication in Actin-based Motility. *J Cell Biol* 136, 6, 1307–1322.

[23] Cerveny, K. L., McCaffery, J. M., and Jensen, R. E. 2001. Division of mitochondria requires a novel DNM1-interacting protein, Net2p. *Molecular biology of the cell* 12, 2, 309–321.

[24] Chakrabarti, R., Ji, W.-K., Stan, R. V., Juan Sanz, J. de, Ryan, T. A., and Higgs, H. N. 2018. INF2-mediated actin polymerization at the ER stimulates mitochondrial calcium uptake, inner membrane constriction, and division. *The Journal of cell biology* 217, 1, 251–268.

[25] Chen, H. and Chan, D. C. 2009. Mitochondrial dynamics--fusion, fission, movement, and mitophagy--in neurodegenerative diseases. *Human molecular genetics* 18, R2, R169-76.

[26] Chen, H., Chomyn, A., and Chan, D. C. 2005. Disruption of fusion results in mitochondrial heterogeneity and dysfunction. *The Journal of biological chemistry* 280, 28, 26185–26192.

[27] Chen, T.-J., Gehler, S., Shaw, A. E., Bamburg, J. R., and Letourneau, P. C. 2006. Cdc42 participates in the regulation of ADF/cofilin and retinal growth cone filopodia by brain derived neurotrophic factor. *Journal of neurobiology* 66, 2, 103–114.

[28] Chen, Z., Wang, C., Yu, N., Si, L., Zhu, L., Zeng, A., Liu, Z., and Wang, X. 2019. INF2 regulates oxidative stress-induced apoptosis in epidermal HaCaT cells by modulating the HIF1 signaling pathway. *Biomedicine & pharmacotherapy = Biomedecine & pharmacotherapie* 111, 151–161.

[29] Chhabra, E. S. and Higgs, H. N. 2006. INF2 Is a WASP homology 2 motif-containing formin that severs actin filaments and accelerates both polymerization and depolymerization. *The Journal of biological chemistry* 281, 36, 26754–26767.

[30] Chhabra, E. S., Ramabhadran, V., Gerber, S. A., and Higgs, H. N. 2009. INF2 is an endoplasmic reticulum-associated formin protein. *Journal of cell science* 122, Pt 9, 1430–1440.

[31] Cho, B., Cho, H. M., Jo, Y., Kim, H. D., Song, M., Moon, C., Kim, H., Kim, K., Sesaki, H., Im Rhyu, J., Kim, H., and Sun, W. 2017. Constriction of the mitochondrial inner compartment is a priming event for mitochondrial division. *Nature communications* 8, 15754.

[32] CHOI, D. 1988. Glutamate neurotoxicity and diseases of the nervous system. *Neuron* 1, 8, 623–634.

[33] Chua, B. T., Volbracht, C., Tan, K. O., Li, R., Yu, V. C., and Li, P. 2003. Mitochondrial translocation of cofilin is an early step in apoptosis induction. *Nature cell biology* 5, 12, 1083–1089.

[34] Cichon, J., Sun, C., Chen, B., Jiang, M., Chen, X. A., Sun, Y., Wang, Y., and Chen, G. 2012. Cofilin aggregation blocks intracellular trafficking and induces synaptic loss in hippocampal neurons. *The Journal of biological chemistry* 287, 6, 3919–3929.

[35] Coles, C. H. and Bradke, F. 2015. Coordinating neuronal actin-microtubule dynamics. *Current biology : CB* 25, 15, R677-91.

[36] Culmsee, C. and Landshamer, S. 2006. Molecular insights into mechanisms of the cell death program: role in the progression of neurodegenerative disorders. *Current Alzheimer research* 3, 4, 269–283.

[37] Culmsee, C., Zhu, C., Landshamer, S., Becattini, B., Wagner, E., Pellecchia, M., Pellechia, M., Blomgren, K., and Plesnila, N. 2005. Apoptosis-inducing factor triggered by poly(ADP-ribose) polymerase and Bid mediates neuronal cell death after oxygen-glucose deprivation and focal cerebral ischemia. *The Journal of neuroscience : the official journal of the Society for Neuroscience* 25, 44, 10262–10272.

[38] da Silva, J. S. and Dotti, C. G. 2002. Breaking the neuronal sphere: regulation of the actin cytoskeleton in neuritogenesis. *Nature reviews. Neuroscience* 3, 9, 694–704.

[39] Dagda, R. K., Cherra, S. J., Kulich, S. M., Tandon, A., Park, D., and Chu, C. T. 2009. Loss of PINK1 function promotes mitophagy through effects on oxidative stress and mitochondrial fission. *The Journal of biological chemistry* 284, 20, 13843–13855.

[40] Dang, C. V., O'Donnell, K. A., Zeller, K. I., Nguyen, T., Osthus, R. C., and Li, F. 2006. The c-Myc target gene network. *Seminars in cancer biology* 16, 4, 253–264.

[41] Davis, J. B. and Maher, P. 1994. Protein kinase C activation inhibits glutamate-induced cytotoxicity in a neuronal cell line. *Brain Research* 652, 1, 169–173.

[42] Dawitz, J., Kroon, T., Hjorth, J. J. J., and Meredith, R. M. 2011. Functional calcium imaging in developing cortical networks. *Journal of visualized experiments : JoVE*, 56.

[43] Deng, Y., Wei, J., Cheng, J., Zhong, P., Xiong, Z., Liu, A., Lin, L., Chen, S., and Yan, Z. 2016. Partial Amelioration of Synaptic and Cognitive Deficits by Inhibiting Cofilin Dephosphorylation in an Animal Model of Alzheimer's Disease. *Journal of Alzheimer's disease : JAD* 53, 4, 1419–1432.

[44] Diemert, S., Dolga, A. M., Tobaben, S., Grohm, J., Pfeifer, S., Oexler, E., and Culmsee, C. 2012. Impedance measurement for real time detection of neuronal cell death. *Journal of neuroscience methods* 203, 1, 69–77.

[45] Dixon, S. J., Lemberg, K. M., Lamprecht, M. R., Skouta, R., Zaitsev, E. M., Gleason, C. E., Patel, D. N., Bauer, A. J., Cantley, A. M., Yang, W. S., Morrison, B., and Stockwell, B. R. 2012. Ferroptosis: an iron-dependent form of nonapoptotic cell death. *Cell* 149, 5, 1060–1072.

[46] Dong, X.-x., Wang, Y., and Qin, Z.-h. 2009. Molecular mechanisms of excitotoxicity and their relevance to pathogenesis of neurodegenerative diseases. *Acta pharmacologica Sinica* 30, 4, 379–387.

[47] Duffney, L. J., Zhong, P., Wei, J., Matas, E., Cheng, J., Qin, L., Ma, K., Dietz, D. M., Kajiwara, Y., Buxbaum, J. D., and Yan, Z. 2015. Autism-like Deficits in Shank3-Deficient Mice Are Rescued by Targeting Actin Regulators. *Cell reports* 11, 9, 1400–1413.

[48] Elgass, K., Pakay, J., Ryan, M. T., and Palmer, C. S. 2013. Recent advances into the understanding of mitochondrial fission. *Biochimica et biophysica acta* 1833, 1, 150–161.

[49] Filadi, R., Greotti, E., Turacchio, G., Luini, A., Pozzan, T., and Pizzo, P. 2015. Mitofusin 2 ablation increases endoplasmic reticulum-mitochondria coupling. *Proceedings of the National Academy of Sciences of the United States of America* 112, 17, E2174-81.

[50] Filichia, E., Hoffer, B., Qi, X., and Luo, Y. 2016. Inhibition of Drp1 mitochondrial translocation provides neural protection in dopaminergic system in a Parkinson's disease model induced by MPTP. *Scientific reports* 6, 32656.

[51] Flynn, K. C., Hellal, F., Neukirchen, D., Jacob, S., Tahirovic, S., Dupraz, S., Stern, S., Garvalov, B. K., Gurniak, C., Shaw, A. E., Meyn, L., Wedlich-Söldner, R., Bamburg, J. R., Small, J. V., Witke, W., and Bradke, F. 2012. ADF/cofilin-mediated actin retrograde flow directs neurite formation in the developing brain. *Neuron* 76, 6, 1091–1107.

[52] Frank, S., Gaume, B., Bergmann-Leitner, E. S., Leitner, W. W., Robert, E. G., Catez, F., Smith, C. L., and Youle, R. J. 2001. The Role of Dynamin-Related Protein 1, a Mediator of Mitochondrial Fission, in Apoptosis. *Developmental cell* 1, 4, 515–525.

[53] Frederick, R. L. and Shaw, J. M. 2007. Moving mitochondria: establishing distribution of an essential organelle. *Traffic (Copenhagen, Denmark)* 8, 12, 1668–1675.

[54] Friedman, J. R. and Nunnari, J. 2014. Mitochondrial form and function. *Nature* 505, 7483, 335–343.

[55] Fu, W., Liu, Y., and Yin, H. 2019. Mitochondrial Dynamics: Biogenesis, Fission, Fusion, and Mitophagy in the Regulation of Stem Cell Behaviors. *Stem cells international* 2019, 9757201.

[56] Gawlowski, T., Suarez, J., Scott, B., Torres-Gonzalez, M., Wang, H., Schwappacher, R., Han, X., Yates, J. R., Hoshijima, M., and Dillmann, W. 2012. Modulation of dynamin-related protein 1 (DRP1) function by increased O-linked-β-N-acetylglucosamine modification (O-GlcNAc) in cardiac myocytes. *The Journal of biological chemistry* 287, 35, 30024–30034.

[57] Gellert, M., Hanschmann, E.-M., Lepka, K., Berndt, C., and Lillig, C. H. 2015. Redox regulation of cytoskeletal dynamics during differentiation and de-differentiation. *Biochimica et biophysica acta* 1850, 8, 1575–1587.

[58] Glancy, B., Willis, W. T., Chess, D. J., and Balaban, R. S. 2013. Effect of calcium on the oxidative phosphorylation cascade in skeletal muscle mitochondria. *Biochemistry* 52, 16, 2793–2809.

[59] Goetzman, E. S. and Prochownik, E. V. 2018. The Role for Myc in Coordinating Glycolysis, Oxidative Phosphorylation, Glutaminolysis, and Fatty Acid Metabolism in Normal and Neoplastic Tissues. *Frontiers in endocrinology* 9, 129.

[60] Gohla, A., Birkenfeld, J., and Bokoch, G. M. 2005. Chronophin, a novel HAD-type serine protein phosphatase, regulates cofilin-dependent actin dynamics. *Nature cell biology* 7, 1, 21–29.

[61] Good, P. F. 1998. Mitochondria & Free Radicals in Neurodegenerative Diseases. *Neurology* 50, 5, 1523.

[62] Goodson, M., Rust, M. B., Witke, W., Bannerman, D., Mott, R., Ponting, C. P., and Flint, J. 2012. Cofilin-1: a modulator of anxiety in mice. *PLoS genetics* 8, 10, e1002970.

[63] Grienberger, C. and Konnerth, A. 2012. Imaging calcium in neurons. *Neuron* 73, 5, 862–885.

[64] Grohm, J., Kim, S.-W., Mamrak, U., Tobaben, S., Cassidy-Stone, A., Nunnari, J., Plesnila, N., and Culmsee, C. 2012. Inhibition of Drp1 provides neuroprotection in vitro and in vivo. *Cell death and differentiation* 19, 9, 1446–1458.

[65] Grohm, J., Plesnila, N., and Culmsee, C. 2010. Bid mediates fission, membrane permeabilization and peri-nuclear accumulation of mitochondria as a prerequisite for oxidative neuronal cell death. *Brain, behavior, and immunity* 24, 5, 831–838.

[66] Gu, J., Lee, C. W., Fan, Y., Komlos, D., Tang, X., Sun, C., Yu, K., Hartzell, H. C., Chen, G., Bamburg, J. R., and Zheng, J. Q. 2010. ADF/cofilin-mediated actin dynamics regulate AMPA receptor trafficking during synaptic plasticity. *Nature neuroscience* 13, 10, 1208–1215.

[67] Gurniak, C. B., Chevessier, F., Jokwitz, M., Jönsson, F., Perlas, E., Richter, H., Matern, G., Boyl, P. P., Chaponnier, C., Fürst, D., Schröder, R., and Witke, W. 2014. Severe protein aggregate myopathy in a knockout mouse model points to an essential role of cofilin2 in sarcomeric actin exchange and muscle maintenance. *European journal of cell biology* 93, 5-6, 252–266.

[68] Gurniak, C. B., Perlas, E., and Witke, W. 2005. The actin depolymerizing factor n-cofilin is essential for neural tube morphogenesis and neural crest cell migration. *Developmental biology* 278, 1, 231–241.

[69] Halliwell, B. 1992. Reactive oxygen species and the central nervous system. *Journal of neurochemistry* 59, 5, 1609–1623.

[70] Hanschmann, E.-M., Lönn, M. E., Schütte, L. D., Funke, M., Godoy, J. R., Eitner, S., Hudemann, C., and Lillig, C. H. 2010. Both thioredoxin 2 and glutaredoxin 2 contribute to the reduction of the mitochondrial 2-Cys peroxiredoxin Prx3. *The Journal of biological chemistry* 285, 52, 40699–40705.

[71] Hatch, A. L., Gurel, P. S., and Higgs, H. N. 2014. Novel roles for actin in mitochondrial fission. *Journal of cell science* 127, Pt 21, 4549–4560.

[72] Hatch, A. L., Ji, W.-K., Merrill, R. A., Strack, S., and Higgs, H. N. 2016. Actin filaments as dynamic reservoirs for Drp1 recruitment. *Molecular biology of the cell* 27, 20, 3109–3121.

[73] Higgs, H. N. 2005. Formin proteins: a domain-based approach. *Trends in biochemical sciences* 30, 6, 342–353.

[74] Hild, G., Kalmár, L., Kardos, R., Nyitrai, M., and Bugyi, B. 2014. The other side of the coin: functional and structural versatility of ADF/cofilins. *European journal of cell biology* 93, 5-6, 238–251.

[75] Hodneland Nilsson, L. I., Nitschke Pettersen, I. K., Nikolaisen, J., Micklem, D., Avsnes Dale, H., Vatne Røsland, G., Lorens, J., and Tronstad, K. J. 2015. A new live-cell reporter strategy to simultaneously monitor mitochondrial biogenesis and morphology. *Scientific reports* 5, 17217.

[76] Hoffmann, L., Rust, M. B., and Culmsee, C. 2019. Actin(g) on mitochondria - a role for cofilin1 in neuronal cell death pathways. *Biological chemistry* 400, 9, 1089–1097.

[77] Hotulainen, P. and Hoogenraad, C. C. 2010. Actin in dendritic spines: connecting dynamics to function. *J Cell Biol* 189, 4, 619–629.

[78] Hotulainen, P., Llano, O., Smirnov, S., Tanhuanpää, K., Faix, J., Rivera, C., and Lappalainen, P. 2009. Defining mechanisms of actin polymerization and depolymerization during dendritic spine morphogenesis. *The Journal of cell biology* 185, 2, 323–339.

[79] Huang, T. Y., Minamide, L. S., Bamburg, J. R., and Bokoch, G. M. 2008. Chronophin mediates an ATP-sensing mechanism for cofilin dephosphorylation and neuronal cofilin-actin rod formation. *Developmental cell* 15, 5, 691–703.

[80] Huang, X., Sun, L., Ji, S., Zhao, T., Zhang, W., Xu, J., Zhang, J., Wang, Y., Wang, X., Franzini-Armstrong, C., Zheng, M., and Cheng, H. 2013. Kissing and nanotunneling mediate intermitochondrial communication in the heart. *Proceedings of the National Academy of Sciences of the United States of America* 110, 8, 2846–2851.

[81] Hynd, M. R., Scott, H. L., and Dodd, P. R. 2004. Glutamate-mediated excitotoxicity and neurodegeneration in Alzheimer's disease. *Neurochemistry international* 45, 5, 583–595.

[82] Ježek, J., Cooper, K. F., and Strich, R. 2018. Reactive Oxygen Species and Mitochondrial Dynamics: The Yin and Yang of Mitochondrial Dysfunction and Cancer Progression. *Antioxidants (Basel, Switzerland)* 7, 1.

[83] Ji, W.-K., Hatch, A. L., Merrill, R. A., Strack, S., and Higgs, H. N. 2015. Actin filaments target the oligomeric maturation of the dynamin GTPase Drp1 to mitochondrial fission sites. *eLife* 4, e11553.

[84] Karbowski, M., Lee, Y.-J., Gaume, B., Jeong, S.-Y., Frank, S., Nechushtan, A., Santel, A., Fuller, M., Smith, C. L., and Youle, R. J. 2002. Spatial and temporal association of Bax with mitochondrial fission sites, Drp1, and Mfn2 during apoptosis. *J Cell Biol* 159, 6, 931–938.

[85] Kim, G. H., Kim, J. E., Rhie, S. J., and Yoon, S. 2015. The Role of Oxidative Stress in Neurodegenerative Diseases. *Experimental Neurobiology* 24, 4, 325–340.

[86] Kim, J.-S., Huang, T. Y., and Bokoch, G. M. 2009. Reactive oxygen species regulate a slingshot-cofilin activation pathway. *Molecular biology of the cell* 20, 11, 2650–2660.

[87] Kim, J.-w., Tchernyshyov, I., Semenza, G. L., and Dang, C. V. 2006. HIF-1-mediated expression of pyruvate dehydrogenase kinase: a metabolic switch required for cellular adaptation to hypoxia. *Cell metabolism* 3, 3, 177–185.

[88] Klamt, F., Zdanov, S., Levine, R. L., Pariser, A., Zhang, Y., Zhang, B., Yu, L.-R., Veenstra, T. D., and Shacter, E. 2009. Oxidant-induced apoptosis is mediated by oxidation of the actin-regulatory protein cofilin. *Nature cell biology* 11, 10, 1241–1246.

[89] Koch, D., Spiwoks-Becker, I., Sabanov, V., Sinning, A., Dugladze, T., Stellmacher, A., Ahuja, R., Grimm, J., Schüler, S., Müller, A., Angenstein, F., Ahmed, T., Diesler, A., Moser, M., Tom Dieck, S., Spessert, R., Boeckers, T. M., Fässler, R., Hübner, C. A., Balschun, D., Gloveli, T., Kessels, M. M., and Qualmann, B. 2011. Proper synaptic vesicle formation and neuronal network activity critically rely on syndapin I. *The EMBO journal* 30, 24, 4955–4969.

[90] Korobova, F., Ramabhadran, V., and Higgs, H. N. 2013. An actin-dependent step in mitochondrial fission mediated by the ER-associated formin INF2. *Science (New York, N.Y.)* 339, 6118, 464–467.

[91] Kotiadis, V. N., Leadsham, J. E., Bastow, E. L., Gheeraert, A., Whybrew, J. M., Bard, M., Lappalainen, P., and Gourlay, C. W. 2012. Identification of new surfaces of cofilin that link mitochondrial function to the control of multi-drug resistance. *Journal of cell science* 125, 9, 2288–2299.

[92] Koutsilieri, E. and Riederer, P. 2007. Excitotoxicity and new antiglutamatergic strategies in Parkinson's disease and Alzheimer's disease. *Parkinsonism & Related Disorders* 13, S329-S331.

[93] Kritis, A. A., Stamoula, E. G., Paniskaki, K. A., and Vavilis, T. D. 2015. Researching glutamate - induced cytotoxicity in different cell lines: a comparative/collective analysis/study. *Frontiers in cellular neuroscience* 9, 91.

[94] Kuznetsov, A. V., Janakiraman, M., Margreiter, R., and Troppmair, J. 2004. Regulating cell survival by controlling cellular energy production: novel functions for ancient signaling pathways? *FEBS letters* 577, 1-2, 1–4.

[95] Lackner, L. L. 2014. Shaping the dynamic mitochondrial network. *BMC biology* 12, 35.

[96] Lackner, L. L. and Nunnari, J. M. 2009. The molecular mechanism and cellular functions of mitochondrial division. *Biochimica et biophysica acta* 1792, 12, 1138–1144.

[97] Landshamer, S., Hoehn, M., Barth, N., Duvezin-Caubet, S., Schwake, G., Tobaben, S., Kazhdan, I., Becattini, B., Zahler, S., Vollmar, A., Pellecchia, M., Reichert, A., Plesnila, N., Wagner, E., and Culmsee, C. 2008. Bid-induced release of AIF from mitochondria causes immediate neuronal cell death. *Cell death and differentiation* 15, 10, 1553–1563.

[98] Lavorato, M., Iyer, V. R., Dewight, W., Cupo, R. R., Debattisti, V., Gomez, L., La Fuente, S. de, Zhao, Y.-T., Valdivia, H. H., Hajnóczky, G., and Franzini-Armstrong, C. 2017. Increased mitochondrial nanotunneling activity, induced by calcium imbalance, affects intermitochondrial matrix exchanges. *Proceedings of the National Academy of Sciences of the United States of America* 114, 5, E849-E858.

[99] Lemasters, J. J., Nieminen, A.-L., Qian, T., Trost, L. C., Elmore, S. P., Nishimura, Y., Crowe, R. A., Cascio, W. E., Bradham, C. A., Brenner, D. A., and Herman, B. 1998. The mitochondrial permeability transition in cell death: a common mechanism in necrosis, apoptosis and autophagy. *Biochimica et Biophysica Acta (BBA) - Bioenergetics* 1366, 1-2, 177–196.

[100] Lewinska, A., Klukowska-Rötzler, J., Deregowska, A., Adamczyk-Grochala, J., and Wnuk, M. 2019. c-Myc activation promotes cofilin-mediated F-actin cytoskeleton remodeling and telomere homeostasis as a response to oxidant-based DNA damage in medulloblastoma cells. *Redox biology* 24, 101163.

[101] Li, G., Zhou, J., Budhraja, A., Hu, X., Chen, Y., Cheng, Q., Liu, L., Zhou, T., Li, P., Liu, E., and Gao, N. 2015. Mitochondrial translocation and interaction of cofilin and Drp1 are required for erucin-induced mitochondrial fission and apoptosis. *Oncotarget* 6, 3, 1834–1849.

[102] Li, S., Xu, S., Roelofs, B. A., Boyman, L., Lederer, W. J., Sesaki, H., and Karbowski, M. 2015. Transient assembly of F-actin on the outer mitochondrial membrane contributes to mitochondrial fission. *The Journal of cell biology* 208, 1, 109–123.

[103] Liao, Y., Hao, Y., Chen, H., He, Q., Yuan, Z., and Cheng, J. 2015. Mitochondrial calcium uniporter protein MCU is involved in oxidative stress-induced cell death. *Protein & cell* 6, 6, 434–442.

[104] Liesa, M., Palacín, M., and Zorzano, A. 2009. Mitochondrial dynamics in mammalian health and disease. *Physiological reviews* 89, 3, 799–845.

[105] Lin, M. T. and Beal, M. F. 2006. Mitochondrial dysfunction and oxidative stress in neurodegenerative diseases. *Nature* 443, 7113, 787–795.

[106] Liu, T., Wang, F., LePochat, P., Woo, J.-A. A., Bukhari, M. Z., Hong, K. W., Trotter, C., and Kang, D. E. 2017. Cofilin-mediated Neuronal Apoptosis via p53 Translocation and PLD1 Regulation. *Scientific reports* 7, 1, 11532.

[107] Luo, S., Uehara, H., and Shacter, E. 2014. Taurine chloramine-induced inactivation of cofilin protein through methionine oxidation. *Free radical biology & medicine* 75, 84–94.

[108] Maciver, S. K. and Weeds, A. G. 1994. Actophorin preferentially binds monomeric ADP-Actin over ATP-bound actin: consequences for cell locomotion. *FEBS letters* 347, 2-3, 251–256.

[109] Mai, S., Klinkenberg, M., Auburger, G., Bereiter-Hahn, J., and Jendrach, M. 2010. Decreased expression of Drp1 and Fis1 mediates mitochondrial elongation in

senescent cells and enhances resistance to oxidative stress through PINK1. *Journal of cell science* 123, 6, 917–926.

[110] Mangione, M. C. and Gould, K. L. 2019. Molecular form and function of the cytokinetic ring. *Journal of cell science* 132, 12.

[111] Manor, U., Bartholomew, S., Golani, G., Christenson, E., Kozlov, M., Higgs, H., Spudich, J., and Lippincott-Schwartz, J. 2015. A mitochondria-anchored isoform of the actin-nucleating spire protein regulates mitochondrial division. *eLife* 4.

[112] Mattson, M. P. 2007. Calcium and neurodegeneration. *Aging cell* 6, 3, 337–350.

[113] Mattson, M. P., Gleichmann, M., and Cheng, A. 2008. Mitochondria in neuroplasticity and neurological disorders. *Neuron* 60, 5, 748–766.

[114] Miller, D. M., Thomas, S. D., Islam, A., Muench, D., and Sedoris, K. 2012. c-Myc and cancer metabolism. *Clinical cancer research : an official journal of the American Association for Cancer Research* 18, 20, 5546–5553.

[115] Minamide, L. S., Maiti, S., Boyle, J. A., Davis, R. C., Coppinger, J. A., Bao, Y., Huang, T. Y., Yates, J., Bokoch, G. M., and Bamburg, J. R. 2010. Isolation and characterization of cytoplasmic cofilin-actin rods. *The Journal of biological chemistry* 285, 8, 5450–5460.

[116] Minamide, L. S., Striegl, A. M., Boyle, J. A., Meberg, P. J., and Bamburg, J. R. 2000. Neurodegenerative stimuli induce persistent ADF/cofilin-actin rods that disrupt distal neurite function. *Nature cell biology* 2, 9, 628–636.

[117] Mitchison, T. J. and Cramer, L. P. 1996. Actin-based cell motility and cell locomotion. *Cell* 84, 3, 371–379.

[118] Mizuno, K. 2013. Signaling mechanisms and functional roles of cofilin phosphorylation and dephosphorylation. *Cellular signalling* 25, 2, 457–469.

[119] Moore, A. S. and Holzbaur, E. L. F. 2018. Mitochondrial-cytoskeletal interactions: dynamic associations that facilitate network function and remodeling. *Current Opinion in Physiology* 3, 94–100.

[120] Moore, A. S., Wong, Y. C., Simpson, C. L., and Holzbaur, E. L. F. 2016. Dynamic actin cycling through mitochondrial subpopulations locally regulates the fission-fusion balance within mitochondrial networks. *Nature communications* 7, 12886.

[121] Morimoto, B. H. and Koshland, D. E. 1990. Induction and expression of long- and short-term neurosecretory potentiation in a neural cell line. *Neuron* 5, 6, 875–880.

[122] Moriyama, K., Iida, K., and Yahara, I. 1996. Phosphorylation of Ser-3 of cofilin regulates its essential function on actin. *Genes Cells* 1, 1, 73–86.

[123] Munsie, L., Caron, N., Atwal, R. S., Marsden, I., Wild, E. J., Bamburg, J. R., Tabrizi, S. J., and Truant, R. 2011. Mutant huntingtin causes defective actin remodeling during stress: defining a new role for transglutaminase 2 in neurodegenerative disease. *Human molecular genetics* 20, 10, 1937–1951.

[124] Munsie, L. N., Desmond, C. R., and Truant, R. 2012. Cofilin nuclear-cytoplasmic shuttling affects cofilin-actin rod formation during stress. *Journal of cell science* 125, Pt 17, 3977–3988.

[125] Munsie, L. N. and Truant, R. 2012. The role of the cofilin-actin rod stress response in neurodegenerative diseases uncovers potential new drug targets. *Bioarchitecture* 2, 6, 204–208.

[126] Murphy, T. H., Schnaar, R. L., and Coyle, J. T. 1990. Immature cortical neurons are uniquely sensitive to glutamate toxicity by inhibition of cystine uptake. *The FASEB Journal* 4, 6, 1624–1633.

[127] Neitemeier, S., Jelinek, A., Laino, V., Hoffmann, L., Eisenbach, I., Eying, R., Ganjam, G. K., Dolga, A. M., Oppermann, S., and Culmsee, C. 2017. BID links ferroptosis to mitochondrial cell death pathways. *Redox biology* 12, 558–570.

[128] Nemethova, M., Auinger, S., and Small, J. V. 2008. Building the actin cytoskeleton: filopodia contribute to the construction of contractile bundles in the lamella. *The Journal of cell biology* 180, 6, 1233–1244.

[129] Niwa, R., Nagata-Ohashi, K., Takeichi, M., Mizuno, K., and Uemura, T. 2002. Control of actin reorganization by Slingshot, a family of phosphatases that dephosphorylate ADF/cofilin. *Cell* 108, 2, 233–246.

[130] Nunnari, J. and Suomalainen, A. 2012. Mitochondria: in sickness and in health. *Cell* 148, 6, 1145–1159.

[131] Olesen, J. and Leonardi, M. 2003. The burden of brain diseases in Europe. *European journal of neurology* 10, 5, 471–477.

[132] Olney, J. W. 1969. Brain lesions, obesity, and other disturbances in mice treated with monosodium glutamate. *Science (New York, N.Y.)* 164, 3880, 719–721.

[133] Ordonez, D. G., Lee, M. K., and Feany, M. B. 2018. α-synuclein Induces Mitochondrial Dysfunction through Spectrin and the Actin Cytoskeleton. *Neuron* 97, 1, 108-124.e6.

[134] Pfannstiel, J., Cyrklaff, M., Habermann, A., Stoeva, S., Griffiths, G., Shoeman, R., and Faulstich, H. 2001. Human cofilin forms oligomers exhibiting actin bundling activity. *The Journal of biological chemistry* 276, 52, 49476–49484.

[135] Posadas, I., Pérez-Martínez, F. C., Guerra, J., Sánchez-Verdú, P., and Ceña, V. 2012. Cofilin activation mediates Bax translocation to mitochondria during excitotoxic neuronal death. *Journal of neurochemistry* 120, 4, 515–527.

[136] Qiu, Y., Chen, W. Y., Wang, Z. Y., Liu, F., Wei, M., Ma, C., and Huang, Y. G. 2016. Simvastatin Attenuates Neuropathic Pain by Inhibiting the RhoA/LIMK/Cofilin Pathway. *Neurochemical research* 41, 9, 2457–2469.

[137] Raffaello, A., Mammucari, C., Gherardi, G., and Rizzuto, R. 2016. Calcium at the Center of Cell Signaling: Interplay between Endoplasmic Reticulum, Mitochondria, and Lysosomes. *Trends in biochemical sciences* 41, 12, 1035–1049.

[138] Ramabhadran, V., Korobova, F., Rahme, G. J., and Higgs, H. N. 2011. Splice variant-specific cellular function of the formin INF2 in maintenance of Golgi architecture. *Molecular biology of the cell* 22, 24, 4822–4833.

[139] Rehklau, K., Gurniak, C. B., Conrad, M., Friauf, E., Ott, M., and Rust, M. B. 2012. ADF/cofilin proteins translocate to mitochondria during apoptosis but are not generally required for cell death signaling. *Cell death and differentiation* 19, 6, 958–967.

[140] Rehklau, K., Hoffmann, L., Gurniak, C. B., Ott, M., Witke, W., Scorrano, L., Culmsee, C., and Rust, M. B. 2017. Cofilin1-dependent actin dynamics control DRP1-mediated mitochondrial fission. *Cell death & disease* 8, 10, e3063.

[141] Revenu, C., Athman, R., Robine, S., and Louvard, D. 2004. The co-workers of actin filaments: from cell structures to signals. *Nature reviews. Molecular cell biology* 5, 8, 635–646.

[142] Rogers, G. W., Brand, M. D., Petrosyan, S., Ashok, D., Elorza, A. A., Ferrick, D. A., and Murphy, A. N. 2011. High Throughput Microplate Respiratory Measurements Using Minimal Quantities Of Isolated Mitochondria. *PloS one* 6, 7, e21746.

[143] Ruiz, A., Matute, C., and Alberdi, E. 2010. Intracellular Ca2+ release through ryanodine receptors contributes to AMPA receptor-mediated mitochondrial dysfunction and ER stress in oligodendrocytes. *Cell death & disease* 1, e54.

[144] Rust, M. B. 2015. ADF/cofilin: a crucial regulator of synapse physiology and behavior. *Cellular and molecular life sciences : CMLS* 72, 18, 3521–3529.

[145] Rust, M. B., Gurniak, C. B., Renner, M., Vara, H., Morando, L., Görlich, A., Sassoè-Pognetto, M., Banchaabouchi, M. A., Giustetto, M., Triller, A., Choquet, D., and Witke, W. 2010. Learning, AMPA receptor mobility and synaptic plasticity depend on n-cofilin-mediated actin dynamics. *The EMBO journal* 29, 11, 1889–1902.

[146] Salgo, M. G., Stone, K., Squadrito, G. L., Battista, J. R., and Pryor, W. A. 1995. Peroxynitrite causes DNA nicks in plasmid pBR322. *Biochemical and biophysical research communications* 210, 3, 1025–1030.

[147] Schmitt, S., Saathoff, F., Meissner, L., Schropp, E.-M., Lichtmannegger, J., Schulz, S., Eberhagen, C., Borchard, S., Aichler, M., Adamski, J., Plesnila, N., Rothenfusser, S., Kroemer, G., and Zischka, H. 2013. A semi-automated method for isolating functionally intact mitochondria from cultured cells and tissue biopsies. *Analytical biochemistry* 443, 1, 66–74.

[148] Scott, I. and Youle, R. J. 2010. Mitochondrial fission and fusion. *Essays in biochemistry* 47, 85–98.

[149] Seiler, A., Schneider, M., Förster, H., Roth, S., Wirth, E. K., Culmsee, C., Plesnila, N., Kremmer, E., Rådmark, O., Wurst, W., Bornkamm, G. W., Schweizer, U., and Conrad, M. 2008. Glutathione peroxidase 4 senses and translates oxidative stress into 12/15-lipoxygenase dependent- and AIF-mediated cell death. *Cell metabolism* 8, 3, 237–248.

[150] Shirlee Tan, B. S. P., David Schubert, B. S. P., and Pamela Maher, B. S. P. 2001. Oxytosis: A Novel Form of Programmed Cell Death. *CTMC* 1, 6, 497–506.

[151] Shu, L., Chen, B., Chen, B., Xu, H., Wang, G., Huang, Y., Zhao, Y., Gong, H., Jiang, M., Chen, L., Liu, X., and Wang, Y. 2018. Brain ischemic insult induces cofilin rod formation leading to synaptic dysfunction in neurons. *Journal of cerebral blood flow and metabolism : official journal of the International Society of Cerebral Blood Flow and Metabolism*, 271678X18785567.

[152] Skeberdis, V. A., Lan, J.-y., Opitz, T., Zheng, X., Bennett, M. V.L., and Zukin, R.S. 2001. mGluR1-mediated potentiation of NMDA receptors involves a rise in intracellular calcium and activation of protein kinase C. *Neuropharmacology* 40, 7, 856–865.

[153] Song, Z., Ghochani, M., McCaffery, J. M., Frey, T. G., and Chan, D. C. 2009. Mitofusins and OPA1 mediate sequential steps in mitochondrial membrane fusion. *Molecular biology of the cell* 20, 15, 3525–3532.

[154] Stanika, R. I., Pivovarova, N. B., Brantner, C. A., Watts, C. A., Winters, C. A., and Andrews, S. B. 2009. Coupling diverse routes of calcium entry to mitochondrial dysfunction and glutamate excitotoxicity. *Proceedings of the National Academy of Sciences of the United States of America* 106, 24, 9854–9859.

[155] Stockert, J. C., Horobin, R. W., Colombo, L. L., and Blázquez-Castro, A. 2018. Tetrazolium salts and formazan products in Cell Biology: Viability assessment, fluorescence imaging, and labeling perspectives. *Acta histochemica* 120, 3, 159–167.

[156] Südhof, T. C. 2018. Towards an Understanding of Synapse Formation. *Neuron* 100, 2, 276–293.

[157] Sungur, A. Ö., Stemmler, L., Wöhr, M., and Rust, M. B. 2018. Impaired Object Recognition but Normal Social Behavior and Ultrasonic Communication in Cofilin1 Mutant Mice. *Frontiers in behavioral neuroscience* 12, 25.

[158] Swamy, M., Sirajudeen, K. N. S., and Chandran, G. 2009. Nitric oxide (NO), citrulline-NO cycle enzymes, glutamine synthetase, and oxidative status in kainic acid-mediated excitotoxicity in rat brain. *Drug and chemical toxicology* 32, 4, 326–331.

[159] Tilve, S., Difato, F., and Chieregatti, E. 2015. Cofilin 1 activation prevents the defects in axon elongation and guidance induced by extracellular alpha-synuclein. *Scientific reports* 5, 16524.

[160] Tobaben, S., Grohm, J., Seiler, A., Conrad, M., Plesnila, N., and Culmsee, C. 2011. Bid-mediated mitochondrial damage is a key mechanism in glutamate-induced oxidative stress and AIF-dependent cell death in immortalized HT-22 hippocampal neurons. *Cell death and differentiation* 18, 2, 282–292.

[161] Tojkander, S., Gateva, G., and Lappalainen, P. 2012. Actin stress fibers--assembly, dynamics and biological roles. *Journal of cell science* 125, Pt 8, 1855–1864.

[162] Traaseth, N., Elfering, S., Solien, J., Haynes, V., and Giulivi, C. 2004. Role of calcium signaling in the activation of mitochondrial nitric oxide synthase and citric acid cycle. *Biochimica et biophysica acta* 1658, 1-2, 64–71.

[163] Vander Heiden, M. G., Cantley, L. C., and Thompson, C. B. 2009. Understanding the Warburg effect: the metabolic requirements of cell proliferation. *Science (New York, N.Y.)* 324, 5930, 1029–1033.

[164] Vartiainen, M. K., Mustonen, T., Mattila, P. K., Ojala, P. J., Thesleff, I., Partanen, J., and Lappalainen, P. 2002. The three mouse actin-depolymerizing factor/cofilins evolved to fulfill cell-type-specific requirements for actin dynamics. *Molecular biology of the cell* 13, 1, 183–194.

[165] Vila, M. and Przedborski, S. 2003. Targeting programmed cell death in neurodegenerative diseases. *Nature reviews. Neuroscience* 4, 5, 365–375.

[166] Vincent, A. E., Ng, Y. S., White, K., Davey, T., Mannella, C., Falkous, G., Feeney, C., Schaefer, A. M., McFarland, R., Gorman, G. S., Taylor, R. W., Turnbull, D. M., and

Picard, M. 2016. The Spectrum of Mitochondrial Ultrastructural Defects in Mitochondrial Myopathy. *Scientific reports* 6, 30610.

[167] Vincent, A. E., Turnbull, D. M., Eisner, V., Hajnóczky, G., and Picard, M. 2017. Mitochondrial Nanotunnels. *Trends in cell biology* 27, 11, 787–799.

[168] Wabnitz, G. H., Goursot, C., Jahraus, B., Kirchgessner, H., Hellwig, A., Klemke, M., Konstandin, M. H., and Samstag, Y. 2010. Mitochondrial translocation of oxidized cofilin induces caspase-independent necrotic-like programmed cell death of T cells. *Cell death & disease* 1, e58.

[169] Wang, C., Li, Z., Lu, Y., Du, R., Katiyar, S., Yang, J., Fu, M., Leader, J. E., Quong, A., Novikoff, P. M., and Pestell, R. G. 2006. Cyclin D1 repression of nuclear respiratory factor 1 integrates nuclear DNA synthesis and mitochondrial function. *Proceedings of the National Academy of Sciences of the United States of America* 103, 31, 11567–11572.

[170] Wang, L., Duan, Q., Wang, T., Ahmed, M., Zhang, N., Li, Y., Li, L., and Yao, X. 2015. Mitochondrial Respiratory Chain Inhibitors Involved in ROS Production Induced by Acute High Concentrations of Iodide and the Effects of SOD as a Protective Factor. *Oxidative medicine and cellular longevity* 2015, 217670.

[171] Wang, Y., Nartiss, Y., Steipe, B., McQuibban, G. A., and Kim, P. K. 2012. ROS-induced mitochondrial depolarization initiates PARK2/PARKIN-dependent mitochondrial degradation by autophagy. *Autophagy* 8, 10, 1462–1476.

[172] Welch, M. D., Mallavarapu, A., Rosenblatt, J., and Mitchison, T. J. 1997. Actin dynamics in vivo. *Current opinion in cell biology* 9, 1, 54–61.

[173] WHO. 2018. Global Health Estimates 2016: Deaths by Cause, Age, Sex, by Country and by Region, 2000-2016. *World Health Organization*.

[174] Williams, G. S. B., Boyman, L., and Lederer, W. J. 2015. Mitochondrial calcium and the regulation of metabolism in the heart. *Journal of molecular and cellular cardiology* 78, 35–45.

[175] Wioland, H., Guichard, B., Senju, Y., Myram, S., Lappalainen, P., Jégou, A., and Romet-Lemonne, G. 2017. ADF/Cofilin Accelerates Actin Dynamics by Severing

Filaments and Promoting Their Depolymerization at Both Ends. *Current biology : CB* 27, 13, 1956-1967.e7.

[176] Wolf, M., Zimmermann, A.-M., Görlich, A., Gurniak, C. B., Sassoè-Pognetto, M., Friauf, E., Witke, W., and Rust, M. B. 2015. ADF/Cofilin Controls Synaptic Actin Dynamics and Regulates Synaptic Vesicle Mobilization and Exocytosis. *Cerebral cortex (New York, N.Y. : 1991)* 25, 9, 2863–2875.

[177] Won, S. J., Minnella, A. M., Wu, L., Eun, C. H., Rome, E., Herson, P. S., Shaw, A. E., Bamburg, J. R., and Swanson, R. A. 2018. Cofilin-actin rod formation in neuronal processes after brain ischemia. *PloS one* 13, 10, e0198709.

[178] Wrogemann, K. and Pena, S. D. 1976. Mitochondrial calcium overload: A general mechanism for cell-necrosis in muscle diseases. *Lancet (London, England)* 1, 7961, 672–674.

[179] Wu, J., Prole, D. L., Shen, Y., Lin, Z., Gnanasekaran, A., Liu, Y., Chen, L., Zhou, H., Chen, S. R. W., Usachev, Y. M., Taylor, C. W., and Campbell, R. E. 2014. Red fluorescent genetically encoded Ca2+ indicators for use in mitochondria and endoplasmic reticulum. *The Biochemical journal* 464, 1, 13–22.

[180] Xiong, Z.-G., Zhu, X.-M., Chu, X.-P., Minami, M., Hey, J., Wei, W.-L., MacDonald, J. F., Wemmie, J. A., Price, M. P., Welsh, M. J., and Simon, R. P. 2004. Neuroprotection in ischemia: blocking calcium-permeable acid-sensing ion channels. *Cell* 118, 6, 687–698.

[181] Xu, Q., Huff, L. P., Fujii, M., and Griendling, K. K. 2017. Redox regulation of the actin cytoskeleton and its role in the vascular system. *Free radical biology & medicine* 109, 84–107.

[182] Yamauchi, M., Omote, K., and Ninomiya, T. 1998. Direct evidence for the role of nitric oxide on the glutamate-induced neuronal death in cultured cortical neurons. *Brain Research* 780, 2, 253–259.

[183] Yang, J.-L., Sykora, P., Wilson, D. M., Mattson, M. P., and Bohr, V. A. 2011. The excitatory neurotransmitter glutamate stimulates DNA repair to increase neuronal resiliency. *Mechanisms of ageing and development* 132, 8-9, 405–411.

[184] Yang, L., Long, Q., Liu, J., Tang, H., Li, Y., Bao, F., Qin, D., Pei, D., and Liu, X. 2015. Mitochondrial fusion provides an 'initial metabolic complementation' controlled by mtDNA. *Cellular and molecular life sciences : CMLS* 72, 13, 2585–2598.

[185] Yang, N., Higuchi, O., Ohashi, K., Nagata, K., Wada, A., Kangawa, K., Nishida, E., and Mizuno, K. 1998. Cofilin phosphorylation by LIM-kinase 1 and its role in Rac-mediated actin reorganization. *Nature* 393, 6687, 809–812.

[186] Zamzami, N., Métivier, D., and Kroemer, G. 2000. Quantitation of Mitochondrial Transmembrane Potential in Cells and in Isolated Mitochondria. In *Apoptosis*, J. C. Reed, Ed. Methods in Enzymology v. 322. Academic Press, San Diego, 208–213. DOI=10.1016/S0076-6879(00)22021-1.

[187] Zeller, K. I., Jegga, A. G., Aronow, B. J., O'Donnell, K. A., and Dang, C. V. 2003. An integrated database of genes responsive to the Myc oncogenic transcription factor: identification of direct genomic targets. *Genome biology* 4, 10, R69.

[188] Zhou, Q., Homma, K. J., and Poo, M.-m. 2004. Shrinkage of dendritic spines associated with long-term depression of hippocampal synapses. *Neuron* 44, 5, 749–757.

[189] Zorova, L. D., Popkov, V. A., Plotnikov, E. Y., Silachev, D. N., Pevzner, I. B., Jankauskas, S. S., Babenko, V. A., Zorov, S. D., Balakireva, A. V., Juhaszova, M., Sollott, S. J., and Zorov, D. B. 2018. Mitochondrial membrane potential. *Analytical biochemistry* 552, 50–59.

10 Index of tables

11 Index of figures

12 Presentations and publications

12.1 Poster Presentations

- **Oxidative stress activates mechanisms of regulated necrosis via CYLD**

  L. Hoffmann, I. Eisenbach, GK. Ganjam, C. Culmsee, DPhG Meeting Munich, Germany, 4.10.16-7.10.16

- **CRISPR/Cas9 Bid knockout reveals a key role for BID-mediated mitochondrial damage in ferroptosis**

  A. Jelinek, S. Neitemeier, L. Hoffmann, GK. Ganjam, C. Culmsee, DPhG Meeting Munich, Germany, 4.10.16-7.10.16

- **CRISPR/Cas9 Bid knockout demonstrates a key role for BID as a molecular link in paradigms of oxytosis & ferroptosis**

  A. Jelinek, S. Neitemeier, L. Hoffmann, GK. Ganjam, C. Culmsee, NEUROSCIENCE 2016, San Diego, USA, 12.11-16.11.2016

- **Oxidative stress activates mechanisms of regulated necrosis and mitochondrial demise via CYLD**

  I. Eisenbach, L. Hoffmann, G. K. Ganjam, C. Culmsee, DGPT Meeting Heidelberg, Germany, 6.3.2017-9.3.2017

- **The impact of cofilin1 on mitochondrial dynamics and function**

  L. Hoffmann, K. Rehklau, J. Grohm, M. B. Rust, C. Culmsee, DGPT Meeting Heidelberg, Germany, 6.3.2017-9.3.2017

- **Oxidative stress activates mechanisms of regulated necrosis and mitochondrial demise via CYLD**

  I. Eisenbach, L. Hoffmann, G. K. Ganjam, C. Culmsee, EUROMIT Köln 2017, Germany, 11.6.-15.6.2017

- **The impact of cofilin1 on mitochondrial dynamics and function**

L. Hoffmann, K. Rehklau, J. Grohm, M. B. Rust, C. Culmsee, EUROMIT Köln 2017, Germany, 11.6.-15.6.2017

- **Oxidative stress activates mechanisms of regulated necrosis and mitochondrial demise via CYLD**

  I. Eisenbach, L. Hoffmann, G. K. Ganjam, C. Culmsee, ECDO Meeting Leuven 2017, Belgium, 27.9.-29.9.2017

- **The impact of the actin-regulating protein cofilin1 on mitochondrial dynamics and resilience in neuronal HT22 cells**

  L. Hoffmann, K. Rehklau, J. Grohm, M. B. Rust, C. Culmsee, NEUROSCIENCE 2017, Washington D.C. (USA), 11.11.-15.11.2017

- **The impact of the actin-binding protein cofilin1 on mitochondrial dynamics and function**

  L. Hoffmann, K. Rehklau, J. Grohm, M. B. Rust, C. Culmsee, GRK2213 Retreat 2018, Hannoversch Münden, Germany, 17.1.-18.1.2018

- **The impact of the actin-regulating protein Cofilin1 on mitochondrial dynamics and resilience in neuronal HT22 cells and primary mouse neurons**

  L. Hoffmann, K. Rehklau, M. B. Rust, C. Culmsee, GBM Symposium, Marburg, Germany, 20.9.-22.9.2018

- **CYLD links mechanisms of necroptosis to mitochondrial pathways of ferroptosis in neuronal cells**

  I. Eisenbach, L. Hoffmann, G. K. Ganjam, l. Heyder, M. Daude, W. Diederich, C. Culmsee, Targeting mitochondria, Berlin, Germany, 23.10.-25.10.2018

- **The impact of the actin-regulating protein Cofilin1 on mitochondrial dynamics and resilience in neuronal HT22 cells and primary mouse neurons**

  L. Hoffmann, K. Rehklau, M. B. Rust, C. Culmsee, Targeting mitochondria, Berlin, Germany 23.10.-25.10.2018

- **The impact of the actin-binding protein cofilin1 on mitochondrial dynamics and function**

  L. Hoffmann, K. Rehklau, J. Grohm, M. B. Rust, C. Culmsee, GRK2213 Retreat 2019, Hannoversch Münden, Germany, 15.1.-17.1.2019

- **The impact of the actin-regulating protein Cofilin1 on mitochondrial dynamics and resilience in neuronal HT22 cells and primary mouse neurons**

  L. Hoffmann, K. Rehklau, M. B. Rust, C. Culmsee, International GRK2213 PhD Symposium, Marburg, Germany, 2.-4.04.2019

- **CYLD depletion leads to a metabolic shift in neuronal cells and maintains mitochondrial integrity in a model of ferroptosis**

  I. Eisenbach, L. Hoffmann, G. K. Ganjam, l. Heyder, M. Daude, W. Diederich, C. Culmsee, Targeting mitochondria, Berlin, Germany, 27.10.-29.10.2019

- **Role of the actin-binding proteins cofilin1 and inverted-formin 2 (INF2) on mitochondrial and cellular resilience**

  L. Hoffmann, K. Rehklau, M. B. Rust, C. Culmsee, Targeting mitochondria, Berlin, Germany, 27.10.-29.10.2019

- **The role of the actin-binding protein cofilin1 on mitochondrial morphology and cellular resilience**

  L. Hoffmann, M. B. Rust, C. Culmsee, Mitochondria and Metabolism in Health and Disease, Suzhou, China, 11.11.-15.11.19

12.2 Oral Presentations

- **Role of the actin-regulating protein cofilin1 in mitochondrial and cellular resilience**

  International GBM Symposium, Marburg, Germany, 20.9.-22.9.2018

- **Role of the actin-binding proteins cofilin1 and INF2 on mitochondrial dynamics and cellular resilience**

  Kickoff Meeting of the ACAciA Consortium, Marburg, Germany, 25.06.-26.06.2019

12.3 Publications

- Neitemeier S*, Jelinek A*, Laino V, **Hoffmann L**, Eisenbach I, Eying R, Ganjam GK, Dolga AM, Oppermann S, Culmsee C. BID links ferroptosis to mitochondrial cell death pathways. *Redox Biology* (2017)

- Rehklau K*, **Hoffmann L***, Gurniak CB, Ott M, Witke W, Scorrano L, Culmsee C, Rust MB. Cofilin1-dependent actin dynamics control DRP1-mediated mitochondrial fission. *Cell death and Disease* (2017)

- Ganjam GK*, Terpolilli NA*, Diemert S*, Eisenbach I, **Hoffmann L**, Reuther C, Herden C, Roth J, Plesnila N, Culmsee C. Cylindromatosis mediates neuronal cell death *in vitro* and *in vivo*. *Cell death and Differentiation* (2018)

- **Hoffmann L**, Rust MB, Culmsee C. Actin(g) on mitochondria - a role for cofilin1 in neuronal cell death pathways. *Biological Chemistry* (2019). (Review)

- Keller I*, **Hoffmann L***, Ganjam GK, Heyder L, Daude M, Zhu C, Dobson-Stone C, Diederich W, Plesnila N, Culmsee C. CYLD depletion prevents mitochondrial damage in ferroptosis by inhibiting RIP1 activation and through metabolic re-programming. *(In preparation)*

- **Hoffmann L**, Waclawczyk MS, Hanschmann EM, Rust MB, Culmsee C. Downregulation of the actin-binding protein cofilin1 provides neuroprotection in models of oxidative stress induced cell death. *(In preparation)*

*contributed equally

13 Acknowledgements/Danksagung

Die Seiten 157 bis 158 enthalten personenbezogene Daten und sind deshalb in der elektronischen Version nicht enthalten.

14 Curriculum vitae

Die Seite 159 enthält personenbezogene Daten und ist deshalb in der elektronischen Version nicht enthalten.